Final Report

FDOT Contract No.: BDV31-977-82
UF Contract No.: 0057299

Sinkhole Detection with 3-D Full Elastic Seismic Waveform Tomography

Principal Investigators: Michael C. McVay, Ph.D. (PI)
Khiem Tran, Ph.D. (Co-PI)
Scott Wasman, Ph.D. (Co-PI)

Researcher: Majid Mirzanejad

Department of Civil and Coastal Engineering
Engineering School of Sustainable Infrastructure and Environment
University of Florida
P.O. Box 116580
Gainesville, Florida 32611-6580

Developed for the

David Horhota, Ph.D., P.E., Project Manager

June 2020

DISCLAIMER

The opinions, findings, and conclusions expressed in this publication are those of the authors and not necessarily those of the Florida Department of Transportation or the U.S. Department of Transportation.

Prepared in cooperation with the State of Florida Department of Transportation and the U.S. Department of Transportation.

SI (MODERN METRIC) CONVERSION FACTORS (from FHWA)

APPROXIMATE CONVERSIONS TO SI UNITS

SYMBOL	WHEN YOU KNOW	MULTIPLY BY	TO FIND	SYMBOL
LENGTH				
in	inches	25.4	millimeters	mm
ft	feet	0.305	meters	m
yd	yards	0.914	meters	m
mi	miles	1.61	kilometers	km

SYMBOL	WHEN YOU KNOW	MULTIPLY BY	TO FIND	SYMBOL
AREA				
in^2	square inches	645.2	square millimeters	mm^2
ft^2	square feet	0.093	square meters	m^2
yd^2	square yard	0.836	square meters	m^2
ac	acres	0.405	hectares	ha
mi^2	square miles	2.59	square kilometers	km^2

SYMBOL	WHEN YOU KNOW	MULTIPLY BY	TO FIND	SYMBOL
VOLUME				
fl oz	fluid ounces	29.57	milliliters	mL
gal	gallons	3.785	liters	L
ft^3	cubic feet	0.028	cubic meters	m^3
yd^3	cubic yards	0.765	cubic meters	m^3
NOTE: volumes greater than 1000 L shall be shown in m^3				

SYMBOL	WHEN YOU KNOW	MULTIPLY BY	TO FIND	SYMBOL
MASS				
oz	ounces	28.35	grams	g
lb	pounds	0.454	kilograms	kg
T	short tons (2000 lb)	0.907	megagrams (or "metric ton")	Mg (or "t")

SYMBOL	WHEN YOU KNOW	MULTIPLY BY	TO FIND	SYMBOL
TEMPERATURE (exact degrees)				
°F	Fahrenheit	5 (F-32)/9 or (F-32)/1.8	Celsius	°C

SYMBOL	WHEN YOU KNOW	MULTIPLY BY	TO FIND	SYMBOL
ILLUMINATION				
fc	foot-candles	10.76	lux	lx
fl	foot-Lamberts	3.426	candela/m^2	cd/m^2

SYMBOL	WHEN YOU KNOW	MULTIPLY BY	TO FIND	SYMBOL
FORCE and PRESSURE or STRESS				
Lbf*	poundforce	4.45	newtons	N
kip	kip force	1000	pounds	lbf
lbf/in^2	poundforce per square inch	6.89	kilopascals	kPa

APPROXIMATE CONVERSIONS TO SI UNITS

SYMBOL	WHEN YOU KNOW	MULTIPLY BY	TO FIND	SYMBOL
		LENGTH		
mm	millimeters	0.039	inches	in
m	meters	3.28	feet	ft
m	meters	1.09	yards	yd
km	kilometers	0.621	miles	mi

SYMBOL	WHEN YOU KNOW	MULTIPLY BY	TO FIND	SYMBOL
		AREA		
mm^2	square millimeters	0.0016	square inches	in^2
m^2	square meters	10.764	square feet	ft^2
m^2	square meters	1.195	square yards	yd^2
ha	hectares	2.47	acres	ac
km^2	square kilometers	0.386	square miles	mi^2

SYMBOL	WHEN YOU KNOW	MULTIPLY BY	TO FIND	SYMBOL
		VOLUME		
mL	milliliters	0.034	fluid ounces	fl oz
L	liters	0.264	gallons	gal
m^3	cubic meters	35.314	cubic feet	ft^3
m^3	cubic meters	1.307	cubic yards	yd^3

SYMBOL	WHEN YOU KNOW	MULTIPLY BY	TO FIND	SYMBOL
		MASS		
g	grams	0.035	ounces	oz
kg	kilograms	2.202	pounds	lb
Mg (or "t")	megagrams (or "metric ton")	1.103	short tons (2000 lb)	T

SYMBOL	WHEN YOU KNOW	MULTIPLY BY	TO FIND	SYMBOL
		TEMPERATURE (exact degrees)		
°C	Celsius	1.8C+32	Fahrenheit	°F

SYMBOL	WHEN YOU KNOW	MULTIPLY BY	TO FIND	SYMBOL
		ILLUMINATION		
lx	lux	0.0929	foot-candles	fc
cd/m^2	$candela/m^2$	0.2919	foot-Lamberts	fl

SYMBOL	WHEN YOU KNOW	MULTIPLY BY	TO FIND	SYMBOL
		FORCE and PRESSURE or STRESS		
N	newtons	0.225	poundforce	lbf
kPa	kilopascals	0.145	poundforce per square inch	lbf/in^2

*SI is the symbol for International System of Units. Appropriate rounding should be made to comply with Section 4 of ASTM E380.
(Revised March 2003)

TECHNICAL REPORT DOCUMENTATION PAGE

1. Report No.	2. Government Accession No.	3. Recipient's Catalog No.
4. Title and Subtitle Sinkhole Detection with 3-D Full Elastic Seismic Waveform Tomography		5. Report Date May 2020 6. Performing Organization Code
7. Author(s) Majid Mirzanejad, Khiem T. Tran, Michael C. McVay, and Scott J. Wasman		8. Performing Organization Report No.
9. Performing Organization Name and Address University of Florida – Dept. of Civil and Coastal Engineering Engineering School of Sustainable Infrastructure and Environment 365 Weil Hall – P.O. Box 116580 Gainesville, FL 32611-6580		10. Work Unit No. (TRAIS) 11. Contract or Grant No. BDV31-977-82
12. Sponsoring Agency Name and Address Florida Department of Transportation 605 Suwannee Street, MS 30 Tallahassee, FL 32399		13. Type of Report and Period Covered Final Report 3/1/18 – 5/15/2020 14. Sponsoring Agency Code
15. Supplementary Notes		

16. Abstract

A new 3-D full waveform inversion (FWI) method was developed, optimized, and verified using synthetic and field test data. The goal was to overcome some of the limitations of a previously developed 2-D approach. Particularly, it was expected that the 3-D FWI method could detect out-of-line voids and 3-D features (pinnacles, zones, etc.), be easier to implement for a large volume, and increase overall detection accuracy. To ensure robustness of the developed method, well-known and established techniques for forward modeling and optimization were implemented. Elastic wave equations were solved using a finite difference method implemented in time domain to simulate wave propagation. Boundary truncation techniques of perfectly matched layer (PML) and image technique were used to truncate the testing medium and reduce computational demand. The Gauss-Newton optimization technique was used to minimize the error and update the V_S and V_P model parameters independently. Synthetic tests were carried out to find the best testing configuration and establish maximum void detection depth. These tests revealed optimal receiver-source spacing as equal to the maximum void diameter. Maximum void detection depth was established as 3 times the void diameter from the ground surface. Field verification was carried out at various locations to ensure the 3-D FWI method result validity on noisy field data. Initial tests on a stormwater pipe located at the UF campus proved that the method can successfully be used to detect the depth, direction, and overall shape of the pipe. Further testing at a site in Newberry, FL, showed that the method can detect variable soil-rock layering and identify unknown anomalies. Three shallow voids were detected and verified using SPTs. Overall, there was good agreement between the SPT N-values and inverted results, and the presence of the voids was verified. An attempt was made to extend the void detection depth of the developed method. This was achieved through the application of a modified source to generate more energy at lower frequencies (higher wavelength). The modified source was used at a bridge construction site in Miami, Fl, where a large deep void was detected. Final inversion results showed that using the modified source with the developed method could help increase its void detection capability. Void features including depth and position were successfully detected and characterized. Finally, a novel SPT seismic source method was proposed for the first time. It was based on using SPT device as the source and gathering data with receivers on the ground surface. The SPT seismic method is useful for increasing void detection depth when there is limited access on the surface and the source does not produce enough energy at low frequencies (0-10 Hz). Tests with the SPT seismic approach at the Newberry and Miami, FL sites showed that it can detect shallow voids and very deep voids where there is limited access on the surface (e.g., right of ways). All the results were compared and verified using invasive tests performed at the test site.

17. Key Words	18. Distribution Statement
Full Waveform Inversion, Sinkholes, Anomalies, Shear Wave, Compression Wave, Geophysical, Non-Destructive Testing, Inversion Analysis	No restrictions.

19. Security Classif. (of this report)	20. Security Classif. (of this page)	21. No. of Pages	22. Price
Unclassified	Unclassified	203	

Form DOT F 1700.7 (8-72) Reproduction of completed page authorized

ACKNOWLEDGMENTS

The researchers would like to thank the Florida Department of Transportation (FDOT) for the financial support to carry out this research, as well as the State Materials Office in Gainesville, Florida, for providing access and assisting with many of the field tests (SPT, CPT, and seismic), FDOT's Central Office Geotechnical Group, District 4 Geotechnical Materials Group, as well as Archer-Western and Universal Engineering for Access to the Miami Site.

EXECUTIVE SUMMARY

This research was performed with the goal of developing a 3-D full waveform inversion (FWI) method for the detection of soil-rock layering, 3-D features (e.g., rock pinnacles), as well as anomalies such as voids and pre-collapsed sinkholes using seismic wave data. 3-D simulation and inversion of seismic data can potentially alleviate some of the drawbacks associated with 2-D methods (i.e., out of plane scattering and point source modelling), and hence produce a more accurate result of the subsurface structure. Moreover, using a 2-D grid of sources and receivers on the ground surface can facilitate a more complete data set (e.g. waves out of plane) and, with the computational efforts, will result in a more detailed 3-D view of the underlying features. In addition, collection of all the information of the waveform provides higher resolutions at lower frequencies and reveals more detail of the underlying soil-rock structure.

To incorporate these features, the inversion technique was developed based on a 3-D elastic forward finite difference simulation of 2^{nd} order accuracy in time and space to model wave propagation and the Gauss-Newton optimization technique to minimize the cost function. The cost function defined in the context of this inversion problem was defined as the L2-norm of the residual (difference) of waveforms gathered in the field with that of the simulated data generated through the elastic forward solver. Parameters of interest in the inversion problem are the V_s and V_p velocities of the seismic wave, which are updated cell by cell in an iterative process. The employed optimization method utilizes the information embedded in the second derivative (Hessian) of the cost function and can therefore produce better results compared to methods that only utilize the first derivative (Gradient). Robust boundary truncation techniques (convolutional perfectly matched layer and image technique) were used at the boundaries of the simulated space to absorb incident wave energy and eliminate spurious reflections. Numerical

stability checks for temporal and spatial stability were incorporated to ensure seamless velocity and stress field updates during forward simulation.

To identify the ability of the developed FWI method for subsurface site characterization, synthetic experiments were initially performed for layer and void detection and to establish optimal source-receiver testing configuration as well as determine the maximum void detection depth. The method was expected to provide a detailed 3-D map of the subsurface, including layering features and embedded voids. Synthetic experiments on a realistic model with a variable layering interface suggested that it can be successfully employed in identifying soil-rock layering. Synthetic experiments on the test configuration using a surface-based testing geometry revealed the best receiver and source spacing was equal to the size of the void that was to be detected. For example, a 3-m (10-ft) void could be best detected when a 3-m (10-ft) receiver spacing was used on the ground surface. Any source-receiver spacing less than that only increased data redundancy and did not improve void characterization. Analyses of the void detection depth showed that the method can be used to detect voids as deep as 3 times its size from the surface when used with surface-based test geometry. This means that, for example, a 3-m (10-ft) void can be detected when located up to 9 m (30 ft) from the ground surface.

Finally, field experiments at three sites in Florida were carried out to verify the applicability of the developed 3-D FWI method on noisy data. The first site featured a stormwater pipe beneath an open field on the University of Florida main campus in Gainesville, Florida. The goal was to determine if the 3-D FWI method could detect the depth, direction, and general shape of the pipe. It was subsequently tested on data gathered at a FDOT retention pond located at Newberry, Florida, in a blind class-A prediction. The results suggested that the method

could detect variable soil-rock layering and shallow embedded anomalies. The presence of layering and voids were confirmed using SPTs.

The method was further tested with a large source that produced greater energy at lower frequencies (5-20 Hz). Lower frequency waves are of longer wavelength and can therefore penetrate deeper into materials. This was tested at a bridge construction site in Miami, Florida, where preliminary borings indicated a large void at more than 20-m (66-feet) in depth. The final inverted results revealed a large, non-uniformly shaped void. Comparisons with results of invasive techniques (SPT N-values and sonar images) from the test site validated the method in detecting deep voids using surface testing only.

To improve the capabilities of the FWI method in deep void detection, a novel in-depth source seismic testing approach using the SPT was introduced. The SPT hammer blows were used as an energy source at location of the SPT spoon, generating seismic waves within the subsurface. This approach is particularly useful where surface access is limited (e.g., right of ways) and location of anomaly is unknown. The new method was initially tested at a site in Newberry, Florida, where it detected a deep void (15-m [50-ft] depth). It was subsequently used at a bridge construction site in Miami, Florida. Vertical SPT borings were placed outside of the void area, and the wavefield was detected on the ground surface. The results revealed that the SPT seismic approach can be used to detect voids that would not be encountered with a SPT boring. Inversion results compared with SPT N-values generally matched well throughout the depth and particularly at the void location. The entire data collection process (equipment setup, data collection, and equipment break-down) for each of the test sets can be done in less than 1 day, using a three-person crew. Comparatively, an invasive SPT test with sampling at every 1.5 m (5 ft) can take up to 2 days depending on the site condition and the investigation depth, and

only tests a small volume of material. Overall, the analysis can be expected to take 15-40 hours depending on the test area to complete on a standard desktop computer with 32 cores running at 3.2 GHz and 300 GB of RAM.

TABLE OF CONTENTS

LIST OF FIGURES

Figure page

CHAPTER 1

INTRODUCTION

1.1 Background

Cover collapse and cover subsidence sinkholes are formed due to the spalling, piping, or raveling of the upper sediments (clay, silt, and sands) into cavities or voids within the limestone. They can happen abruptly in a matter of a few hours (cover-collapse) or take several years (cover-subsidence) to occur and are more prevalent in regions with carbonate or evaporitic rock structures. Sinkhole activities in urban settings can cause significant damage to public infrastructure or private property, even leading to loss of life. With increased cost of development and maintenance, there is a great need for efficient and cost-effective methods to accurately image or identify voids and raveling zones beneath the ground surface.

A variety of non-invasive techniques have been developed to image subsurface features such as shallow voids and other anomalies (soft or weak zones or buried objects). The most common techniques are ground penetrating radar (GPR), electrical resistivity tomography (ERT), gravity, and seismic methods. The common concept of these methods for identifying voids lies in the contrast of some properties of the void material with its surrounding features. Each method has its own benefits and drawbacks, as discussed below.

GPR (De Vore, 1998; Bristow and Jol, 2003; Daniels, 2005; Jol, 2008) is one of the most popular non-invasive methods to image subsurface high contrast anomalies. It is based on sending electromagnetic waves into the subsurface using a transmitting antenna and picking up the reflections using a receiving antenna. The transmitting and receiving antennas are usually attached to a single probe and can be used to scan the subsurface quickly and without the need to insert the receiver antenna within the ground. This makes GPR a versatile tool in high traffic

urban environments where there is a need for rapid deployment, as well as in aerial reconnaissance of underground structures in inaccessible environments. The transmitted electromagnetic waves, reflected from the boundaries of anomalies due to their contrasting dielectric properties with the surrounding material, are rapidly displayed on recorded radargrams. These radargrams are usually interpreted to infer subsurface structure and detect voids and other high contrast features.

Generally, the shorter electromagnetic wavelength allows for higher resolution of the GPR image versus seismic methods. However, this comes at the expense of a more limited GPR imaging depth compared to the seismic approach. Moreover, due to a phenomenon known as the skin effect (Hawkins, 1956), electromagnetic radiation rapidly attenuates when propagating in materials with high conductivity, such as water or clay. Thus, GPR is not able to penetrate deep beneath the ground water table or through clay layers (Slob et al., 2010), which generally limits its application to areas of dry subsurface sandy/silty soils. There is also the issue of interpretation of the radargrams. Ringing effects and a lack of robust tomographic methods can lead to discrepancies in the radargrams from one operator to another (Chen and Chow, 2007; Lai et al., 2018).

ERT (Sudha et al., 2009; Cardarelli et al., 2010) is another popular method that can be used to detect underground high contrast anomalies, such as voids. The method is based on the passing of electrical current through the subsurface and measuring the electric potential with an array of electrodes placed on the ground surface, or inside a borehole. Anomalies are highly contrasting due to their higher or lower electrical resistivity compared to the surrounding material, and which is captured by the electric potential in electrode arrays and reflected in the resistivity profiles. The resistivity profile can then be used in an inversion problem to generate an

image of subsurface features. However, the existence of a large volume of rock and soil on top of a deep void masks its presence, and as a result, ERT may only detect shallow voids less than 5-10 m (16-33 ft) depth (Wightman et al., 2003). Note, even within 5-10 m (16-33 ft) depth, local variability of resistivity not associated with sinkholes are very likely and require invasive testing.

Gravity methods (LaFehr, 1980; Paterson and Reeves, 1985; Hansen, 2001) are based on measurements of localized gravity gradients over a test site and used to identify zones of lower or higher gravity values. Gravity measurements are directly related to the soil volume density and can indicate the existence of anomalous low or high subsurface mass. Variability in mass may be due to an empty void, a void filled with lighter or heavier materials (i.e., water, loose soil, or foreign object), a change in the over-lying soil layer thickness, a localized decrease in soil density, or the water table (Greenfield, 1979). Therefore, solely measuring gravity variations cannot verify the main cause of the anomalies in the gravitational field, and more knowledge of the test site is usually required. One way to deal with the uncertainty in gravity data is through the application of time-lapse processing of gravity gradient (DiFrancesco and Talwani, 2002), which allows for the removal of terrain data and enables the analysis to focus only on gravity anomalies that can represent voids or tunnels. Recent research on the gravity gradiometry method using synthetic data suggests that it can be used to detect and characterize elongated voids and tunnels up to 15 m (50 ft) deep (McKenna et al., 2015).

Seismic waves and associated waveforms contain a plethora of information about the medium in which they travel. For instance, buried voids can modulate the frequency content, amplitude and phase of the propagating waveforms, which may be used to detect voids. Actual experimentation with test voids within 5 m (16 ft) of the ground surface show that both body and surface waveforms are affected (Grandjean and Leparoux, 2004). Deeper voids are usually

hidden from surface waves and can only be detected by body waves. The detectability of a void depends on many factors, including the source energy and frequency content, material properties, distance between the void and the receivers, and the ratio of void size to the wavelength of the interacting wave.

Seismic wave-based methods, including refraction tomography (Tran and Hiltunen, 2011) and surface wave approaches like multi-channel analysis of surface waves (MASW; Park et al. 1999), have also been used for anomaly/void detection (Cardarelli et al, 2010; Tran and Hiltunen, 2012; Tran and Sperry, 2018). However, these methods only use a small percentage of the information in the waveform to infer subsurface properties, limiting their ability to provide detailed information of voids. Full waveform inversion (FWI) methods are the most promising way to obtain true 3-D subsurface seismic images for void detection. As documented by Virieux and Operto (2009), the full waveform approach produces higher resolution models of the subsurface structure than approaches that consider only portions of the measured wavefield, such as dispersion curves or first-arrival time. Significant progress on 2-D/3-D FWI methodologies has been made since 2008, for various length scales. They vary from meter-scales (Romdhane et al., 2011; Bretaudeau et al., 2013; Butzer et al., 2013; Fathi et al., 2016; Nguyen and Tran, 2018; Tran et al., 2019; Mirzanejad and Tran, 2019) to km-scales (Ben-Hadj-Ali et al., 2008; Epanomeritakis et al., 2008; Fichtner et al., 2009; Plessix, 2009; Vigh et al., 2011; Warner et al., 2013; Ha et al., 2014; Metivier et al., 2016; Shen et al., 2018).

1.2 Motivation and outline of the study

For the sinkhole detection application, Tran et al. (2013) has shown that the 2-D FWI approach could successfully detect buried voids as well as characterize variable soil-rock layering. However, the 2-D approach requires that the test lines be placed right over the voids. If test lines are off-center of the voids, they will be distorted and shifted, or even invisible,

depending on the distance between the test lines and the voids. Additionally, the 2-D approach does not correctly account for point source modelling and out-of-plane scattering effects. The latter generally require the application of phase and amplitude correction factors. The use of a 3-D FWI approach could eliminate the need for these corrections, as well as detect off-line voids and horizontal variability. In summary, 3-D FWI has the potential of providing a high-resolution 3-D image of the subsurface structure.

Recently, a 3-D Gauss-Newton full-waveform inversion method (3-D GN-FWI) was developed (Tran et al., 2019) and is explained in detail in Chapter 2. It is based on an elastic finite-difference forward model to generate a synthetic wavefield, and a Gauss-Newton approach to minimize the misfit function to extract the material properties on a cellular approach. The Gauss-Newton inversion is well recognized as a robust and effective technique for numerical optimizations of non-linear problems, with faster convergence rates than a traditional gradient method. More importantly, for near-surface imaging, the inverse Hessian matrix used in the Gauss-Newton inversion acts as a weighting function to balance the gradient vector and model updating during the inversion. It reduces the dominancy of Rayleigh waves (less weights for shallow cells) and increases the contribution of body waves in the far-field data (more weights for deeper cells), and thus helps resolve deeper structures. The 3-D GN-FWI method has successfully characterized in-situ soil-rock layering including the existence of soft soil zones. Compared to results of the same field data analyzed by a cross-adjoint 3-D FWI (Nguyen and Tran 2018), S-wave velocity (Vs) profiles from the 3-D GN-FWI are more consistent with SPT N-values (Tran et al., 2019).

In this study, we developed a 3-D GN-FWI method and investigated its capability in detection of soil-rock layering and anomalies (e.g. voids, layering, as well as horizontal

variability – pinnacles, ravel zones, etc.). First, the method was tested on a synthetic dataset obtained from a challenging synthetic model with no embedded voids and variable soil-rock layers. It was then tested in other synthetic studies with an embedded void to find the optimal source/receiver configuration and maximum void detection depth. Subsequently, it was tested at a site on the University of Florida main campus, which featured a buried storm water pipe. The goal was to see if the method could accurately detect and characterize the known cavity and to verify its validity on noisy field data (vs. noise-free synthetic data). Next, the method was tested on field data collected at a retention pond in Newberry, Florida, in a blind study, where no previous knowledge of voids and soil-rock layering existed.

Application of a large source for improved void detection depth was then considered and analyzed. Testing was performed at a bridge construction site located in Miami, Florida, where a large deep void existed. Using the modified source with the heavier drop weight and a larger impact surface increased both the energy and wavelength of seismic waves resulting in the deep void detectability. The results were compared with SPT N-values and sonar images from the test site. Overall, a there was good agreement between all results of all the methods.

Lastly, the method was extended for the energy source embedded in the ground using existing SPT equipment. Specifically, the SPT spoon impacted by the 63 kg (140 lbf) hammer was used as the source, generating seismic waves within the ground from coupling between the spoon and surrounding soil or rock. The wavefield signals were gathered on the ground surface using a 2-D array of geophones. The SPT seismic approach was initially tested at the Newbery site as a proof of concept project and then applied to much greater depth (45 m [150 ft]) at the Miami bridge construction site. The results from both sites showed that the approach can extend the capability of seismic method to detect voids within soil-rock that may otherwise not be

identified with traditional SPT or other low energy surface sources. All seismic results (Vs) were plotted against recorded SPT N values as a function of depth. Data acquisition, analysis, visualization of subsurface features and field verification of the detected voids are elaborated in the following chapters.

CHAPTER 2

DEVELOPMENT OF 3-D FWI ALGORITHM FOR VOID DETECTION

2.1 Introduction

Prior FDOT research (FDOT BDV31-977-29) focused on developing 2-D Full Waveform Inversion (FWI) for soil-rock layering, as well as anomaly (e.g. sinkhole) identification. Successful software was developed and delivered to the FDOT for characterizing soil layering along with results on 5 test sites with invasive testing. Summary findings revealed that 2-D FWI investigation required seismic data be acquired right over the top of the void, which results in multiple test lines, since the void location is generally unknown. In addition, distortion and translation of void was observed (FDOT BDV31-977-29) as result of 3-D effects (e.g. limestone pinnacles). Due to the identified issues, as well as Florida's site variability, FDOT BDV31-977-82 is developing and testing 3-D FWI capabilities.

The goal of this chapter is to develop a computational algorithm of the 3-D FWI method for anomaly/void detection in Florida, using synthetic (computational) waveform data. The work is done through computer simulations employing synthetic models, consisting of cells/cubes with individual *Vs* and *Vp* values. Synthetic models consist of soil-rock layers with typical Florida properties as well as finite 3-D anomalies/voids and an initial velocity profile (3-D) for the whole volume. Next, using the synthetic model, waveform data is generated for a large range of frequencies from 5 to 50 Hz, using a set of receivers and sources (shots) located in uniform 2-D grids on the surface of models (i.e. ground surface). This waveform data is then analyzed (inversion) as if the data was collected from a field test, and a 3-D velocity structure is determined from the waveform data. Comparison of the interpreted models against the true

(physical) models provide bases for the development, implementation and revision of the computational inversion algorithm.

2.2 Development of 3-D FWI algorithm for void detection

A new 3-D FWI algorithm has been successfully developed for detection of voids and characterization of soil-rock layers. The algorithm includes forward modeling for simulation of wave-fields, and model updating (inversion) for extraction of soil-rock properties (Vs and Vp independently). For the forward modeling, the classic velocity-stress staggered-grid finite-difference method was used in combination with perfectly matched layer boundary conditions to solve the equations. For model updating, the Gauss-Newton approach is used to minimize the residuals between the estimated responses obtained by forward simulation and the observed seismic data.

2.2.1 Modeling 3-D wave propagation

The goal of 3-D FWI is to characterize subsurface structures in 3-D domains at high resolution and accuracy. The simulation of wave-fields or the forward modeling plays a critical role in this goal. The forward modeling needs to accurately simulate seismic wave propagation in the field for data comparison (matching). Otherwise inversion artefacts are generated due discrepancy between modelled and field measured data. In addition, a stable and computationally efficient forward solver is required, because a large number of forward simulations are needed in the inversion analysis to reduce the error.

Three-dimensional elastic wave propagation is modelled by a set of the first-order linear partial differential equations for isotropic materials (Eq. 2.1 to Eq. 2.9). The first three equations govern particle velocity, and the remaining equations govern the stress tensor:

$$\dot{v_x} = \frac{1}{\rho}\left(\frac{\partial \sigma_{xx}}{\partial x} + \frac{\partial \sigma_{xy}}{\partial y} + \frac{\partial \sigma_{xz}}{\partial z}\right) + f_x \quad \text{Eq. 2.1}$$

$$\dot{v_y} = \frac{1}{\rho}\left(\frac{\partial \sigma_{xy}}{\partial x} + \frac{\partial \sigma_{yy}}{\partial y} + \frac{\partial \sigma_{yz}}{\partial z}\right) + f_y \quad \text{Eq. 2.2}$$

$$\dot{v_z} = \frac{1}{\rho}\left(\frac{\partial \sigma_{xz}}{\partial x} + \frac{\partial \sigma_{yz}}{\partial y} + \frac{\partial \sigma_{zz}}{\partial z}\right) + f_z \quad \text{Eq. 2.3}$$

$$\dot{\sigma}_{xx} = (\lambda + 2\mu)\frac{\partial v_x}{\partial x} + \lambda\left(\frac{\partial v_y}{\partial y} + \frac{\partial v_z}{\partial z}\right) \quad \text{Eq. 2.4}$$

$$\dot{\sigma}_{yy} = (\lambda + 2\mu)\frac{\partial v_y}{\partial y} + \lambda\left(\frac{\partial v_x}{\partial x} + \frac{\partial v_z}{\partial z}\right) \quad \text{Eq. 2.5}$$

$$\dot{\sigma}_{zz} = (\lambda + 2\mu)\frac{\partial v_z}{\partial z} + \lambda\left(\frac{\partial v_x}{\partial x} + \frac{\partial v_y}{\partial y}\right) \quad \text{Eq. 2.6}$$

$$\dot{\sigma}_{xy} = \mu\left(\frac{\partial v_x}{\partial y} + \frac{\partial v_y}{\partial x}\right) \quad \text{Eq. 2.7}$$

$$\dot{\sigma}_{xz} = \mu\left(\frac{\partial v_x}{\partial z} + \frac{\partial v_z}{\partial x}\right) \quad \text{Eq. 2.8}$$

$$\dot{\sigma}_{yz} = \mu\left(\frac{\partial v_y}{\partial z} + \frac{\partial v_z}{\partial y}\right) \quad \text{Eq. 2.9}$$

where the over-dot denotes the time derivative, (v_x, v_y, v_z) is the particle velocity vector, (f_x, f_y, f_z) is the body force vector, $(\sigma_{xx}, \sigma_{yy}, \sigma_{zz}, \sigma_{xy}, \sigma_{xz}, \sigma_{yz})$ is the stress tensor, ρ is the mass density and μ, λ are Lamé's coefficients. Lamé's coefficients are calculated from S-wave and P-wave velocities (*Vs* and *Vp*) as:

$$\lambda = \rho V_P^2 - 2\rho V_s^2, \ \mu = \rho V_s^2 \quad \text{Eq. 2.10}$$

Derivatives are discretized by using center finite differences. Assuming the equations are verified at the nodes, discretization leads to a velocity-stress staggered-grid as shown in Figure 2.1. The advantages of this technique include: (*i*) source insertion can be expressed by velocity

or stress; (*ii*) a stable and accurate representation for a planar free-surface boundary is easily implemented; (*iii*) the algorithm can be conveniently implemented on scalar, vector, or parallel computers; (*iv*) signal filtering and boundary truncation can be implemented with minimum effort; and (*v*) wave-fields at multiple frequencies can be generated simultaneously in the time domain.

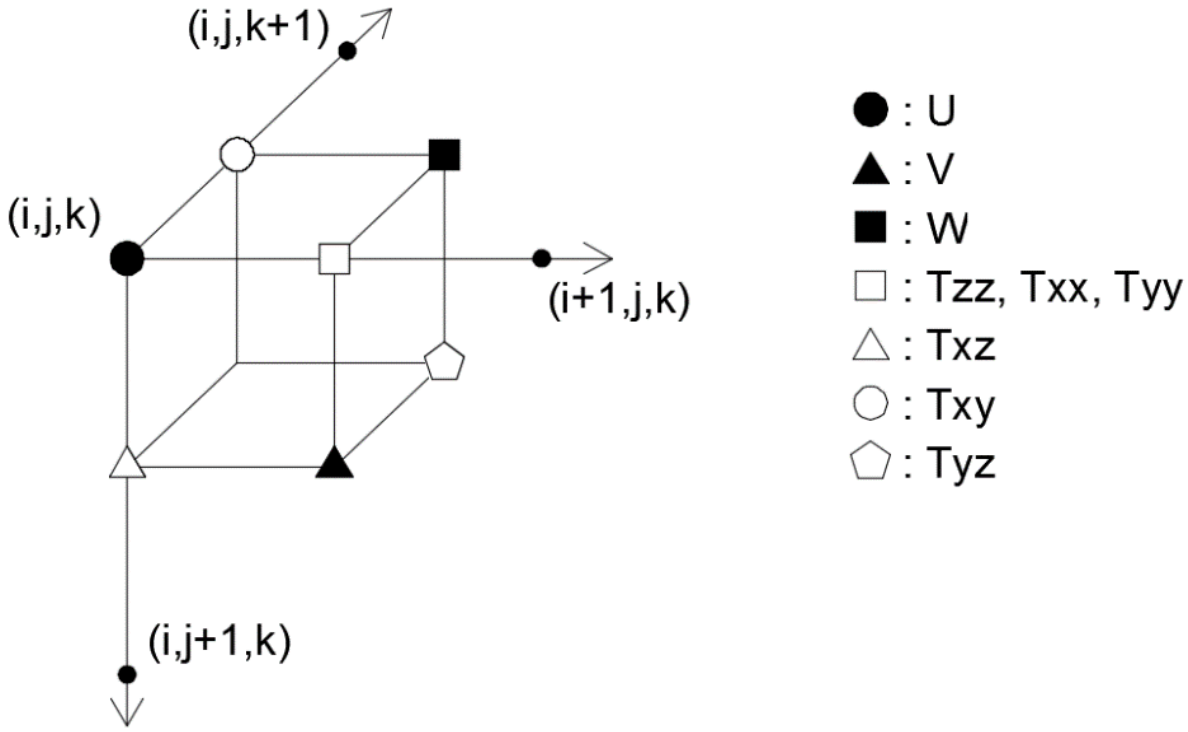

Figure 2.1: Staggered 3-D grid

With each time step, stress and velocities are updated to simulate wave propagation. This is done by converting Eq. 2.1 to Eq. 2.9 into their finite difference forms (Eq. 2.11 through Eq.2-19). The explicit numerical scheme for calculating velocities and stresses is as follows:

$$U_{i,j,k}^{n+\frac{1}{2}} = U_{i,j,k}^{n-\frac{1}{2}} + B_{i,j,k}\frac{\Delta t}{\Delta x}\left(Txx^{n}_{i+\frac{1}{2},j,k} - Txx^{n}_{i-\frac{1}{2},j,k}\right)$$

$$+ B_{i,j,k}\frac{\Delta t}{\Delta y}\left(Txy^{n}_{i,j,k+\frac{1}{2}} - Txy^{n}_{i,j,k-\frac{1}{2}}\right) \qquad \text{Eq. 2.11}$$

$$+ B_{i,j,k}\frac{\Delta t}{\Delta z}\left(Txz^{n}_{i,j+\frac{1}{2},k} - Txz^{n}_{i,j-\frac{1}{2},k}\right)$$

$$V_{i+\frac{1}{2},j+\frac{1}{2},k}^{n+\frac{1}{2}} = V_{i+\frac{1}{2},j+\frac{1}{2},k}^{n-\frac{1}{2}} + B_{i+\frac{1}{2},j+\frac{1}{2},k}\frac{\Delta t}{\Delta x}\left(Txz^{n}_{i+1,j+\frac{1}{2},k} - Txz^{n}_{i,j+\frac{1}{2},k}\right)$$

$$+ B_{i+\frac{1}{2},j+\frac{1}{2},k}\frac{\Delta t}{\Delta y}\left(Tyz^{n}_{i+\frac{1}{2},j+\frac{1}{2},k+\frac{1}{2}} - Tyz^{n}_{i+\frac{1}{2},j+\frac{1}{2},k-\frac{1}{2}}\right) \qquad \text{Eq. 2.12}$$

$$+ B_{i+\frac{1}{2},j+\frac{1}{2},k}\frac{\Delta t}{\Delta z}\left(Tzz^{n}_{i+\frac{1}{2},j+1,k} - Tzz^{n}_{i+\frac{1}{2},j,k}\right)$$

$$W_{i+\frac{1}{2},j,k+\frac{1}{2}}^{n+\frac{1}{2}} = W_{i+\frac{1}{2},j,k+\frac{1}{2}}^{n-\frac{1}{2}} + B_{i+\frac{1}{2},j,k+\frac{1}{2}}\frac{\Delta t}{\Delta x}\left(Txy^{n}_{i+1,j,k+\frac{1}{2}} - Txy^{n}_{i,j,k+\frac{1}{2}}\right)$$

$$+ B_{i+\frac{1}{2},j,k+\frac{1}{2}}\frac{\Delta t}{\Delta y}\left(Tyy^{n}_{i+\frac{1}{2},j,k+1} - Tyy^{n}_{i+\frac{1}{2},j,k}\right) \qquad \text{Eq. 2.13}$$

$$+ B_{i+\frac{1}{2},j,k+\frac{1}{2}}\frac{\Delta t}{\Delta z}\left(Tyz^{n}_{i+\frac{1}{2},j+\frac{1}{2},k+\frac{1}{2}} - Tyz^{n}_{i+\frac{1}{2},j-\frac{1}{2},k+\frac{1}{2}}\right)$$

$$Txx_{i+\frac{1}{2},j,k}^{n+1} = Txx^{n}_{i+\frac{1}{2},j,k} + (L+2M)_{i+\frac{1}{2},j,k}\frac{\Delta t}{\Delta x}\left(U^{n+\frac{1}{2}}_{i+1,j,k} - U^{n+\frac{1}{2}}_{i,j,k}\right)$$

$$+ L_{i+\frac{1}{2},j,k}\frac{\Delta t}{\Delta y}\left(W^{n+\frac{1}{2}}_{i+\frac{1}{2},j,k+\frac{1}{2}} - W^{n+\frac{1}{2}}_{i+\frac{1}{2},j,k-\frac{1}{2}}\right) \qquad \text{Eq. 2.14}$$

$$+ L_{i+\frac{1}{2},j,k}\frac{\Delta t}{\Delta z}\left(V^{n+\frac{1}{2}}_{i+\frac{1}{2},j+\frac{1}{2},k} - V^{n+\frac{1}{2}}_{i+\frac{1}{2},j-\frac{1}{2},k}\right)$$

$$Tyy^{n+1}_{i+\frac{1}{2},j,k} = Tyy^{n}_{i+\frac{1}{2},j,k} + (L+2M)_{i+\frac{1}{2},j,k}\frac{\Delta t}{\Delta y}\left(W^{n+\frac{1}{2}}_{i+\frac{1}{2},j,k+\frac{1}{2}} - W^{n+\frac{1}{2}}_{i+\frac{1}{2},j,k-\frac{1}{2}}\right)$$
$$+ L_{i+\frac{1}{2},j,k}\frac{\Delta t}{\Delta x}\left(U^{n+\frac{1}{2}}_{i+1,j,k} - U^{n+\frac{1}{2}}_{i,j,k}\right) + L_{i+\frac{1}{2},j,k}\frac{\Delta t}{\Delta z}\left(V^{n+\frac{1}{2}}_{i+\frac{1}{2},j+\frac{1}{2},k} - V^{n+\frac{1}{2}}_{i+\frac{1}{2},j-\frac{1}{2},k}\right) \quad \text{Eq. 2.15}$$

$$Tzz^{n+1}_{i+\frac{1}{2},j,k} = Tzz^{n}_{i+\frac{1}{2},j,k} + (L+2M)_{i+\frac{1}{2},j,k}\frac{\Delta t}{\Delta z}\left(V^{n+\frac{1}{2}}_{i+\frac{1}{2},j+\frac{1}{2},k} - V^{n+\frac{1}{2}}_{i+\frac{1}{2},j-\frac{1}{2},k}\right)$$
$$+ L_{i+\frac{1}{2},j,k}\frac{\Delta t}{\Delta x}\left(U^{n+\frac{1}{2}}_{i+1,j,k} - U^{n+\frac{1}{2}}_{i,j,k}\right) + L_{i+\frac{1}{2},j,k}\frac{\Delta t}{\Delta y}\left(W^{n+\frac{1}{2}}_{i+\frac{1}{2},j,k+\frac{1}{2}} - W^{n+\frac{1}{2}}_{i+\frac{1}{2},j,k-\frac{1}{2}}\right) \quad \text{Eq. 2.16}$$

$$Txy^{n+1}_{i,j,k+\frac{1}{2}} = Txy^{n}_{i,j,k+\frac{1}{2}} + M_{i,j,k+\frac{1}{2}}\frac{\Delta t}{\Delta y}\left(U^{n+\frac{1}{2}}_{i,j,k+1} - U^{n+\frac{1}{2}}_{i,j,k}\right)$$
$$+ M_{i,j,k+\frac{1}{2}}\frac{\Delta t}{\Delta x}\left(W^{n+\frac{1}{2}}_{i+\frac{1}{2},j,k+\frac{1}{2}} - W^{n+\frac{1}{2}}_{i-\frac{1}{2},j,k+\frac{1}{2}}\right) \quad \text{Eq. 2.17}$$

$$Txz^{n+1}_{i,j+\frac{1}{2},k} = Txz^{n}_{i,j+\frac{1}{2},k} + M_{i,j+\frac{1}{2},k}\frac{\Delta t}{\Delta z}\left(U^{n+\frac{1}{2}}_{i,j+1,k} - U^{n+\frac{1}{2}}_{i,j,k}\right)$$
$$+ M_{i,j+\frac{1}{2},k}\frac{\Delta t}{\Delta x}\left(V^{n+\frac{1}{2}}_{i+\frac{1}{2},j+\frac{1}{2},k} - V^{n+\frac{1}{2}}_{i-\frac{1}{2},j+\frac{1}{2},k}\right) \quad \text{Eq. 2.18}$$

$$Tyz^{n+1}_{i+\frac{1}{2},j+\frac{1}{2},k+\frac{1}{2}} = Tyz^{n}_{i+\frac{1}{2},j+\frac{1}{2},k+\frac{1}{2}} + M_{i+\frac{1}{2},j+\frac{1}{2},k+\frac{1}{2}}\frac{\Delta t}{\Delta z}\left(W^{n+\frac{1}{2}}_{i+\frac{1}{2},j+1,k+\frac{1}{2}} - W^{n+\frac{1}{2}}_{i+\frac{1}{2},j,k+\frac{1}{2}}\right)$$
$$+ M_{i+\frac{1}{2},j+\frac{1}{2},k+\frac{1}{2}}\frac{\Delta t}{\Delta y}\left(V^{n+\frac{1}{2}}_{i+\frac{1}{2},j+\frac{1}{2},k+1} - V^{n+\frac{1}{2}}_{i+\frac{1}{2},j+\frac{1}{2},k}\right) \quad \text{Eq. 2.19}$$

where i, j, k are the indicial location of the current point in the x, z, and y directions, respectively; n represents the current time step while U, V, and W are the particle velocities in the x, z, and y directions. B is the reciprocal of the density at the location indicated by the indices and T represent the stress component in each direction. M and L are the Lame's coefficients mentioned earlier.

In order to maintain stability of the simulation, the time interval (sampling rate) Δt must satisfy the Courant-Friedrichs-Levy (CFL) stability criterion. The numerical stability condition for this explicit scheme is:

$$v_{\max}\Delta t\sqrt{\frac{1}{\Delta x^2+\Delta y^2+\Delta z^2}}\le 1, \qquad \text{Eq. 2.20}$$

where $v_{\max}$ is the maximum P-wave velocity of the medium, and Δx, Δy and Δz is the grid spacing selected to satisfy at least ten points per minimum expected wavelength to avoid numerical dispersion or:

$$\Delta x, \Delta y, \Delta z \le dh = \frac{\lambda_{min}}{10}, \qquad \text{Eq. 2.21}$$

where $\lambda_{min} = \frac{v_{ave}}{f_{max}}$, v_{ave} is the average S-wave velocity in the media, f_{max} is the maximum frequency of the source. During inversion, Δt is allowed to change due to different $v_{\max}$ values, which ensures that the measured wave fields are interpolated to the same sampling rate for comparison to the estimated wave fields at every iteration. Note, using a fixed small sampling rate will maintain stability of the simulation through iterations, but it will increase the required computer time.

2.2.1.1 Boundary conditions

Special conditions are required at the boundaries of the modeled domain when simulating wave propagation with finite difference equations. A model without boundary conditions will have boundaries that act like rigid walls, i.e. all incoming waves will be reflect off of the boundary back into the domain. These reflections do not accurately represent the infinite media from which data are collected in the field. An ideal model will allow the wave to pass through the boundary without any reflection. For the domain, a free-surface boundary condition is

applied on the top boundary (surface), while perfectly matched layers (PML) are applied at the other boundaries (i.e. sides and bottom).

2.2.1.1.1 Free surface condition

The free surface condition, applied at the surface ($z = 0$), occurs naturally in the field when the medium being modeled encounters open air. This allows the normal stress (σ_{zz}) and the shear stresses (σ_{xz}, σ_{yz}) to be set to zero (Tran and McVay, 2012). This condition is critical when implementing the staggered grid and the need to numerically calculate $\frac{\partial \sigma_{xz}}{\partial z}$, $\frac{\partial \sigma_{yz}}{\partial z}$, and $\frac{\partial v_z}{\partial z}$ at the surface without the grid points for σ_{xz}, σ_{yz}, and v_z above the surface.

The surface condition is carried out in two steps. The first is done by substituting zero for σ_{xx} into Eq. 2.4 and solving for $\frac{\partial v_z}{\partial z}$.

$$\frac{\partial v_z}{\partial z} = -\frac{\lambda}{\lambda + 2\mu}\left(\frac{\partial v_x}{\partial x} + \frac{\partial v_y}{\partial y}\right) \qquad \text{Eq. 2.22}$$

Eq. 2.22 is then expressed in terms of the staggered grid,

$$\left(\frac{\partial V}{\partial z}\right)^{n+\frac{1}{2}}_{i+\frac{1}{2},1,k} = -\frac{L_{i+\frac{1}{2},1,k}}{(L+2M)_{i+\frac{1}{2},1,k}}\left(\frac{1}{dx}\left(U^{n+\frac{1}{2}}_{i+1,1,k} - U^{n+\frac{1}{2}}_{i,1,k}\right) + \frac{1}{dy}\left(W^{n+\frac{1}{2}}_{i+\frac{1}{2},1,k+\frac{1}{2}} - W^{n+\frac{1}{2}}_{i+\frac{1}{2},1,k-\frac{1}{2}}\right)\right) \qquad \text{Eq. 2.23}$$

where the z-coordinate remains at the surface ($j = 1$). Eq. 2.23 is used whenever σ_{xx} is calculated at the surface.

The second step is done by setting the remaining stresses (σ_{xz} and σ_{yz}) to zero and determining the slope of the shear stresses at the surface mathematically (Figure 2.2 and Eq. 2.24, Eq. 2.25). These equations are used when calculating both the velocities in x and y directions on the surface.

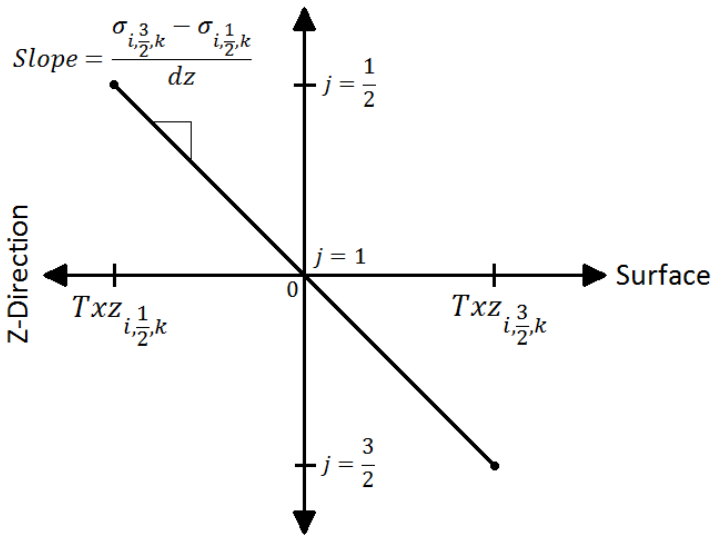

Figure 2.2: $\frac{\partial \sigma}{\partial z}$ surface plot

$$\left(\frac{\partial Txz}{\partial z}\right)^{n}_{i,j,k} = \frac{1}{dz}\left(Txz^{n}_{i,\frac{3}{2},k} - Txz^{n}_{i,\frac{1}{2},k}\right) = \frac{1}{dz}\left(Txz^{n}_{i,\frac{3}{2},k} - \left(-Txz^{n}_{i,\frac{3}{2},k}\right)\right)$$

$$= \frac{2}{dz} Txz^{n}_{i,\frac{3}{2},k} \qquad \text{Eq. 2.24}$$

$$\left(\frac{\partial Tyz}{\partial z}\right)^{n}_{i+\frac{1}{2},j,k+\frac{1}{2}} = \frac{1}{dz}\left(Tyz^{n}_{i+\frac{1}{2},\frac{3}{2},k} - Tyz^{n}_{i+\frac{1}{2},\frac{1}{2},k+\frac{1}{2}}\right)$$

$$= \frac{1}{dz}\left(Tyz^{n}_{i+\frac{1}{2},\frac{3}{2},k+\frac{1}{2}} - \left(-Tyz^{n}_{i+\frac{1}{2},\frac{3}{2},k+\frac{1}{2}}\right)\right) = \frac{2}{dz} Tyz^{n}_{i+\frac{1}{2},\frac{3}{2},k+\frac{1}{2}} \qquad \text{Eq. 2.25}$$

2.2.1.1.2 Perfectly matched layer condition

The remaining boundaries utilize an absorbing condition known as the perfectly matched layer (PML), which attenuates any waves near the boundary (Figure 2.3). Note, the boundary model is critical to ensure that no boundary reflections mask low amplitude late arrival signals from anomalies or weak zones, i.e. lower V values.

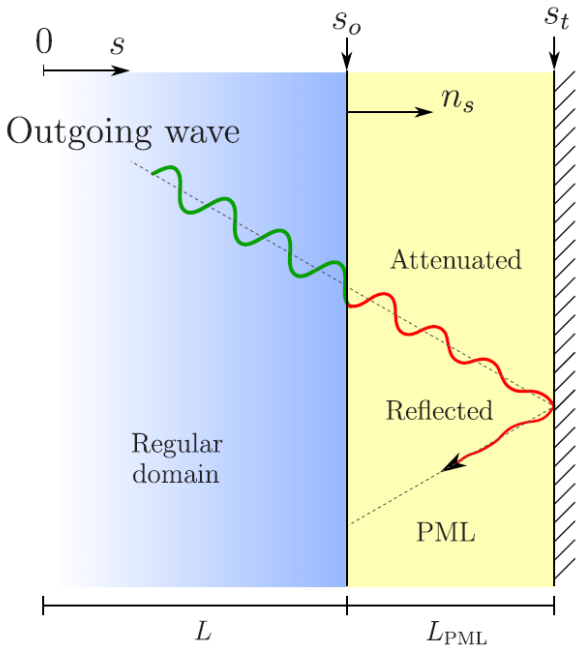

Figure 2.3: Perfectly matched layer on original domain (Fathi et al., 2015)

The dampening effect is carried out by extending the staggered grid beyond the modelled domain, Figure 2.3. Parameter S_o represents the original boundary while S_t is the boundary of the added domain with additional grid points. Each added grid point reduces the wave amplitude based on a and b parameters which are derived using several variables and constants:

$$b_x = e^{-\left(\frac{d_x}{k_x}+\alpha_x\right)\Delta t} \qquad \text{Eq. 2.26}$$

$$a_x = \frac{d_x}{k_x(d_x + k_x\alpha_x)}(b_x - 1) \qquad \text{Eq. 2.27}$$

where k_x is set to one to allow for the PML condition to replicate the classical PML coordinate transformation; α_x is calculated based on the current grid point and the central frequency while d_x represents the damping profile such that $d_x = 0$ inside the original domain and $d_x > 0$ in the perfectly matched layer. a_x and b_x are implemented after the calculation of each stress and velocity derivative ∂_x, by creating the memory variable ψ_x and applying it to Eq. 2.29.

$$\psi_x^n = b_x \psi_x^{n-1} + a_x (\partial_x)^{n+\frac{1}{2}}$$ Eq. 2.28

$$\partial_{\tilde{x}} = \frac{1}{k_x} \partial_x + \psi_x$$ Eq. 2.29

All bottom and side wave reflections are cancelled when the boundary conditions discussed above are applied, allowing for proper modeling of infinite mediums such as those found in the field.

As an example, Figure 2.4 presents 3-D wave propagation in a homogeneous medium with (left) and without (right) the PML conditions. The medium has *Vs* of 200 m/s (600 ft/s) and *Vp* of 400 m/s (1,332 ft/s) for the entire domain. The source is located on the free surface (depth z =0). With the implementation of the PML, almost no reflected signals from boundaries are observed (Figure 2.4, left column). Whereas, significant reflected signals from boundaries are seen after 0.3 s (Figure 2.4, right column) without the PML.

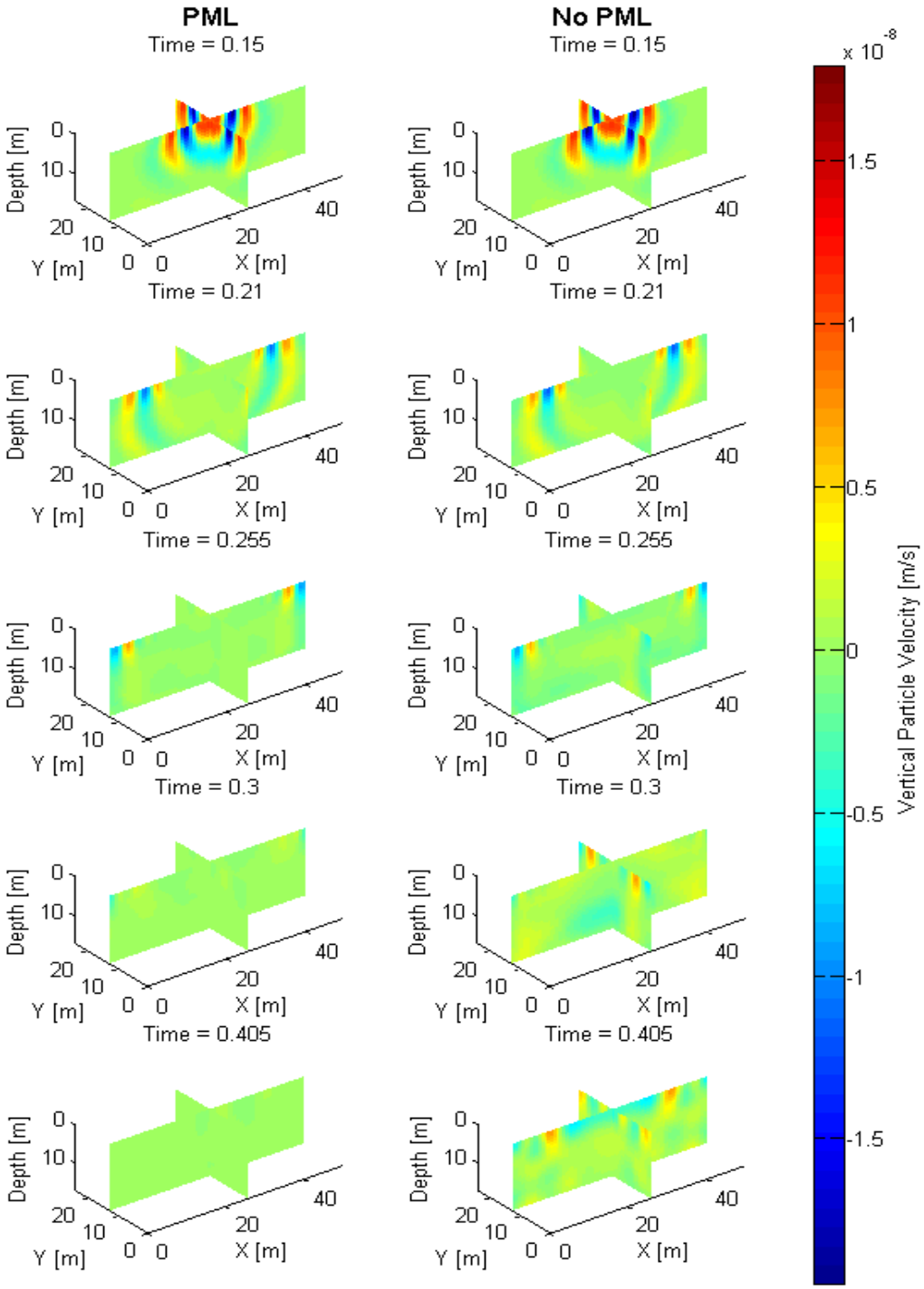

Figure 2.4: 3-D wave propagation with and without the perfectly matched layer (PML) boundary truncation.

2.2.2 3-D forward modeling implementation

After development of the recurrence equations and boundary conditions, a simulation was run with a homogeneous medium to verify that waves were propagating properly using the implemented 3-D wave equation solution. The medium has *Vs* of 200 m/s (666 ft/s) and *Vp* that is generated from the S-wave velocity (Fig. 2.5) with a constant Poisson's ratio of 0.33 for an entire domain: 36 m x 9 m x18 m ($120' \times 30' \times 60'$). A stagger-grid of 49 x 13 x 25 cells (15,925 total) each of which was 0.75 m x 0.75 m x 0.75 m ($2.5' \times 2.5' \times 2.5'$) was used in the simulation.

The initial conditions are set to satisfy equilibrium at time *t=0*, i.e., stress and velocity are zero everywhere in the medium. Then the medium was perturbed by changing the vertical stress at a source which was modeled with the Ricker wavelet R(t):

$$R(t) = (1 - 2\pi^2 f_c^2 (t - t_0)^2).\exp(-\pi^2 f_c^2 (t - t_0)^2), \qquad \text{Eq. 2.30}$$

where f_c is the central frequency and t_0 is the delay time (time shift).

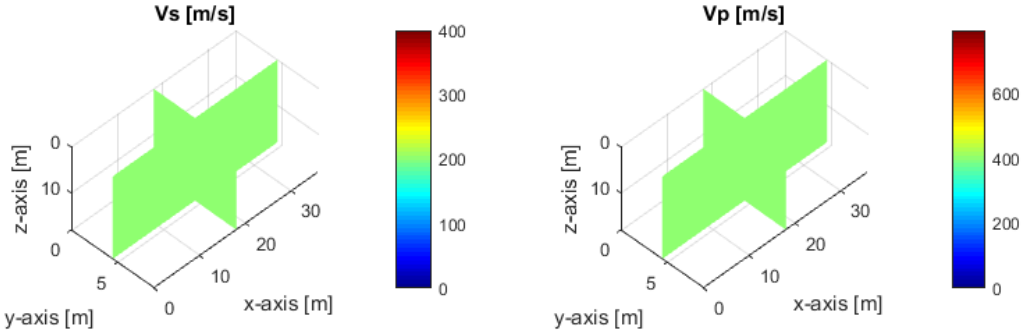

Figure 2.5: S-wave velocity V_S, P-wave velocity V_P profile for forward modeling

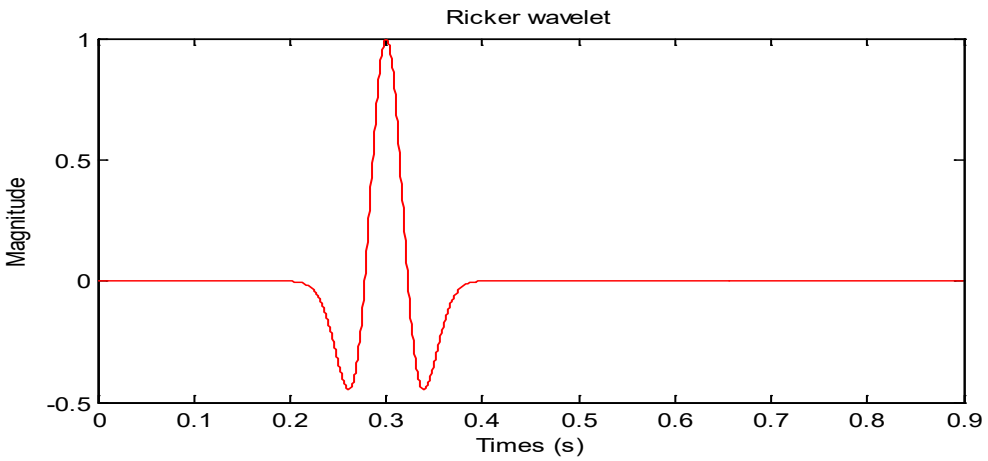

Figure 2.6: Ricker wavelet as source signature

The source was located on the surface at 18 m (60 ft) in x-direction and at 3 m (10 ft) in y-direction. For the source signature, the Ricker wavelet had a central frequency f_c = 15 Hz and a delay time t_0 = 0.3 s (Figure 2.6). Data were simulated for the whole medium at each time step to allow for 3-D images of wave propagation (Figure 2.7). Waveform data were extracted for four parallel receiver lines with a total of 96 receivers for the one source. The receiver lines were equally located at every 3 m (10 ft) in the y-direction (from 0 to 9 m [0 to 30 ft]), and 24 receivers for each line were spaced 1.5 m (5 ft) apart along the x- direction (from 0.75 to 35.25 m [2.5 to 115 ft]). The recorded data were the particle velocity in vertical direction (z-component) of the surface cells at the receiver locations (Figure 2.8).

The recorded waveform data showed a steady wave movement throughout the medium with no reflections, as expected from a homogeneous model. Waveform magnitudes decreased with increasing source-receiver distance. Signals recorded at the receivers at the same distance from the source in any direction had the same magnitude and phase, which showed the accuracy of 3-D forward modeling.

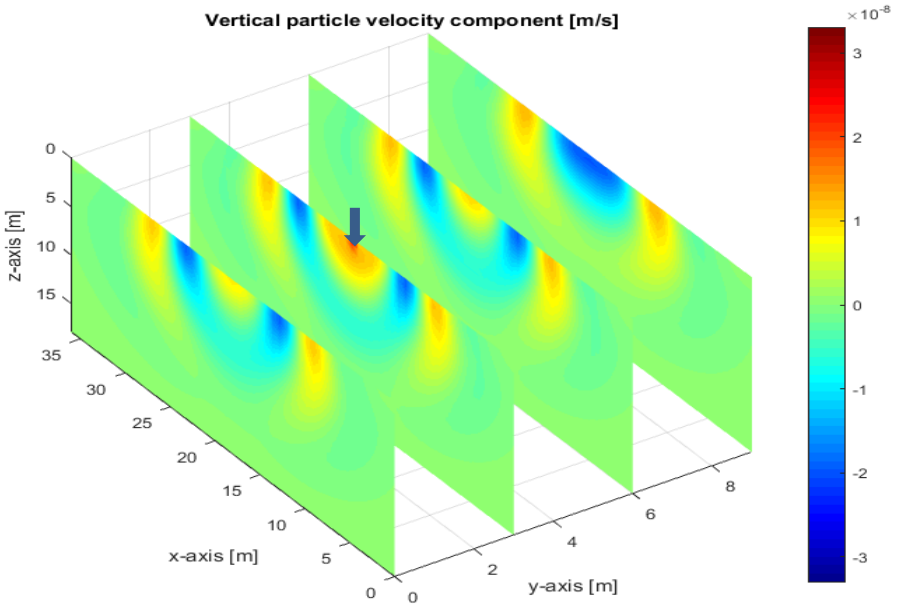

Figure 2.7: Wave propagation at t=0.35 s from a source located on the surface (arrow)

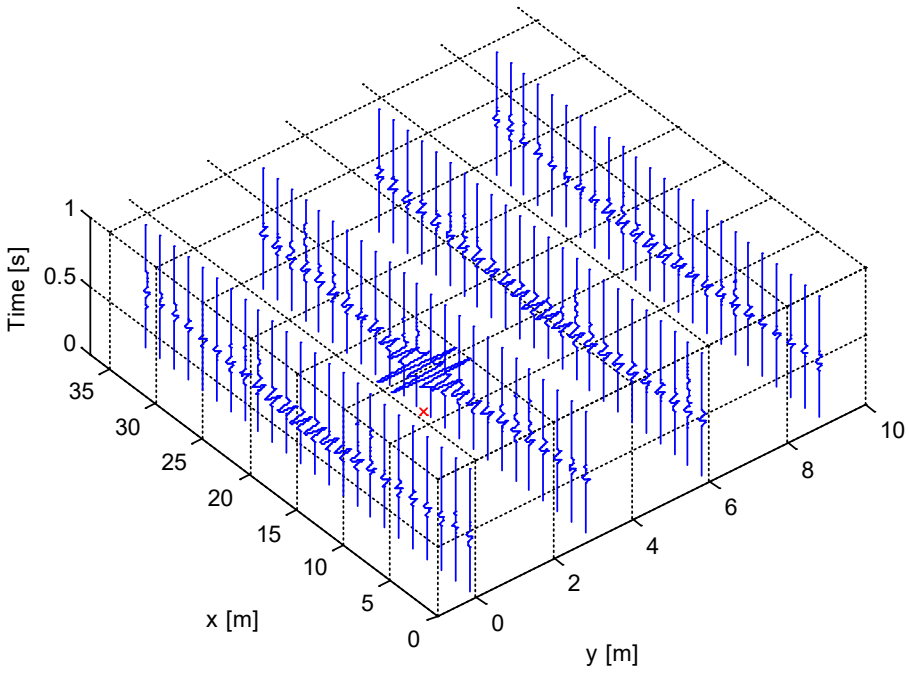

Figure 2.8: Wavefield at receiver locations

2.2.3 Inversion model updating

Equally important in the 3-D analysis is the inversion model that adjusts the individual cell properties (*Vs*, and *Vp*) in order that the measured results at the receivers match the predicted full waveform results from the forward model. For model updating in the inversion, the Gauss-Newton method is used, as it is more robust and converges faster than the gradient method for numerical optimization of non-linear problems. From our previous 2-D FWI study on real experimental data, it is necessary to use the Gauss-Newton method to obtain acceptable/required accuracy for detection of embedded anomalies/voids, and especially reduce inversion artifacts. Although the Gauss-Newton method provides inversion results with higher accuracy, it requires intensive computing of individual elements of the Jacobian matrix along with a huge memory to store the Jacobian and the approximate Hessian matrices. To save RAM, time-domain wave-fields and Jacobian elements obtained from forward modeling simulations (one by one) are converted into the frequency domain and stored for only a few frequencies (3 to 5 frequencies for each inversion), instead of storing for thousands of time steps. Using the discrete Fourier transformation, we convert signals from the time to the frequency domain with

$$\tilde{u}(\mathbf{x},\omega) = \sum_{l=1}^{nt} \exp(\sqrt{-1}\omega l\Delta t) u(\mathbf{x}, l\Delta t)\Delta t \ , \qquad \text{Eq. 2.31}$$

where $\tilde{u}(\mathbf{x},\omega)$ is the frequency domain signal for the space location $\mathbf{x}=(x,y,z)$ and frequency ω, $u(\mathbf{x}, l\Delta t)$ is the time domain signal at the space location $\mathbf{x}$ and time $t= l\Delta t$, Δt is the time sampling, and nt is the number of time steps. Eq. 2.31 is used for all signals (wave-fields, Jacobian and Hessian matrix elements) in following Equations (Eq. 2.32 to Eq. 2.34) on the solution strategy.

The Gauss-Newton method involves minimizing the residual between the estimated responses obtained by forward simulation and the observed seismic data from field testing. The residual is defined as:

$$\Delta \mathbf{d}_{i,j} = \mathbf{F}_{i,j}(\mathbf{m}) - \mathbf{d}_{i,j}, \qquad \text{Eq. 2.32}$$

where indices *i* and *j* denote the *i*-th shot and *j*-th receiver, respectively, and the column vector $\mathbf{F}_{i,j}$ (**m**) is the estimated seismic data associated with the model **m**, and obtained from the solution of the wave equations described by Eq. 2.1 to Eq. 2.9 for the *i*-th shot and *j*-th receiver. Model **m** is a column vector consisting of *Vp* and *Vs* of all cells of the medium. The column vector $\mathbf{d}_{i,j}$ is the observed data for the *i*-th shot and *j*-th receiver. A set of observed data (column vector **d,** combined from all $\mathbf{d}_{i,j}$) includes signals created from all shots and measured by all receivers. Both the shots and receivers are located in 2-D uniform grids on the ground surface.

To minimize the residual, a least-squares error E(**m**) is introduced as:

$$\mathrm{E}(\mathbf{m}) = \frac{1}{2}\Delta \mathbf{d}^t \Delta \mathbf{d}, \quad \textit{and} \quad \Delta \mathbf{d} = \left\{\Delta \mathbf{d}_{i,j},\ i = 1,...NS,\ j = 1...NR\right\} \qquad \text{Eq. 2.33}$$

where the superscript *t* denotes the matrix transpose, *NS* and *NR* are the numbers of shots and receivers, and $\Delta\mathbf{d}$ is a column vector, which is the combination of residuals $\Delta\mathbf{d}_{i,j}$ for all shots and receivers. If the number of frequencies is *NF*, the size of $\Delta\mathbf{d}$ is $NF \times NS \times NR$. The updated material description (*Vs, Vp* of cells), $\mathbf{m}^{n+1}$, is obtained from Gauss-Newton gradient approach for minimization of the error E(**m**) at the $(n+1)$-th iteration from the *n*-th iteration or:

$$\mathbf{m}^{n+1} = \mathbf{m}^{n} - \alpha^{n}\left[\mathbf{J}^t \mathbf{J} + \lambda_1 \mathbf{P}^t \mathbf{P} + \lambda_2 \mathbf{I}^t \mathbf{I}\ \right]^{-1} \mathbf{J}^t \Delta \mathbf{d}, \qquad \text{Eq. 2.34}$$

where **J** is the Jacobian matrix, or derivative of the wave field with respect to individual model parameters (*Vs, Vp* of cells). **I** is the identity matrix, and **P** is a matrix whose elements are determined using a Laplacian operator:

$$P_p \Delta \mathbf{m} = (\Delta m_p)^L + (\Delta m_p)^R + (\Delta m_p)^F + (\Delta m_p)^B + (\Delta m_p)^A + (\Delta m_p)^U - 6(\Delta m_p). \qquad \text{Eq. 2.35}$$

where the superscripts *L*, *R*, *F*, *B, A* and *U* refer to six adjacent cells (left, right, front, back, above, and under) of the cell referring to the model parameter m_p, and P_p is the *p*-th row of the matrix **P** whose elements are either 1, -6, or 0. Coefficients λ_1 and λ_2 are constants, and α^n is the optimal step length.

The main challenge for the use of Gauss-Newton method is the computation of the partial derivative of the wave-field (matrix **J**) with respect to the model parameters (m_p). One approach is to take the partial derivative of the wave-field with respect to a model parameter (m_p) for the *i*-th shot and *j*-th receiver explicitly through two forward simulations with and without the model perturbation as:

$$\mathrm{J}_{i,j}^{p} = \frac{\partial \mathbf{F}_{i,j}(\mathbf{m})}{\partial m_p} = \frac{\mathbf{F}_{i,j}\left(\mathbf{m}+\Delta m_p\right) - \mathbf{F}_{i,j}\left(\mathbf{m}\right)}{\Delta m_p} \qquad \text{Eq. 2.36}$$

By perturbing the individual model parameters (unknowns), a total of $NS \times (M+1)$ forward simulations are required to calculate the matrix **J**, where *M* is the number of unknowns. This requires significant computer time, i.e. many thousands of model parameters within 3-D profiles. Another more efficient approach is to expand the implicit approach developed for 2-D time-domain FWI (Sheen et al., 2006; Tran and McVay, 2012; Tran et al., 2013) to evaluate the derivative of the wave-field for the 3-D problem.

The same Jacobian component of Eq. 2.36 can be obtained by propagating the virtual sources at the parameter location to the receivers. Also, based on the reciprocity of wave propagation, waveforms are identical if a source and a receiver are switched. Thus, the Jacobian matrix (**J)** can be determined by convolution of the virtual sources and backward wave-fields, which are both obtained from forward simulations (Eq. 2.1 to Eq. 2.9). This approach requires only (*NS*+*NR*) forward simulations for the calculation of matrix **J.** Finally, the partial derivative

of the wave-field with respect to a model parameter (m_p) for the *i*-th shot and *j*-th receiver can be implicitly calculated as:

$$J_{i,j}^{p} = F_x * R_x + F_y * R_y + F_z * R_z \quad \text{Eq. 2.37}$$

where F_x, F_y, and F_z are virtual sources calculated from forward wave-fields, which are generated by a source at the *i*-th shot location and recorded at the location of model parameter m_p in directions x, y, and z, respectively. R_x, R_y, and R_z are backward wave-fields generated by a source at the *r*-th receiver location and recorded at the model parameter m_p location in directions x, y, and z, respectively. The * in Eq. 2.37 denotes the convolution.

For verification, shown in Figure 2.9 is a comparison of partial derivative of the wave-fields calculated explicitly and implicitly by Eq. 2.36 and Eq. 2.37, respectively. The tested model was 18 × 40 × 40 m ($60' \times 130' \times 130'$) (depth × length × width) in the z, x, and y directions. It consisted of 3 horizontal layers with *Vs* values of 300, 400, 600 m/s (1,000, 1,332, 2,000 ft/s) and *Vp* values of 600, 800, 1200 m/s (2,000, 2,664, 4,000 ft/s) as shown in Figure 2.9a at a vertical plane of y = 20 m (y=66 ft) (middle of the domain). The medium was divided into 1 × 1 × 1 m ($3.3 \times 3.3 \times 3.3$ ft) cells, and a Ricker wavelet of 15 Hz central frequency was used for the wave simulation. The source and receiver were both vertical and located on the free surface (depth 0 m [0 ft]). The model parameters, m_p were *Vs* and *Vp* of a cell at depth of 12 m (40 ft). Shown in Figure 2.9b are derivative wave-fields calculated by Eq. 2.36 (explicit) and Eq. 2.37 (implicit) with respect to *Vp* and *Vs* of the cell. It is noted that derivative wave-field calculated by Eq. 2.36 was convolved with the source signature to account for the scale of the source signature used for the backward wave-fields in Eq. 2.37. Evident from Figure 2.9b, the implicit and explicit derivative wave-fields are identical, but the implicit approach is much more efficient and will be used in subsequent work. As the derivative wave-fields calculated by Eq.

2.37 are scaled by the source signature used for the backward wave-fields, the residuals (Eq. 2.33) must be convolved with the same source signature before using model updating in Eq. 2.34.

(a)

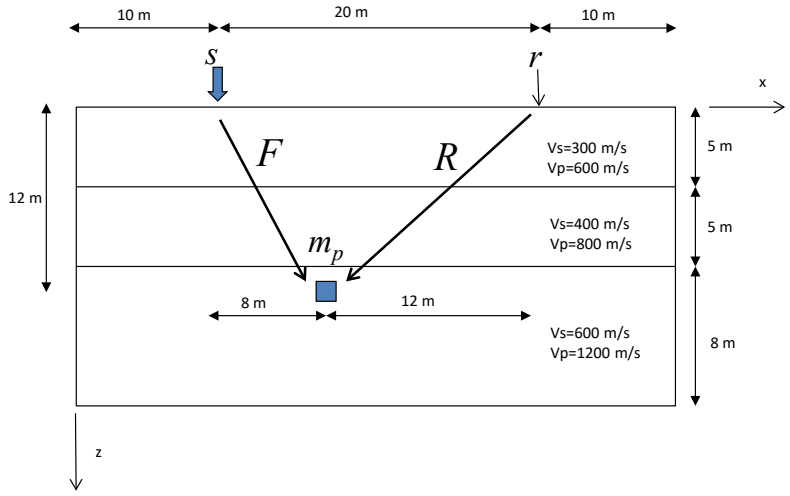

(b)

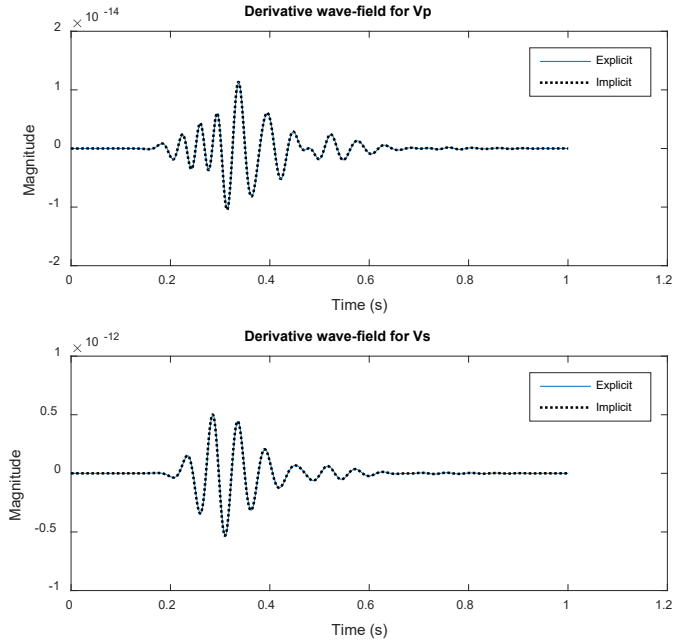

Figure 2.9: Derivative wavefield comparison: (a) schematic diagram of the model, s and r denote for vertical source and vertical receiver and (b) derivative wave-fields with respect to V_p and V_s of a cell at 12-m (40-ft) depth calculated by Eq. 2.36 (Explicit) and Eq. 2.37 (Implicit).

2.3 Application

2.3.1 Layer profile without void

The developed 3-D FWI algorithm was tested on a synthetic model of variable high- and low-velocity soil-rock layers with no void. Surface-based waveform data were calculated for a test configuration (i.e. 2-D uniform grids of shots and receivers as shown in Figure 2.10), and then input to the 3-D FWI algorithm as if they were acquired from field testing. The *Vs* and *Vp* structures underneath the receiver and shot area were extracted from the inversion analyses, and compared to the true profile for evaluation of the algorithm.

The model was 18 × 36 × 9 m ($60' \times 120' \times 30'$) (depth × length × width), consisting of 4 soil layers (Figure 2.11a) with a low-velocity third layer. The 4 layers have *Vs* values of 200 m/s (666 ft/s), 400 m/s (1,332 ft/s), 200 m/s (666 ft/s) and 600 m/s (2,000 ft/s), and *Vp* is twice that of *Vs*. The mass density was 1,800 kg/m^3 (112.37 lbf/ft^3) for the whole model. Synthetic waveform data were computed using the solution of Eq. 2.1 to Eq. 2.9, with a test configuration of 96 receivers and 52 shots (sources) located in 2-D uniform grids (Figure 2.10). The receiver grid was 4 × 24 at 3 m (10 ft) spacing in the shorter direction and 1.5 m (5 ft) spacing in the longer direction, and the source grid was 4 × 13 at 3 m (10 ft) spacing in both directions. Sources and receivers were all vertical and located on the free surface (0-m depth). The Ricker wavelet with 15 Hz central frequency was used for the source signature.

A basic 1D initial model with *Vs* and *Vp* linearly increasing with depth (Figure 2.11b) was used for the inversion. The *Vs* increased from 200 m/s (666 ft/s) on the free surface (0-m depth) to 600 m/s (2,000 ft/s) at the bottom of the model (18-m [60-ft] depth), and the *Vp* was twice that of *Vs*. The same dataset (created by Ricker wavelet source of 15 Hz central frequency) were filtered through two frequency bandwidths: 5-20 Hz and 5-30 Hz, and were used for the

two inversion runs. The first run began with the lower frequency range (5-20 Hz) with the initial model (Figure 2.11b). The second run was performed with the higher frequency range (5-30 Hz) using the inverted result from the first run as the input model.

Vs and *Vp* values of the individual cells were updated simultaneously by Eq. 2.35 during the inversion analysis. The stopping criterion was set at the point when the least-squares error changed less than 1% from one iteration to the next for 3 consecutive iterations, or if a preset maximum number of iterations (30) had been reached. The first and second runs stopped after 22 and 30 iterations, respectively. The two runs took approximately 36 hours in total on a computer with 32 cores having 3.46 GHz each and 256 GB of memory; approximately 220 GB of memory was used in the analyses.

The least-squares errors for all 52 iterations of the two inversion runs were normalized by the initial error of the first iteration and are displayed in Figure 2.12. The error reduced from 1.0 (normalized) at the first iteration to less than 0.13 at the final iteration (iteration 52). The error increased when adding data from 20 to 30 Hz, because the model was not adjusted to the shorter wavelength signals. Figure 2.13 shows a comparison of observed data at 5- 30 Hz, for the estimated data associated with the initial model and the final inverted result at iteration 52. Clearly, the full waveform match improved significantly during inversion. The observed and final estimated data agrees quite well with no cycle skipping, suggesting that the 1D initial model is sufficient.

Results of the two inversion runs are shown in Figure 2.11. The result at 5-20 Hz (Figure 2.11c) is comparable to the true model (Figure 2.11a), showing a 4-layer profile in both *Vs* and *Vp* images along with the low-velocity third layer. The result at 5-30 Hz (Figure 2.11d) is very similar to the true model (Figure 2.11a). The inverted result was improved considerably during

the second run by adding the higher frequency influences, particularly for the top two layers. Also, the variable layer interfaces were accurately characterized, and the true *Vs* and *Vp* values of all layers were recovered.

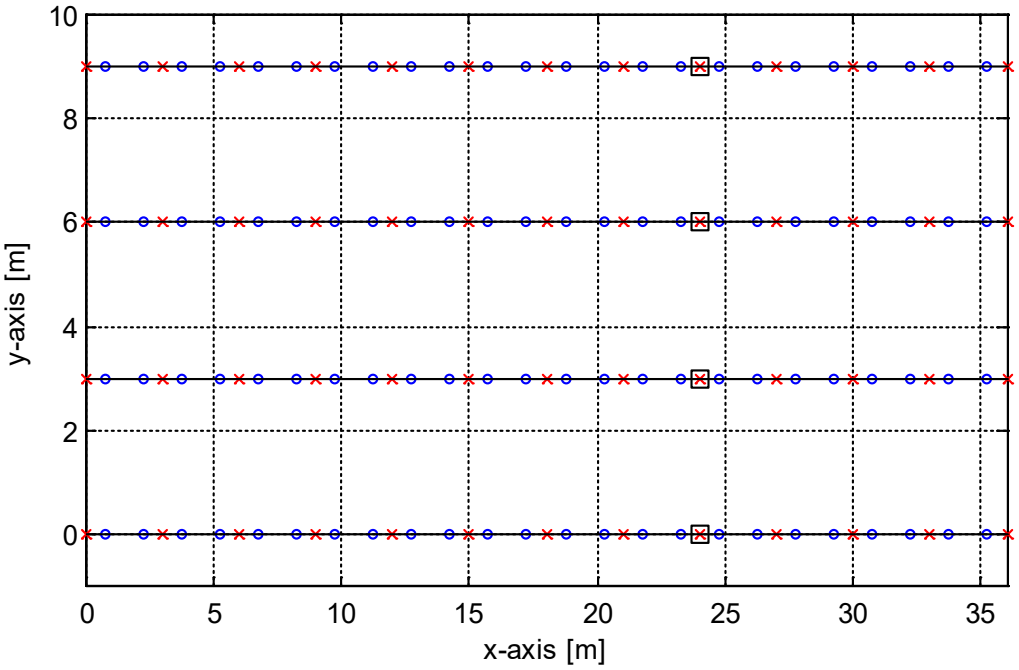

Figure 2.10: Test configuration: source (cross), receiver (circle).

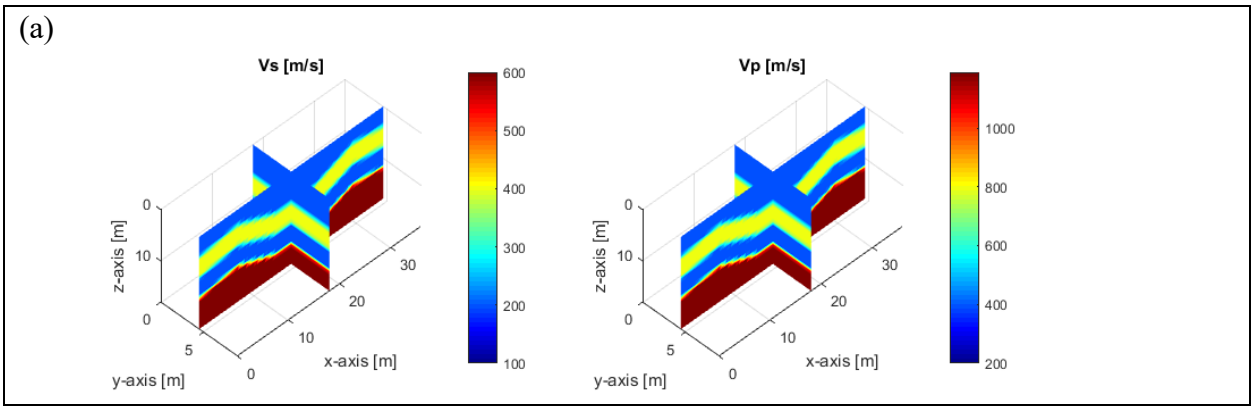

Figure 2.11: Synthetic model: distribution of V_s and V_p: (a) true model used to generate synthetic data for inversion analysis; (b) initial model used at the beginning of inversion; and (c) and (d) inverted models with data at 5-20 Hz and 5-30 Hz, respectively.

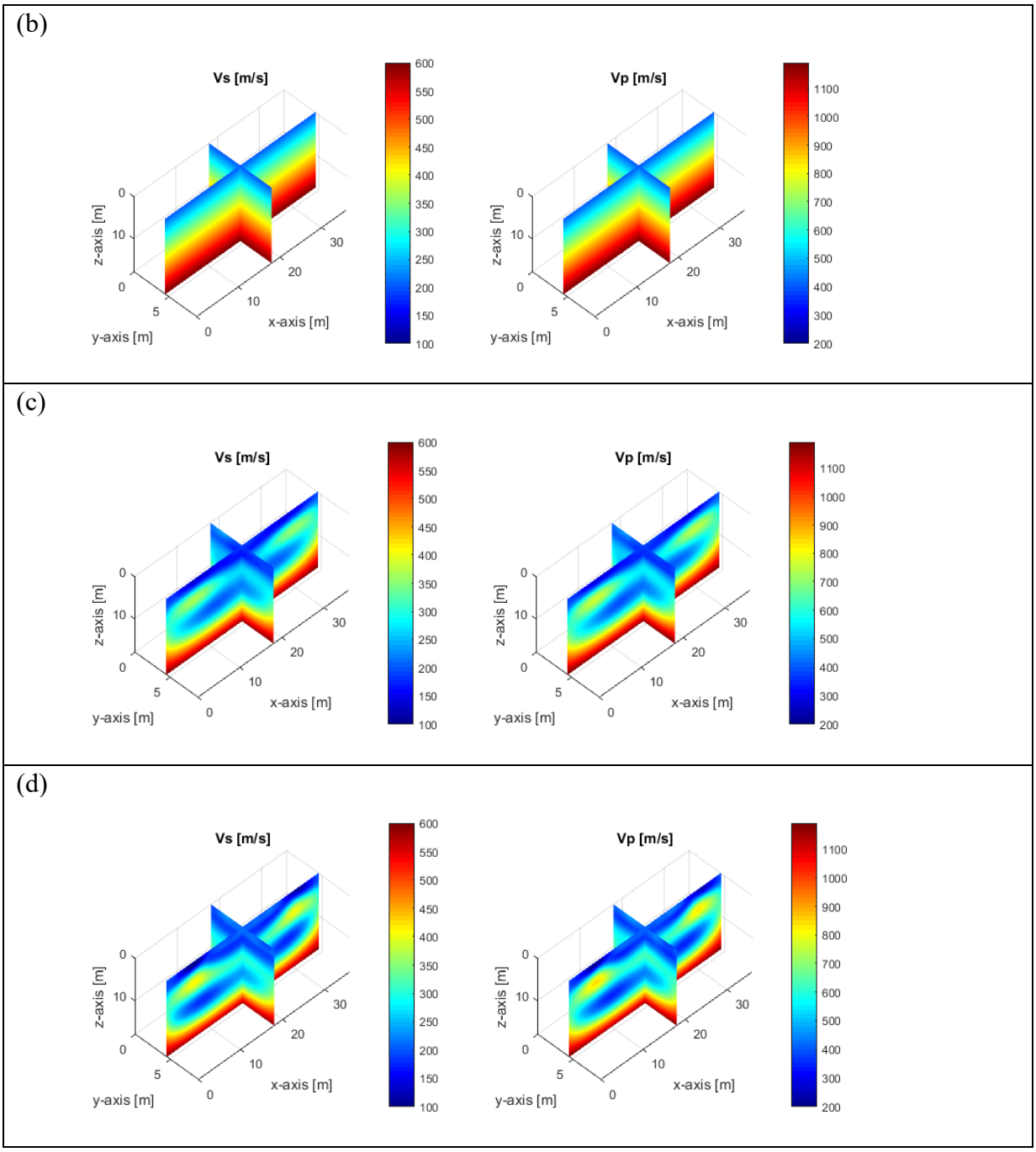

Figure 2.11: Synthetic model: distribution of V_s and V_p: (a) true model used to generate synthetic data for inversion analysis; (b) initial model used at the beginning of inversion; and (c) and (d) inverted models with data at 5-20 Hz and 5-30 Hz, respectively.

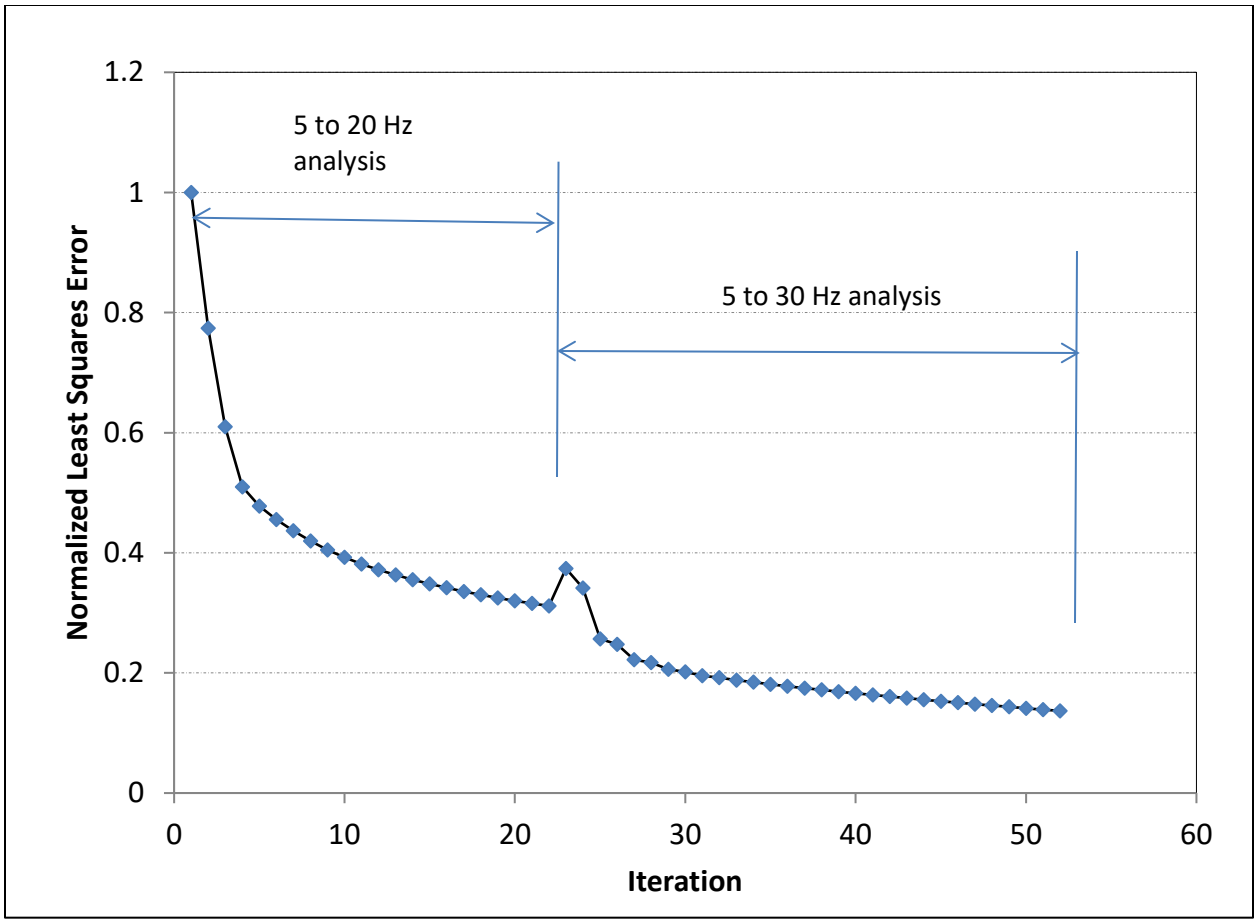

Figure 2.12: Synthetic model: normalized least squares error versus the iteration number for both inversion runs at 5-20 Hz and 5-30 Hz. The error defines the degree of match between the estimated and observed waveforms during the inversion analysis. The error increases at higher frequencies because the model is not yet appropriate to produce the recorded wave propagation of shorter wavelengths.

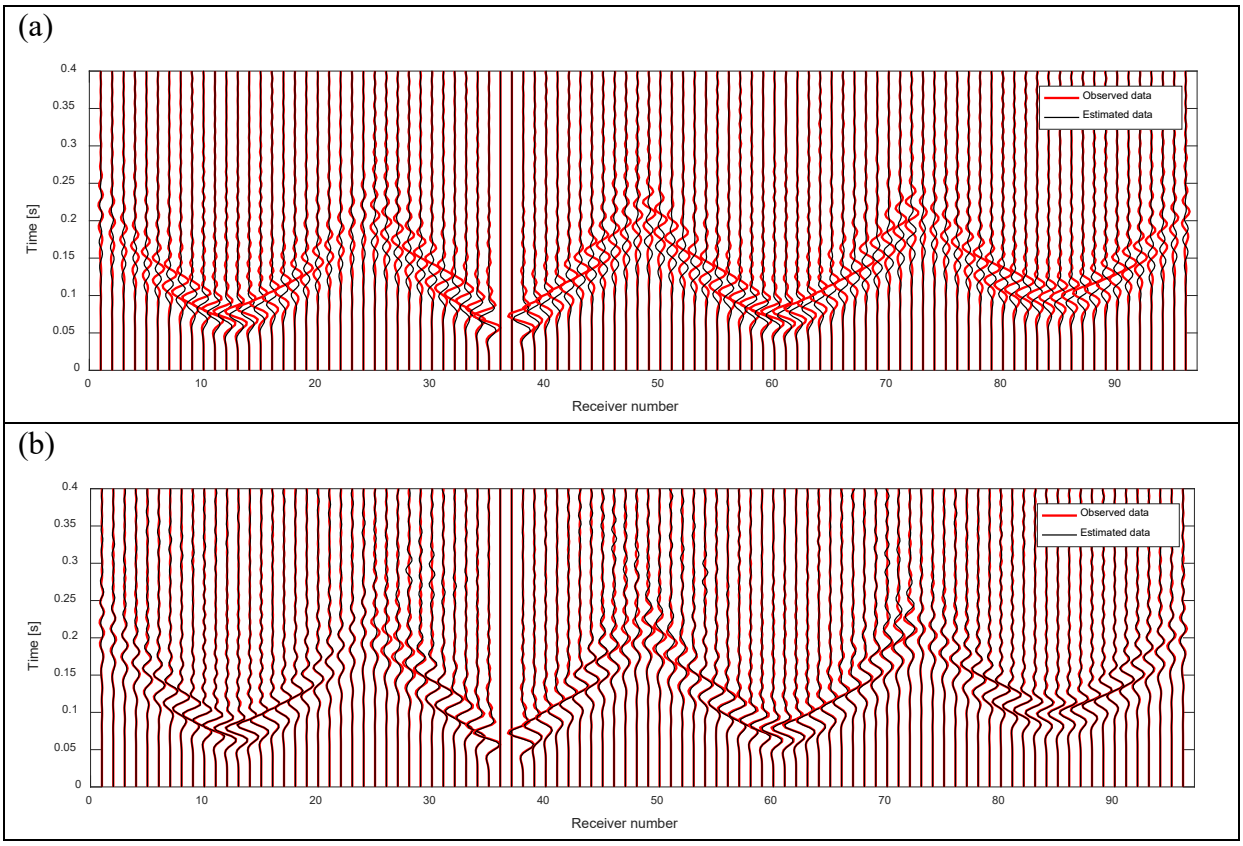

Figure 2.13: Synthetic model: waveform comparison for a sample shot associated with (a) the initial model and (b) the final inverted model.

2.4 Conclusion

A 3-D FWI algorithm for void detection has been developed for seismic wave analysis as part of this research. Convolutional perfectly matched layers, as well as parallelizing computations have been developed/implemented to reduce required computer time for 3-D waveform analyses. The FWI algorithm was tested on a synthetic model without a void. The inverted results show great aptitude for FWI to characterize soil-rock layering (strong over weak) using only surface data. The variable layer interfaces were accurately characterized, and true *Vs* and *Vp* values of layers were recovered.

CHAPTER 3

OPTIMIZATION OF THE TEST CONFIGURATION FOR 3-D FULL WAVEFORM VOID DETECTION

3.1 Introduction

After development of the 3-D FWI algorithm, the work focused on developing efficient test configurations (source and receiver locations) and investigation of the optimal frequency range of seismic data required for detection of voids in Florida geology. To achieve this, several parametric studies were performed with synthetic (computational) models. The objective was to relate the sizes and embedment depths of targeted voids to the test configurations and frequency content of measured data. The test configurations and required frequency range identified in this chapter will be applied to field experiments in Chapter 5 to minimize both field testing and data analysis efforts.

For the parametric studies, two synthetic models (hypothetical soil-rock profiles) were designed to represent the typical Florida geological condition with soils underlain by variable bedrock. One model includes a large void (4.5 m [15 ft] in diameter), and the other includes a small void (3 m [10 ft] in diameter). For each model, wave-fields were simulated with a range of test configurations and analyzed by the developed 3-D FWI algorithm (Chapter 2). For the work, 2-D uniform grids of receivers and shots at various spacing at 3 m (10 ft), 4.5 m (15 ft), and 6 m (20 ft) were studied on the ground surface. Subsequently, accuracy and resolution of inverted profiles were compared between the simulations to identify optimal test configurations.

The investigation also focused on identifying the properties of active source signatures. Specifically, a source signature can only generate a wave-field in a limited band of frequencies for an individual blow. However, both low frequency components (long wavelengths) are required for deep subsurface investigation and high frequency components (short wavelengths)

are needed for higher resolution. The study developed the optimal frequency for the active source properties (drop height, and sizes of impact plates) for the field experiments presented in the following chapters.

3.2 Large embedded void (4.5-m [15-ft] diameter at 9-m [30-ft] depth)

3.2.1 Test configuration

The developed 3-D FWI algorithm in Chapter 2 was tested on a synthetic model consisting of two soil-rock layers and a large buried void. The model domain of 36 m x 24 m x18 m ($120' \times 80 \times 60'$) (length x width x depth) consists of a soil layer overlying limestone, with Vs of 300 m/s (1,000 ft/s) and 600 m/s (2,000 ft/s), respectively (Figure 3.1, left). Poisson's ratio of 0.33 was assumed for the entire medium to calculate Vp (Figure 3.1, right). The void is 4.5 m x 4.5 m x 4.5 m ($15' \times 15' \times 15'$) with Vs = 0 m/s (Vs = 0 ft/s), Vp = 300 m/s (Vp = 1,000 ft/s) (air filled void), and located 9 m (30 ft) (two void diameters) below the ground surface.

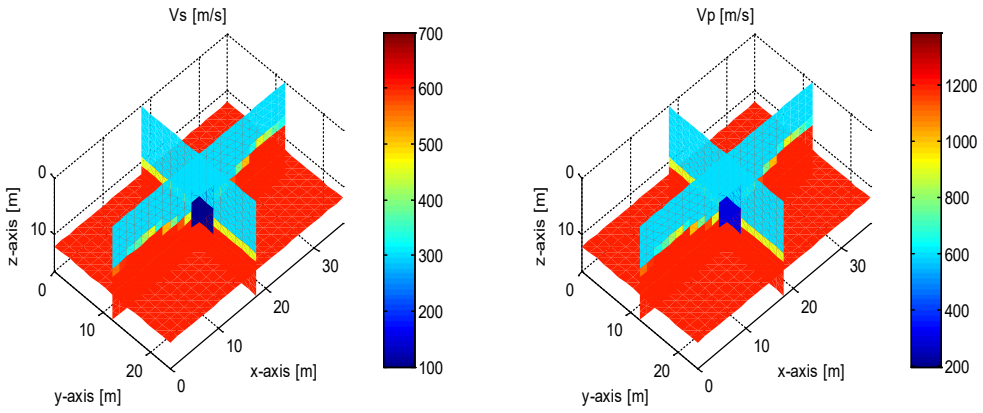

Figure 3.1: Synthetic model with a large void of 4.5-m (15-ft) diameter at 9-m (30-ft) depth

Three test configurations were analyzed to investigate the minimum number of sources and receivers that enabled a successful recovery of the subsurface geometrical and material related features including that of the embedded void. The tests were carried out in an increasing

order of source and receiver spacing on the surface starting from the least dense configuration pattern of 24 receivers and 35 shots and ending with the closest configuration of 96 receivers and 117 shots. Parameters such as the size of the grid, ease of setup in the field, and the number of receivers required for the recovery of the subsurface structure play an important role in determining source and receiver placement positions on the surface.

Shown in Figure 3.2 is the least dense test configuration plan that includes 24 receivers and 35 shots (sources) placed in a uniform grid of 6 × 4 at 6 m (20 ft) spacing for receivers (circles) and 7 × 5 at 6 m (20 ft) spacing for shots (crosses) in the x and y directions. Figure 3.3 depicts the test configuration plan for the medium dense shot and receiver placement case with a uniform grid of 8 × 5 at 4.5 m (15 ft) spacing for receivers and 9 × 6 at 4.5 m (15 ft) spacing for shots in the x and y directions. Lastly, Figure 3.4 shows the densest test configuration for a uniform grid of 12 × 8 at 3 m (10 ft) spacing for receivers and 13 × 9 at 3 m (10 ft) spacing for shots in the x and y directions. Note that all the geophone spacing used in the analysis are less than two void diameters.

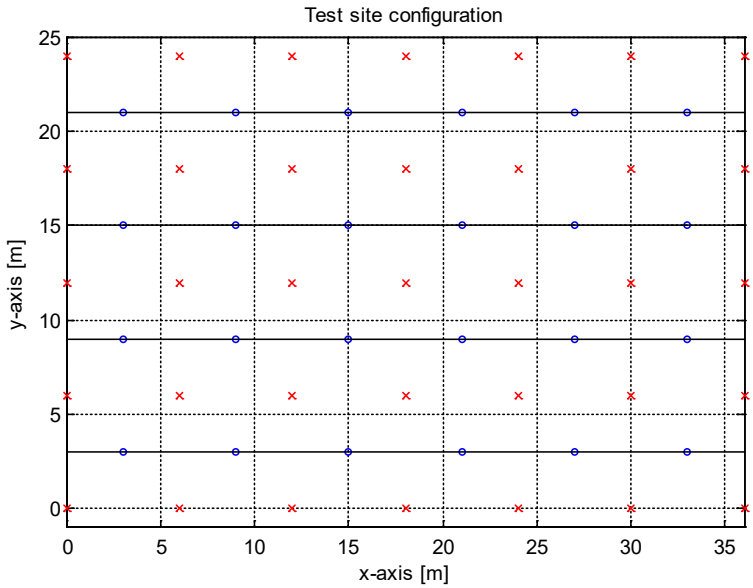

Figure 3.2: Test configuration 1: 24 receivers (circle) and 35 shots (cross) both at 6-m (20-ft) spacing.

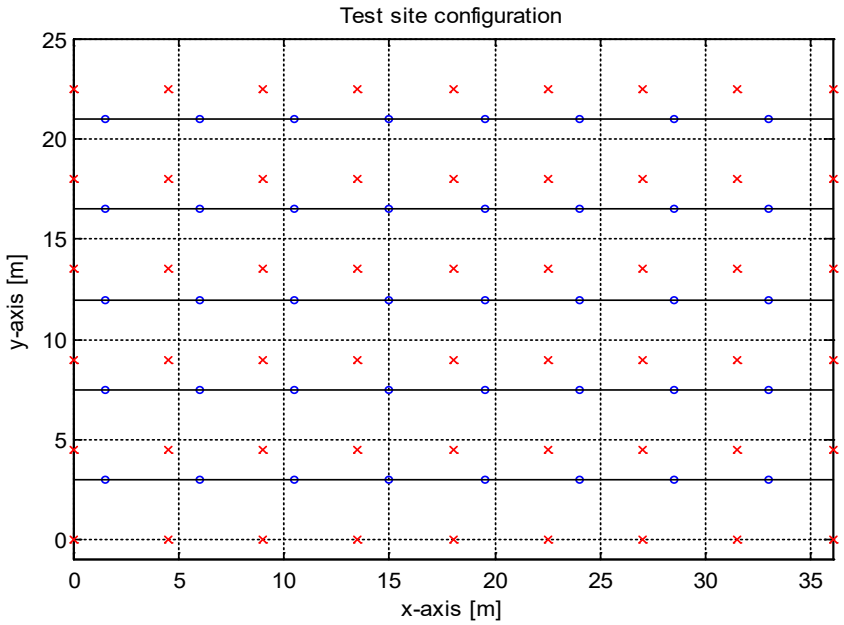

Figure 3.3: Test configuration 2: 40 receivers (circle) and 54 shots (cross) both at 4.5-m (15-ft) spacing.

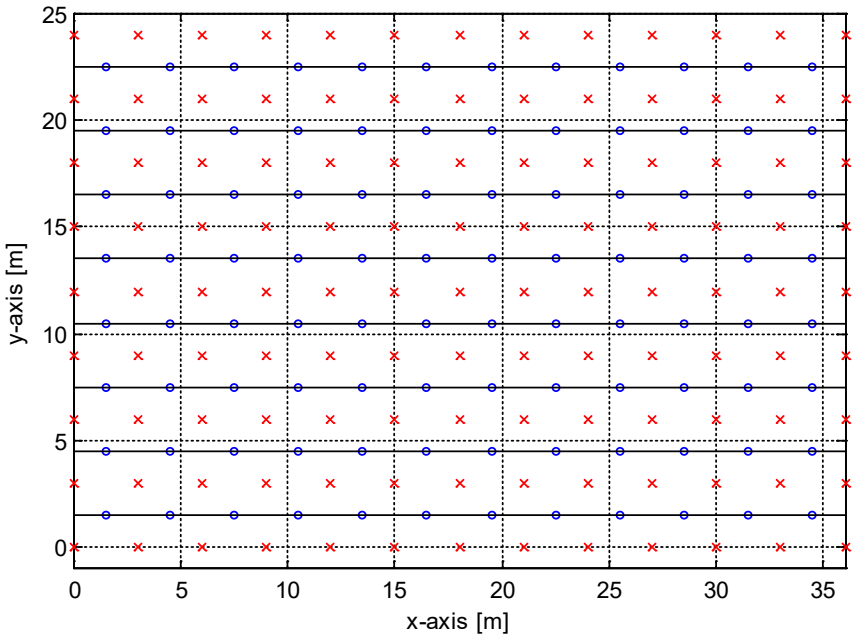

Figure 3.4: Test configuration 3: 96 receivers (circle) and 117 shots (cross) both at 3-m (10-ft) spacing.

3.2.2 Results for test configuration 1 (24 receivers)

The inversion analysis was first carried out for the least dense source and receiver configuration (Figure 3.2) of 24 receivers and 35 shots. The initial model used in the analysis was comprised of a 1-D velocity profile that linearly increased with depth with a Vs value of 300 m/s (1,000 ft/s) on the free surface (0-m depth) to 600 m/s (2,000 ft/s) at the bottom of the model (18-m [60-ft] depth) and a Vp value twice that of Vs (Figure 3.5b). Two inversion runs were conducted. The first run began with the low frequency range (5-25 Hz) data using the initial model described above. The second run was performed with the higher frequency range (5-35 Hz) data using the inverted results from first run as the input model. The first and second runs stopped after 20 and 17 iterations, respectively. Normalized least-squares error for all iterations of the two inversion runs are shown in Figure 3.6, where the error reduced from 1.0 at the onset of the first iteration to about 0.1 at the final iteration (iteration 20) of the first run, and to 0.02 in the second run.

The true model features including the void and the layer outline were recovered after the first inversion (Figure 3.5c). The second run with higher frequency data < 35 Hz improved the inverted model from the first run, particularly in the vicinity of the void region (Figure 3.5d). For a better view of the void, 2-D profile comparisons between true model and inverted model for Vs and Vp are presented for vertical profile (distance y = 12 m [y = 40 ft], Figure 3.7) and horizontal profile (depth z = 9 m [z = 30 ft], Figure 3.8). Apparently, both layers are well characterized, and the void is located correctly.

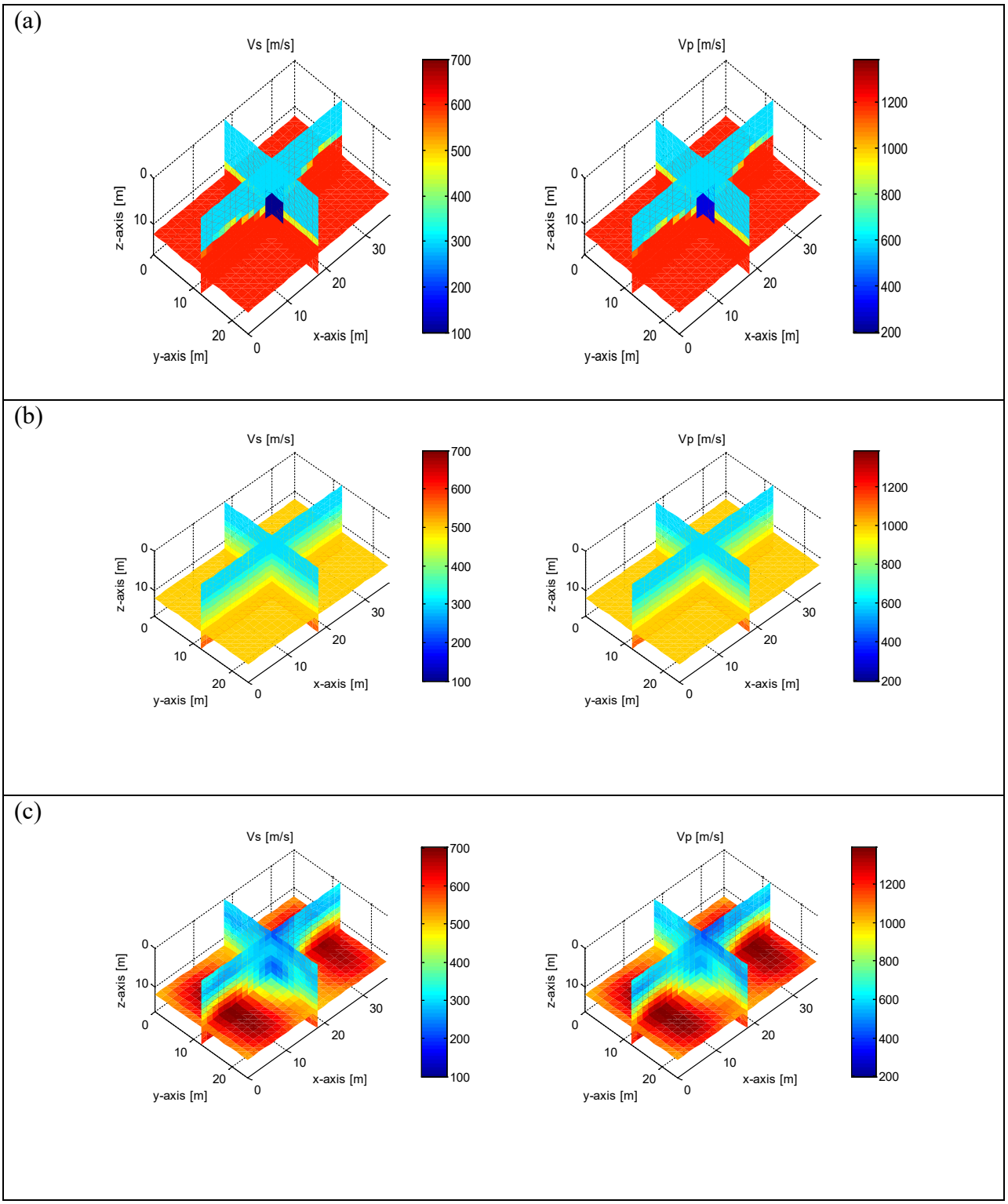

Figure 3.5: Synthetic model of S-wave and P-wave velocities (m/s): (a) true model; (b) initial model; (c) inverted model at 5-25 Hz; (d) inverted model at 5-35 Hz (big void, 24 receivers)

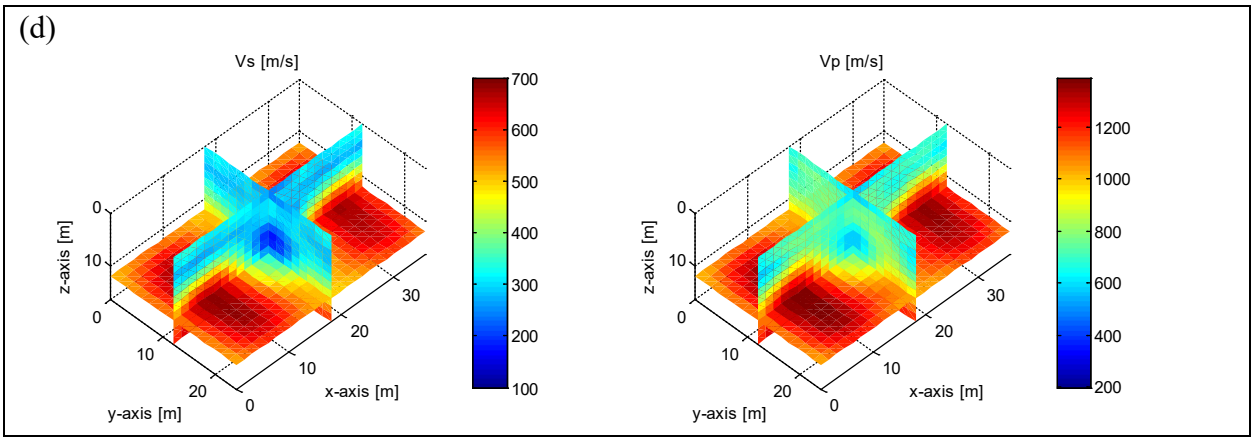

Figure 3.5: Synthetic model of S-wave and P-wave velocities (m/s): (a) true model; (b) initial model; (c) inverted model at 5-25 Hz; (d) inverted model at 5-35 Hz (big void, 24 receivers)

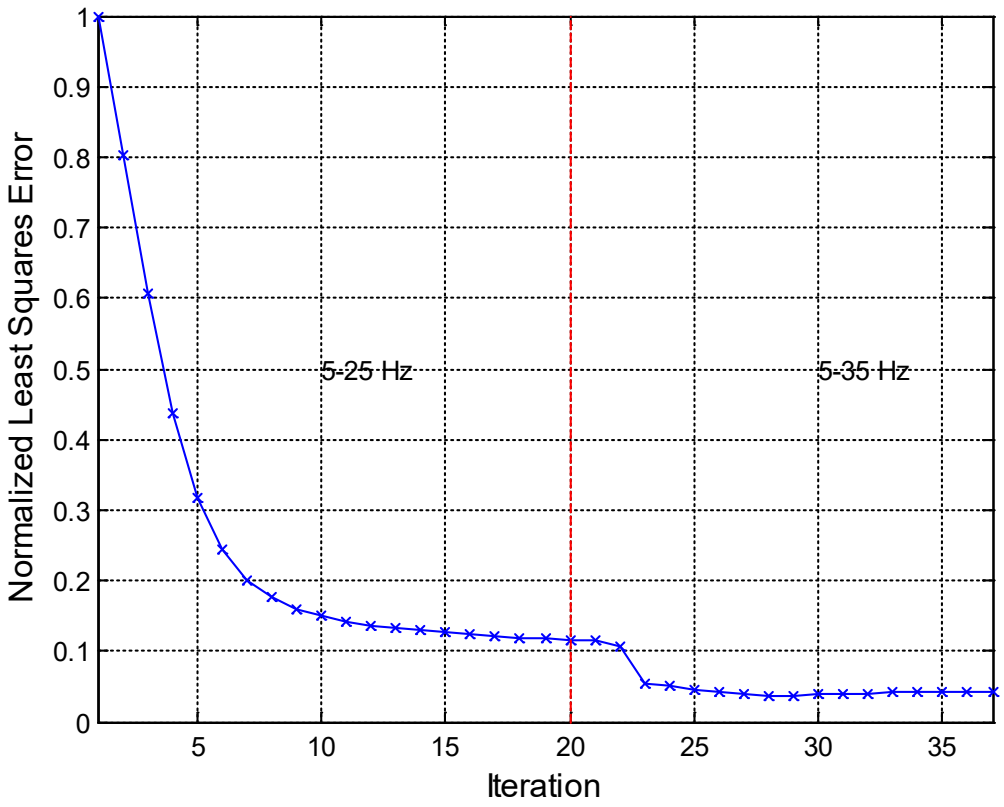

Figure 3.6: Normalized least square error (big void, 24 receivers)

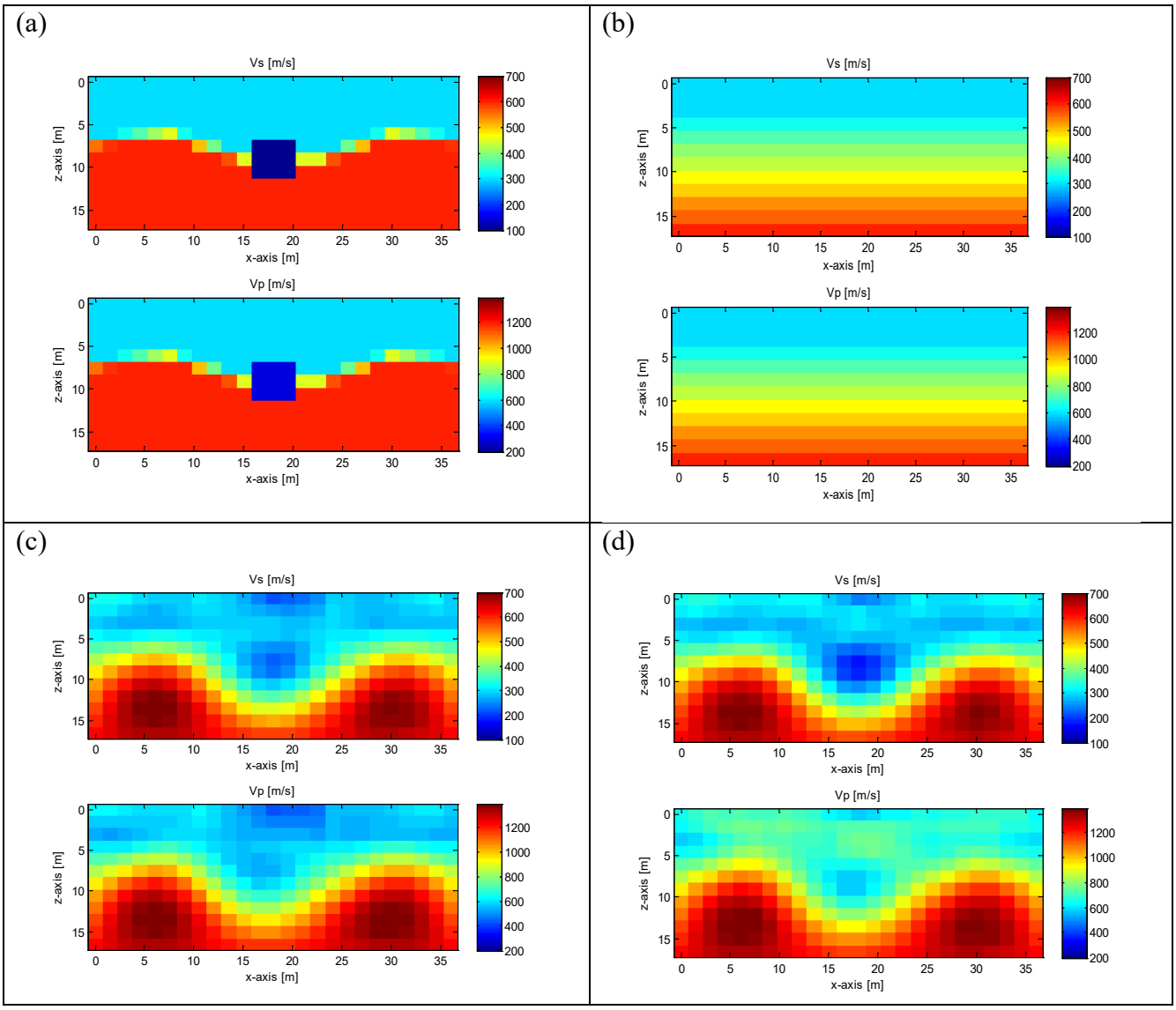

Figure 3.7: Vertical view of V_S and V_P (m/s) at the center of the void (y=12 m [y=40 ft]): (a) true model; (b) initial model; (c) inverted model at 5-25 Hz; (d) inverted model at 5-35 Hz (big void, 24 receivers).

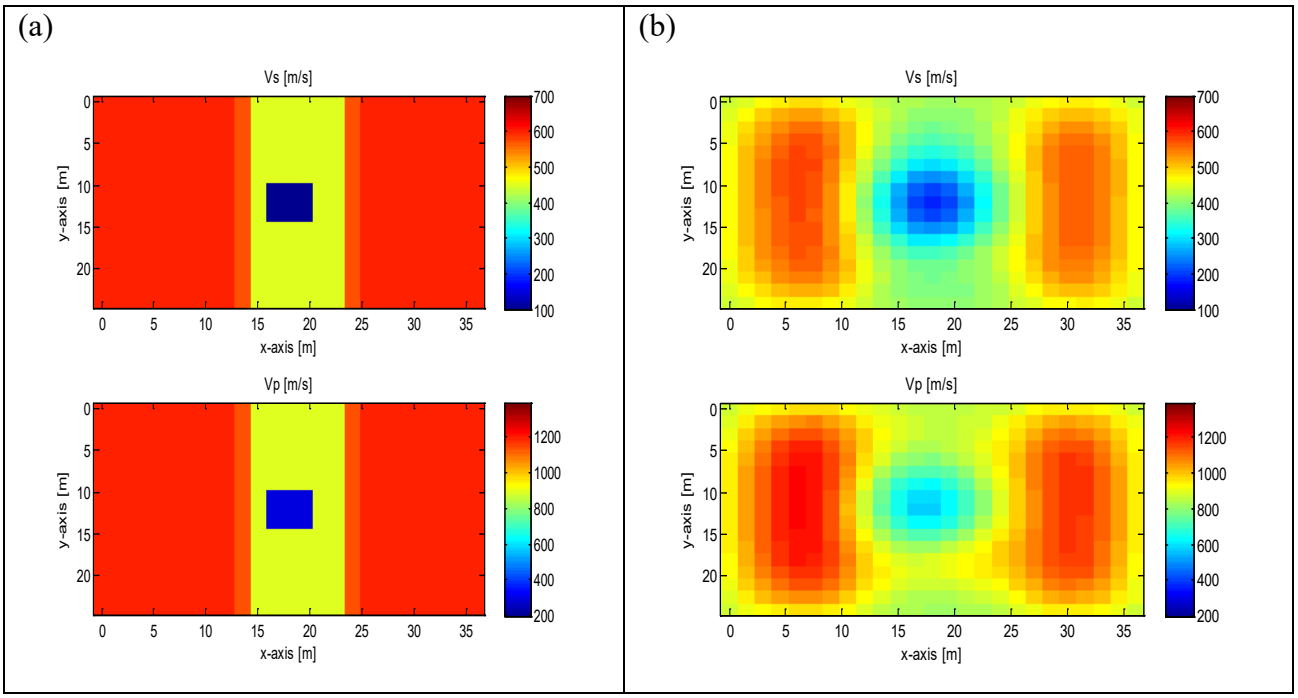

Figure 3.8: Horizontal view of (a) the true model and (b) the final inverted model for V_S and V_P at 9-m (30-ft) depth (big void, 24 receivers)

3.2.3 Results for test configuration 2 (40 receivers)

After the successful recovery of the subsurface features, including the position and shape of the void using a test configuration of 24 receivers, the inversion was tried with a test configuration of 40 receivers and 54 shots (Figure 3.3) to assess there are any improvements in the results, particularly for the P-wave velocity profile occurring in the void region. The inversion began with the same 1-D linearly increasing velocity profile of 300 m/s (1,000 ft/s) at the surface to 600 m/s (2,000 ft/s) at the bottom of the model for the V_S profile and V_P values twice that of V_S (Figure 3.9b).

Two inversion runs were again conducted, with the first run for the low frequency range (5-25 Hz) data using the initial model (Figure 3.9b) as input and the second run for higher frequency range (5-35 Hz) data using the result of the first run. The first and second runs stopped after 20 and 17 iterations, respectively. Normalized least squares error for all iterations of the two inversion runs are shown in Figure 3.10, where the error was reduced from 1.0 at the onset

of the first iteration to about 0.1 at the final iteration (iteration 20) of the first run, and 0.04 on the second run.

Similar to the previous case of 24 receivers, the true model features including the void and layer outline, along with velocity values are clearly recovered after the first run (Figures 3.9c). The second run with higher frequency data up to 35 Hz improved the inverted model from the first run, particularly around the void region (Figures 3.9d). The most noticeable improvement from the increase in the number of receivers from 24 in the previous analysis to 40 in the current analysis can be seen in P-wave velocity inversion results, where the void features are more clearly visualized (Figures 3.9d, right). Two-dimensional profile comparisons between true model and inverted model for V_S and V_P are presented in Figure 3.11 for vertical profile (distance y = 12 m [40 ft]) and in Figure 3.12 for the horizontal profile (depth z = 9 m [30 ft]). Improvements in void characterization, particularly for Vp profile are clearly seen in both figures.

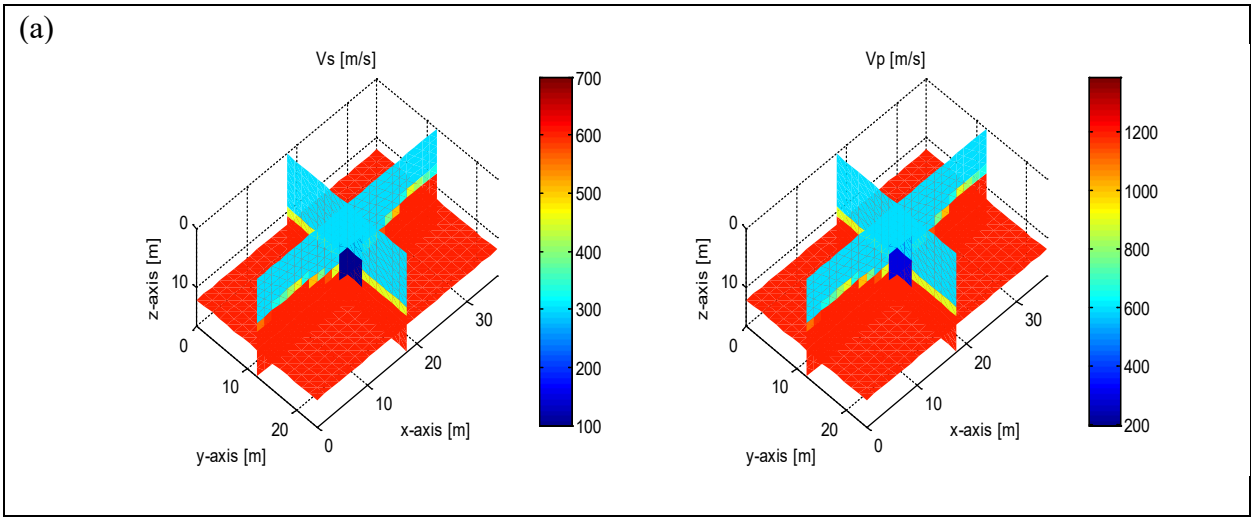

Figure 3.9: Synthetic model of S-wave and P-wave velocities (m/s): (a) true model; (b) initial model; (c) inverted model at 5-25 Hz; (d) inverted model at 5-35 Hz (big void, 40 receivers)

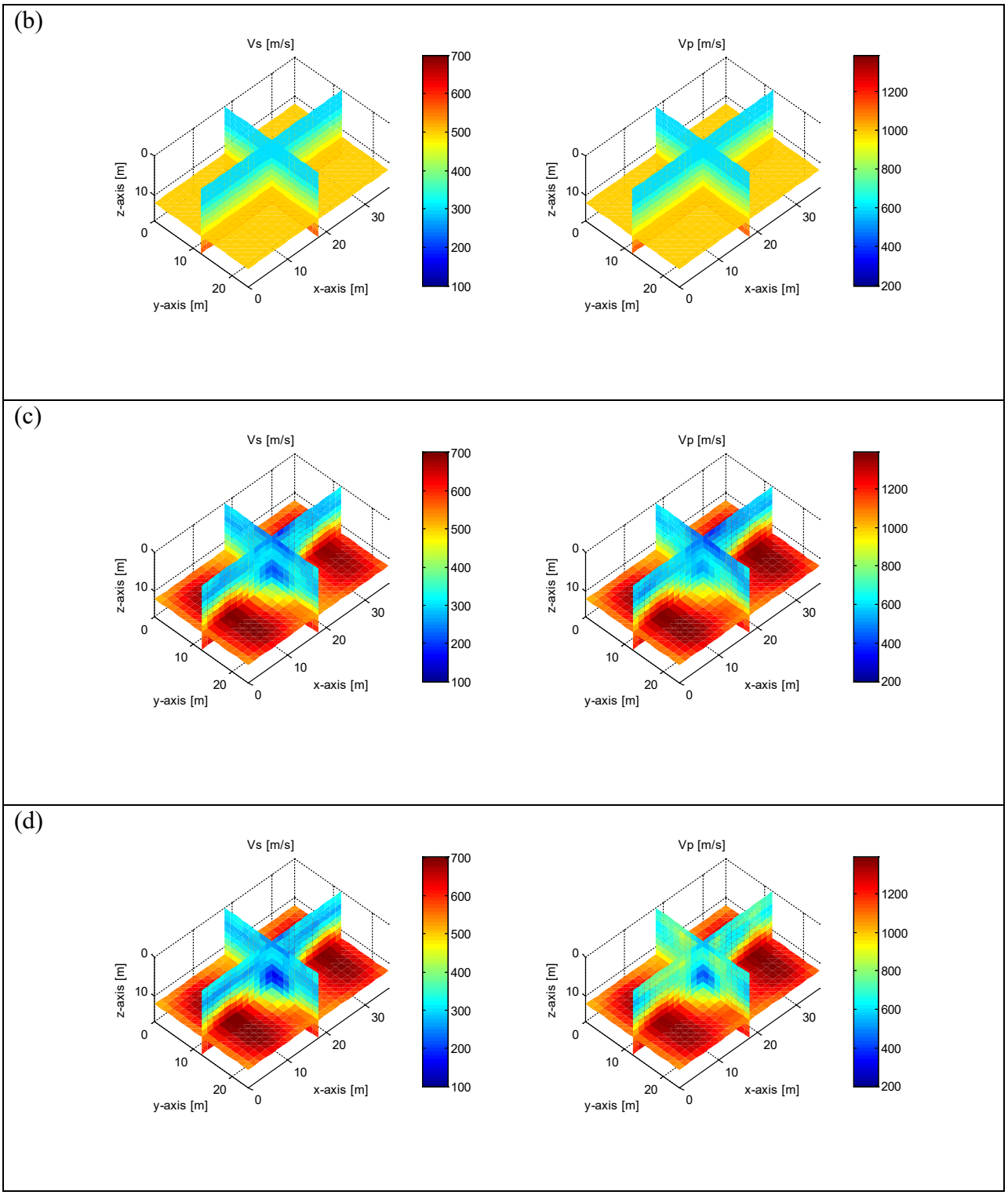

Figure 3.9: Synthetic model of S-wave and P-wave velocities (m/s): (a) true model; (b) initial model; (c) inverted model at 5-25 Hz; (d) inverted model at 5-35 Hz (big void, 40 receivers)

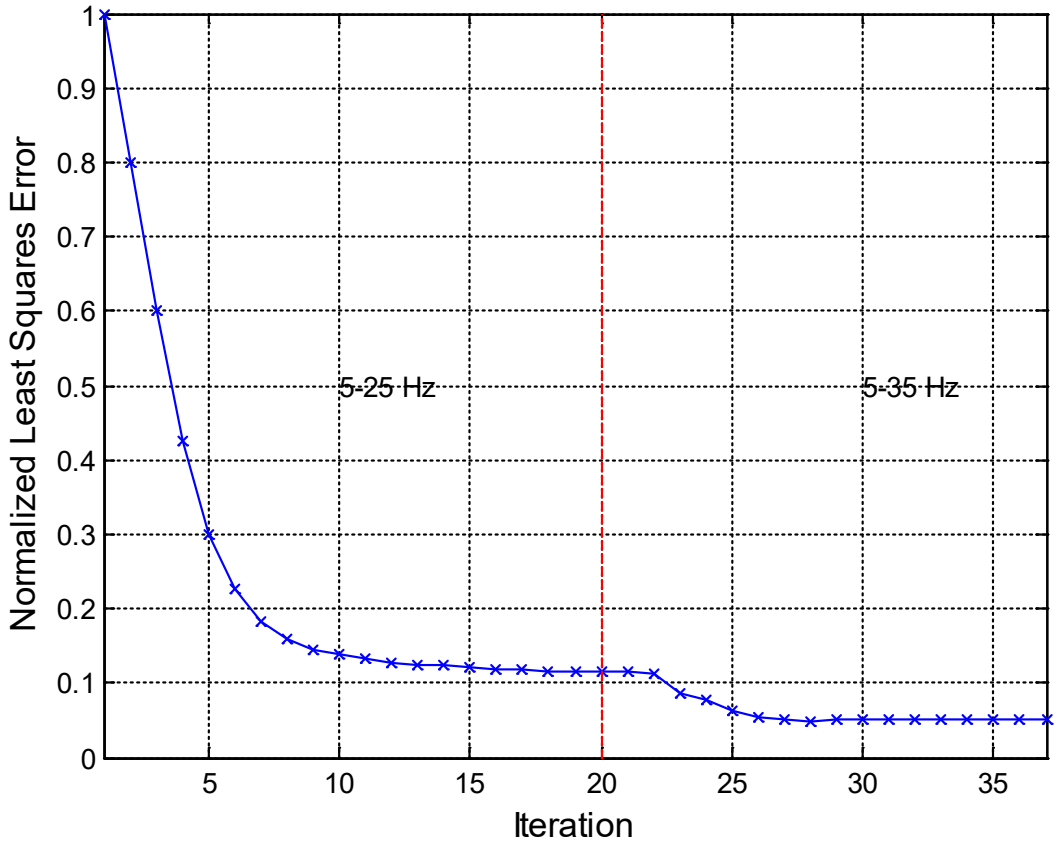

Figure 3.10: Normalized least square error (big void, 40 receivers)

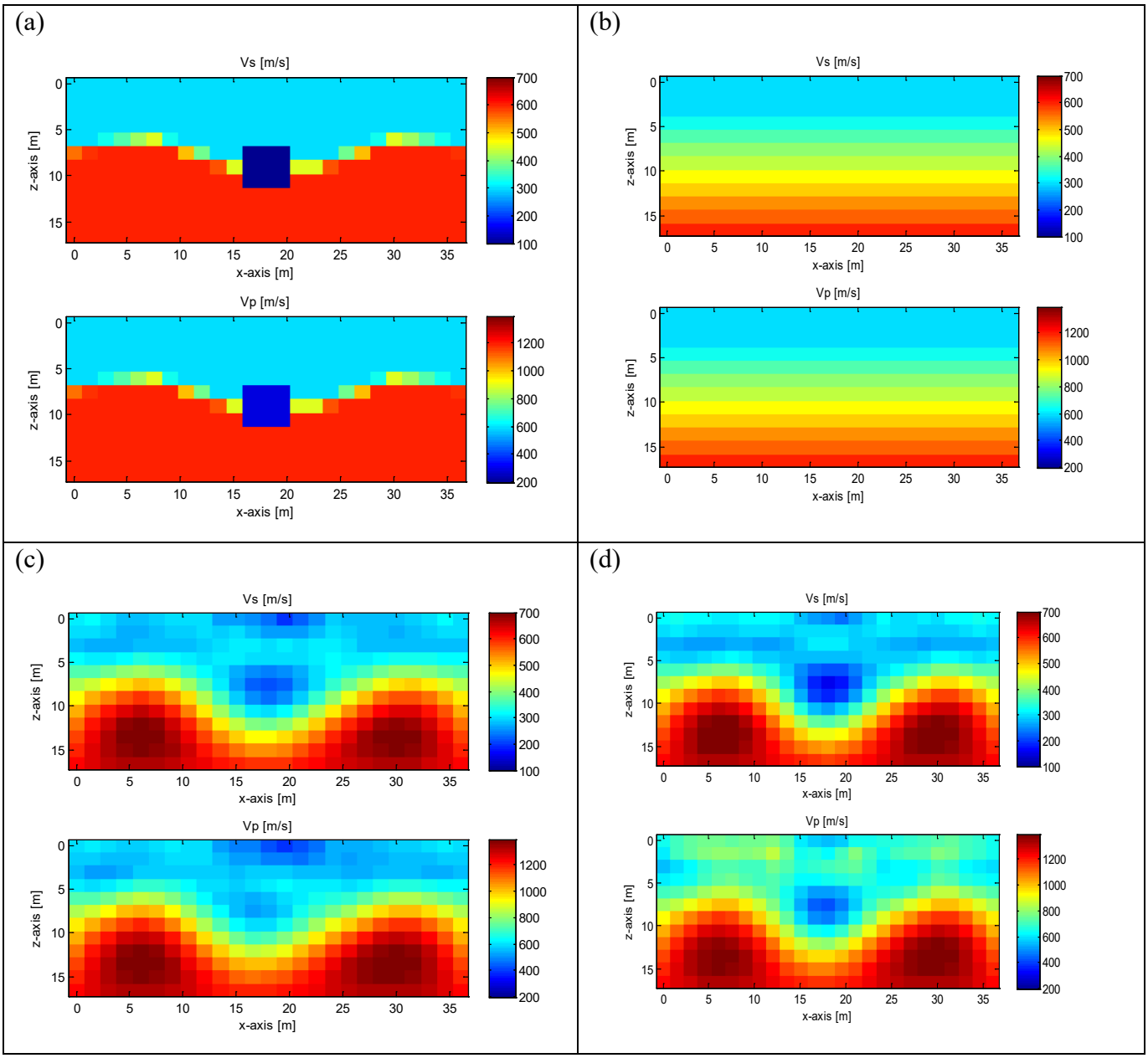

Figure 3.11: Vertical view of V_S and V_P (m/s) at the center of the void: (a) true model; (b) initial model; (c) inverted model at 5-25 Hz; (d) inverted model at 5-35 Hz (big void, 40 receivers).

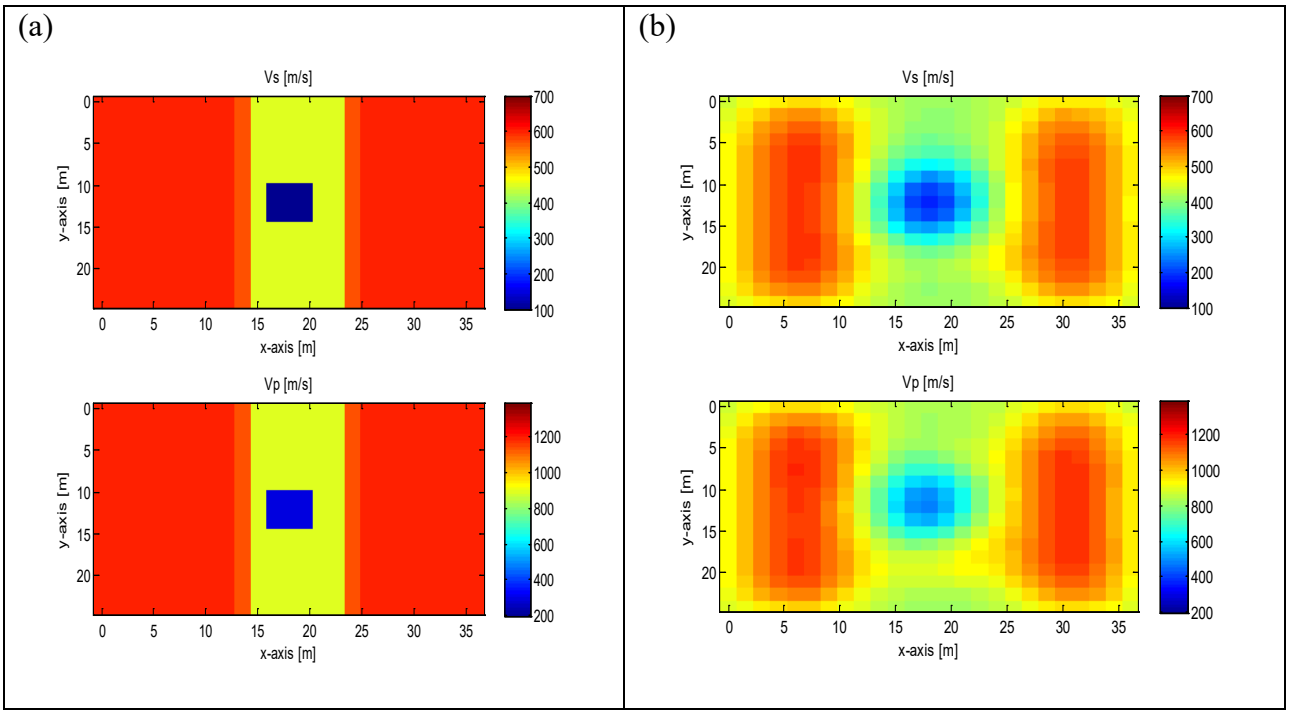

Figure 3.12: Horizontal view of (a) the true model and (b) the inverted model for V_s and V_p at 9-m (30-ft) depth (big void, 40 receivers)

3.2.4 Results for test configuration 3 (96 receivers)

Finally, the inversion was tried on the densest test configuration - 96 receivers and 117 shots (Figure 3.4) to identify any possible improvements over the previous two test configurations of 24 and 40 receivers. Similar to the two previous cases, the inversion began with a 1-D linearly increasing velocity profile of 300 m/s (1,000 ft/s) at the surface to 600 m/s (2,000 ft/s) at the bottom of the model for the V_S profile and V_P values twice that of V_S (Figure 3.13b). Again, two inversion runs were conducted with the first run for the low frequency range (5-25 Hz) data using the initial model (Figure 3-13 b) as input and the second run with the higher frequency range (5-35 Hz) data using the results of the first run as input. Normalized least-squares error for all iterations of the two inversion runs are shown in Figure 3.14. The error reduced from 1.0 at the start of the first iteration to less than 0.1 at the end of the analysis (iteration 34).

As expected from the previous two analyses, true model features including the void geometry and position were correctly characterized (Figures 3.13c and 3.13-D). However, increasing the number of receivers and shots from 40 and 54 respectively in the previous analysis to 96 and 117 in the current analysis, did not lead to any noticeable improvements in the inverted results. This is also evident from the comparison of vertical 2-D profiles (distance y = 12 m [40 ft], Figure 3.15) and horizontal profile (depth z = 9 m [30 ft], Figure 3.16) of velocity to that of the previous analysis (Figures 3.11 and 3.12), where a comparison of the inverted result and the true model is presented. The results suggest that using a receiver and shot spacing smaller than the targeted void diameter is not necessary, or a dense test configuration leads to data redundancy.

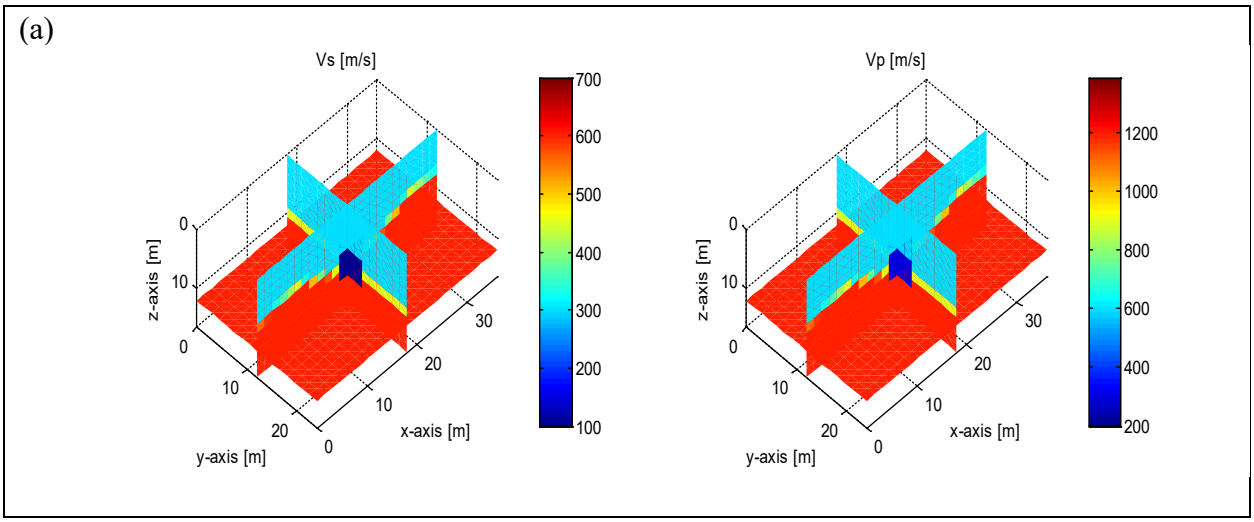

Figure 3.13: Synthetic model of V_S and V_P (m/s): (a) true model; (b) initial model; (c) inverted model at 5-25 Hz; (d) inverted model at 5-35 Hz (big void, 96 receivers)

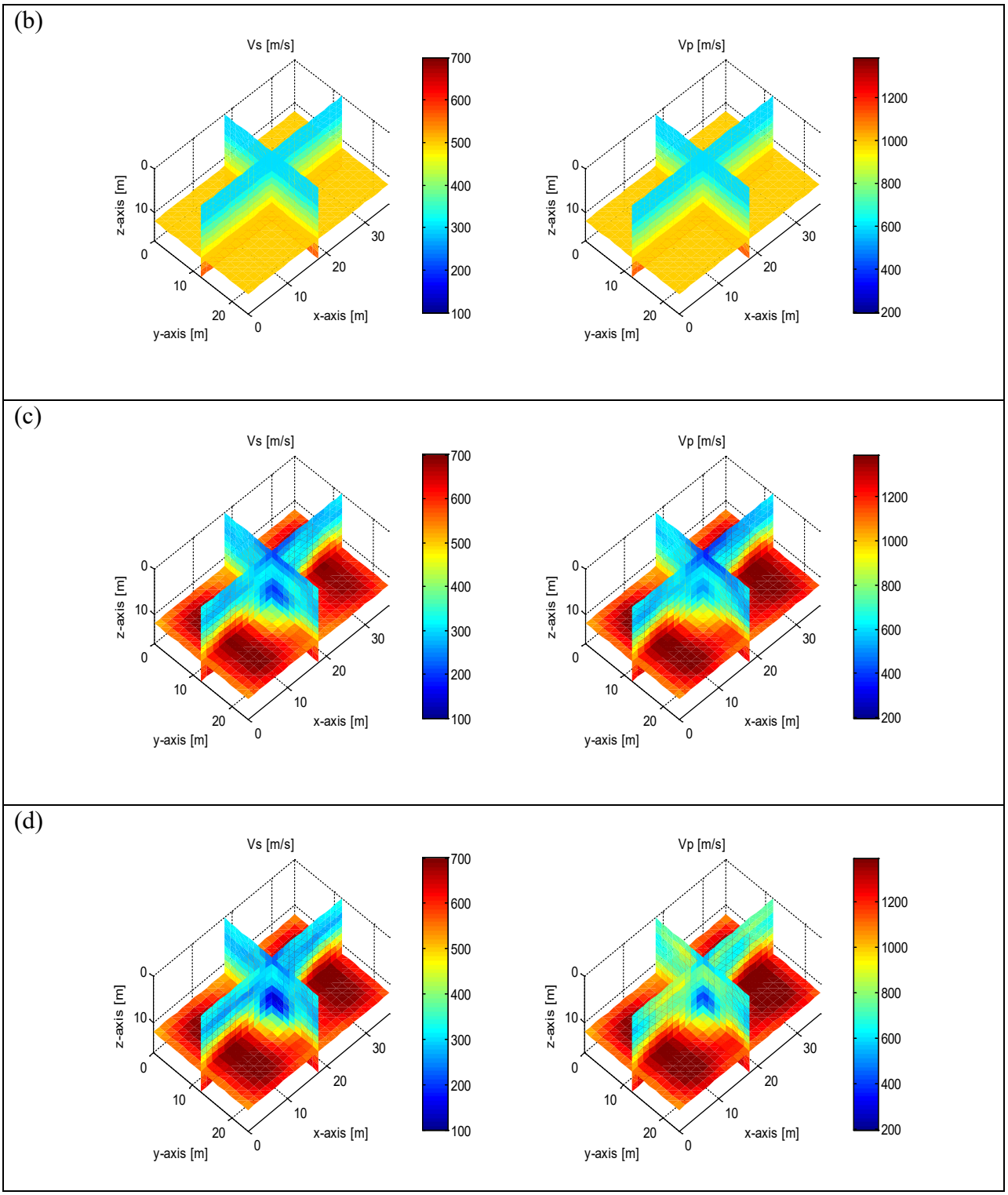

Figure 3.13: Synthetic model of V_S and V_P (m/s): (a) true model; (b) initial model; (c) inverted model at 5-25 Hz; (d) inverted model at 5-35 Hz (big void, 96 receivers)

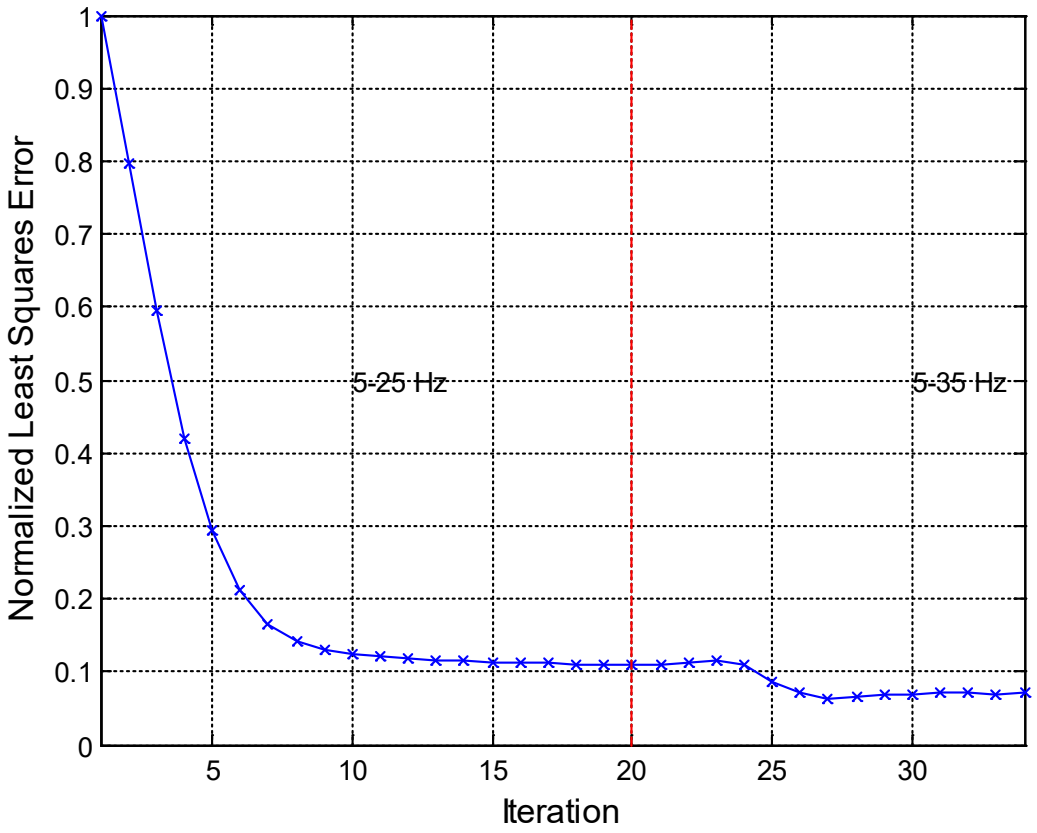

Figure 3.14: Normalized least square error (big void, 96 receivers)

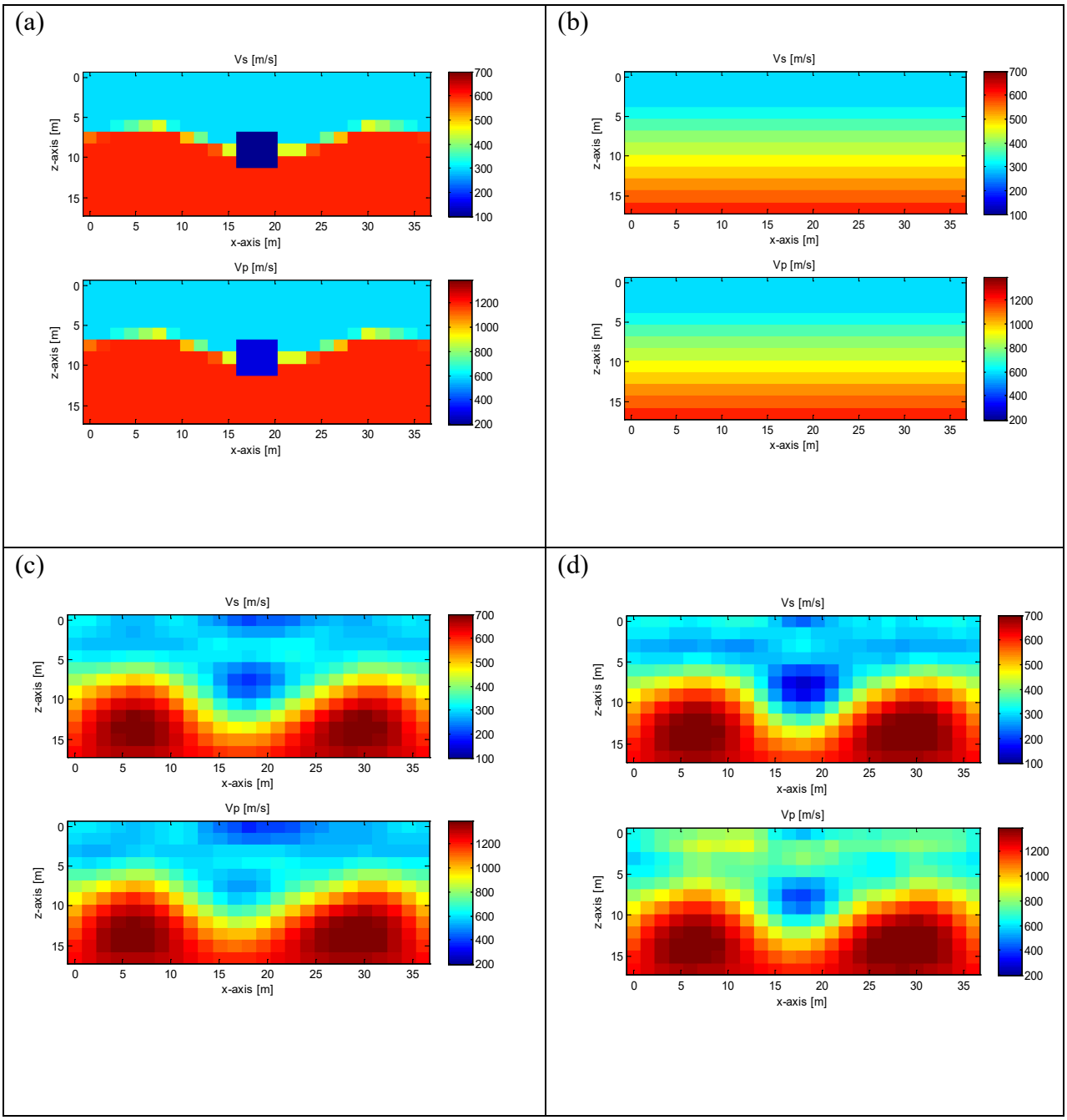

Figure 3.15: Vertical view of V_S and V_P (m/s) at the center of the void: (a) True model; (b) Initial model; (c) Inverted model at 5-25 Hz; (d) Inverted model at 5-35 Hz (big void, 96 receivers).

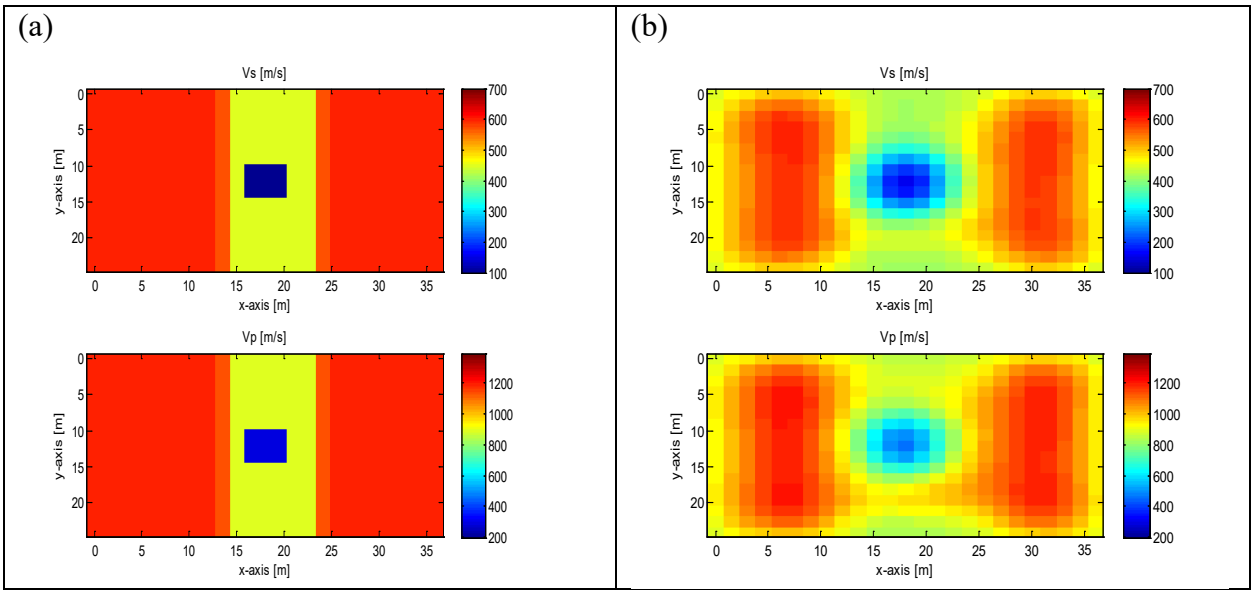

Figure 3.16: Horizontal view of (a) the true model and (b) the inverted model for V_S and V_P at 9-m (30-ft) depth (big void, 96 receivers)

3.3 Small embedded void (3-m [10-ft] diameter at 9-m [30-ft] depth)

3.3.1 Test configuration

With the successful recovery of a large void, the 3-D FWI algorithm was then tested on a smaller void of 3 m (10 ft) diameter embedded at the depth of 3 void diameters (depth z = 9m [30 ft]) as shown in Figure 3.17 a. The same three test configurations ranging from 24 to 96 receivers were used with uniform receiver grids of 6 × 4 at 6 m (20 ft), 8 × 5 at 4.5 m (15 ft), and 12 × 8 at 3 m (10 ft) spacing (circles), as well as shot grids of 7 × 5 at 6 m (20 ft), 9 × 6 at 4.5 m (15 ft), and 13 × 9 at 3 m (10 ft) spacing (crosses), respectively (Figures 3.2, 3.3 and 3.4).

3.3.2 Results for test configuration 1 (24 receivers)

The inversion was first tried on the least dense source and receiver spacing configurations (Figure 3.2) of 24 receivers and 35 shots. The initial model used in the analysis was comprised of a 1-D velocity profile that linearly increased with depth having a V_S value of 300 m/s (1,000 ft/s) on the free surface (0-m depth) to 600 m/s (2,000 ft/s) at the bottom of the model (18-m [60-ft] depth) and a V_P value twice that of V_S (Figure 3.17 b). Similar to the large void cases, two

inversion runs were conducted. The first run began with the low frequency range (5-25 Hz) data using the initial model (Figure 3.17b) and the second run employing the higher frequency range (5-35 Hz) data using the results from the first run as input.

Part of the true model features such as the model layering and velocity values for each layer were successfully recovered (Figures 3.17 c and d). However, the inversion was not successful at identifying or locating the void. This can be better visualized using a 2-D profile comparison between the true model and the inverted results for the 2-D vertical (distance y = 12 m [40 ft], Figure 3.18) and horizontal (depth z = 9 m [30 ft], Figure 3.19) profiles of the medium. Evident, the void location is only vaguely shown in Figure 3.19. A third inversion at higher frequency range (5-50 Hz) was also attempted, but again there was no improvement. It is believed that the lack of void characterization is due to the void's depth (3 void diameters), as well as the coarseness of shot and receiver configuration (shot and receiver spacing = 2 void diameters).

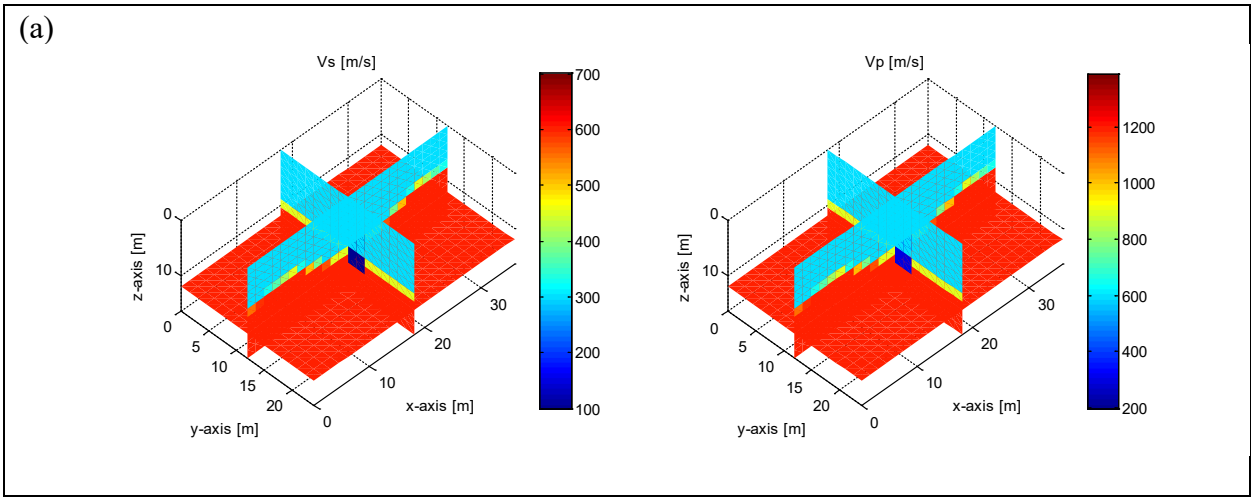

Figure 3.17: Synthetic model of S-wave and P-wave velocities (m/s): (a) true model; (b) initial model; (c) inverted model at 5-25 Hz; (d) inverted model at 5-35 Hz (small void, 24 receivers)

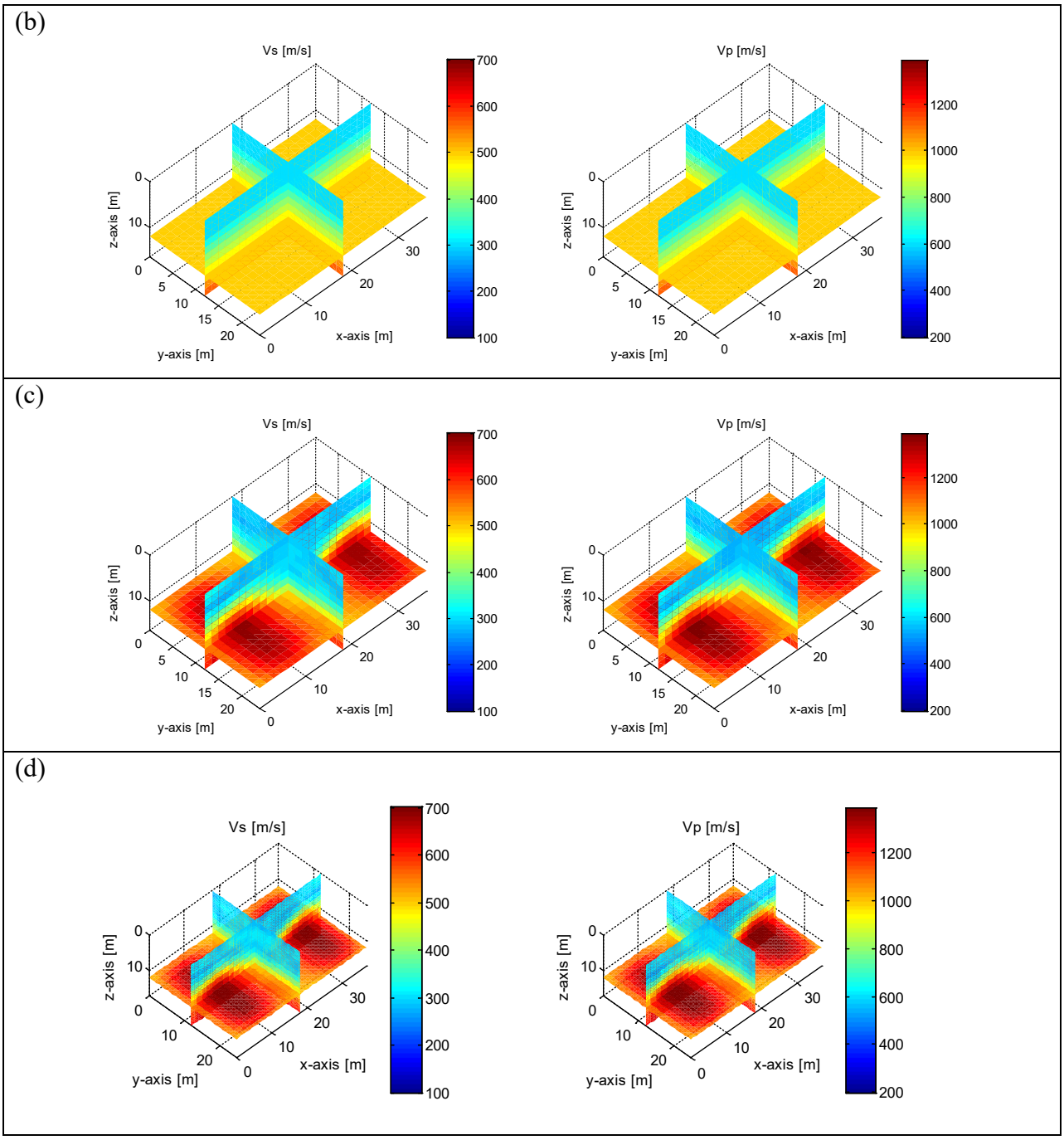

Figure 3.17: Synthetic model of S-wave and P-wave velocities (m/s): (a) true model; (b) initial model; (c) inverted model at 5-25 Hz; (d) inverted model at 5-35 Hz (small void, 24 receivers)

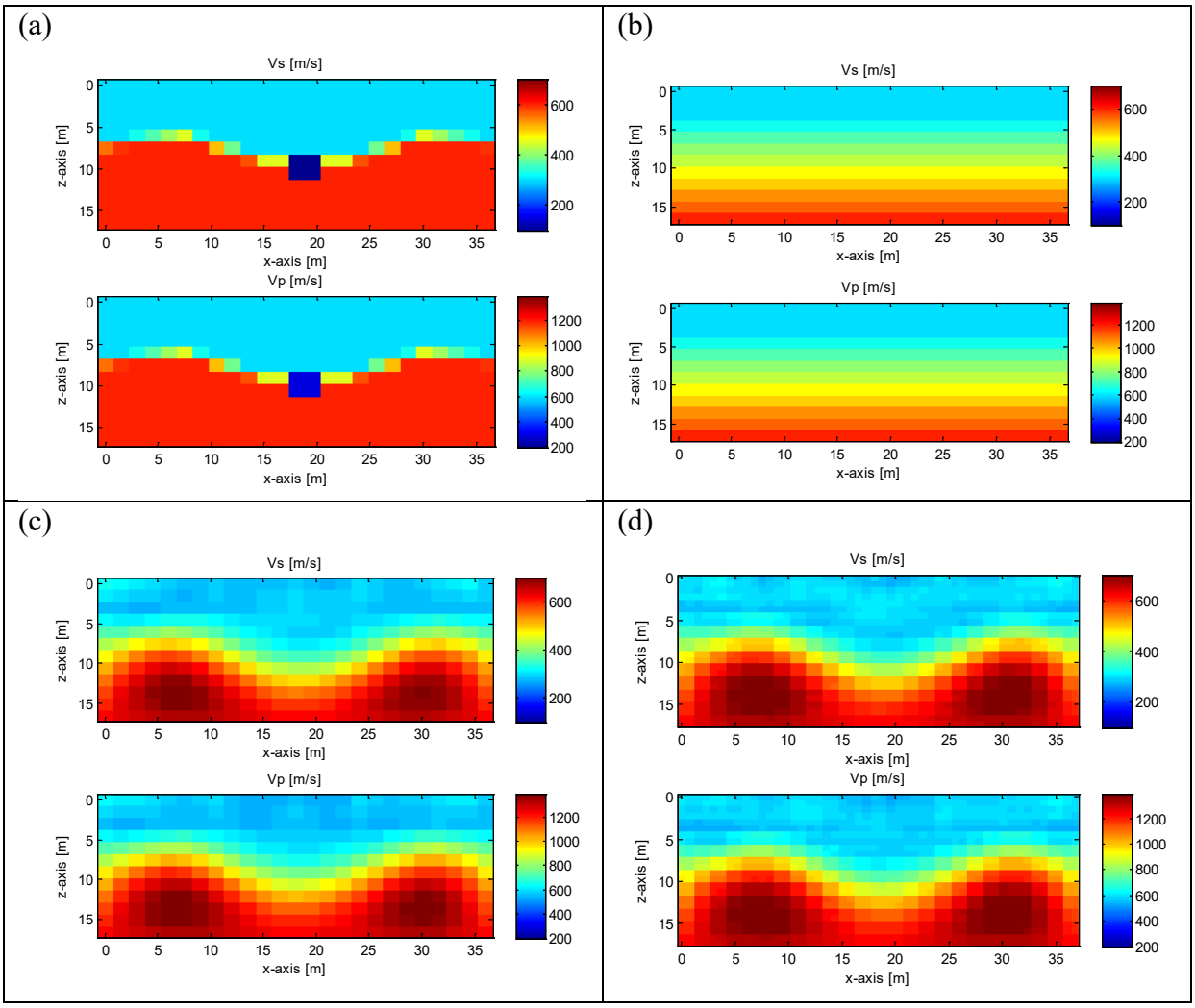

Figure 3.18: Vertical view of V_S and V_P (m/s) at the center of the void (y=12 m [y=40 ft]): (a) true model; (b) initial model; (c) inverted model at 5-25 Hz; (d) inverted model at 5-35 Hz (small void, 24 receivers).

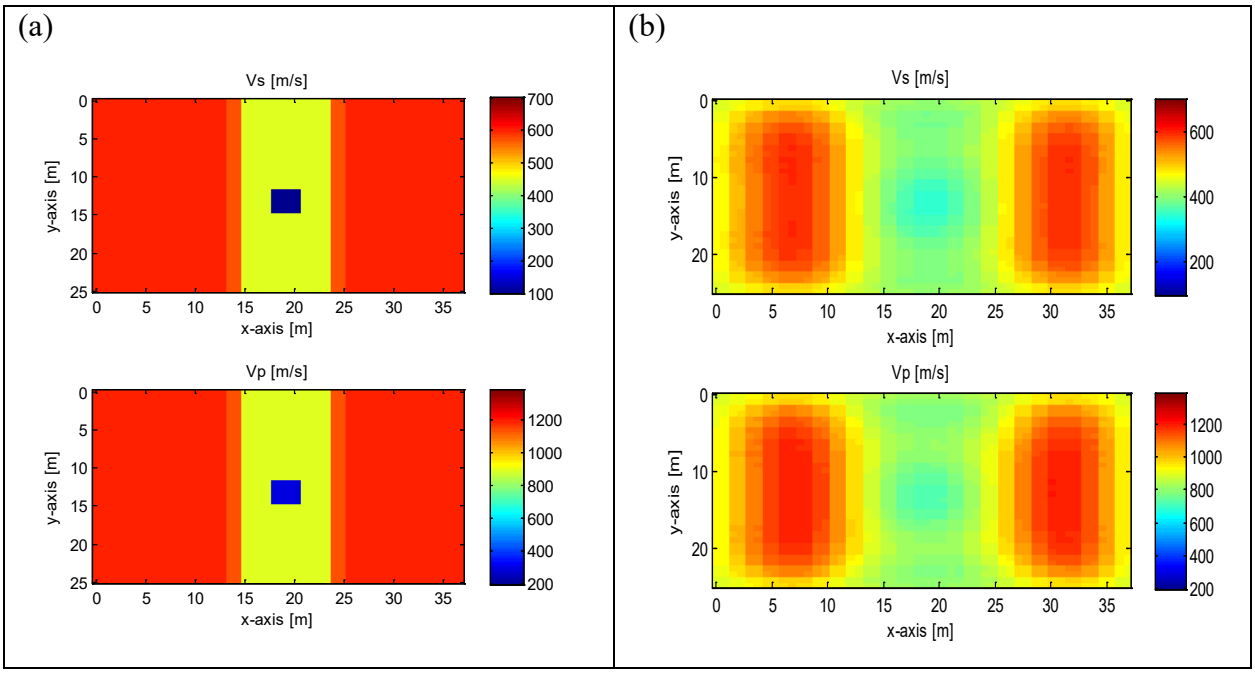

Figure 3.19: Horizontal view of (a) the true model and (b) the inverted model for V_S and V_P at 9-m (30-ft) depth (small void, 24 receivers)

3.3.3 Results for test configuration 2 (40 receivers)

To improve the results, the inversion was performed using test configuration 2 with 40 receivers and 54 shots (Figure 3.3) placed at 4.5 m (15 ft) spacing that is less than twice the void size of 3 m (10 ft). Similar to the previous analyses, the initial model consisted of a 1-D linearly increasing velocity profile of V_S value increasing from 300 m/s (1,000 ft/s) on the frees surface (0-m depth) to 600 m/s (2,000 ft/s) at the bottom of the model (18-m [60-ft] depth) and V_P twice that of V_S (Figure 3.20 b). The first inversion run began with the low frequency range (2.25 Hz) data using the initial model (Figure 3.20 b) and the second run employed the higher frequency range (5-35 Hz) data using the results of the first run as input.

Again, only part of the true model features such as model layering and velocity values for each layer were characterized (Figures 3.20 c and d). Two-dimensional profile comparisons between the true model and the inverted results at a vertical distance y = 12 m (40 ft), (Figure

3.21) and horizontal depth z = 9 m (30 ft) (Figure 3.22) show that the void is not correctly characterized. Figure 3.22 only vaguely shows the possible existence of a void.

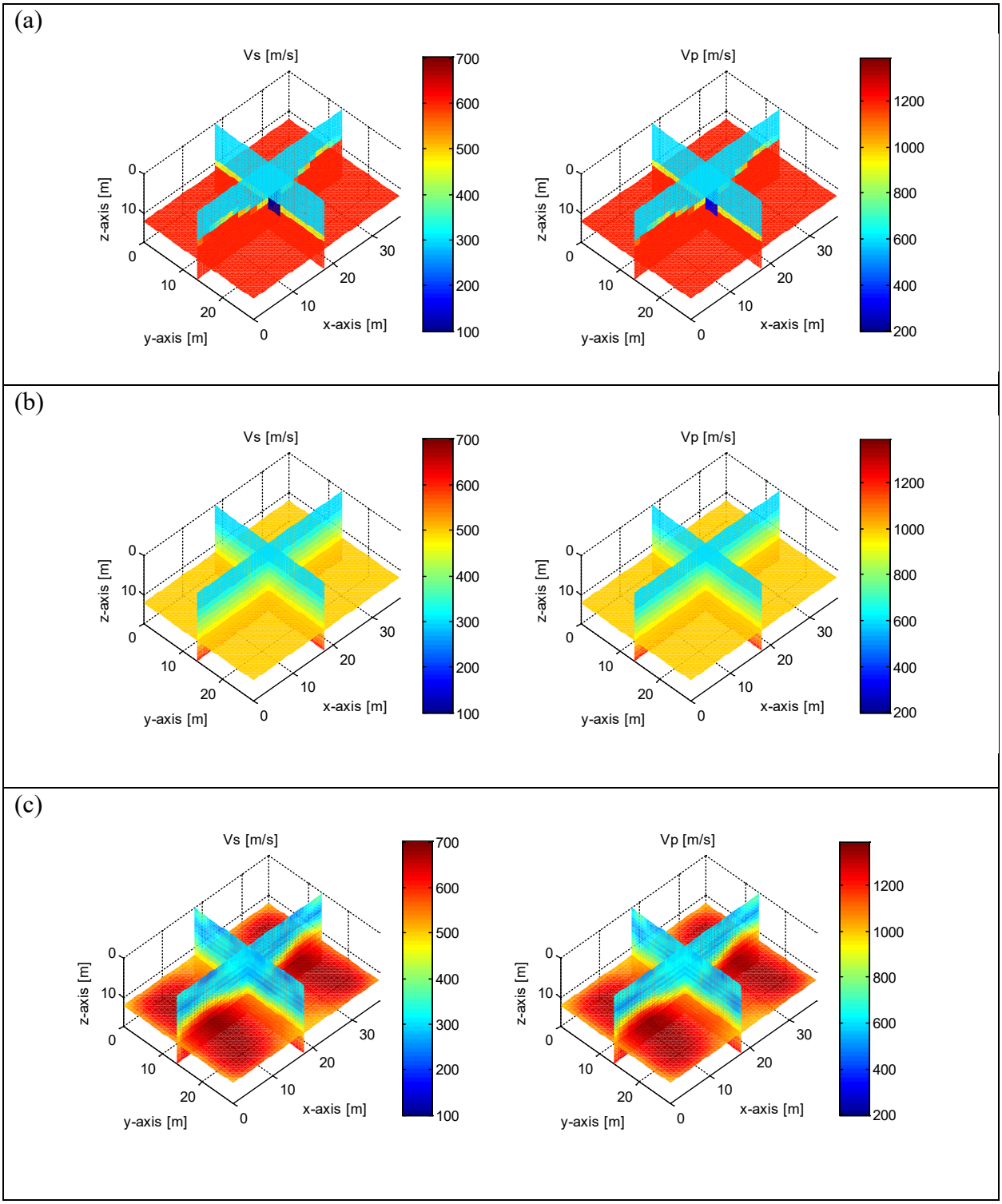

Figure 3.20: Synthetic model of S-wave and P-wave velocities (m/s): (a) true model; (b) initial model; (c) inverted model at 5-25 Hz; (d) inverted model at 5-35 Hz (small void, 40 receivers)

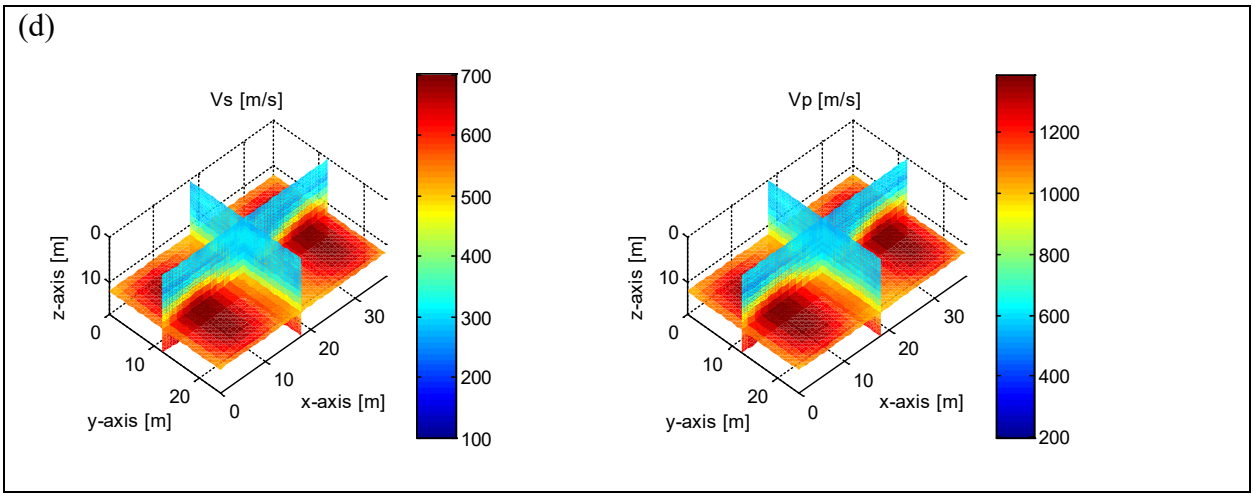

Figure 3.20: Synthetic model of S-wave and P-wave velocities (m/s): (a) true model; (b) initial model; (c) inverted model at 5-25 Hz; (d) inverted model at 5-35 Hz (small void, 40 receivers)

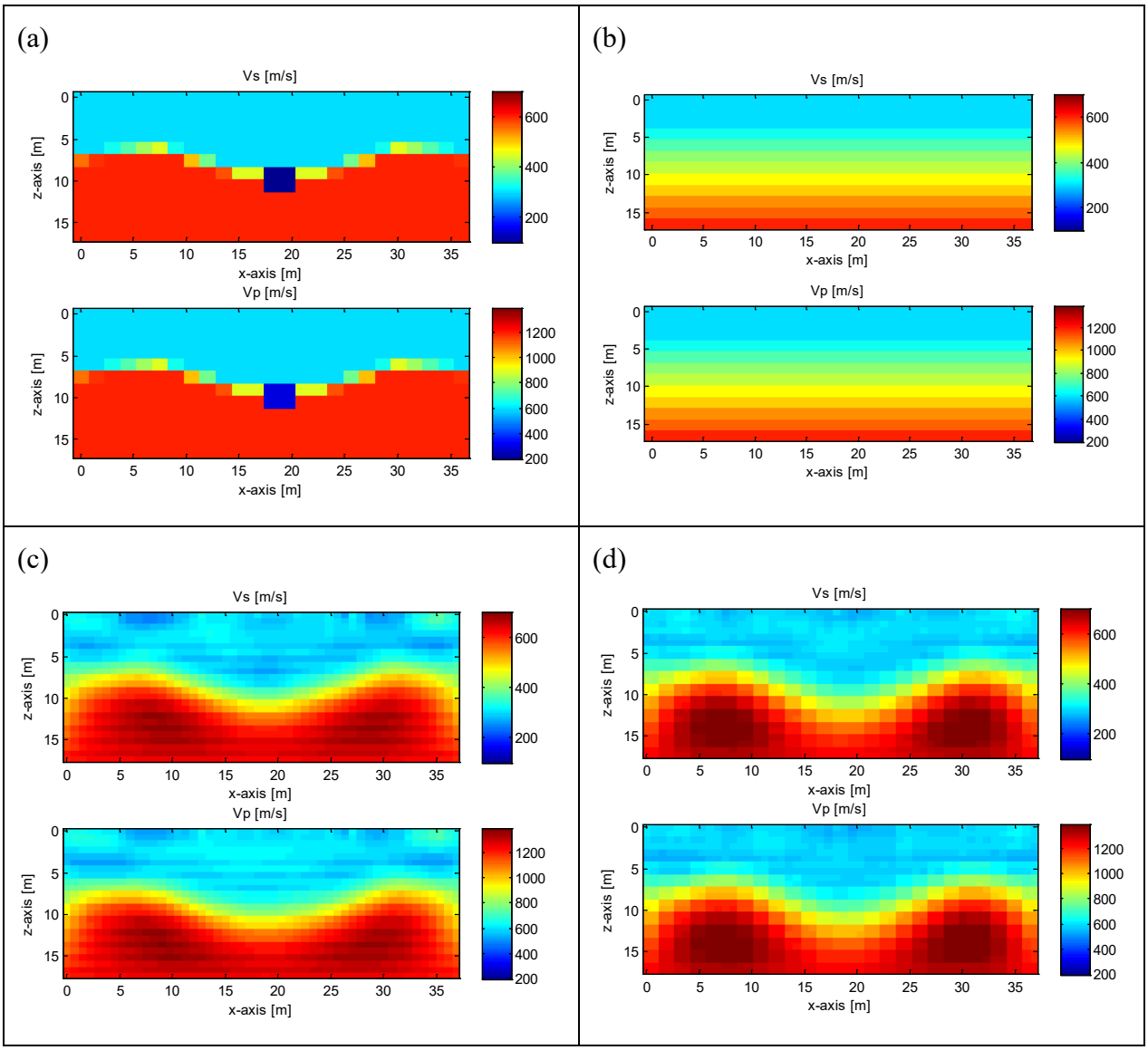

Figure 3.21: Vertical view of V_s and V_p (m/s) at the center of the void: (a) true model; (b) initial model; (c) inverted model at 5-25 Hz; (d) inverted model at 5-35 Hz (small void, 40 receivers).

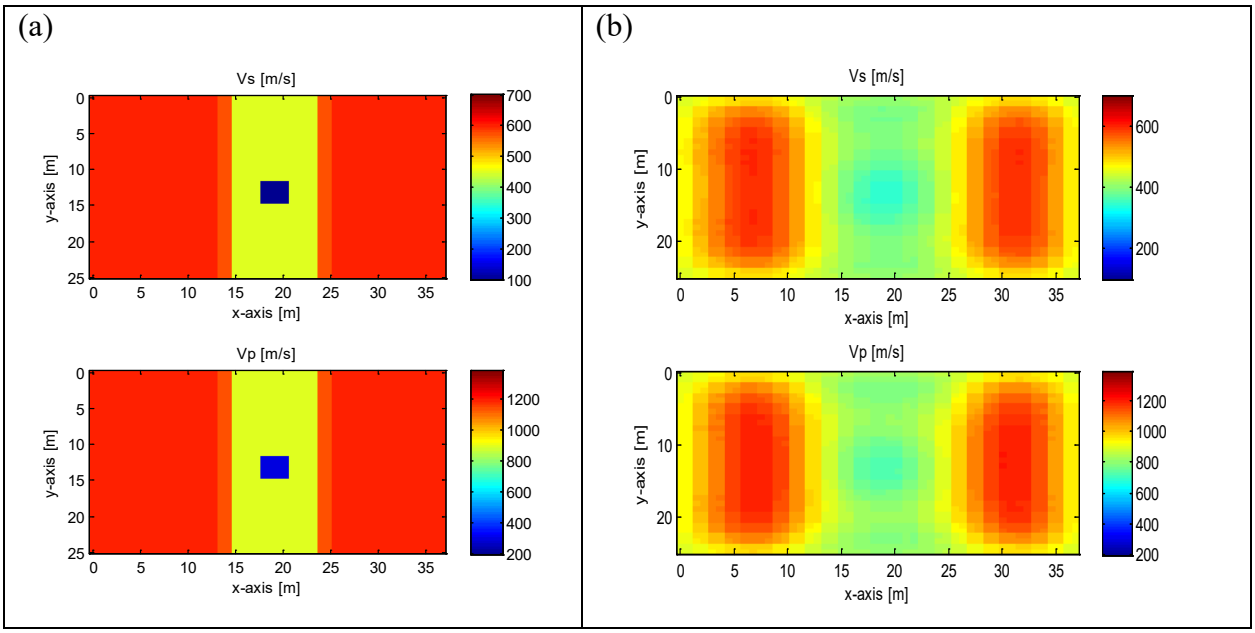

Figure 3.22: Horizontal view of (a) the true model and (b) the inverted model for V_S and V_P at 9-m (30-ft) depth (small void, 40 receivers)

3.3.4 Results for test configuration 3 (96 receivers)

Finally, the inversion was tried with test configuration 3, which consists of 96 receivers and 117 shots (Figure 3.4). Like previous cases, a 1-D linearly increasing velocity profile with a value of 300 m/s (1,000 ft/s) at the surface (0-m depth) to 600 m/s (2,000 ft/s) at the bottom of the model for V_S and twice that for V_P is used (Figure 3.23 b).

Similar to the results from the previous two analyses of test configurations 1 and 2, true model features including the layer interface geometry, position and layer velocity values are successfully recovered and characterized (Figures 3.23c and 3.23-D). There has also been an improvement in void characterization. This is mostly evident from the comparison of the vertical profile (distance y = 12 m [y = 40 ft], Figure 3.24) and horizontal profile (depth z = 9 m [z = 30 ft], Figure 3.25) to that of the previous analyses (Figures 3.18, 3.19, 3.21 and 3.22), particularly for high frequency range (5-33 Hz) data. The void position, shape, and velocity values are successfully recovered, as shown in Figures 3.24d and particularly 3.25b. Normalized least-

squares error for all iterations of the two inversion runs are shown in 3.26, where the error reduced from 1.0 at the start of the first iteration to less than 0.05 at the end of the first run (iteration 16) and further in the second run.

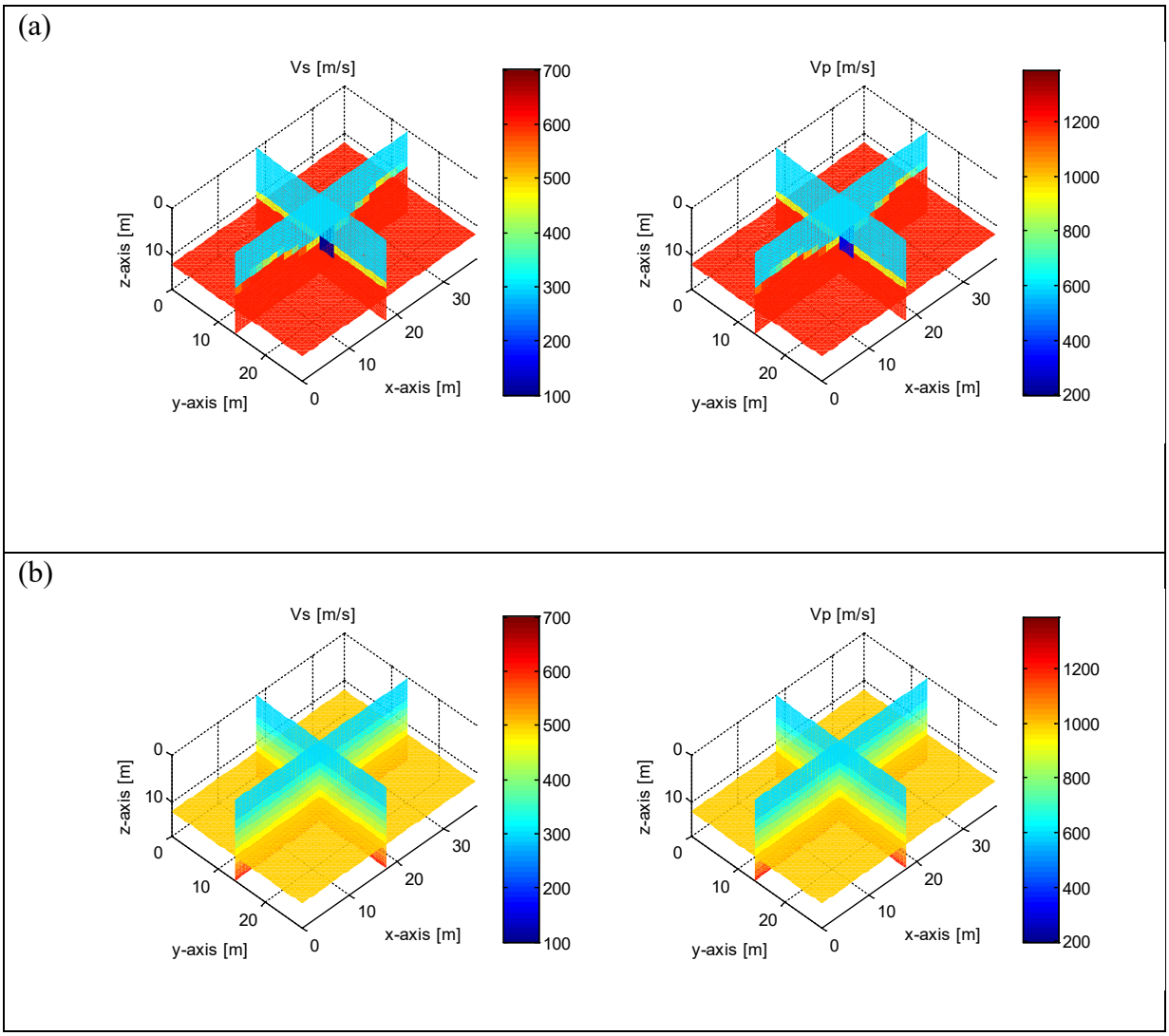

Figure 3.23: Synthetic model of S-wave and P-wave velocities (m/s): (a) true model; (b) initial model; (c) inverted model at 5-25 Hz; (d) inverted model at 5-35 Hz (small void, 96 receivers)

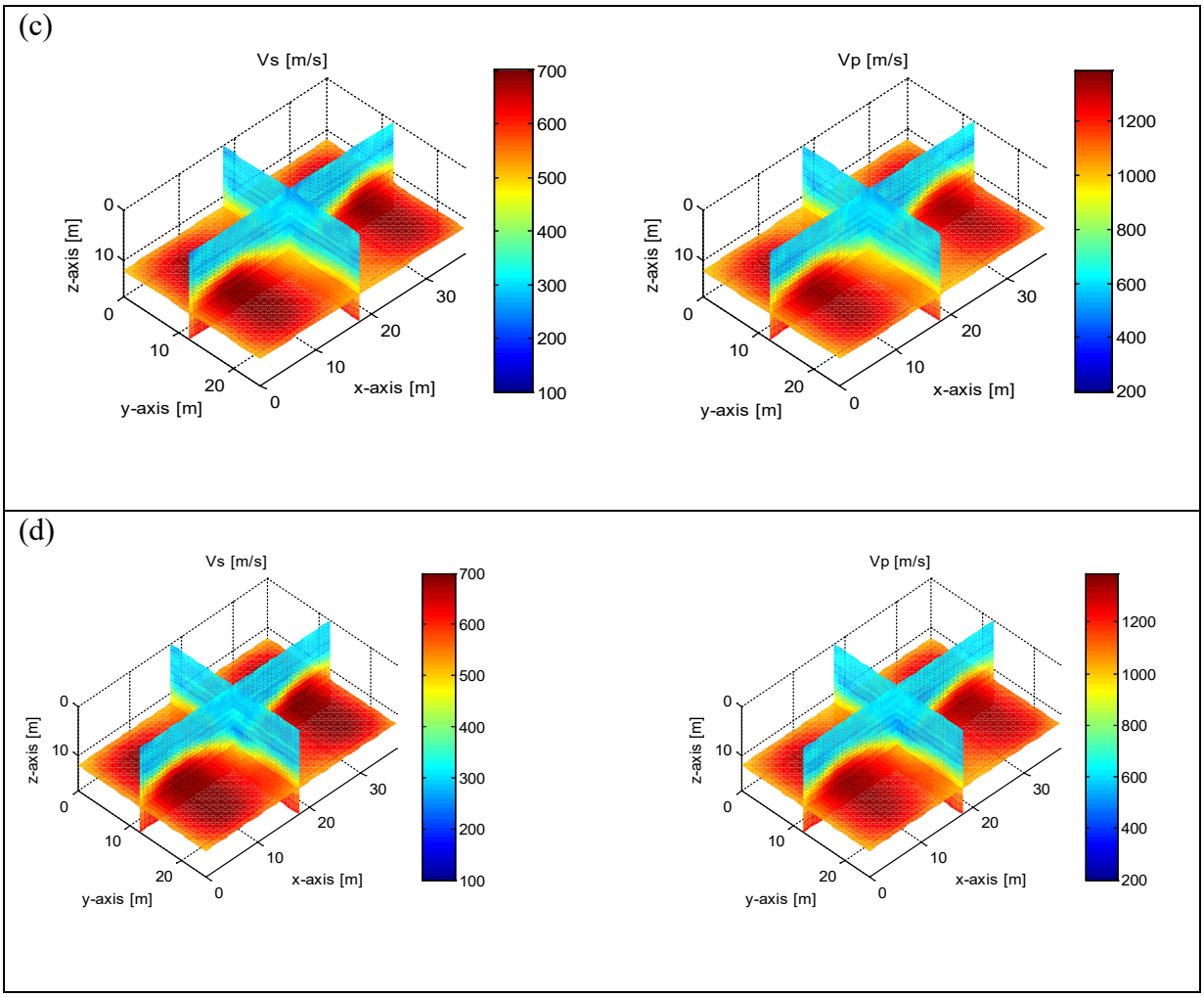

Figure 3.23: Synthetic model of S-wave and P-wave velocities (m/s): (a) true model; (b) initial model; (c) inverted model at 5-25 Hz; (d) inverted model at 5-35 Hz (small void, 96 receivers)

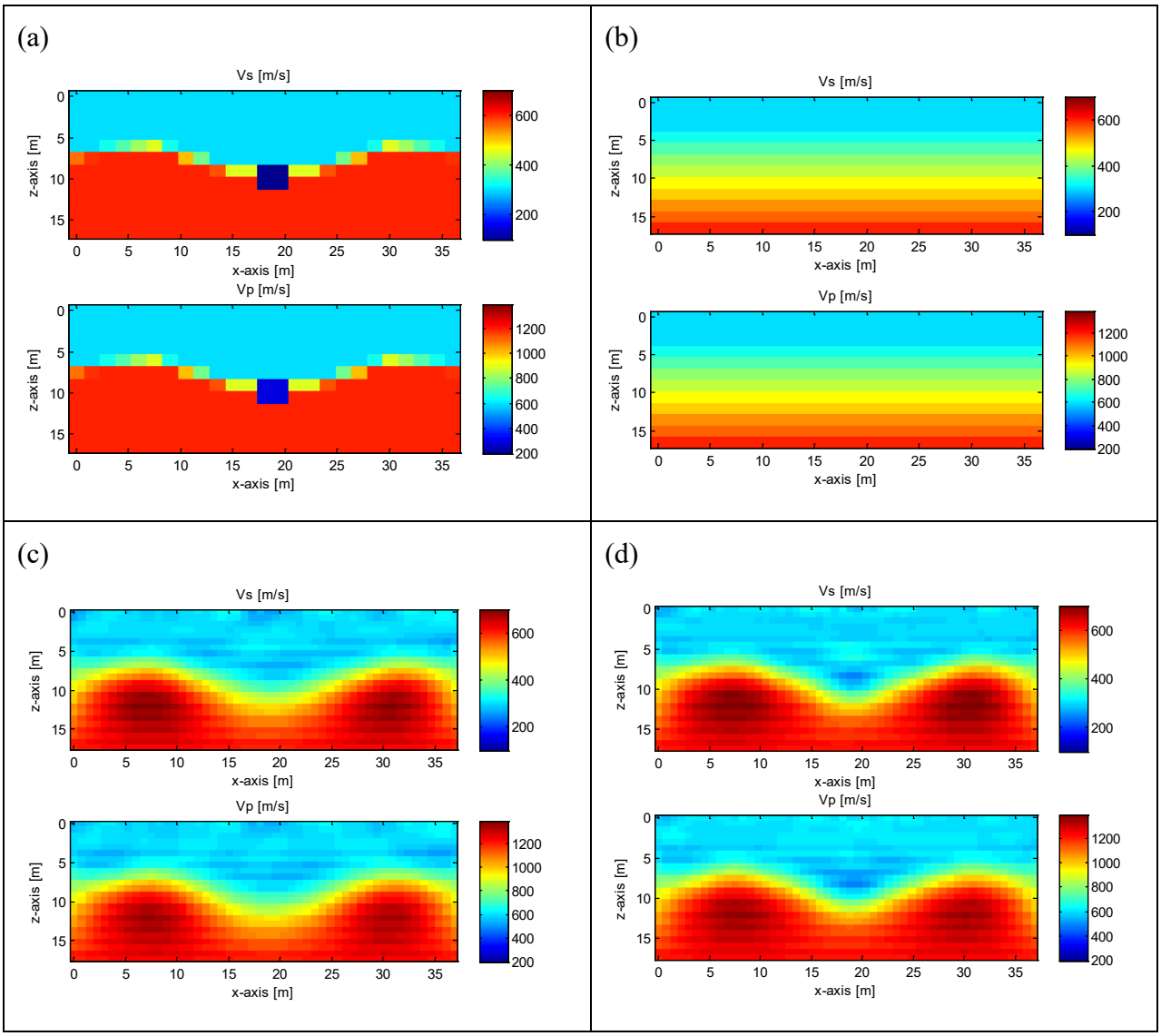

Figure 3.24: Vertical view of V_S and V_P (m/s) at the center of the void: (a) true model; (b) initial model; (c) inverted model at 5-25 Hz; (d) inverted model at 5-35 Hz (small void, 96 receivers).

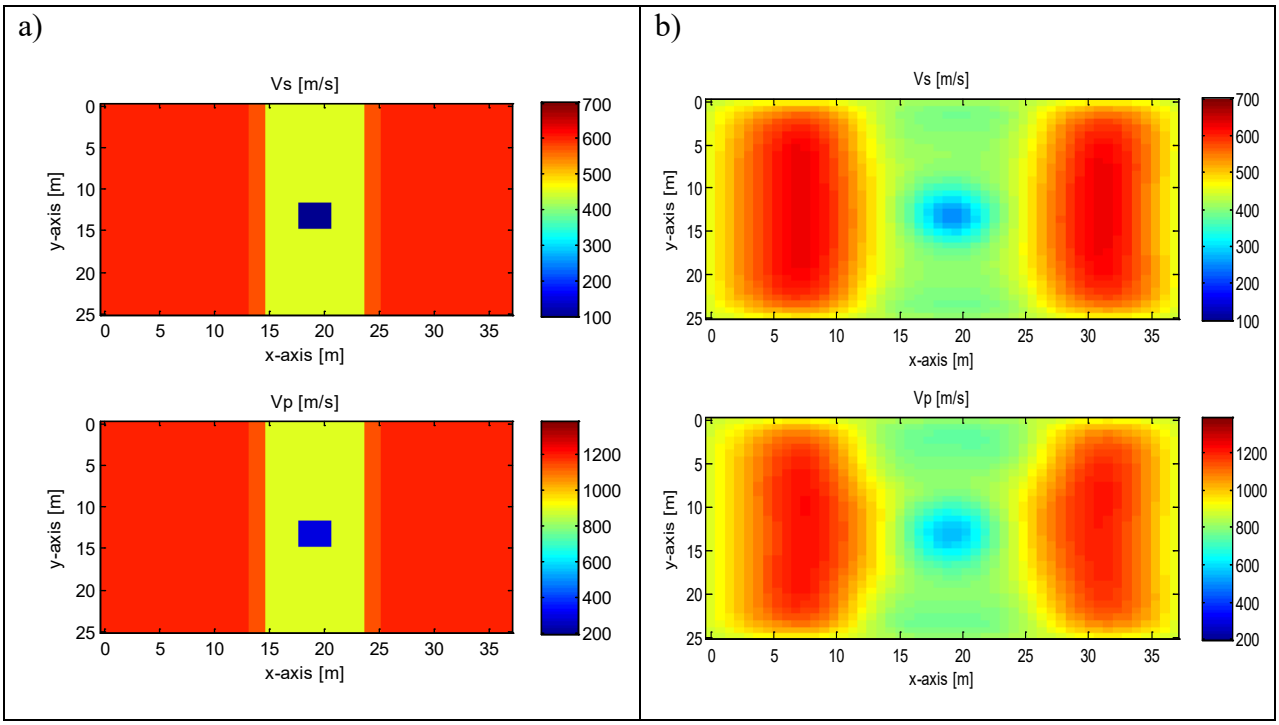

Figure 3.25: Horizontal view of (a) the true model and (b) the inverted model for V_S and V_P at 9-m (30-ft) depth (small void, 96 receivers)

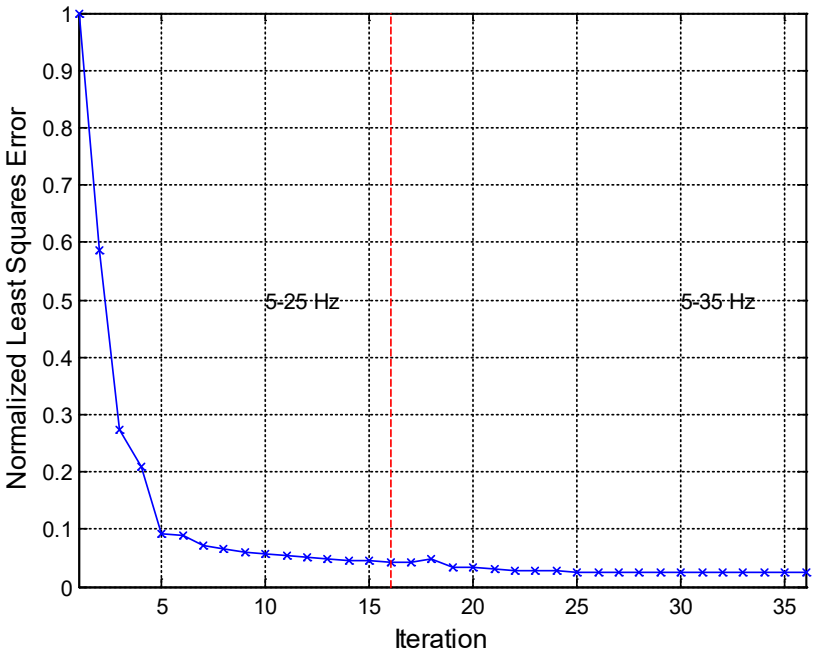

Figure 3.26: Normalized least square error (small void, 96 receivers)

3.4 Conclusion

Optimization of field test configurations (source and receiver locations) were performed using the 3-D FWI algorithm developed in Chapter 2. The goal was to find the minimum number of receivers and shots (maximum spacing) and the optimal frequency range of seismic data that enabled a successful characterization of variable layers and embedded voids. Three test configurations utilizing 2-D uniform grids of geophones and sources placed at 3-m (10-ft) to 6-m (20-ft) spacing on the ground surface were analyzed. Each test configuration was tested on two synthetic models with variable soil-rock layers and embedded voids using different frequency ranges of signal. Accuracy and resolution of inverted profiles were compared between simulations to identify the optimal test configuration.

The 3-D analyses were first performed on the model with the larger void, 4.5-m (15-ft) diameter at 9-m (30-ft) depth. Analyses of all three test configurations at 3-m (10-ft), 4.5-m (15-ft), and 6-m (20-ft) spacing were shown to successfully recover variable layers, as well as the void. The results suggested that the geophone and source spacing equal to the void diameter (4.5 m [15 ft]) was the optimal spacing. Using the smaller geophone-source spacing only produced data redundancy and did not improve the inverted results.

Next, the inversion analyses were performed on a model with a smaller void, 3-m (10-ft) diameter at a deeper depth compared to void diameter, 9 m (30 ft) (3 times void diameter). The 3-D analyses showed that all the shot and receiver configurations could produce successful recovery of variable layers. However, only the densest test configuration of geophone-shot spacing equal to the void diameter (3 m [10 ft]) was able to accurately recover both the void size and its position. The other two configurations at 4.5-m (15-ft) and 6-m (20-ft) spacing vaguely showed the void location.

From the results of the analyses performed in this chapter, both geophone and shot spacing at 1 to 2 diameters of a targeted void is recommended for field testing. Both geophone and shot spacing of 3 m (10 feet) were subsequently used for field experiments (Chapter 5). At such spacing, voids of 1.5-m (5-ft) diameter or larger should be characterized, with maximum buried depths to be determined in Chapter 4. The optimal frequency range of seismic data was identified as 5 to 35 Hz, which were later used in selection of the active source equipment for the field experiments. Sample data with various drop heights and weights (propelled energy generator source) as well as sizes of impact plates will be investigated at each site before conducting seismic surveys. The selected drop height, weight and plate size will be kept constant for the entire data acquisition process at each site.

CHAPTER 4

DETERMINATION OF MAXIMUM VOID DETECTION DEPTH USING SURFACE ACQUISITION GEOMETRY

4.1 Introduction

One of the tasks of this research was to determine the maximum depth at which a void can be identified and characterized with confidence, using only surface measurements of seismic waves. To achieve this goal, several parametric studies were performed using synthetic models. The models have characteristics of typical Florida geological conditions (e.g. layering) with variable soil and rock features and an embedded void placed at varying depths. This study will assist in interpreting inverted results of the field experimental data analyzed by the developed 3-D FWI algorithm in Chapter 2. The numerical results in this chapter will help determine whether an identified void/anomaly is real, or just an inversion artifact due to noise in field experimental data.

For the study, two different void sizes representing a larger (4.5 m [15 ft] diameter) and a smaller (3 m [10 ft] diameter) void are individually embedded below the ground surface at depths of two, three, and four void diameters. A 2-D uniform grid of shots and receivers were then used on the free surface employing the optimal receiver/shot spacing of one void diameter identified in Chapter 3. The wave-fields were then simulated for each model and analyzed using the developed 3-D FWI algorithm. The inverted results were subsequently compared to the true (synthetic) models and were then appraised of their accuracy of the recovered void features, by their size, position and material properties (V_S and V_P values) within the void. The effect of the active source frequency band on void characterization is also further investigated, and the optimal frequency range is identified for field experiments discussed in Chapter 5.

4.2 Large embedded void (4.5-m [15-ft] diameter)

4.2.1 Models and test configuration

The developed 3-D FWI algorithm in Chapter 2 is first tested on synthetic models of variable soil-rock profiles with a large embedded buried void at various depths. A model domain of 45 m x 27 m x 19.5 m ($150' \times 90' \times 65'$) (length x width x depth) is used in the current analysis. The model space has been enlarged compared to that of Chapter 3 to accommodate for varying void depths (2, 3 and 4 void diameters). The existence of multiple soil layers at deeper depths, as well as the attenuation and reflection of the propagating waves makes surface-based deep void characterization a difficult task to achieve. Having sufficient ray coverage at the desired void depth is an essential part of any successful void characterization.

Shown in Figure 4.1 is the test configuration of 60 receivers and 77 shots that are placed in a staggered pattern on the ground surface (0-m [0-ft] depth). The staggered placement of receivers relative to sources helps with reducing receiver-source coupling as well as ease of placement in the field for real data acquisition. To carry out the analyses, three different void depths representing shallow, medium and deep depth voids were used. Shown in Figures 4.2, 4.3 and 4.4 are the 3-D depictions of the studied soil profiles and void depths corresponding to two, three and four void diameters, respectively. The increase in the number of layers corresponding to an increase in void depth is to account for realistic soil layering. It should be noted that the depth of analysis for the deep void (Figure 4.4) has been increased to 28.5 m (95 ft) to accommodate the deeper void, which was placed at four void dimeters (18 m [60 ft]) from the ground surface (0-m [0-ft] depth).

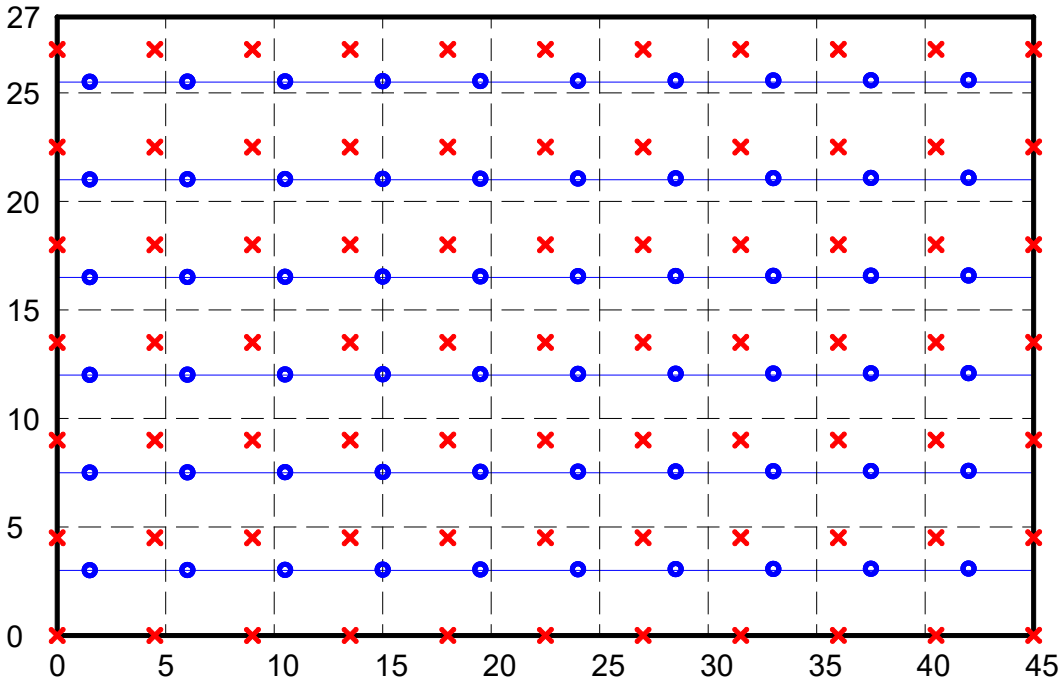

Figure 4.1: Test configuration: 60 receivers (circle) and 77 shots (cross) both at 4.5-m (15-ft) spacing

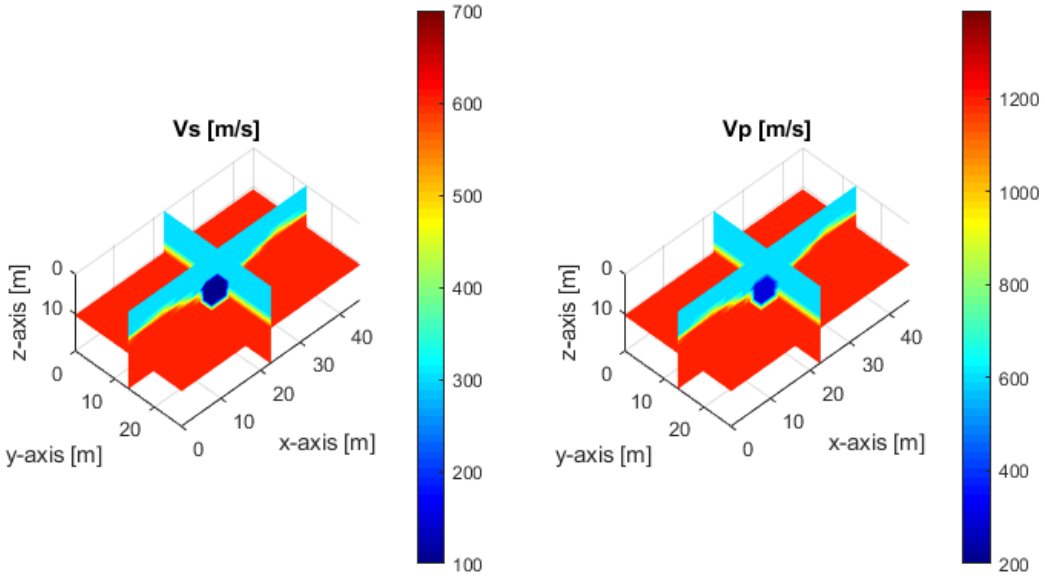

Figure 4.2: Synthetic model with a large void of 4.5-m (15-ft) diameter at 2 void diameter (9.0-m [30-ft]) depth

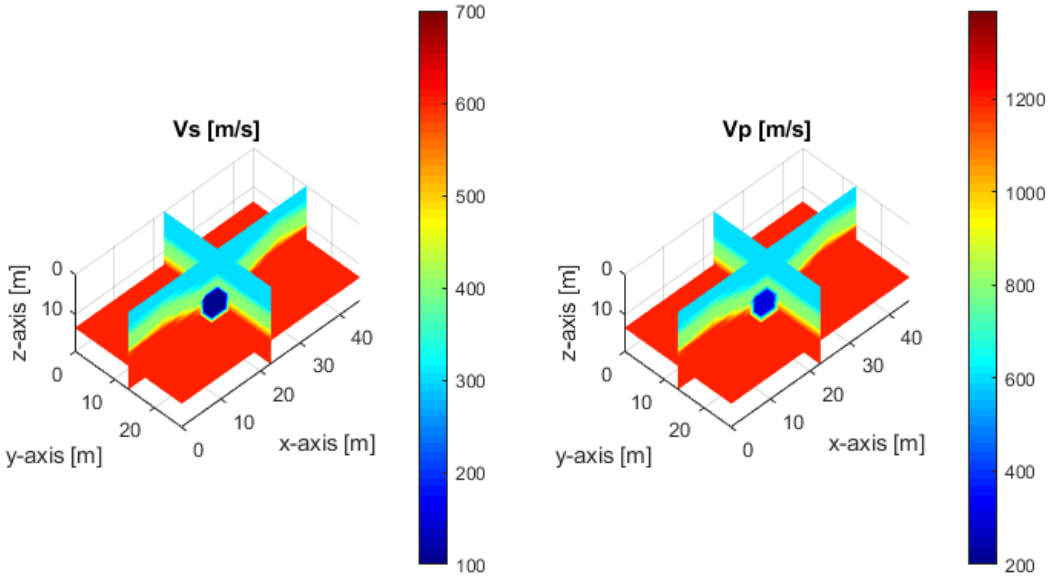

Figure 4.3: Synthetic model with a large void of 4.5-m (15-ft) diameter at 3 void diameter (13.5-m [45-ft]) depth

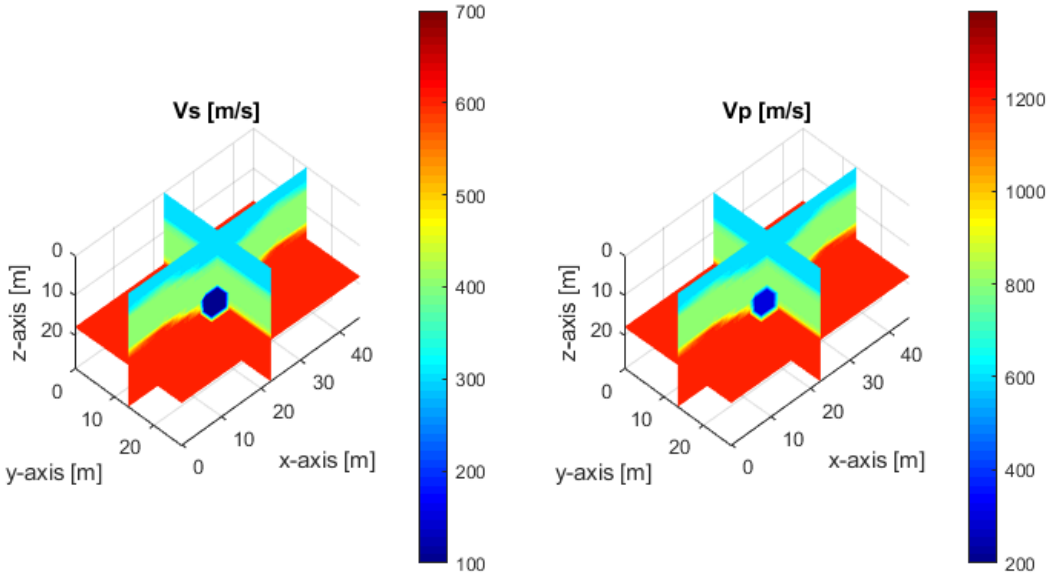

Figure 4.4: Synthetic model with a large void of 4.5-m (15-ft) diameter at 4 void diameter (18-m [60-ft]) depth

4.2.2 Results for shallow void (depth of 2 void diameters)

The inversion was initially performed on the shallow void using the test configuration of 60 receivers and 77 shots (Figure 4.1) with receivers/sources placed at one void diameter (4.5 m [15 ft]) spacing on the ground surface (0-m depth). The true model (Figure 4.5 a) consists of two layers with V_S of 300 m/s (1,000 ft/s) for the top layer and 600 m/s (2,000 ft/s) for the bottom layer and V_P twice that of V_S. The 4.5-m (15-ft) diameter void was embedded at two void diameters (9-m [30-ft] depth) from the surface (0-m [0-ft] depth). The initial model (Figure 4.5 b) used in the analysis consists of a 1-D velocity profile that is linearly increased with depth with V_S of 300 m/s (1,000 ft/s) on the surface (0-m [0-ft] depth) to 600 m/s (2,000 ft/s) at the bottom of the model (19.5-m [65-ft] depth) and V_P twice that of V_S. Two inversions were performed with the first run using the low frequency range data (5-25 Hz) and the second run using the high frequency range data (5-35 Hz). The low frequency data (5-25 Hz) was run using the initial model described above (Figure 4.5 b) and the high frequency data (5-35 Hz) was performed on the results of the first run as the input model. The first and second runs were set to stop after 20 and 40 iterations, respectively. Normalized least-squares error for all iterations of the two inversion runs is shown in Figure 4.6, where the error reduced from 1 at the onset of the first iteration to about 0.2 at the end of the first run (iteration 20) and to 0.1 at the end of the second run (iteration 60).

True model features including the layer outline and void position and material properties (V_S and V_P values) were successfully recovered after the first run (Figure 4.5c). The second run (Figure 4.5d) with higher frequency data of up to 35 Hz improved the results, particularly for the material properties (V_S and V_P values) of the void. For better view of the void, 2-D profile comparison between the true and inverted models are presented for vertical (distance y = 13.5 m

[y = 45 ft], Figure 4.7) and horizontal profiles (depth z = 9 m [z = 30 ft], Figure 4.8). It is observed that layers are clearly characterized, and the void is located and identified correctly.

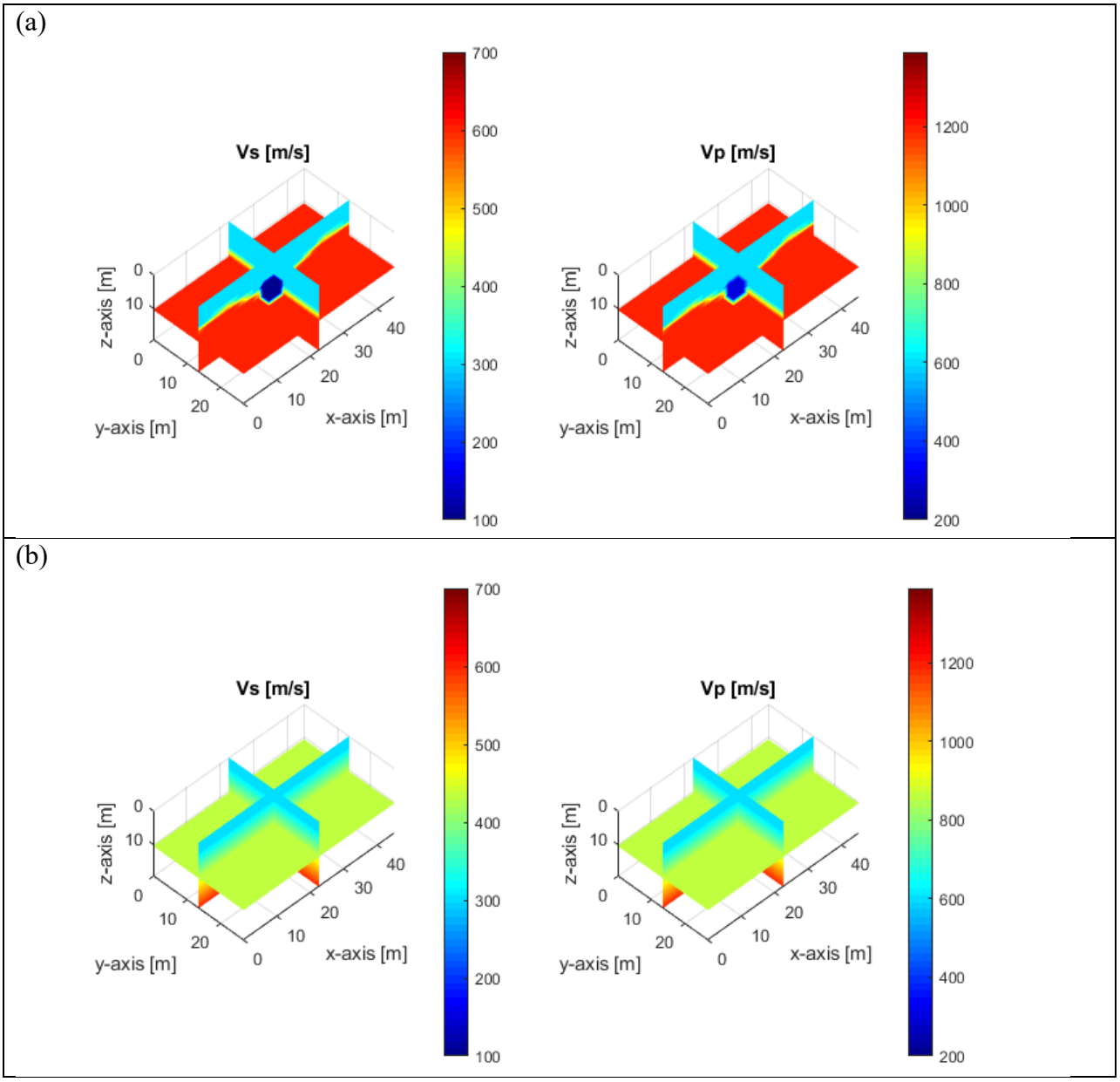

Figure 4.5: Synthetic model of S-wave and P-wave velocities (m/s): (a) true model; (b) initial model; (c) inverted model at 5-25 Hz; (d) inverted model at 5-35 Hz (big void, 2 void diameters)

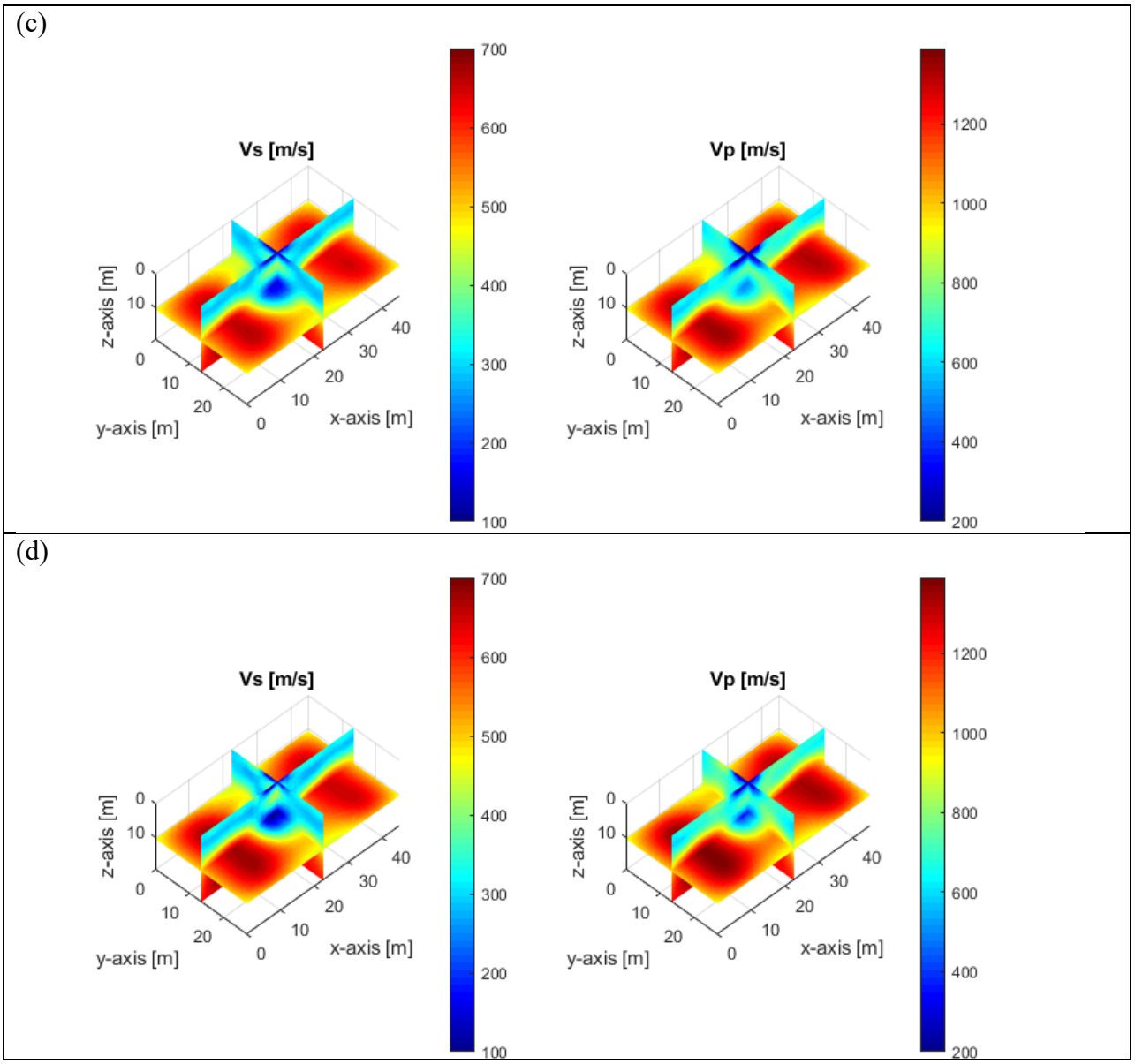

Figure 4.5: Synthetic model of S-wave and P-wave velocities (m/s): (a) true model; (b) initial model; (c) inverted model at 5-25 Hz; (d) inverted model at 5-35 Hz (big void, 2 void diameters)

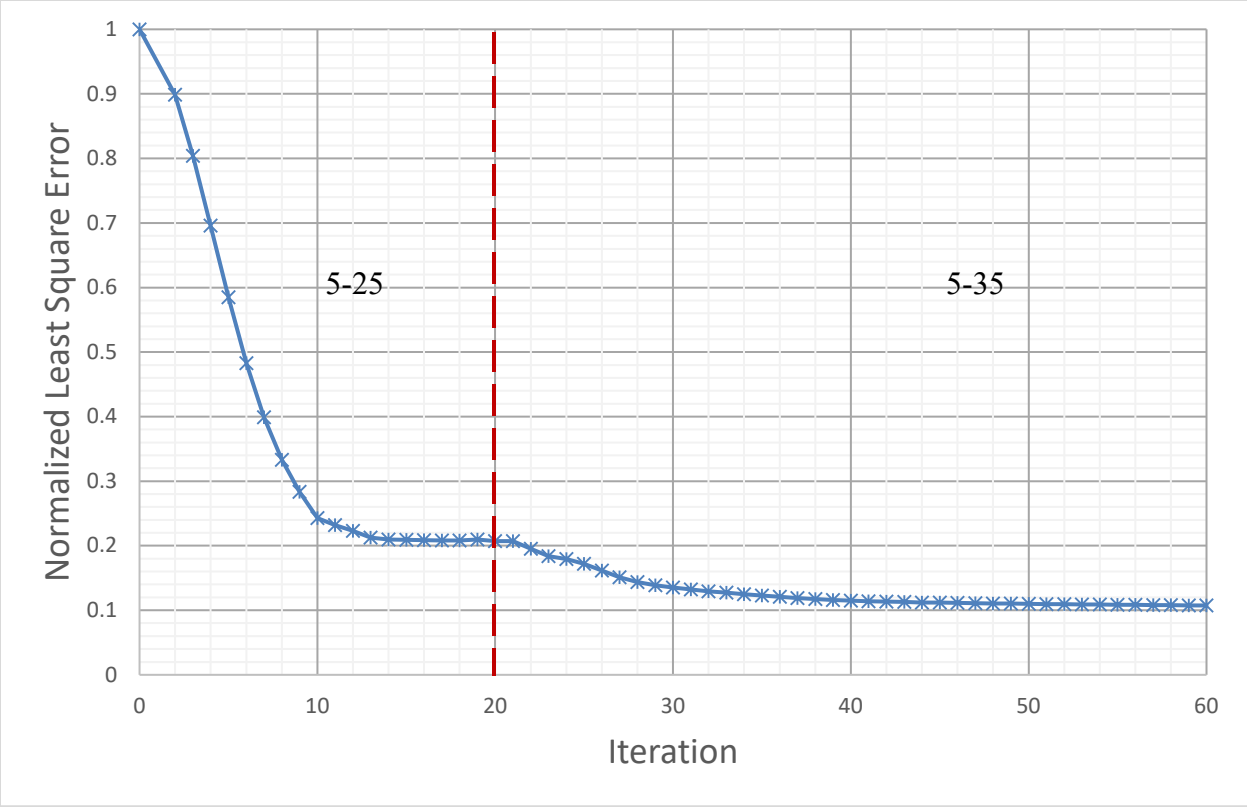

Figure 4.6: Normalized least-squares error (big void, 2 void diameters)

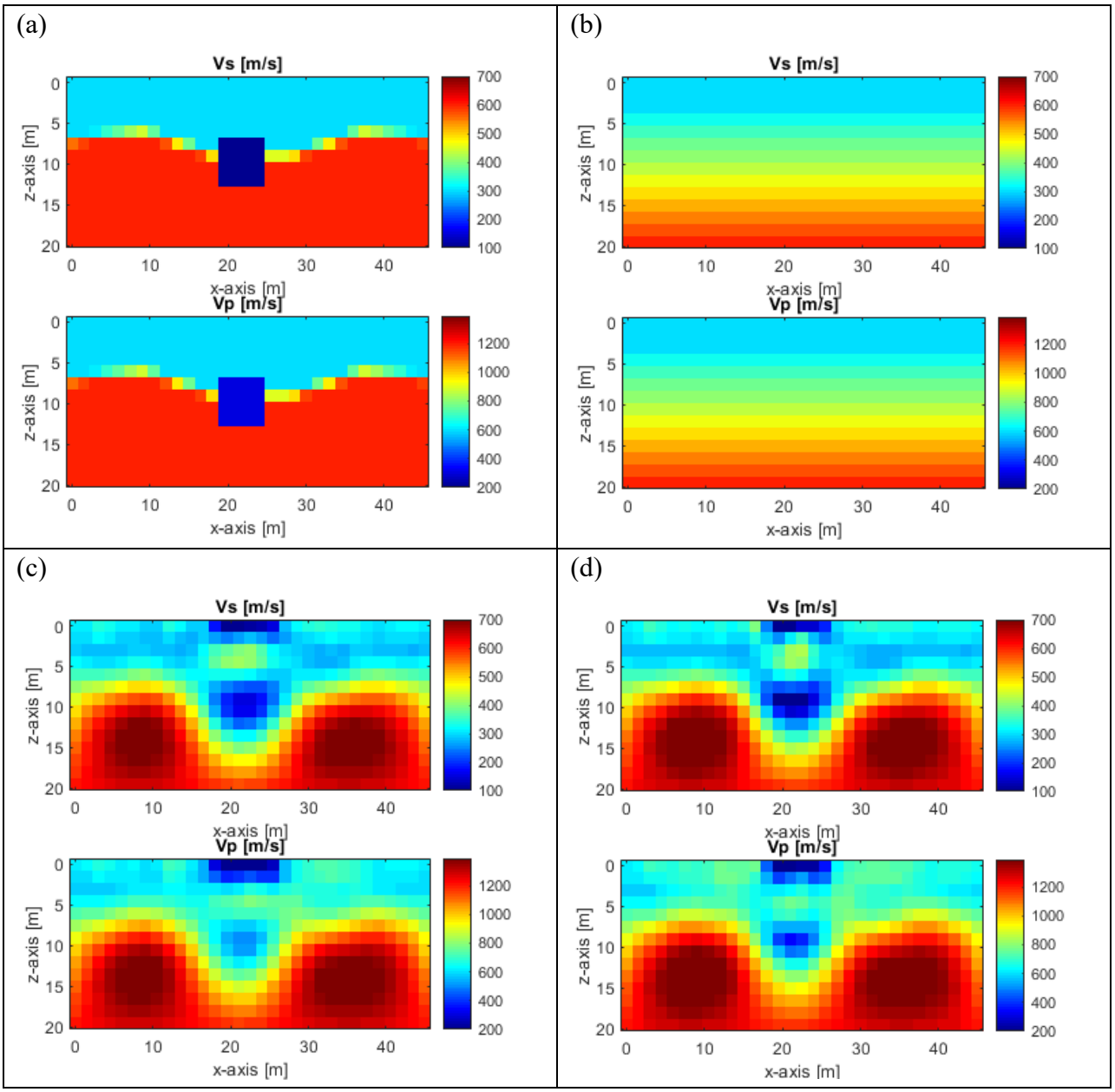

Figure 4.7: Vertical view of V_S and V_P (m/s) at the center of the void (y=13.5 m [y=45 ft]): (a) true model; (b) initial model; (c) inverted model at 5-25 Hz; (d) inverted model at 5-35 Hz (big void, 2 void diameters).

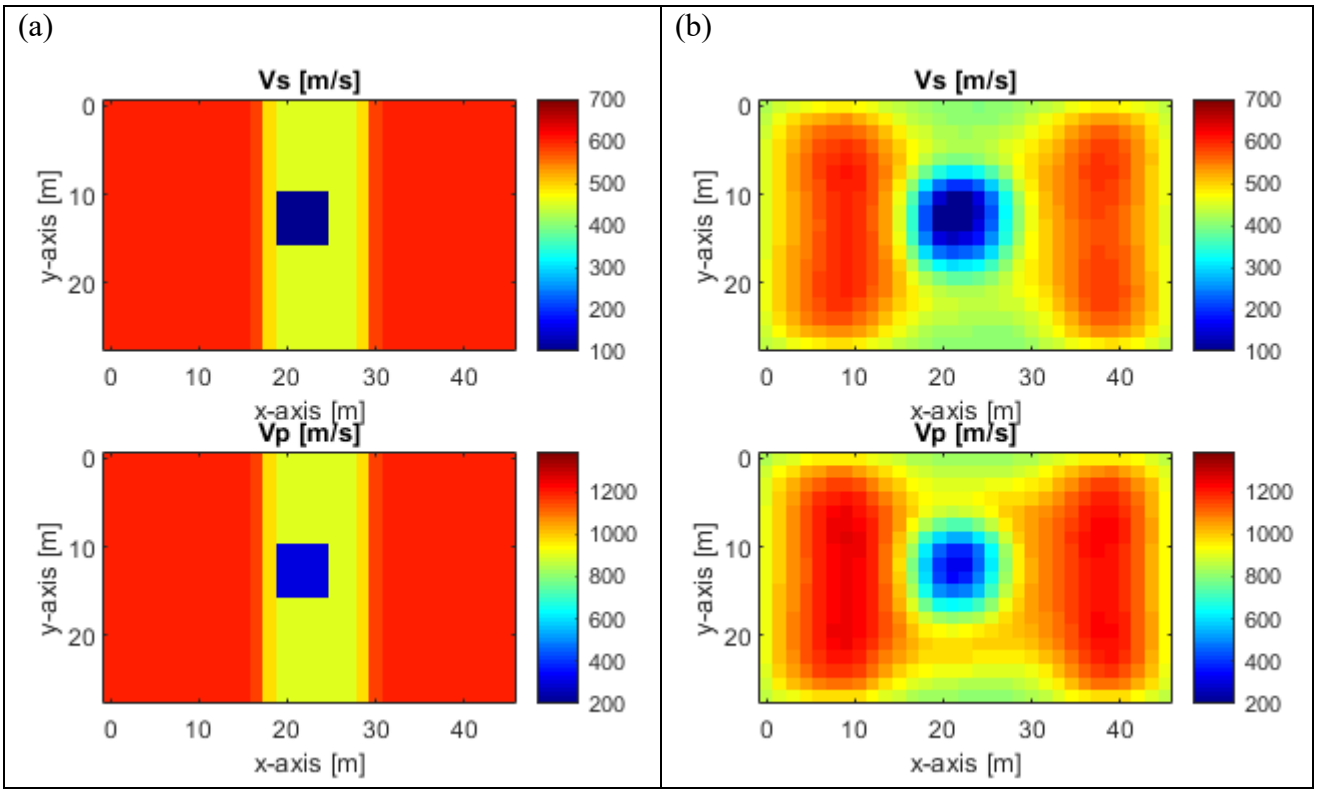

Figure 4.8: Horizontal view of (a) the true model and (b) the final inverted model for V_S and V_P at 9-m (30-ft) depth (big void, 2 void diameters)

4.2.3 Results for medium-depth void (depth of 3 void diameters)

Subsequently, the inversion was carried out on the medium-depth void using the same test configuration of 60 receivers and 77 shots (Figure 4.1). The true model (Figure 4.9 a) consists of three layers with V_S of 300 m/s (1,000 ft/s), 400 m/s (1,332 ft/s) and 600 m/s (2,000 ft/s) for the top, middle and bottom layers, respectively. The 4.5 m (15 ft) diameter void is embedded at three void diameters (13.5-m [45-ft] depth) from the surface (0-m [0-ft] depth).

Like the case of a shallow void (2 void diameter), the initial model (Figure 4.9 b) used in the analysis consists of a 1-D velocity profile that linearly increased with depth. Two inversions were performed in the same fashion as the shallow void analysis. Normalized least-squares error for all iterations of the two inversion runs is shown in Figure 4-10, where the error reduced from

1 at the onset of the first iteration to about 0.15 at the end of the first run (iteration 20) and to 0.1 at the end of the second run (iteration 60).

Part of the true model features including the second layer interface as well as the existence of the void were successfully recovered in the first run (Figure 4.9 c). The second run (Figure 4.9 d) with the higher frequency data of up to 35 Hz had significantly improved recovery of void features (size and position) and material properties (V_S and V_P values). 2-D profile comparison between the true and inverted models are presented for vertical (distance y = 13.5 m [y = 45 ft], Figure 4.11) and horizontal profiles (depth z = 13.5 m [z = 45 ft], Figure 4.12). Evident, void features including size, position and material properties are successfully recovered and characterized.

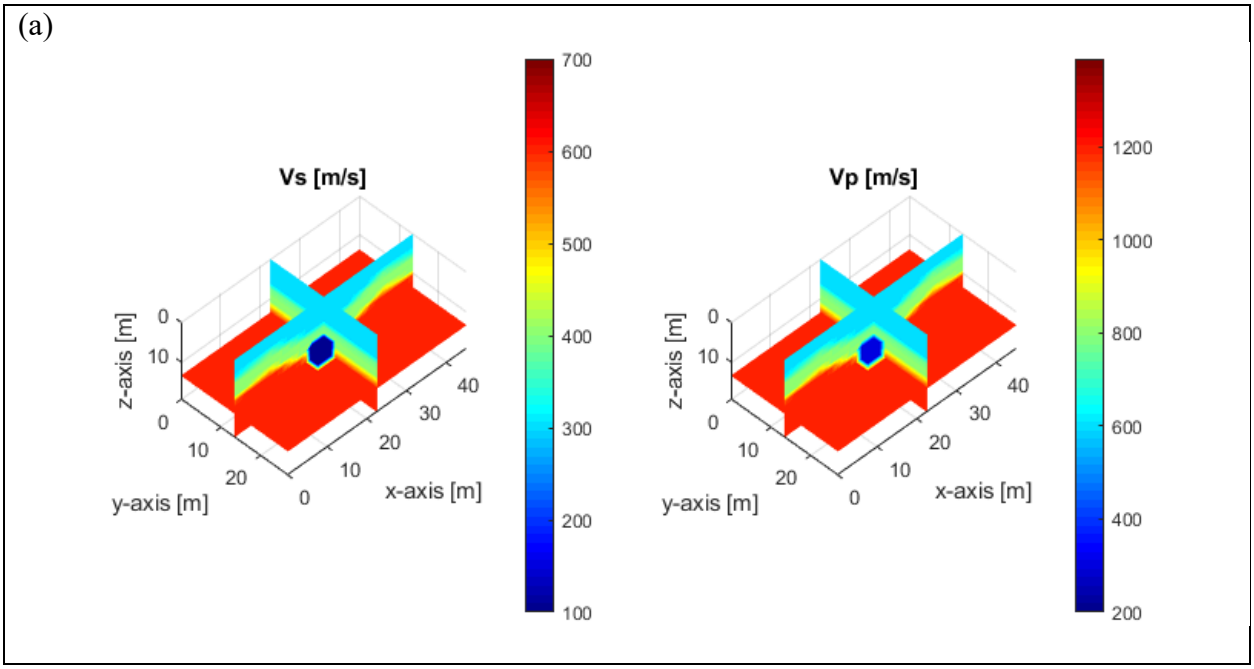

Figure 4.9: Synthetic model of S-wave and P-wave velocities (m/s): (a) true model (b) initial model; (c) inverted model at 5-25 Hz; (d) inverted model at 5-35 Hz (big void, 3 void diameters)

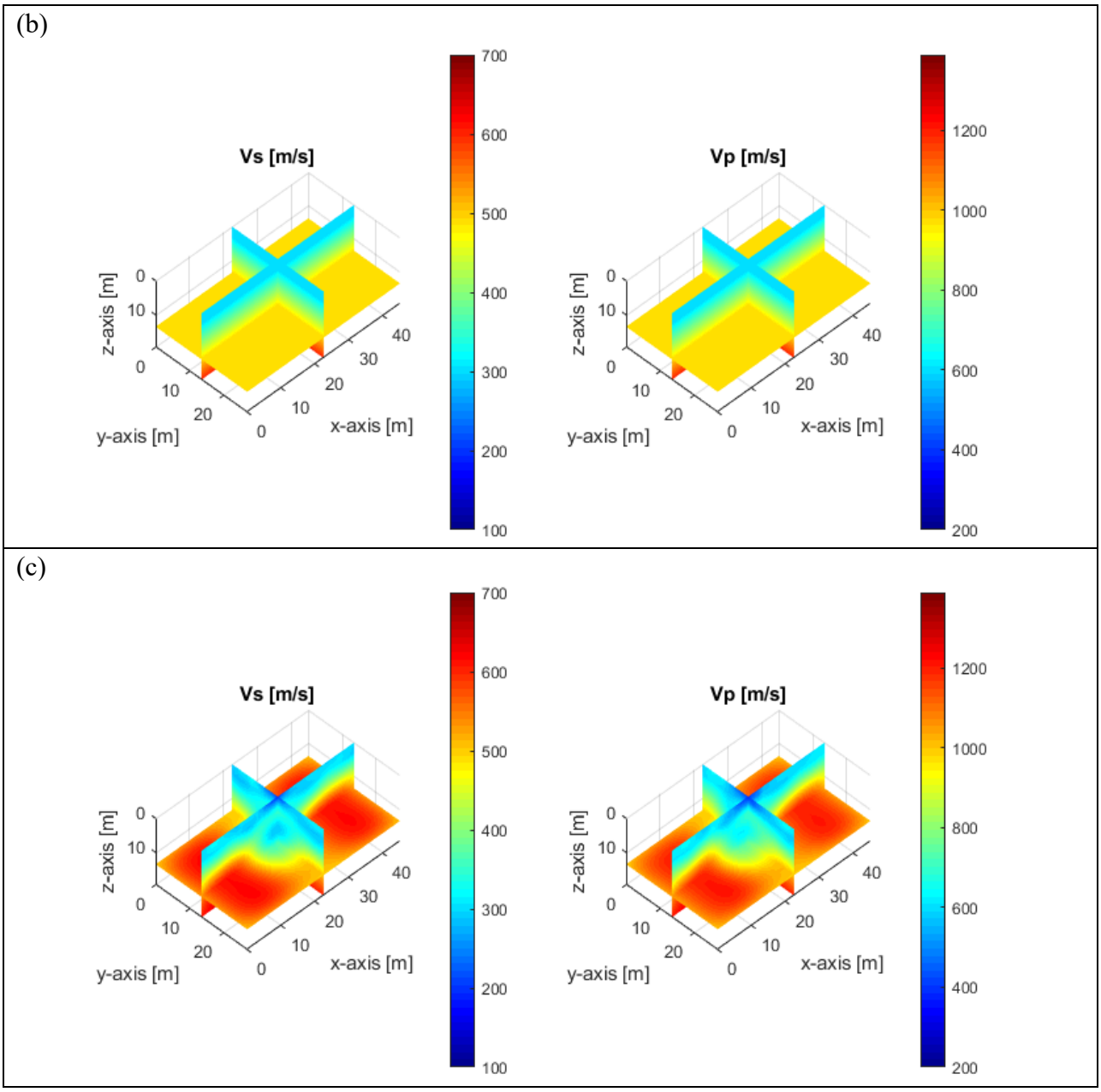

Figure 4.9: Synthetic model of S-wave and P-wave velocities (m/s): (a) true model (b) initial model; (c) inverted model at 5-25 Hz; (d) inverted model at 5-35 Hz (big void, 3 void diameters)

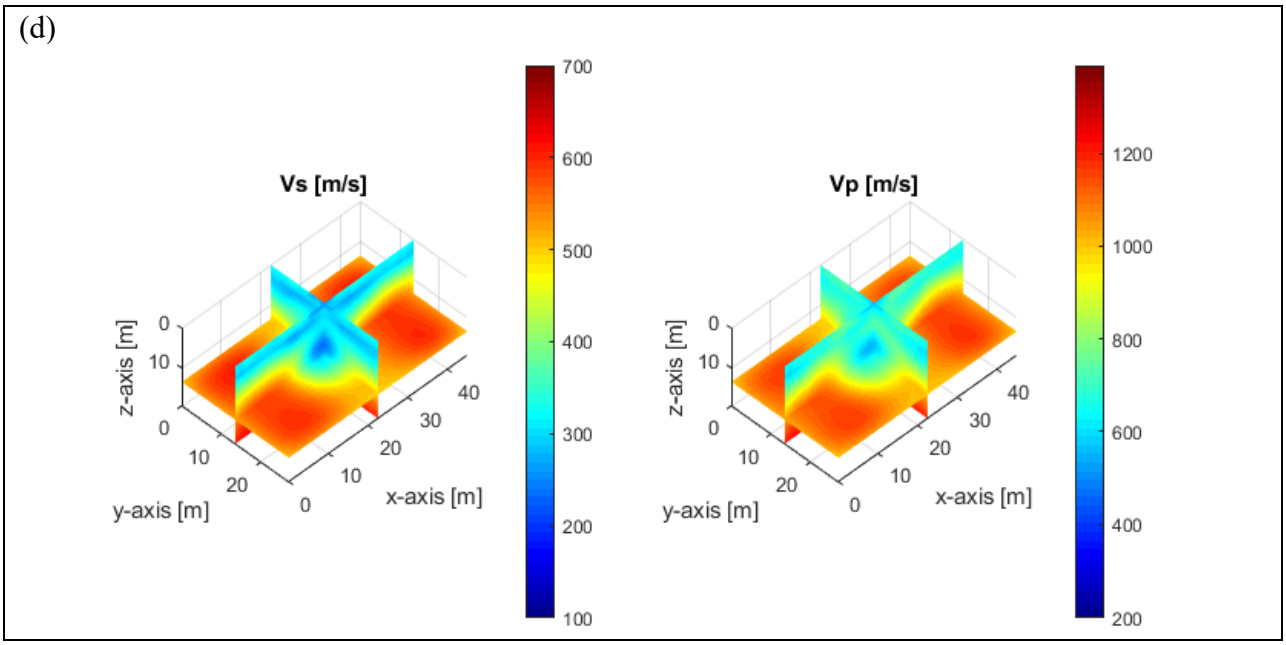

Figure 4.9: Synthetic model of S-wave and P-wave velocities (m/s): (a) true model (b) initial model; (c) inverted model at 5-25 Hz; (d) inverted model at 5-35 Hz (big void, 3 void diameters)

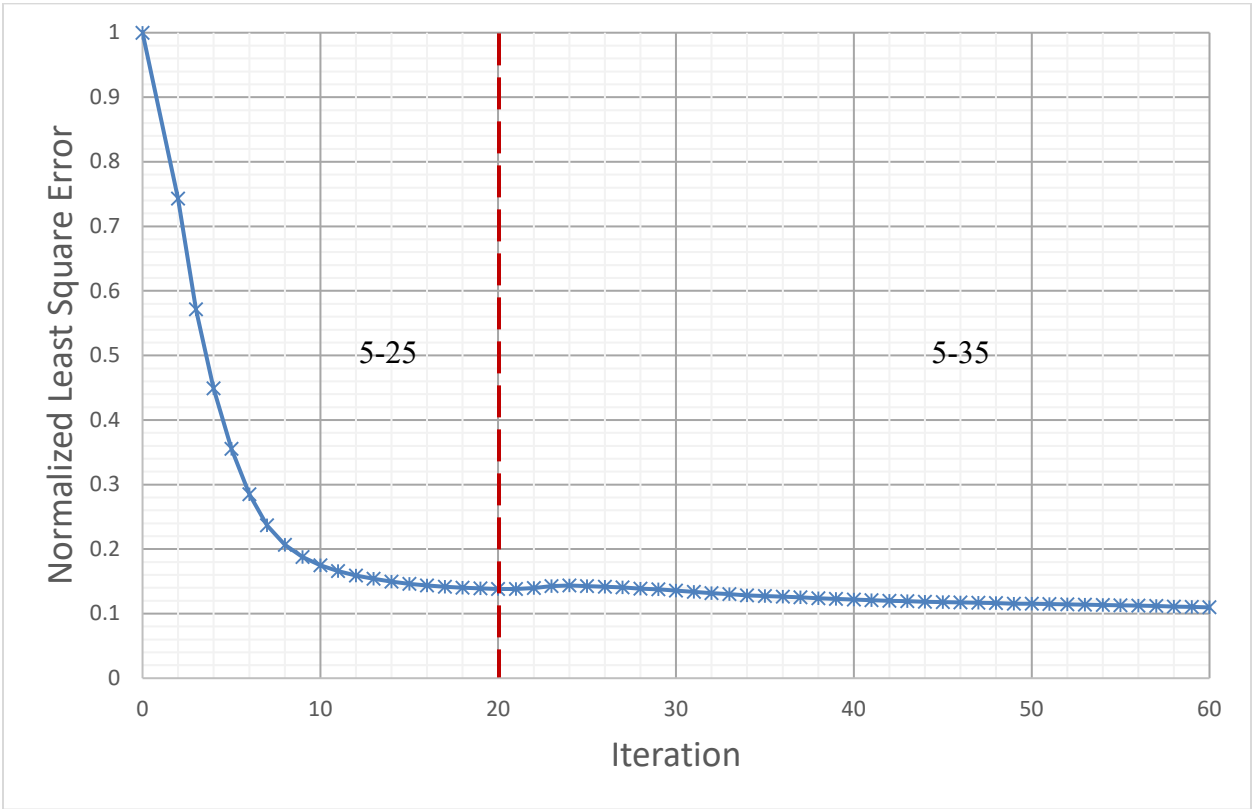

Figure 4.10: Normalized least-squares error (big void, 3 void diameters)

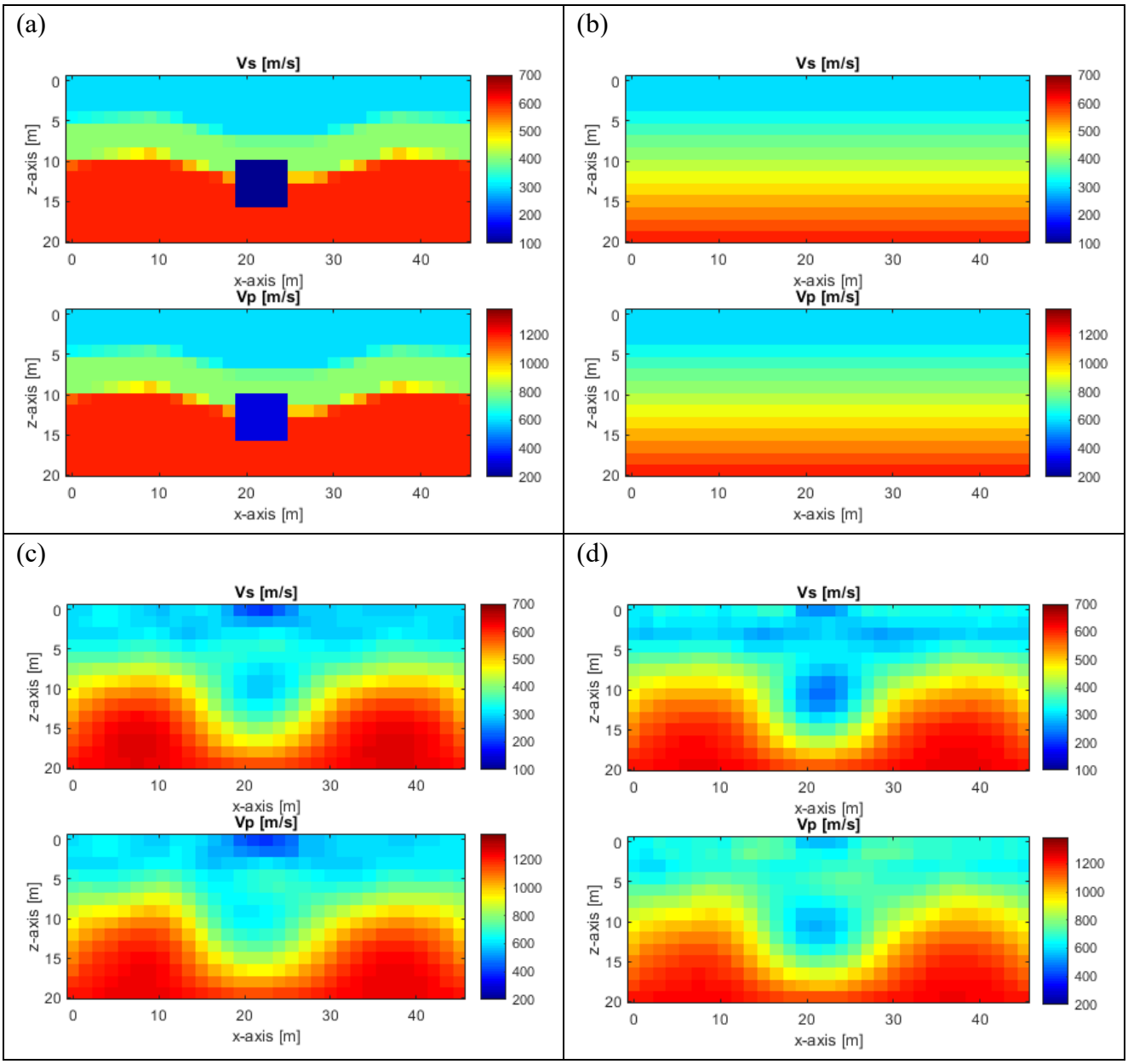

Figure 4.11: Vertical view of V_S and V_P (m/s) at the center of the void: (a) true model; (b) initial model; (c) inverted model at 5-25 Hz; (d) inverted model at 5-35 Hz (big void, 3 void diameters)

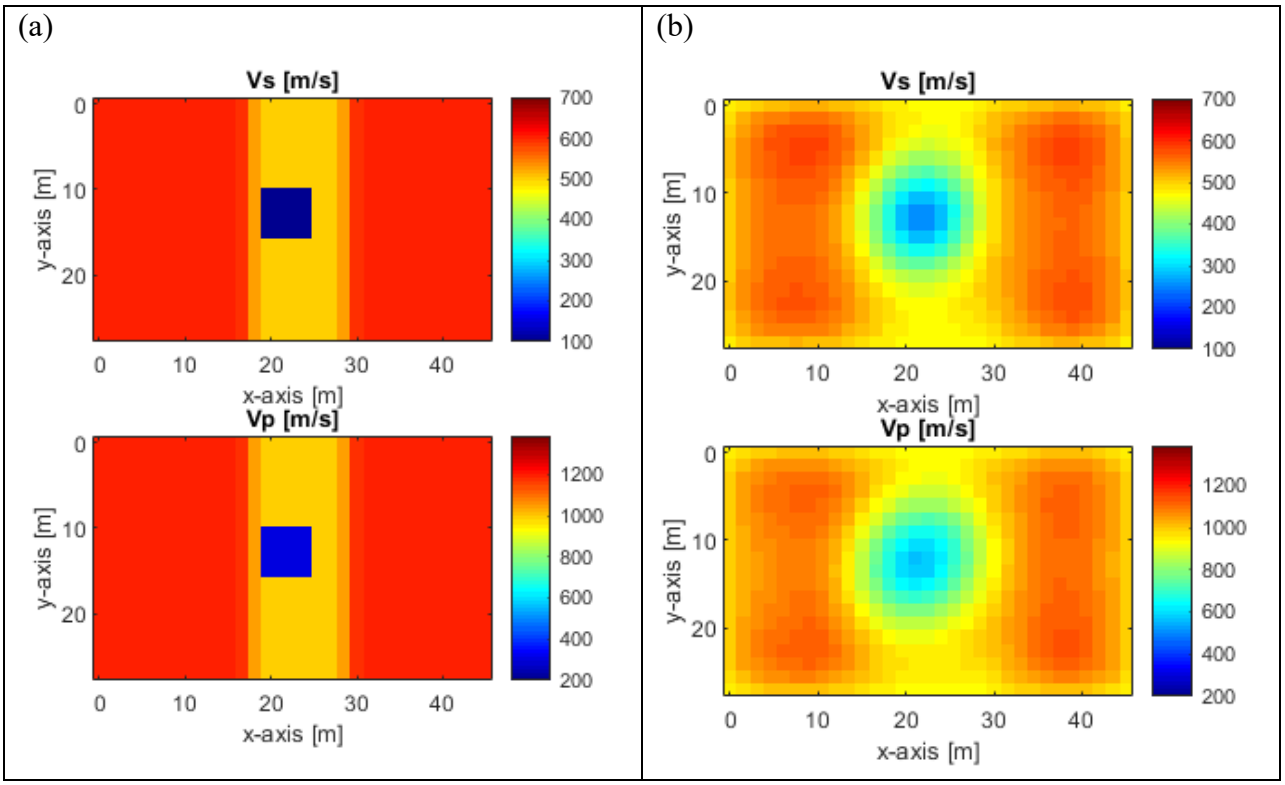

Figure 4.12: Horizontal view of (a) the true model and (b) the inverted model for V_S and V_P at 13.5-m (45-ft) depth (big void, 3 void diameters)

4.2.4 Results for deep void (depth of 4 void diameters)

Finally, the inversion was tried on a deep void embedded at 4 void depths from the ground surface. It should be noted that in order to accommodate the void, the model depth had to be increased to 28.5 m (95 ft) from 19.5 m (65 ft) used in the previous two analyses (shallow and medium-depth void). Again, two inversion runs were performed at two different frequency ranges. Normalized least-squares error for all iterations of the two inversion runs is shown in Figure 4.14, where the error reduced from 1 at the first iteration to about 0.08 at the end of the first run (iteration 20) and to 0.02 at the end of the second run (iteration 60).

Part of the true model features including layer positions and void outline are recovered and visualized for the low frequency (Figure 4.13c) and high frequency data (Figure 4.13-D). The 2-D profile comparison between the true and inverted models are presented for vertical

(distance y = 13.5 m [y = 45 ft], Figure 4.15) and horizontal profiles (depth z = 18 m [z = 60 ft] Figure 4.16). Even though, there is indication of an anomaly at the void location, the void size and material properties (V_S and V_P values) are not characterized. This outcome suggests that the current surface-based 3-D FWI algorithm with the identified surface sources and frequency ranges might not be able to completely recover anomalies located at depths equal to or bigger than four void diameters.

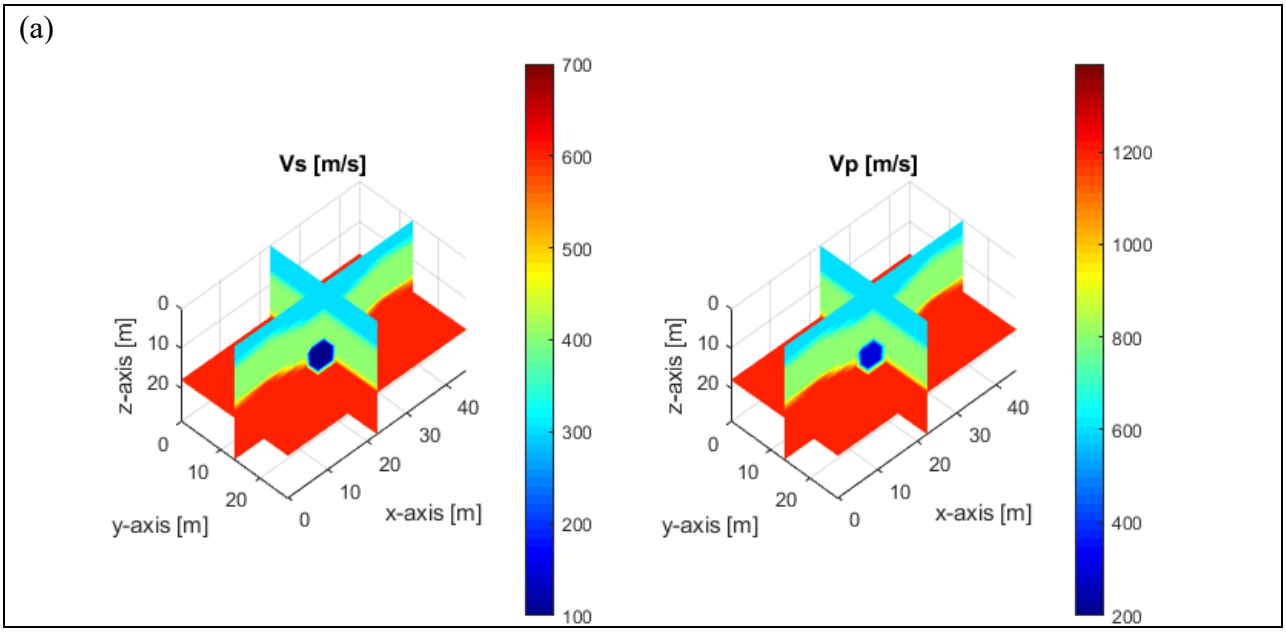

Figure 4.13: Synthetic model of V_S and V_P (m/s): (a) true model; (b) initial model; (c) inverted model at 5-25 Hz; (d) inverted model at 5-35 Hz (big void, 4 void diameters)

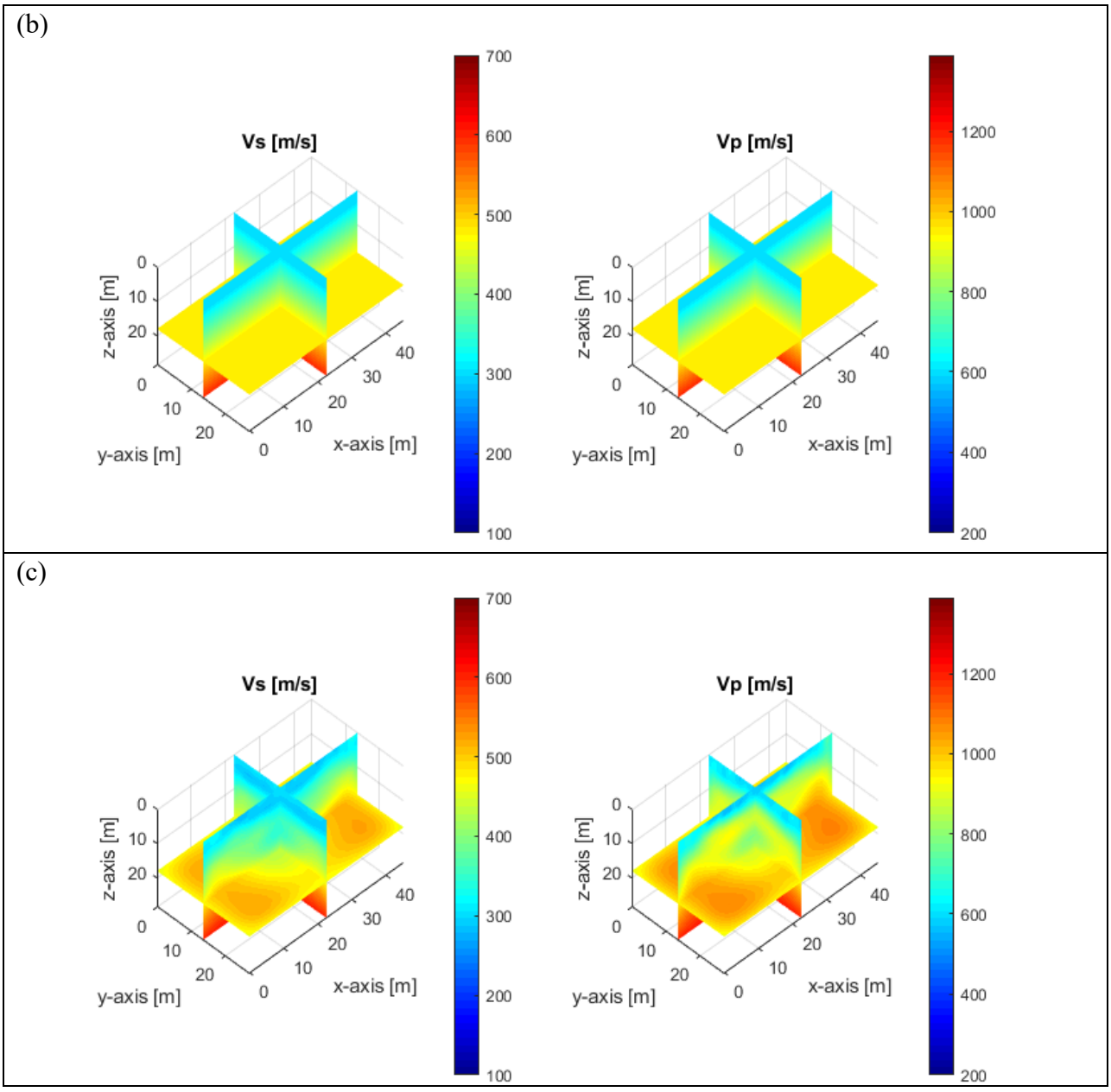

Figure 4.13: Synthetic model of V_S and V_P (m/s): (a) true model; (b) initial model; (c) inverted model at 5-25 Hz; (d) inverted model at 5-35 Hz (big void, 4 void diameters)

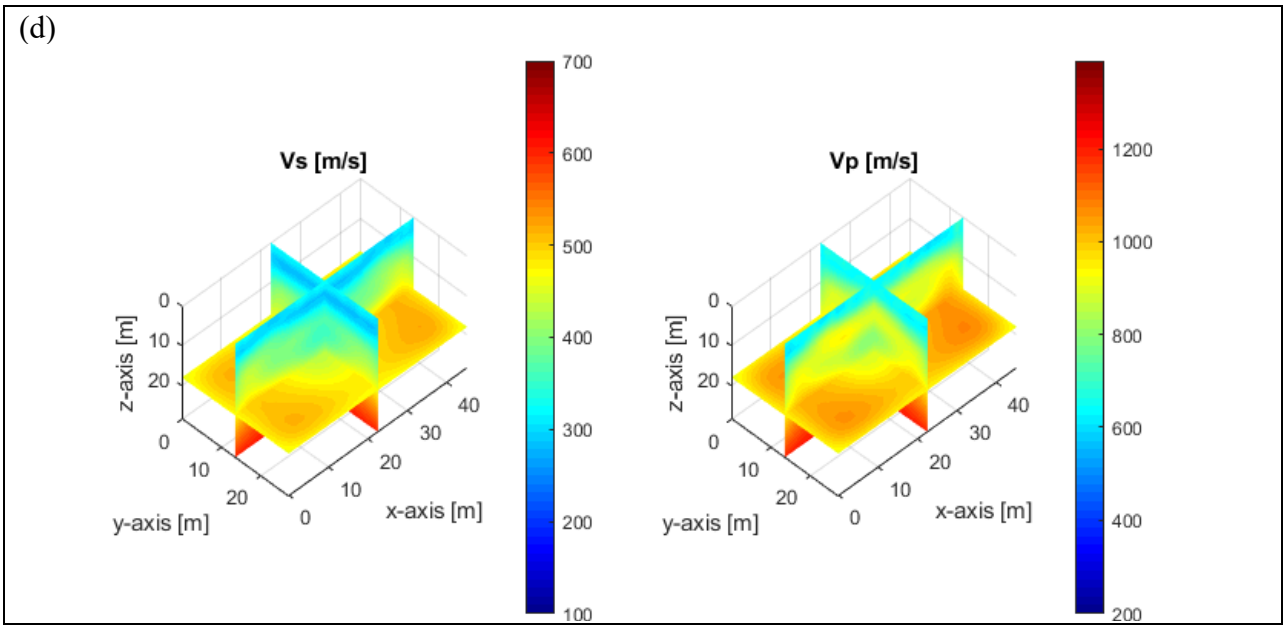

Figure 4.13: Synthetic model of V_S and V_P (m/s): (a) true model; (b) initial model; (c) inverted model at 5-25 Hz; (d) inverted model at 5-35 Hz (big void, 4 void diameters)

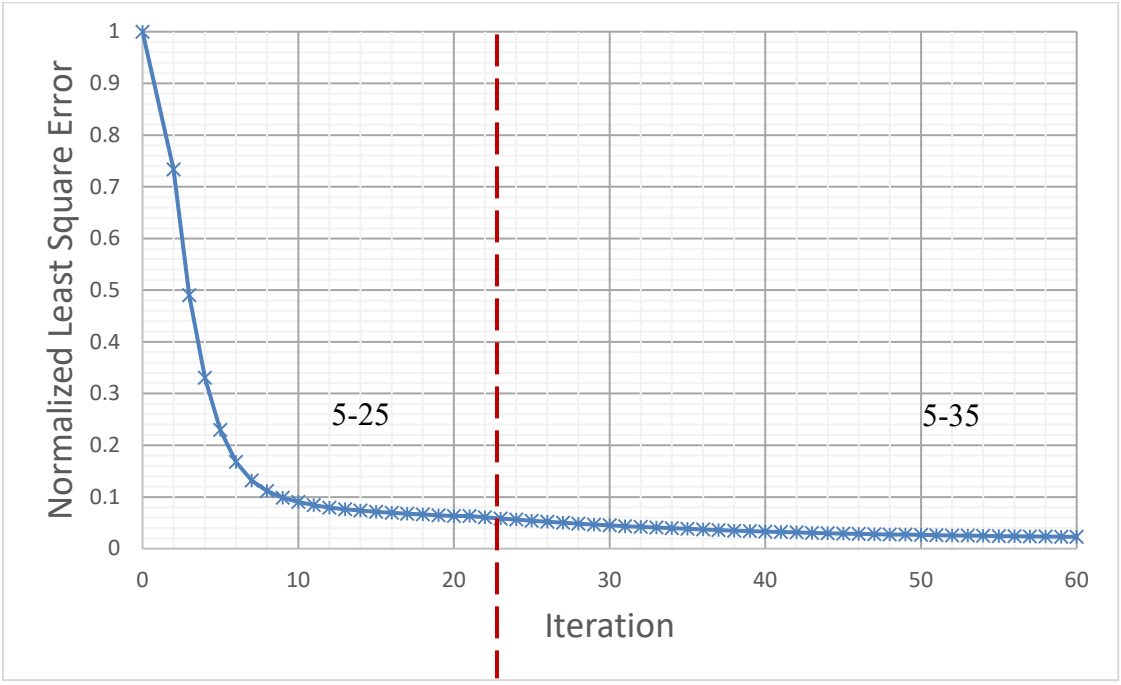

Figure 4.14: Normalized least-squares error (big void, 4 void diameters)

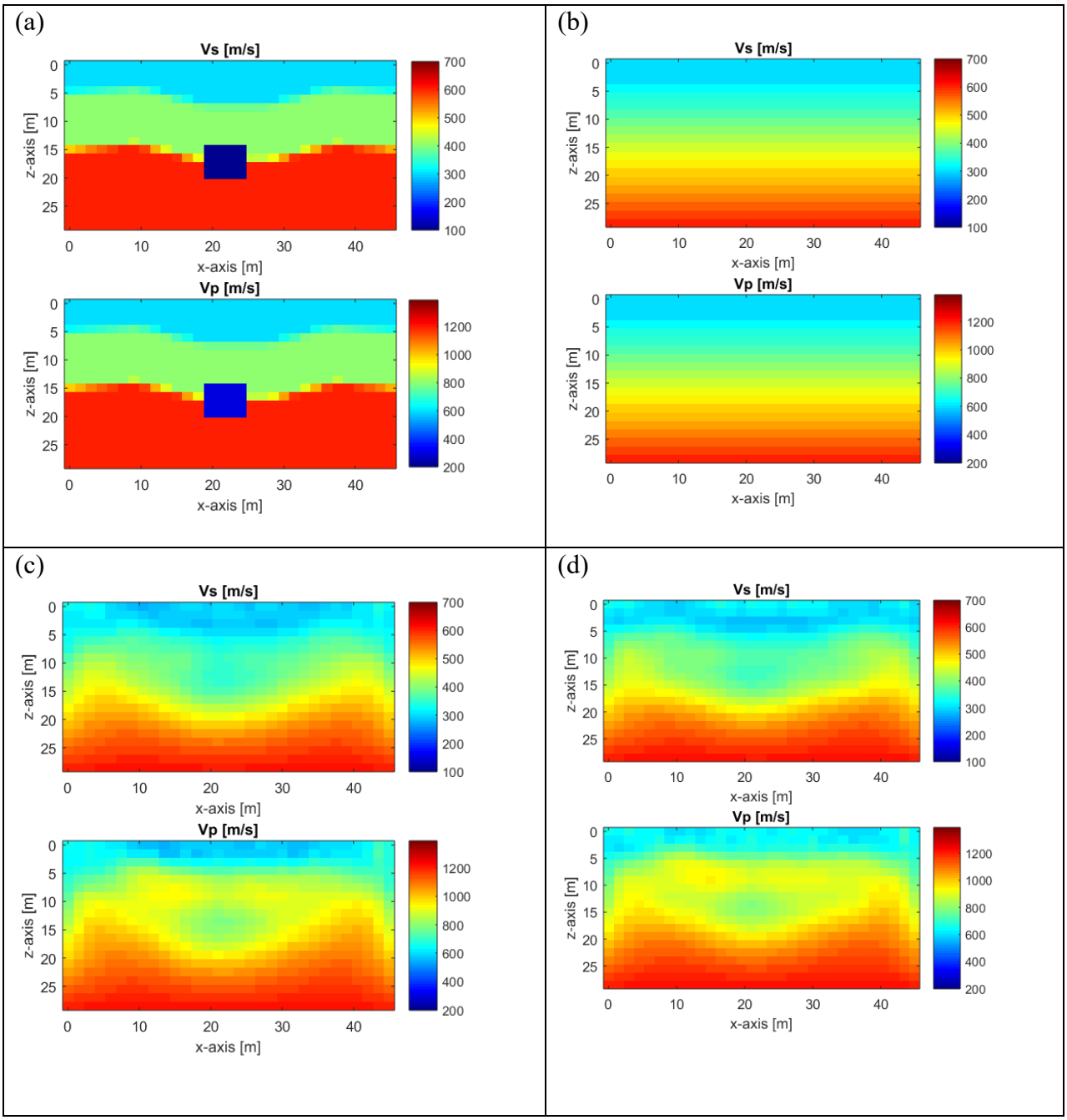

Figure 4.15: Vertical view of V_S and V_P (m/s) at the center of the void: (a) true model; (b) initial model; (c) inverted model at 5-25 Hz; (d) inverted model at 5-35 Hz (big void, 4 void diameters).

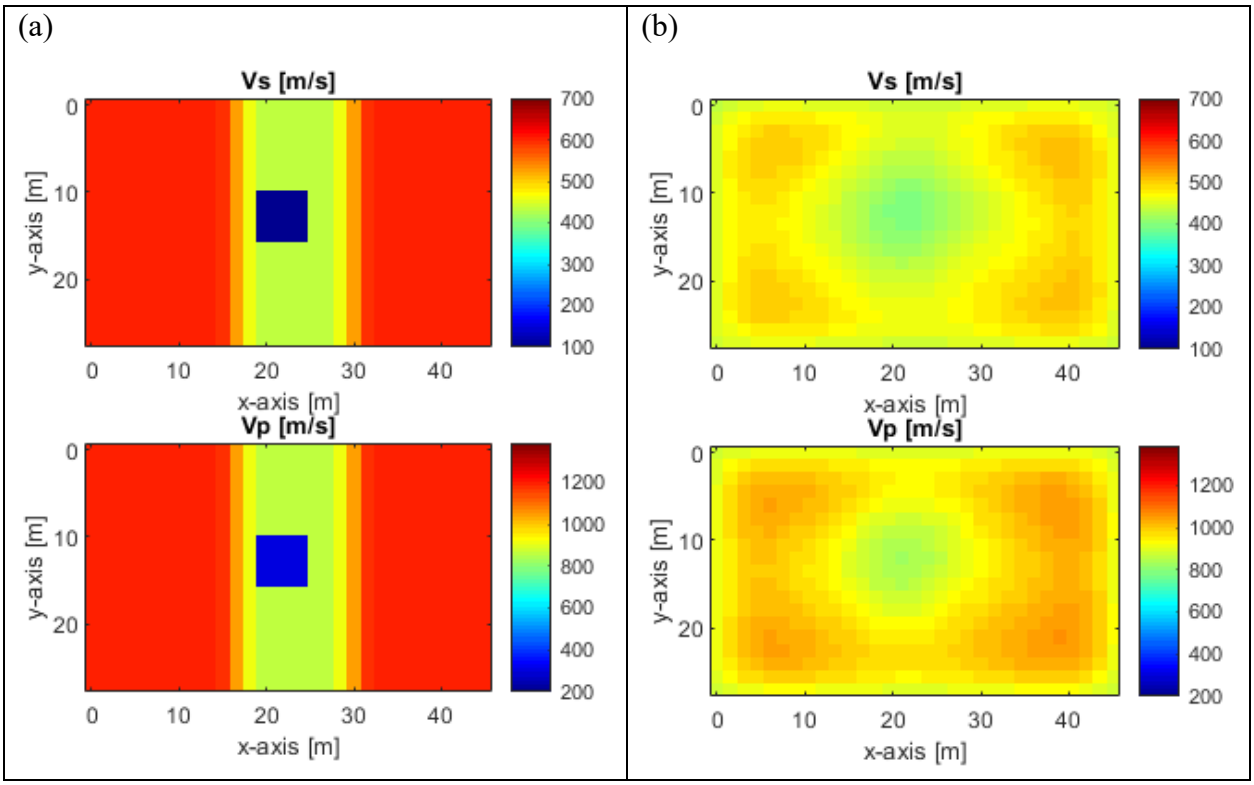

Figure 4.16: Horizontal view of (a) the true model and (b) the inverted model for V_S and V_P at 18-m depth (big void, 4 void diameters)

4.3 Small embedded void (3-m [10-ft] diameter)

4.3.1 Models and test configuration

The developed 3-D FWI algorithm of Chapter 2 was subsequently tested on synthetic models of varying soil-rock profiles with a small embedded void located at various depths. A model domain of 36 m x 24 m x 18 m ($120' \times 80' \times 60'$) (length x width x depth) was used for the analysis. The model was reduced in size compared to that of the large embedded void study (Section 4.2) to account for the reduced receiver-source spacing of 3 m (10 ft) (compared to 4.5 m [15 ft]). Note that given the association of the void depth with the void diameter, the embedded anomalies are closer to the ground surface for the smaller (3 m [10 ft] diameter) void than the larger (4.5 m [15 ft] diameter) void analyzed in the previous section. A two-layer profile was used for the small void model study.

Shown in Figure 4.17 is the test configuration of 96 receivers and 117 shots placed in a staggered grid pattern on the ground surface (0-m depth). Figures 4.18, 4.19 and 4.20 are the 3-D depictions of the studied soil profiles and void depth positions corresponding to two, three and four void diameters, respectively.

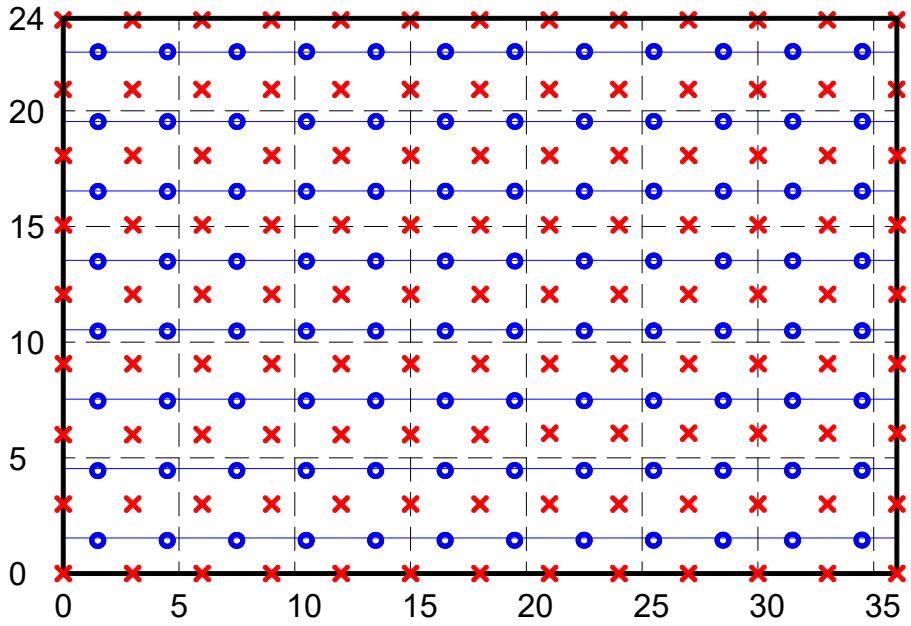

Figure 4.17: Test configuration: 96 receivers (circle) and 117 shots (cross) both at 3-m (10-ft) spacing

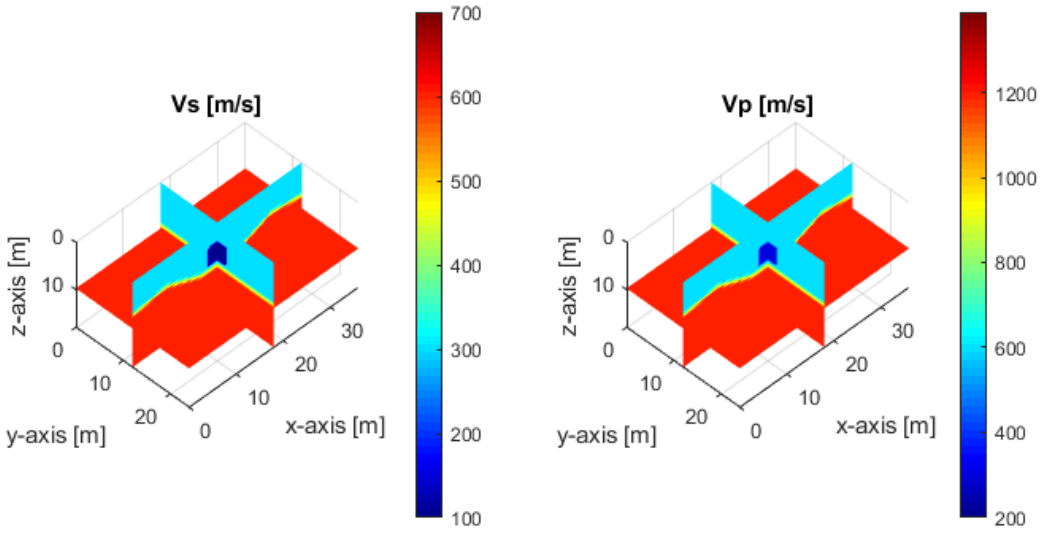

Figure 4.18: Synthetic model with a small void of 3-m (10-ft) diameter at 2 void diameter (6-m [20-ft]) depth

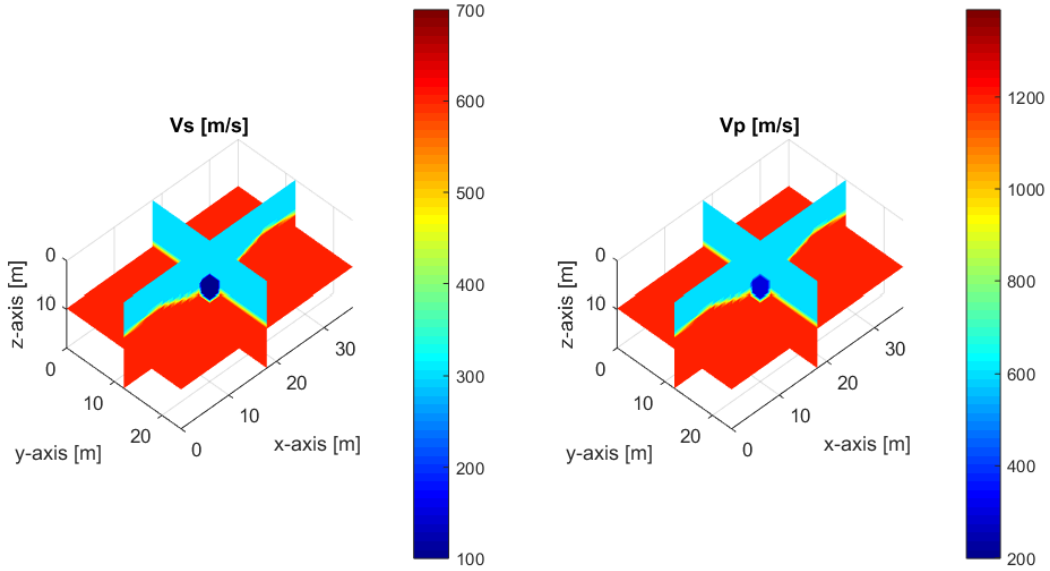

Figure 4.19: Synthetic model with a small void of 3-m (10-ft) diameter at 3 void diameter (9-m [30-ft]) depth

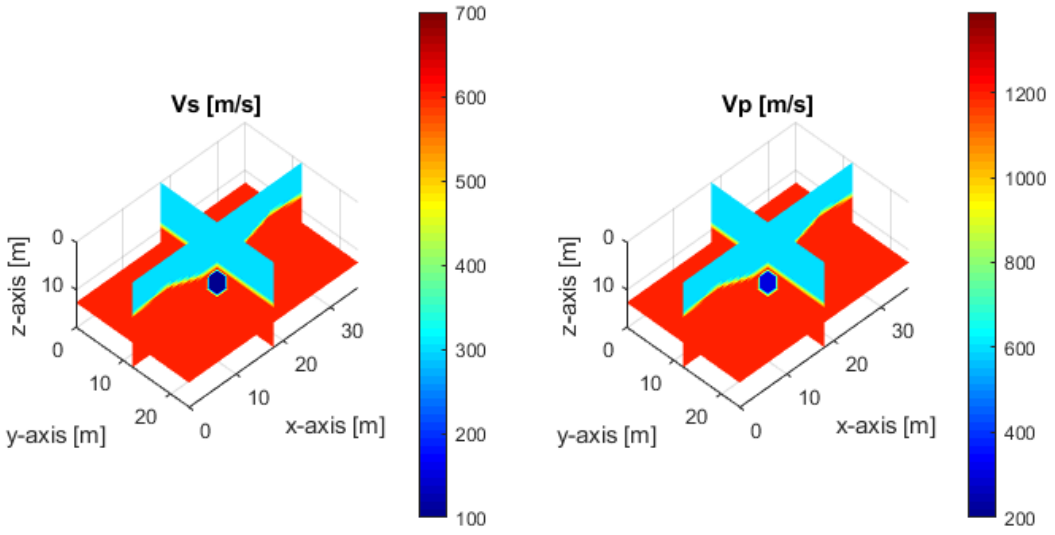

Figure 4.20: Synthetic model with a small void of 3-m (10-ft) diameter at 4 void diameter (12-m [40-ft]) depth

4.3.2 Results for shallow void (depth of 2 void diameters)

The inversion was first performed on the shallow void, using a test configuration of 96 receivers and 117 shots (Figure 4.17) with receivers/sources placed at one void diameter (3 m [10 ft]) spacing on the ground surface (0-m [0-ft] depth). The true model (Figure 4.21 a) consists of two layers with V_S of 300 m/s (1,000 ft/s) for the top layer and 600 m/s (2,000 ft/s) for the bottom layer and Vp twice that of V_S. The 3 m diameter void is embedded above the layer interface at two void diameters (6-m [20-ft] depth) from the ground surface (0-m [0-ft] depth). The initial model (Figure 4.21 b) used in the analysis consisted of a 1-D velocity profile that linearly increases with depth: V_S of 300 m/s (1,000 ft/s) on the surface (0-m [0-ft] depth) to 600 m/s (2,000 ft/s) at the bottom of the model (18-m [60-ft] depth) and V_P twice that of V_S was employed. Two inversions were again performed with the first run using the low frequency range data (5-25 Hz) and the second run using high frequency range data (5-35 Hz). The low frequency data (5-25 Hz) was run using the initial model described above (Figure 4.21 b) and the high

frequency data (5-35 Hz) was performed on the results of the first run as the input model. The first and second runs were set to stop after 20 iterations each. Normalized least-squares error for all iterations of the two inversion runs is shown in Figure 4.22, where the error reduced from 1 at the start of the first iteration to about 0.22 at the end of the first run (iteration 20) and to 0.15 at the end of the second run (iteration 40).

True model features including the layer outline as well as void size and position were successfully recovered after the first run (Figure 4.21c). The second run (Figure 4.21d) with higher frequency data of up to 35 Hz did not result in noticeable improvements in the results. 2-D profile comparison between the true and inverted models are presented for vertical (distance y = 12 m [y = 40 ft], Figure 4.23) and horizontal profiles (depth z = 6 m [z = 20 ft], Figure 4.24). Evident, the layer and void features are clearly recovered, and velocity values are well characterized.

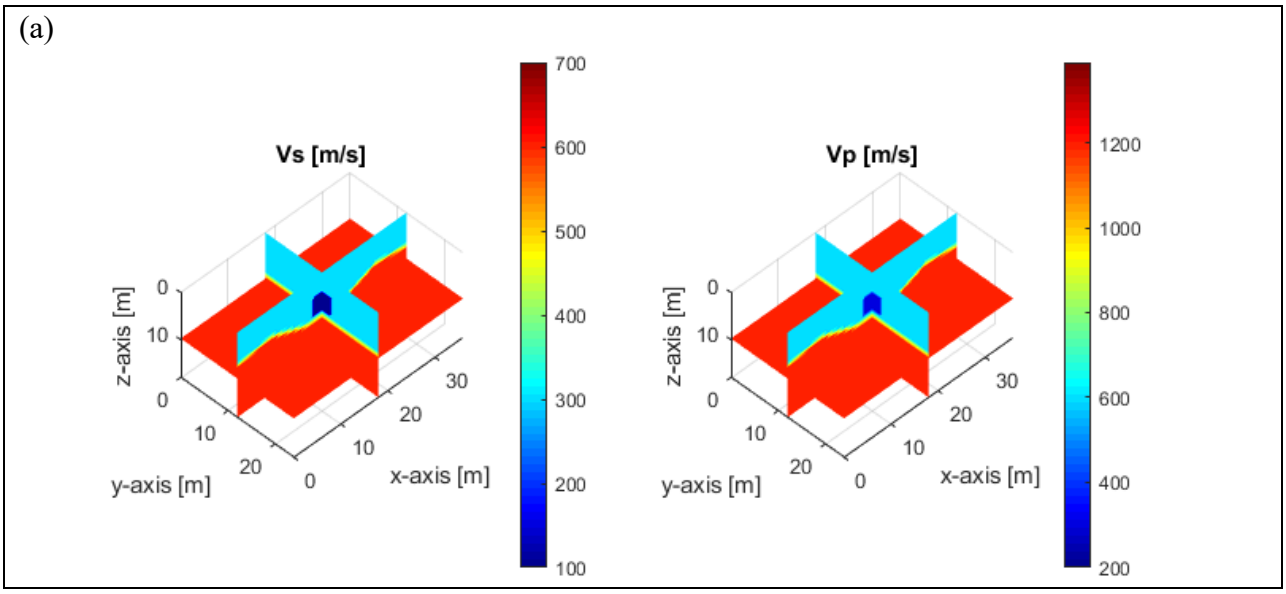

Figure 4.21: Synthetic model of S-wave and P-wave velocities (m/s): (a) true model; (b) initial model; (c) inverted model at 5-25 Hz; (d) inverted model at 5-35 Hz (small void, 2 void diameters)

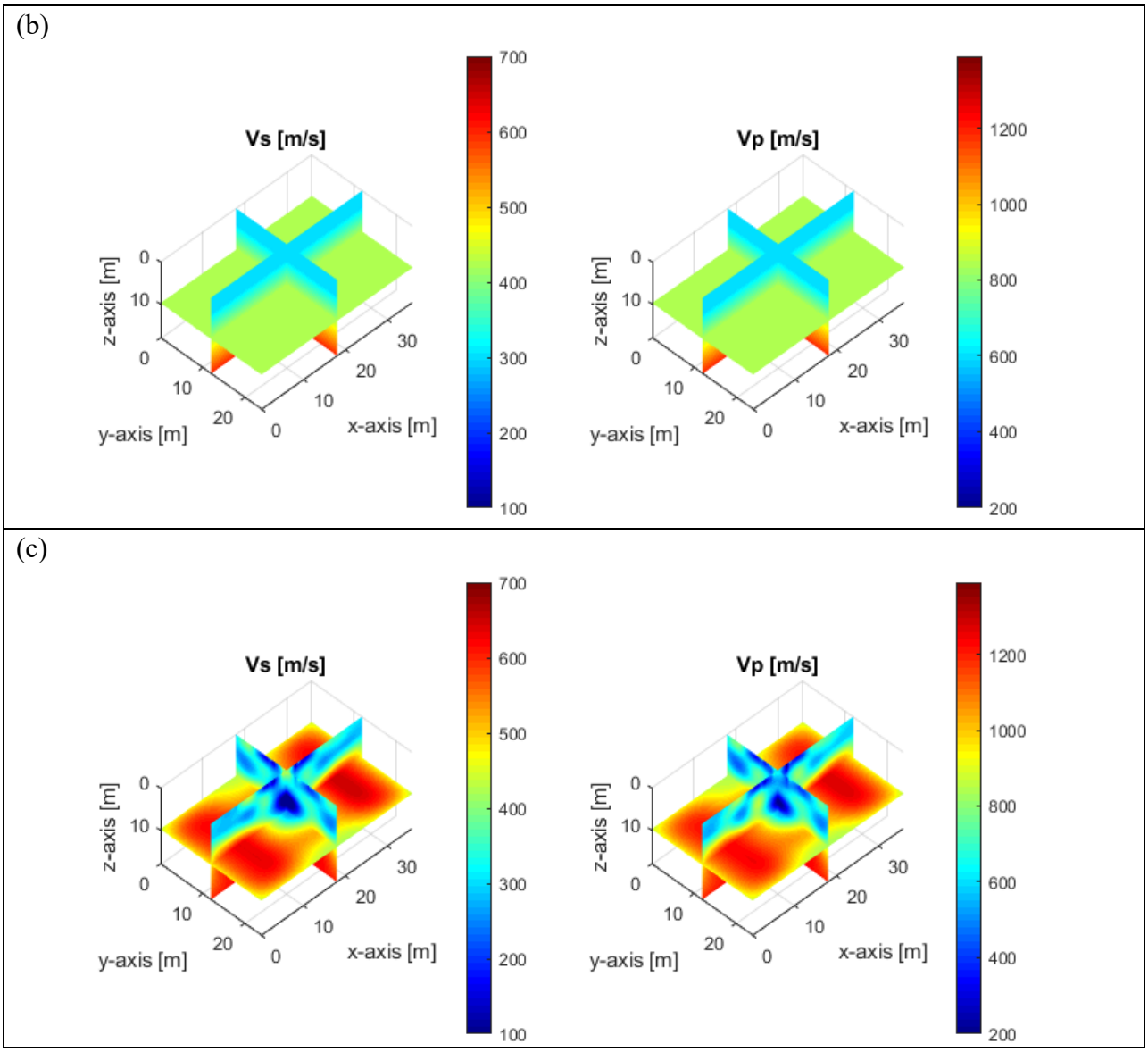

Figure 4.21: Synthetic model of S-wave and P-wave velocities (m/s): (a) true model; (b) initial model; (c) inverted model at 5-25 Hz; (d) inverted model at 5-35 Hz (small void, 2 void diameters)

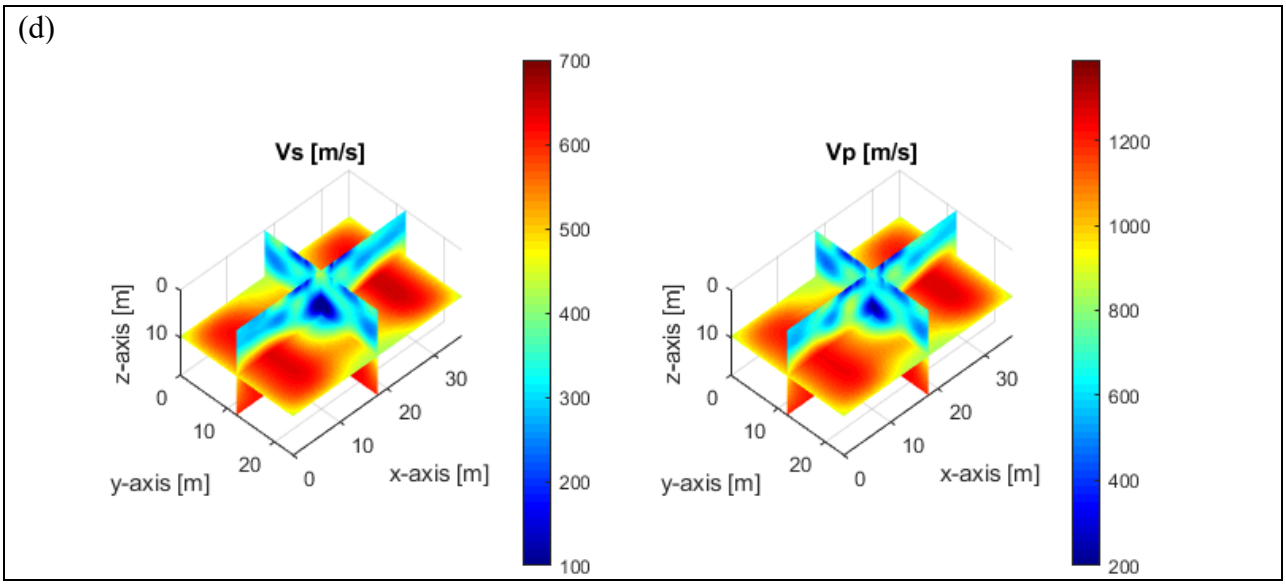

Figure 4.21: Synthetic model of S-wave and P-wave velocities (m/s): (a) true model; (b) initial model; (c) inverted model at 5-25 Hz; (d) inverted model at 5-35 Hz (small void, 2 void diameters)

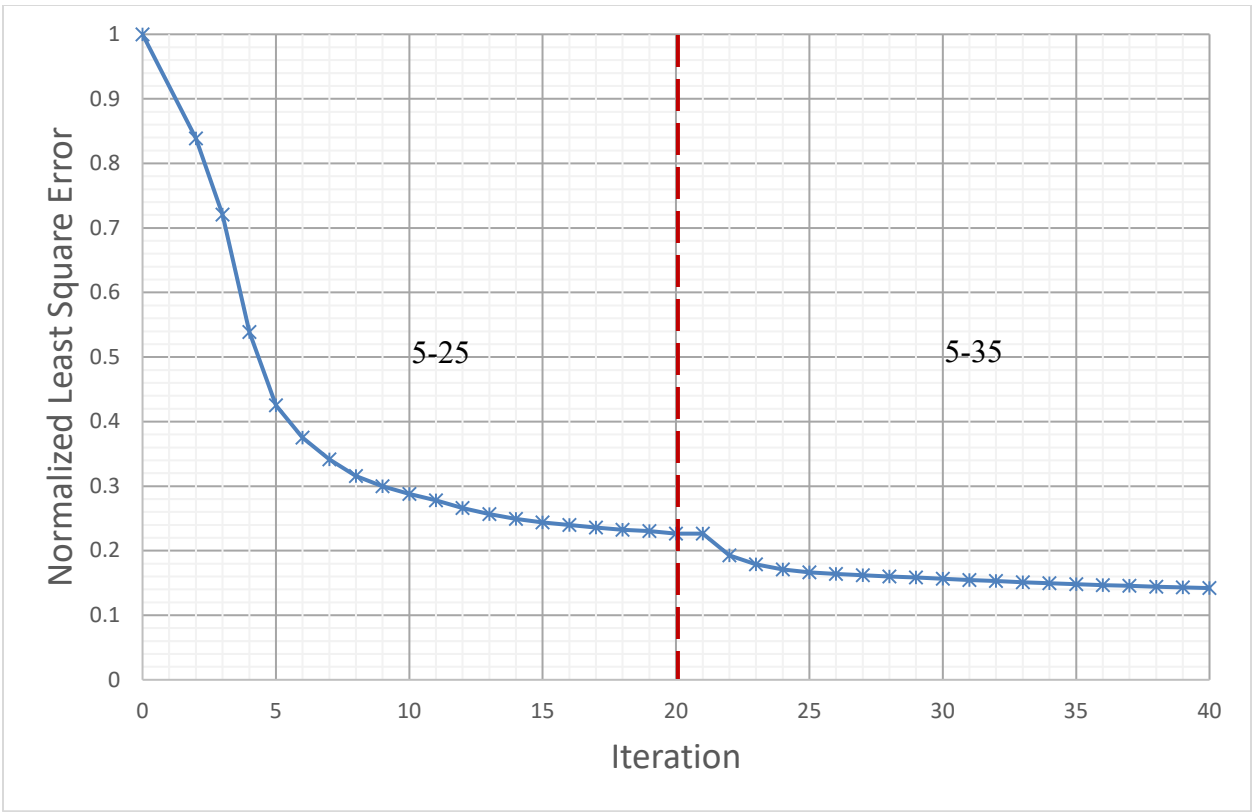

Figure 4.22: Normalized least squares error (small void, 2 void diameters)

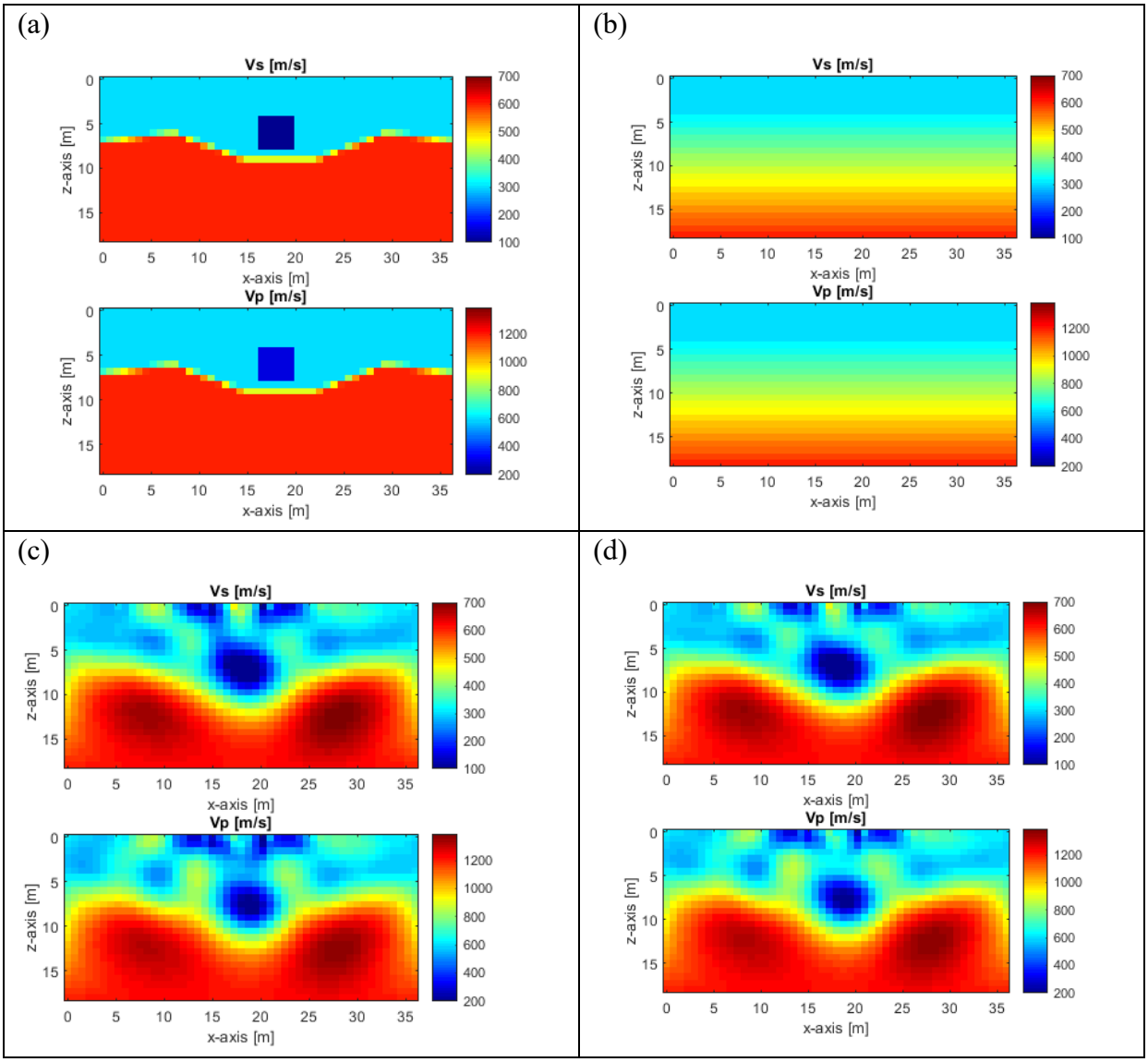

Figure 4.23: Vertical view of V_S and V_P (m/s) at the center of the void (y=12 m [y=40 ft]): (a) true model; (b) initial model; (c) inverted model at 5-25 Hz; (d) inverted model at 5-35 Hz (small void, 2 void diameters).

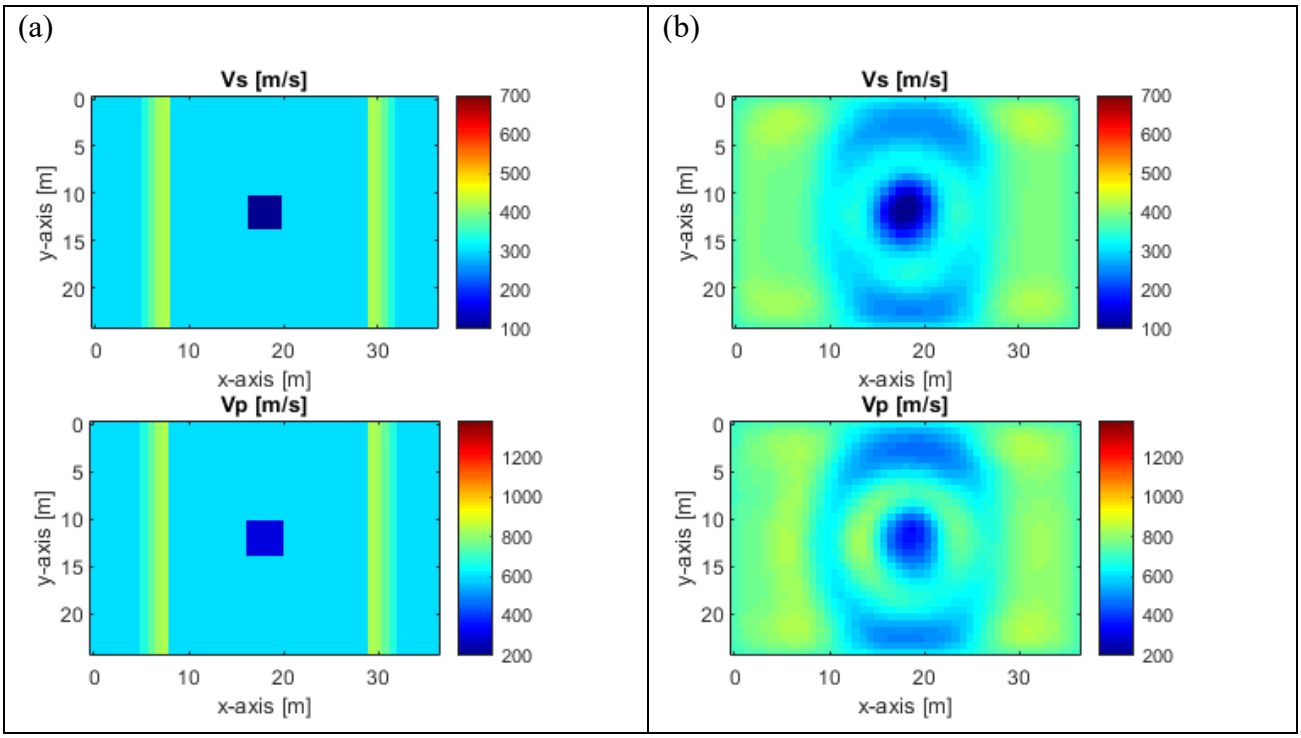

Figure 4.24: Horizontal view of (a) the true model and (b) the inverted model for V_S and V_P at 6-m (20-ft) depth (small void, 2 void diameters)

4.3.3 Results for medium-depth void (depth of 3 void diameters)

The analysis was then performed on the medium-depth void model, in the same fashion with a linear initial model (Figure 4.25b) with two separate inversion analyses with data in the 5-25 Hz and 5-35 Hz ranges. Normalized least-squares error for all iterations of the two runs is shown in Figure 4.26, where the error reduced from 1 at the start of the first iterations to about 0.15 at the end of the first run (iteration 20) and to 0.05 at the end of the second run (iteration 40).

True model features including layer interface and void feature (position and material properties V_S and V_P) were characterized after the first run (Figure 4.25c). The second run (Figure 4.25d) with frequency data up to 35 Hz did not make any noticeable improvements in the inversion results. 2-D profile comparison between the true and inverted models are presented for

vertical (distance y = 12 m [y = 40 ft], Figure 4.27) and horizontal profiles (depth z = 9 m [z = 30 ft], Figure 4.28). Evident, the layer and void features including position, geometry and velocity values were successfully recovered.

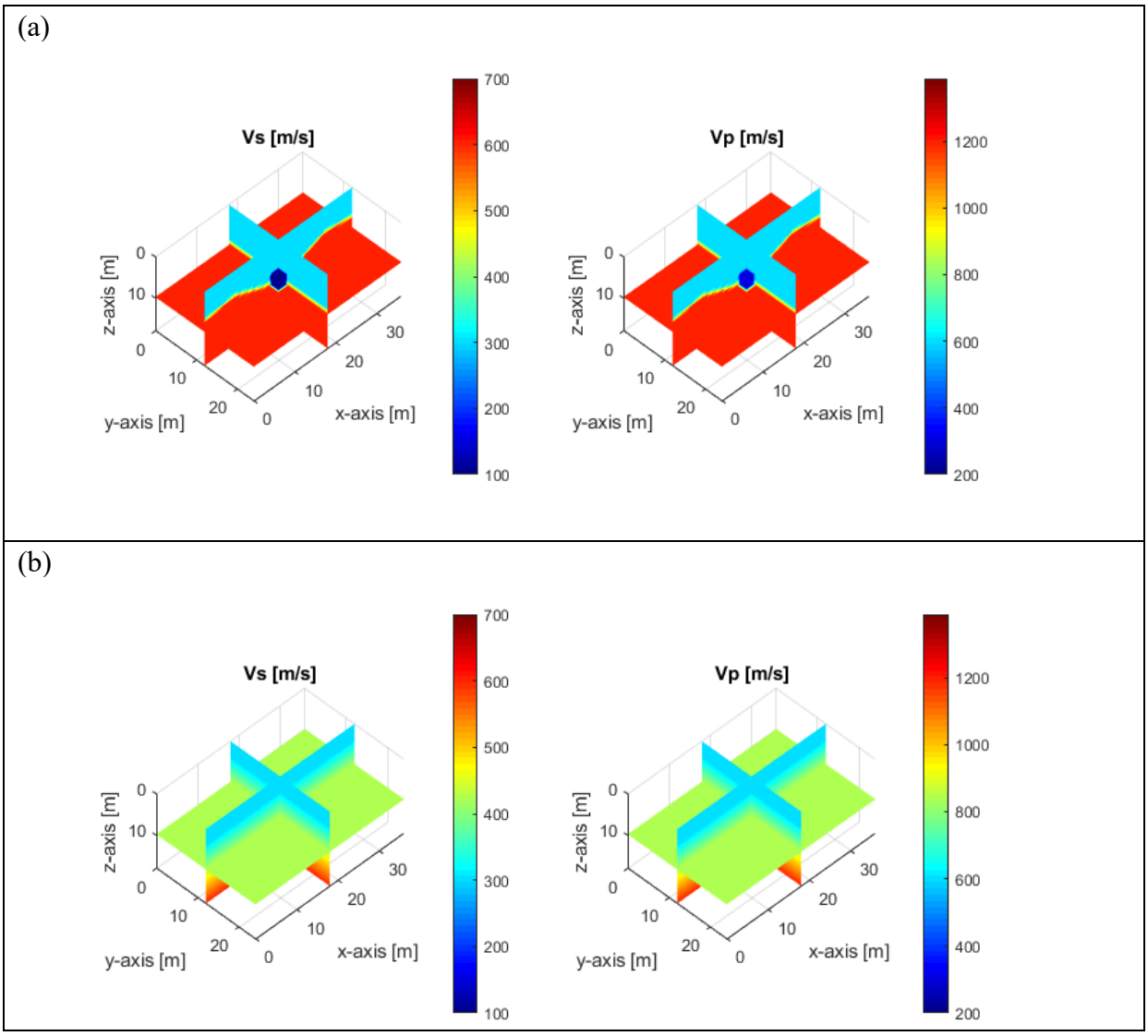

Figure 4.25: Synthetic model of S-wave and P-wave velocities (m/s): (a) true model; (b) initial model; (c) Inverted model at 5-25 Hz; (d) Inverted model at 5-35 Hz (small void, 3 void diameters)

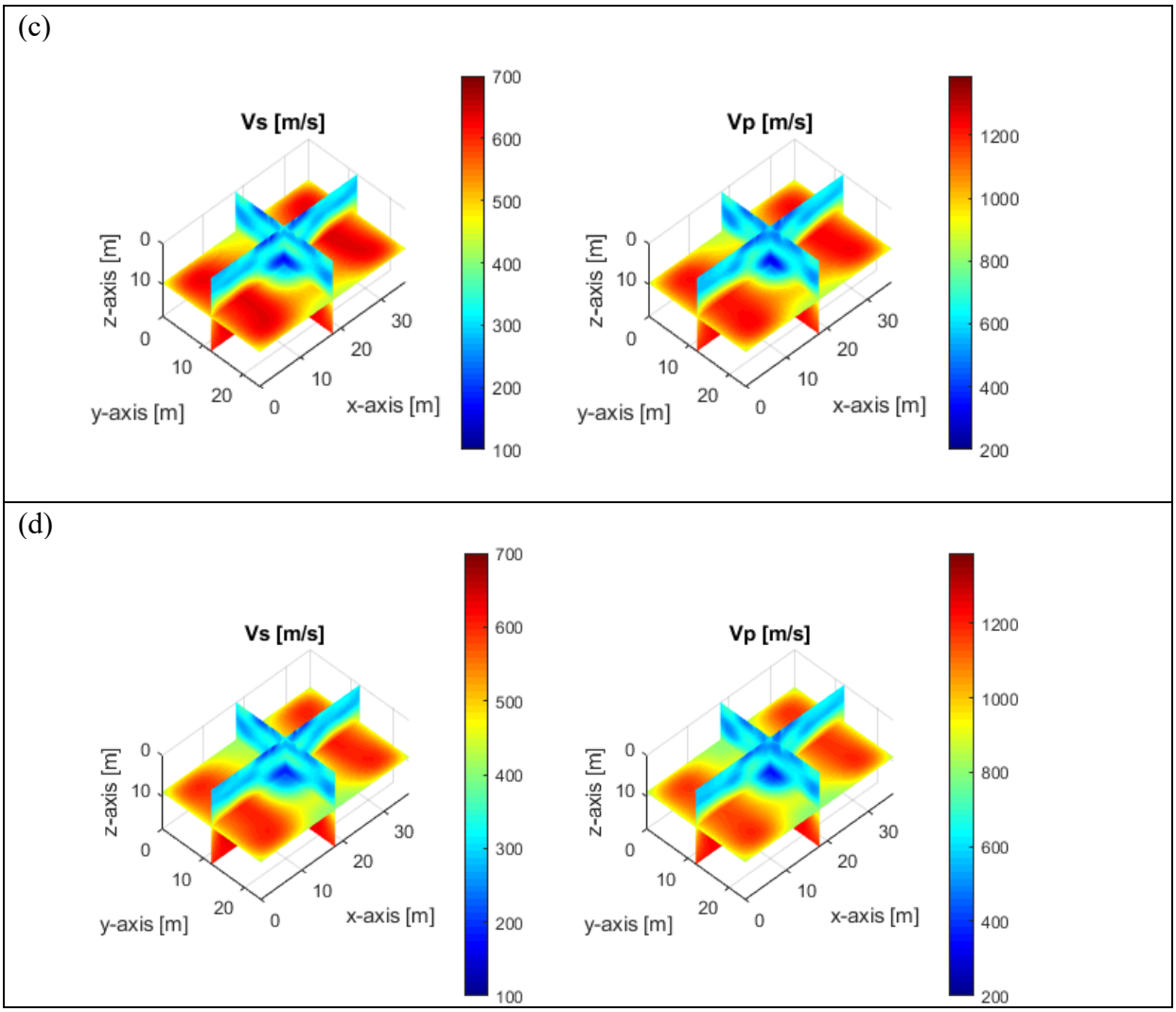

Figure 4.25: Synthetic model of S-wave and P-wave velocities (m/s): (a) true model; (b) initial model; (c) Inverted model at 5-25 Hz; (d) Inverted model at 5-35 Hz (small void, 3 void diameters)

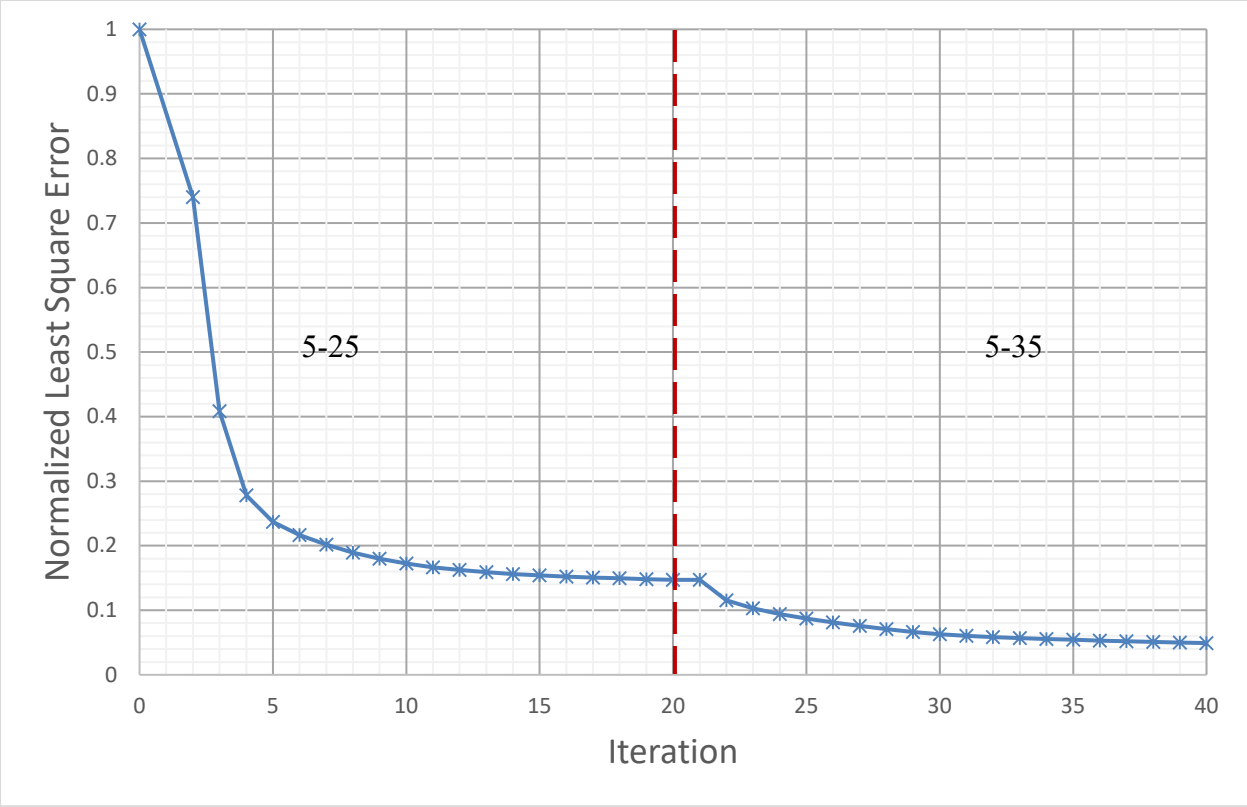

Figure 4.26: Normalized least squares error (small void, 3 void diameters)

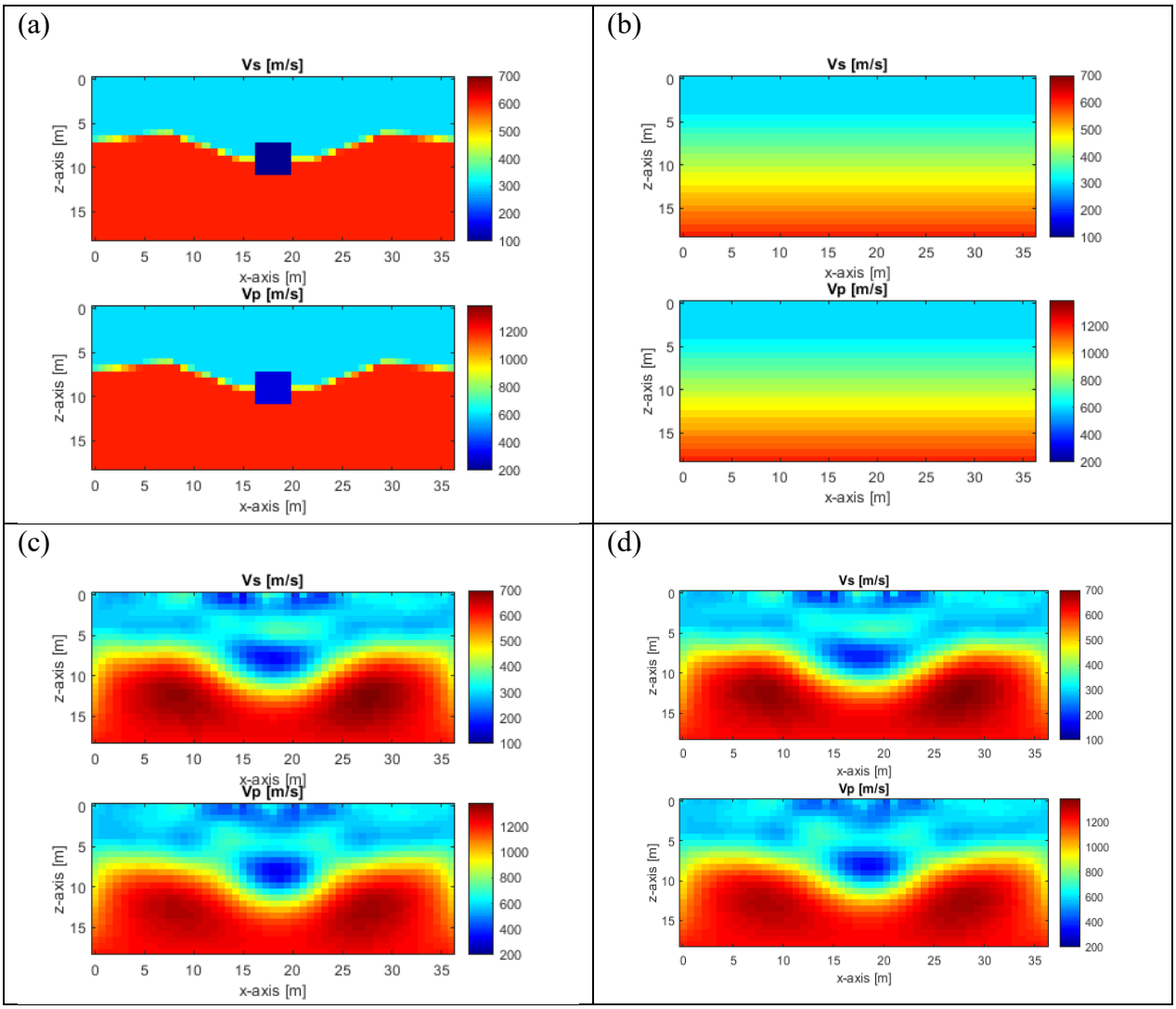

Figure 4.27: Vertical view of V_S and V_P (m/s) at the center of the void: (a) true model; (b) initial model; (c) inverted model at 5-25 Hz; (d) inverted model at 5-35 Hz (small void, 3 void diameters).

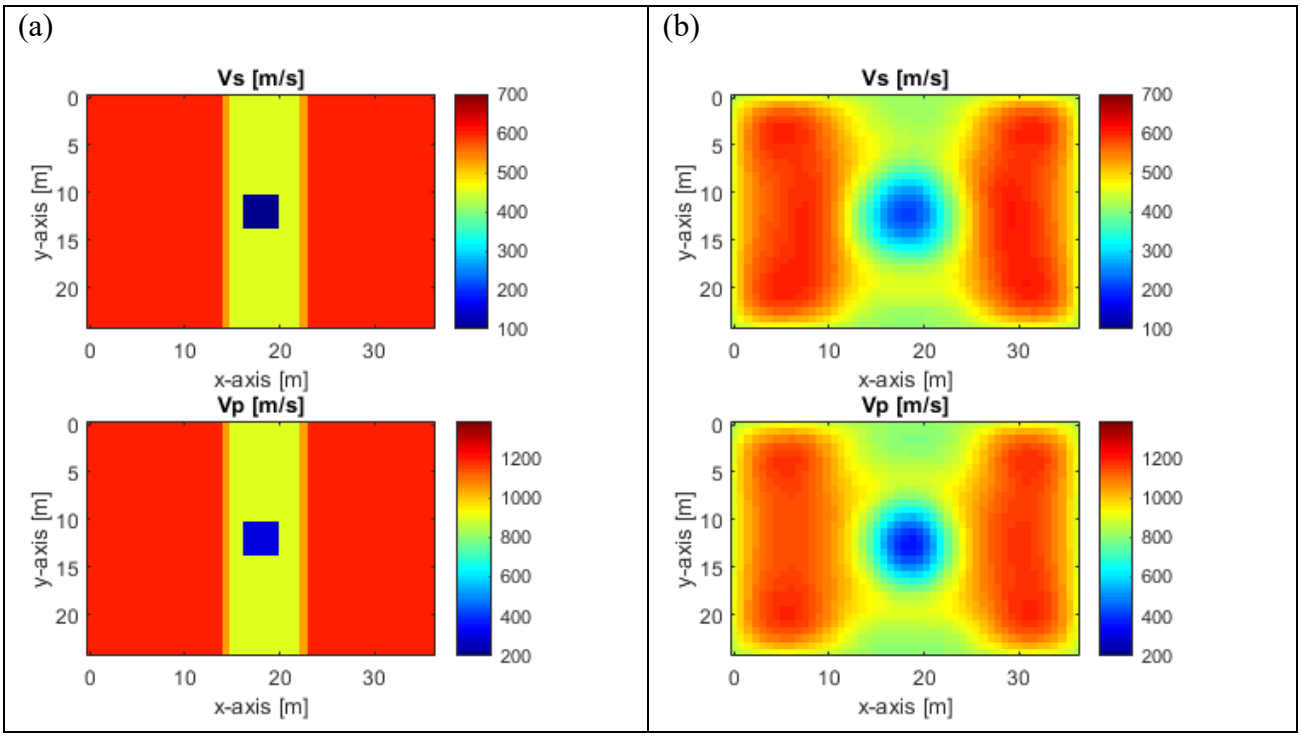

Figure 4.28: Horizontal view of (a) the true model and (b) the final inverted model for V_S and V_P at 9-m (30-ft) depth (small void, 3 void diameters)

4.3.4 Results for deep void (depth of 4 void diameters)

Finally, the same inversion analysis was conducted on the model with the void embedded at the depth of 4 void diameters. The first and second inversion runs were set to stop after 20 and 40 iterations, respectively. Normalized least-squares error for all iterations of the two inversion runs is shown in Figure 4.30, where the error reduced from 1 at the start of the first iteration to about 0.06 at the end of the first run (iteration 20) and 0.02 at the end of the second run (iteration 60).

Features of the true model, including the layer interface position, geometry and material properties (Vs and Vp values) were successfully recovered (Figure 4.29 c and d). However, the inversion algorithm could not successfully recover the void features. 2-D profile comparisons between true and inverted models are presented for vertical (distance y = 12 m [y = 40 ft], Figure 4.31) and horizontal profiles (depth z = 12 m [z = 40 ft], Figure 4.32). There is some indication

of an anomaly at the void location, but the void size and material properties (Vs and Vp values) are not characterized.

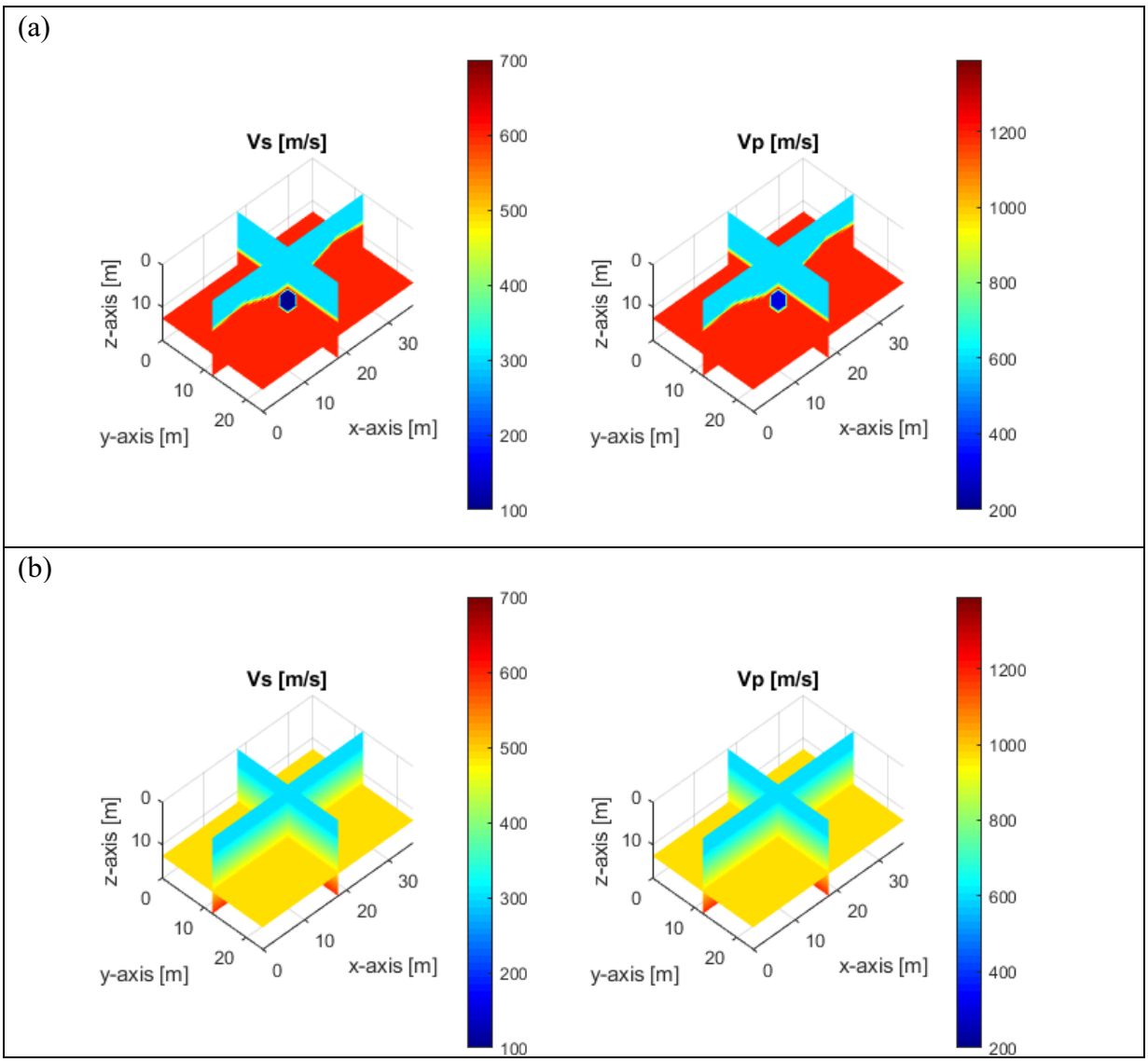

Figure 4.29: Synthetic model of S-wave and P-wave velocities (m/s): (a) true model; (b) initial model; c) inverted model at 5-25 Hz; d) inverted model at 5-35 Hz (small void, 4 void diameters)

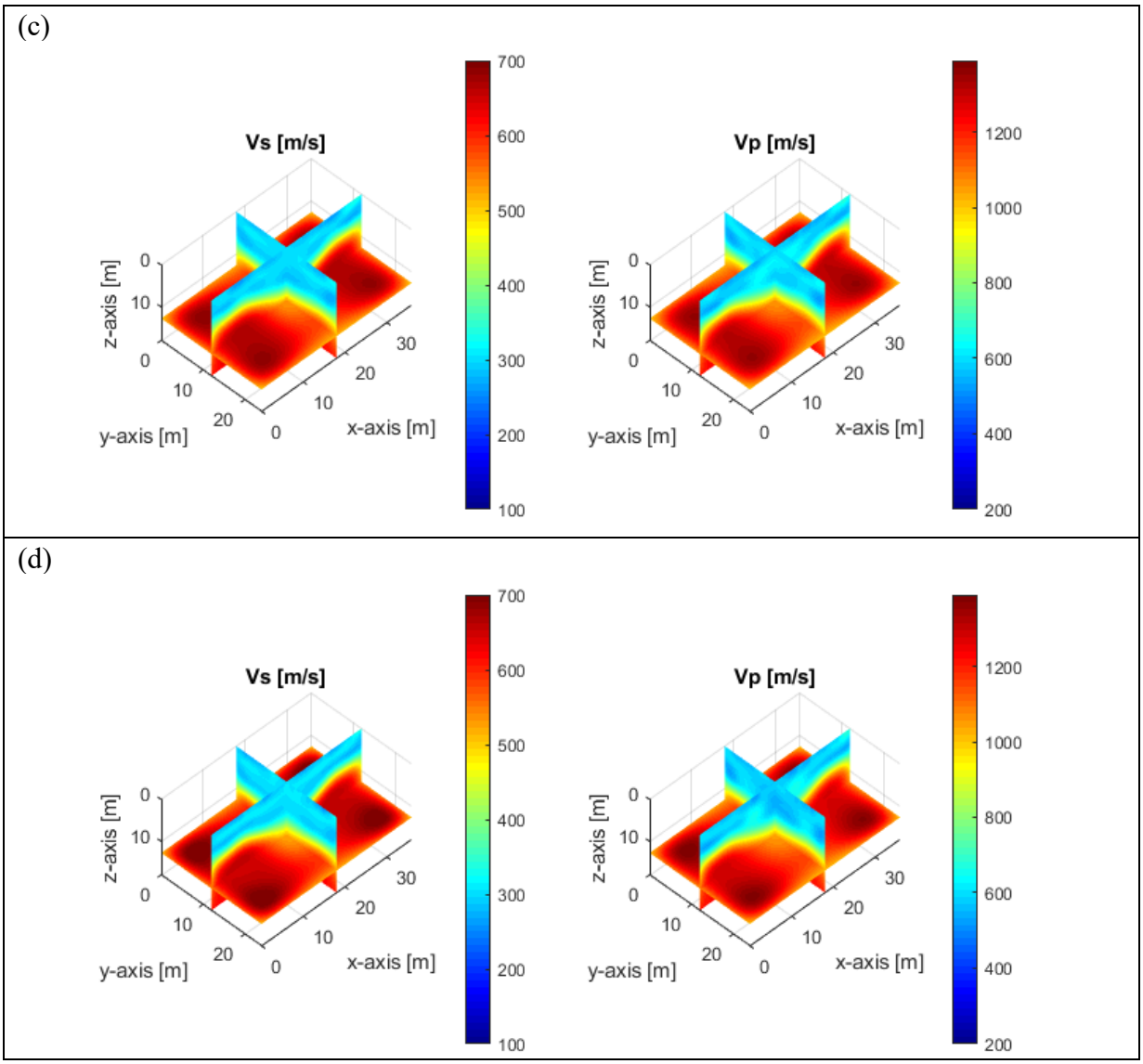

Figure 4.29: Synthetic model of S-wave and P-wave velocities (m/s): (a) true model; (b) initial model; c) inverted model at 5-25 Hz; d) inverted model at 5-35 Hz (small void, 4 void diameters)

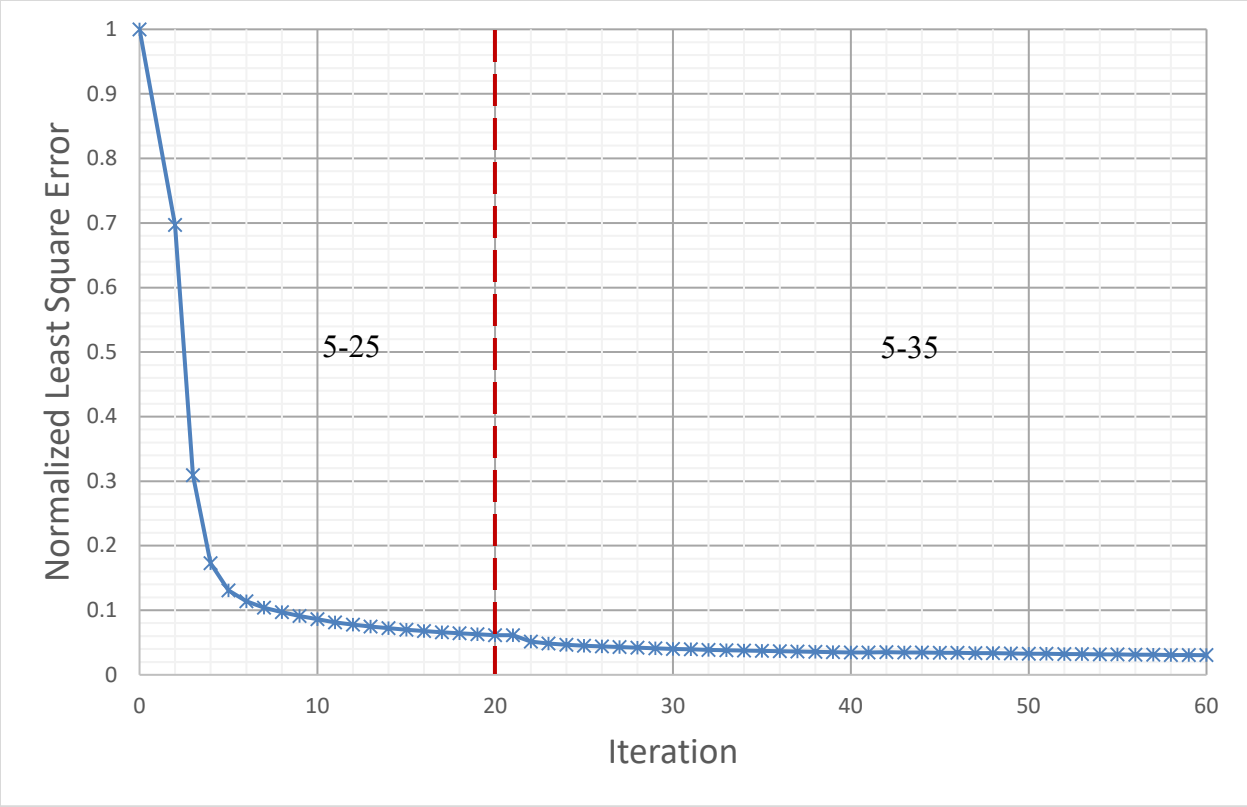

Figure 4.30: Normalized least square error (small void, 4 void diameters)

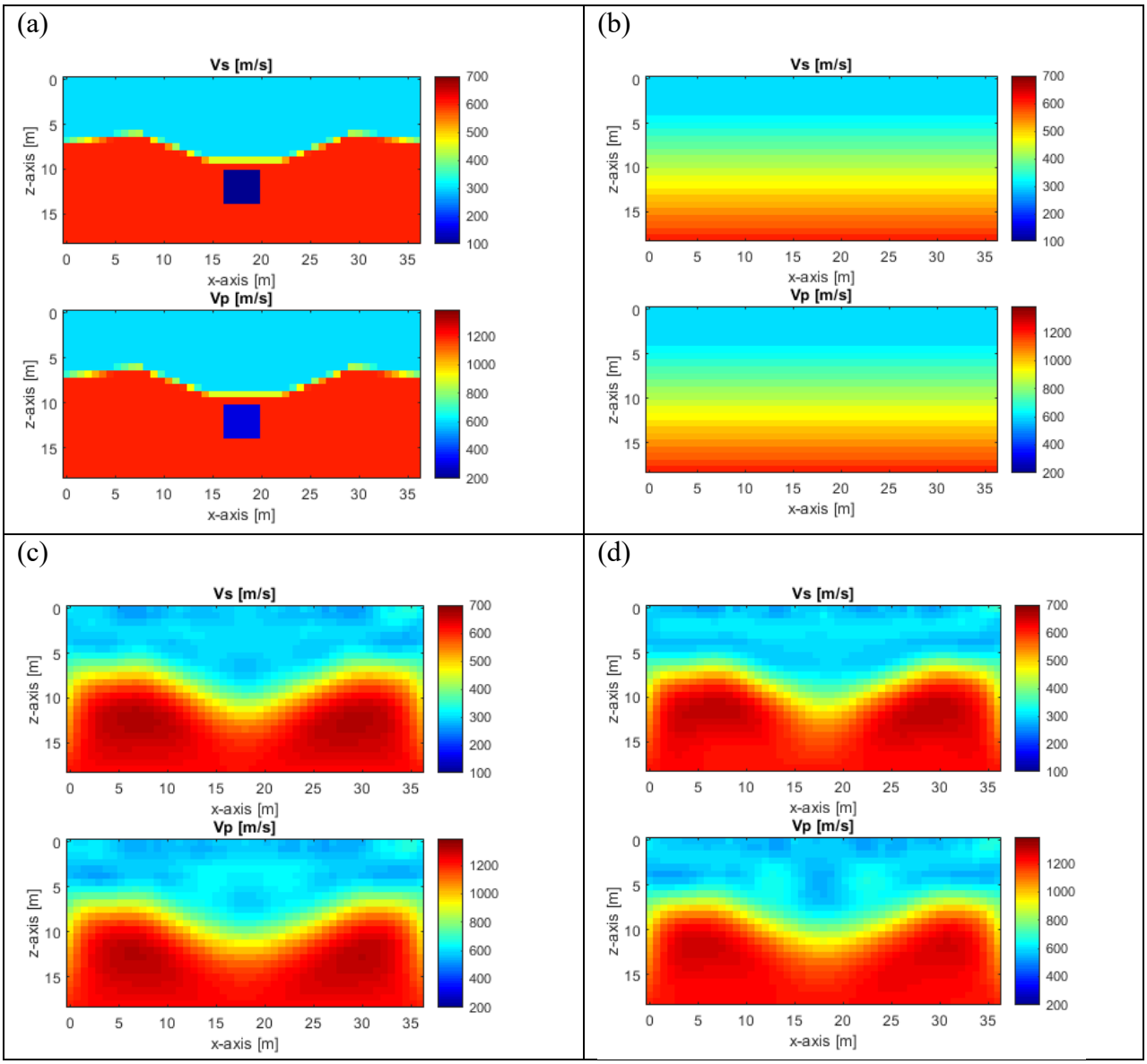

Figure 4.31: Vertical view of V_S and V_P (m/s) at the center of the void: (a) true model; (b) initial model; (c) inverted model at 5-25 Hz; (d) inverted model at 5-35 Hz (small void, 4 void diameter).

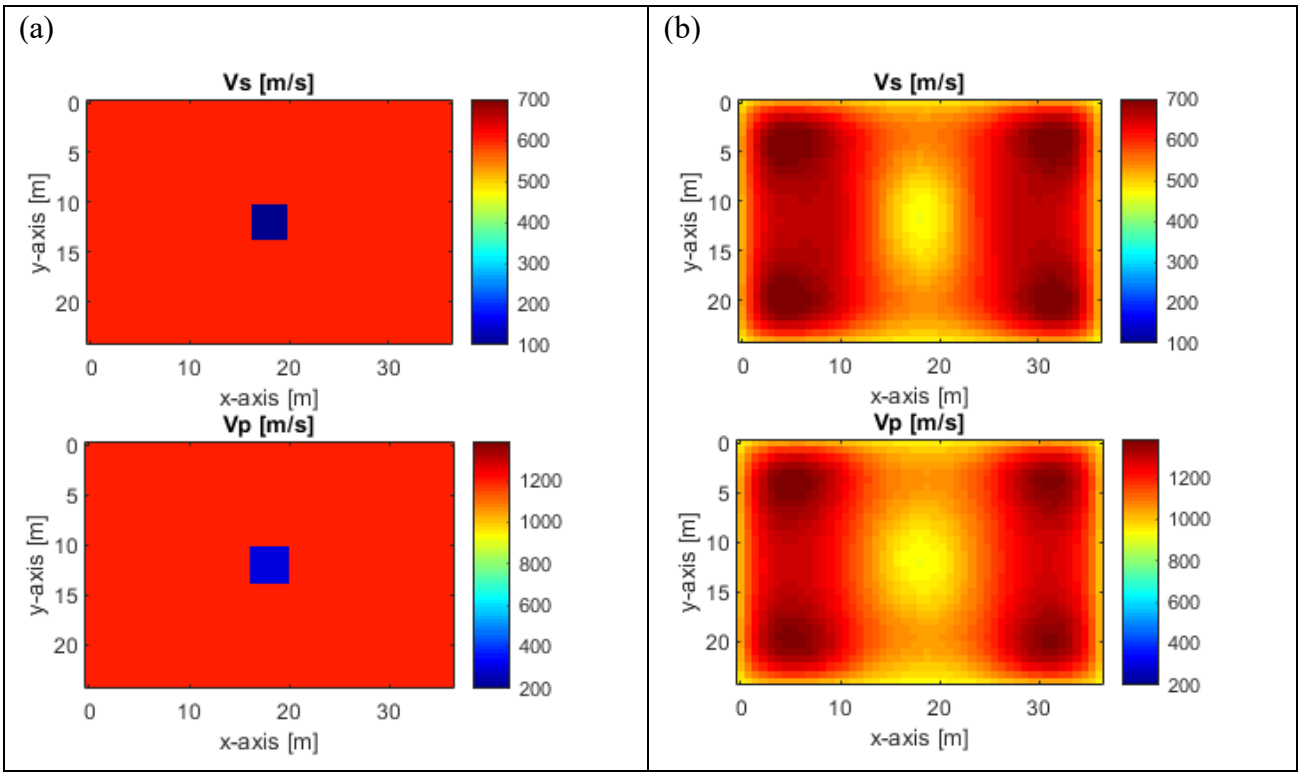

Figure 4.32: Horizontal view of (a) the true model and (b) the final inverted model for V_S and V_P at 12-m depth (small void, 4 void diameter)

4.4 Conclusion

Three dimensional FWI parametric studies were performed on synthetic data to determine the maximum depth of characterizing embedded voids. The objective was to establish a guideline for subsequent field work (Chapter 5) to verify the validity of void characterization. Specifically, the study was to identify the maximum depth as a function of void diameter that the anomaly can be identified/verified with high certainty. In total, three different void depth scenarios were tested with a void embedded at two, three and four void diameters from the ground surface. Based on the results of Chapter 3, a uniform 2-D grid of geophones and sources were placed at one void diameter spacing on the ground surface. Two different void sizes of 3 m (10 ft) and 4.5 m (15 ft) were separately tested for each embedment depth and at different

frequency ranges. Accuracy and resolution of the inverted profiles were subsequently compared to the true model and the maximum characterization depth was identified.

The analyses initiated on the model with the larger void, 4.5 m (15 ft) diameter. The void was embedded at 9 m (30 ft), 13.5 m (45 ft) and 18 m (60 ft) depths corresponding to two, three and four void diameters from the ground surface, respectively. The inverted results suggested that the maximum depth at which void features including its geometry, position and material properties can fully be characterized is 3 void diameters from the ground surface. Even though the existence of a void may be estimated at a depth of 4 void diameters, the lack of detailed recovered features is problematic.

The analyses were next performed on the model with the smaller void, 3 m (10 ft) diameter. The void was similarly embedded at 6 m (20 ft), 9 m (30 ft), and 12 m (40 ft) depths corresponding to two, three and four void diameters from the ground surface, respectively. It was again suggested by results of the inversion analyses that the maximum depth of characterization was again 3 void diameters from the ground surface. For the deeper void at 4 diameters depth, there was again some indication of an anomaly at the void location, however the void size and material properties (Vs and Vp values) were not characterized.

From the results of the synthetic model simulations, the maximum depth at which a void can be identified and characterized with confidence is 3 void diameters from the ground surface. This suggests that a void detected at depths larger than 3 void diameters may be an artifact and not reflect true site conditions. The guidelines for characterization of void depth that are established in this chapter will be used in the field experimental/analyses study, Chapter 5. Finally, the study suggests that the optimal frequency range, 5 to 35 Hz, should be within the

range of the active source (properties based on height of drop weight and size of impact plate) in field experiments of Chapter 5.

CHAPTER 5

FIELD VERIFICATION OF THE DEVELOPED 3-D FULL WAVEFORM INVERSION METHOD

5.1 Introduction

The objective of the final task was the field verification of the developed (Chapter 2) 3-D Full Waveform Inversion (FWI) method for identifying soil-rock layers, pinnacles, voids, etc., at Florida sites using a 2-D array of shots and receivers in a grid pattern on the ground surface, as well as testing an alternate testing configuration for increased void depth detection, when surface access is limited. Chapters 3 and 4 used the developed 3-D FWI algorithm in a synthetic study to find the optimal source and receiver placement (ground surface) for maximum depth of void detection. Specifically, it was shown in Chapter 3 that using a staggered grid of shots/receivers placed at a minimum spacing of one void diameter on the ground surface should result in the best void characterization. Chapter 4 identified that voids and other subsurface anomalies are best detected if located less than 3 void diameters from the ground surface.

One of the important findings of the field work is that seismic ground surface surveying is greatly influenced by horizontal surface wave propagation at shallow depths, with feature detection controlled by size and distance between source, object and sensors. For instance, the detection of soil or rock layers, and pinnacles, are more likely because of the larger surface area and associated reflection of the propagating body wave energy off each versus a small void at large depth.

Another important development of this chapter is the 3-D visualization of the 3-D FWI results including soil-rock layering, features (e.g. pinnacles) as well as voids. The method was first used at a site in Gainesville, Florida, for soil-rock characterization and compared with SPT N-values. It was then tested at a site containing a buried storm water pipe on the University of

Florida main campus. Next, it was used in two areas of a large retention pond in Newberry, Florida. For the Newberry, Florida site, of interest was the unknown subsurface features including soil-rock layering, pinnacles as well as the detection of unknown voids.

The next development from the field work was the use of a larger source aimed at producing more energy at lower frequencies (5-20 Hz), with longer wavelengths (50 m-100 m [150-300 ft]). It was expected that the longer wavelengths could penetrate deeper into the underlying subsurface revealing deeper structures. The test was carried out at a bridge construction site in Miami, Florida. A large deep void was encountered during a preliminary SPT investigation and its extent was verified using sonar imaging. The goal here was to see if the 3-D FWI method could identify the large deep void using surface testing only.

The final development of the field work was the coupling of the in-depth SPT source test data with the developed 3-D FWI method. This effort was carried out at both the Newberry and Miami test sites. The goal was to extend the imaging range for void detection to more than three void diameters from the ground surface in places where there are limitations in terms of source energy (e.g., small source) or surface access (e.g., right of way). In-depth source data are rich in body waves and are less affected by surface dispersion effects. The approach has the potential to image low velocity anomalies such as voids and ravel zones throughout the subsurface in the vicinity of the SPT borehole which is of great interest in the design and construction of deep foundations for bridges and other civil engineering projects. Data acquisition, analysis, visualization, and confirmation (invasive testing) details are elaborated in the following sections.

5.2 Gainesville FDOT retention pond soil-rock characterization

The field work started with the objective of characterizing both soil-rock layering and pinnacle formations. The testing configuration consisted of 96 receivers and 52 shots (Figure 5.1). The seismic wave-fields were generated by a propelled energy generator (PEG, 40 kg [88 lbf] model) as shown in Figure 5.2b, and simultaneously recorded by 48 4.5-Hz vertical geophones in two stages. In each stage, the 48 geophones were placed for a half of the receiver grid, and 52 shots were applied for the entire source grid (4 × 13). As the same impact load (same drop weight and height of the PEG) was applied at each shot location, the collected data from the two stages were simply combined to produce 96-channel shot gathers. Four SPT borings were also conducted at a distance of 24 m (80 ft) (x = 24 m [80 ft]) on each geophone line for verification of seismic results.

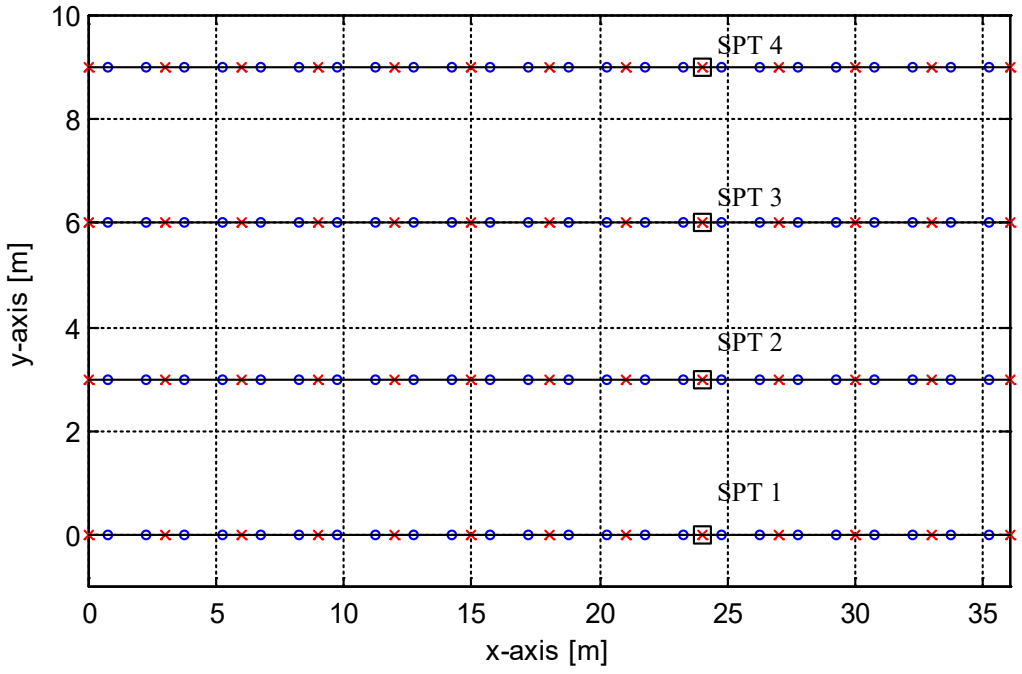

Figure 5.1: Test configuration used for field experiments: source (cross), receiver (circle), standard penetration tests, SPT (square).

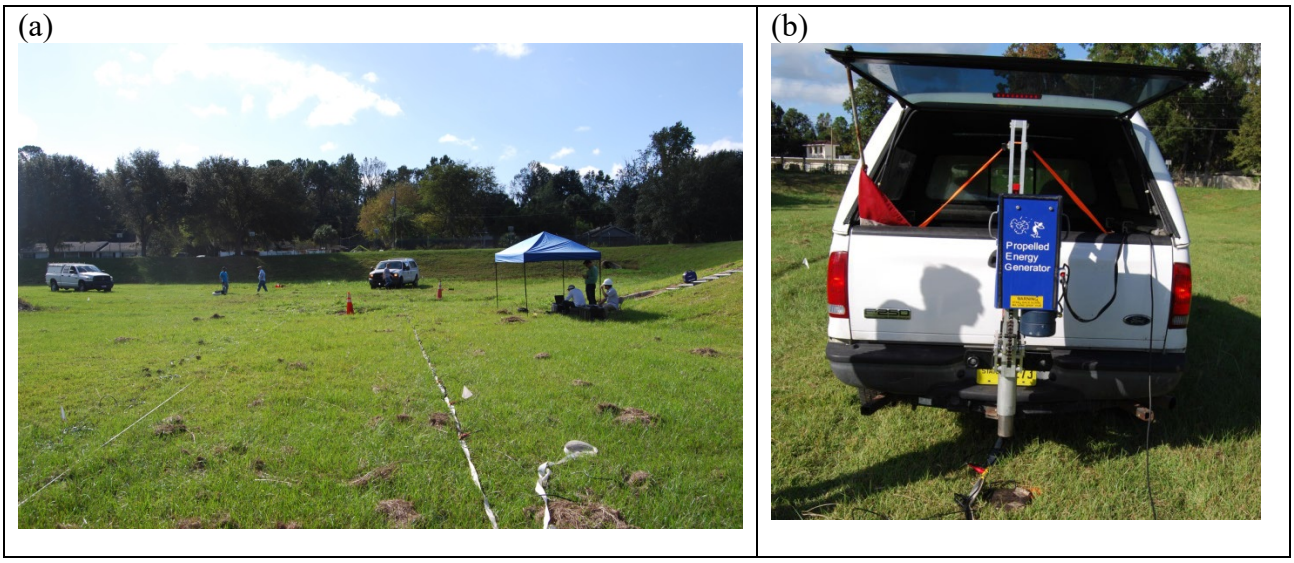

Figure 5.2: Field experiment: (a) test site and (b) propelled energy generator

A 1D initial model was developed via spectral analysis of the measured field data for a sample shot with one line of 24 geophones (Figure 5.3). Rayleigh wave velocities (Vr) were determined from 250 m/s (830 ft/s) to 400 m/s (1,330 ft/s) at the frequency range of 12 to 50 Hz. As Vs is similar to Vr, the Vs near the ground surface associated with high frequency data was known to be approximately 250 m/s (830 ft/s). A half space with Vs of 400 m/s (1,330 ft/s) was assumed at the start with half of the maximum wavelength associated with the data, 12 Hz, for grid depth or 16.7 m (55 ft) (velocity/frequency/2 = 400/12/2 = 16.7 m). Like the case of synthetic model (Chapters 2 to 4), the initial model (Figure 5.4a) was established having Vs increasing with depth from 250 m/s (830 ft/s) at the surface to 400 m/s (1,330 ft/s) (Vs of the half space) at the bottom of the model. The depth of model was taken as a half of the longer dimension of test area (or 18 m [60 ft]) to maintain good signal coverage in the analyzed domain. The Vp was estimated from Vs using a constant Poisson's ratio of 1/3 for the entire medium, which was taken as the middle value of the range from ¼ to ½ for general soils. The mass density was assumed as 1800 kg/m^3 (112.4 lb/ft^3) for the whole medium and kept constant during inversion. Efforts to invert the mass density of medium from the measured wave-field have been

shown to be unsuccessful. This can be explained that most of the energy in wave-fields measured on the surface are Rayleigh waves that are not very sensitive to the mass density.

Measured field data were filtered through the two frequency bandwidths of 5-20 Hz and 5-30 Hz, and used in two sequential inversion runs. The first run at 5 - 20 Hz began with the initial model shown in Figure 5.4a, and the second run began with the results of the first inverted run. During inversion, estimated waveform data are adjusted by an offset-dependent correction factor of the form $y(r) = A \cdot r^{\alpha}$ to compensate for amplitude damping effects caused by inelastic response that cannot be accounted for with the elastic model. Where r is the source-receiver offset, and the factor A and exponent α were determined with an iterative least-squares inversion, which minimizes the energy of waveform residuals. For forward simulation, a source signature was estimated by deconvolution of the measured data with the Green's function, which was explicitly calculated by forward simulation with an assumed Ricker wavelet source. The source signature was updated at the beginning of each iteration to account for the change in the Green's function during inversion due to updated model parameters.

The medium of $18 \times 36 \times 9\ m$ $(60' \times 120' \times 30')$ $(depth \times length \times width)$ was divided into 13,824 cells of $0.75 \times 0.75 \times 0.75\ m$ $(2.5' \times 2.5' \times 2.5')$. Each 0.75 m (2.5 ft) cell size was selected as half of the smaller geophone spacing (1.5 m [5 ft]) to conveniently assign sources and receivers to discretized nodes. The same cell size was used for both inversion runs. Vs and Vp of all cells were updated independently and simultaneously during each inversion. The first and second inversion runs stopped at 21 and 9 iterations, respectively. The total computer time was about 26 hours on a typical workstation computer with 32 cores running at 3.46 GHz and 256 GB of RAM.

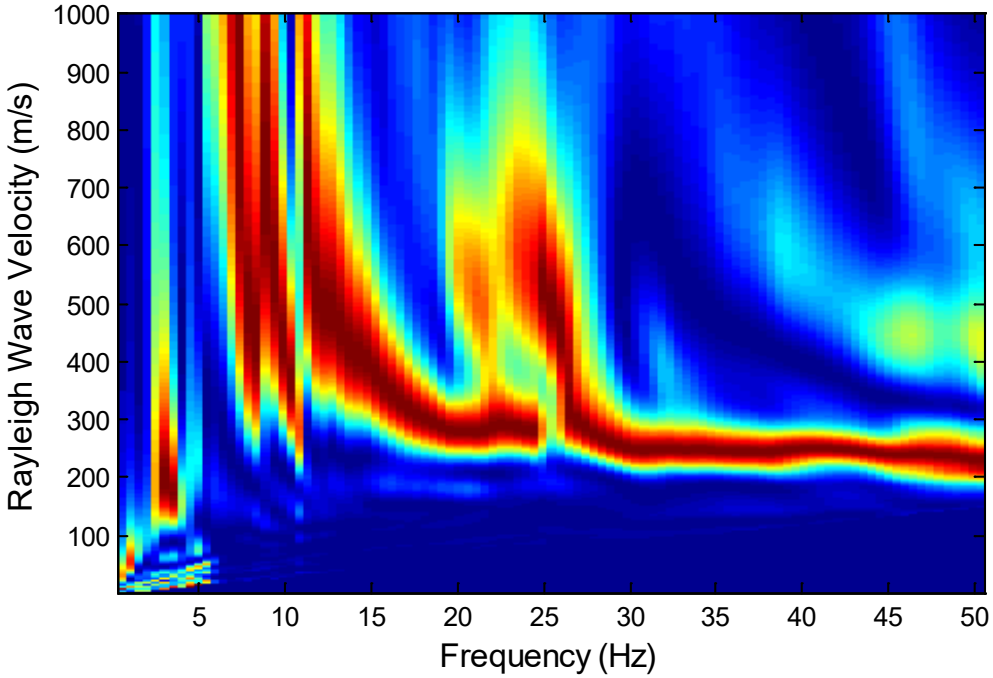

Figure 5.3: Field experiment: spectral analysis of measured data for one sample shot and one line of 24 geophones.

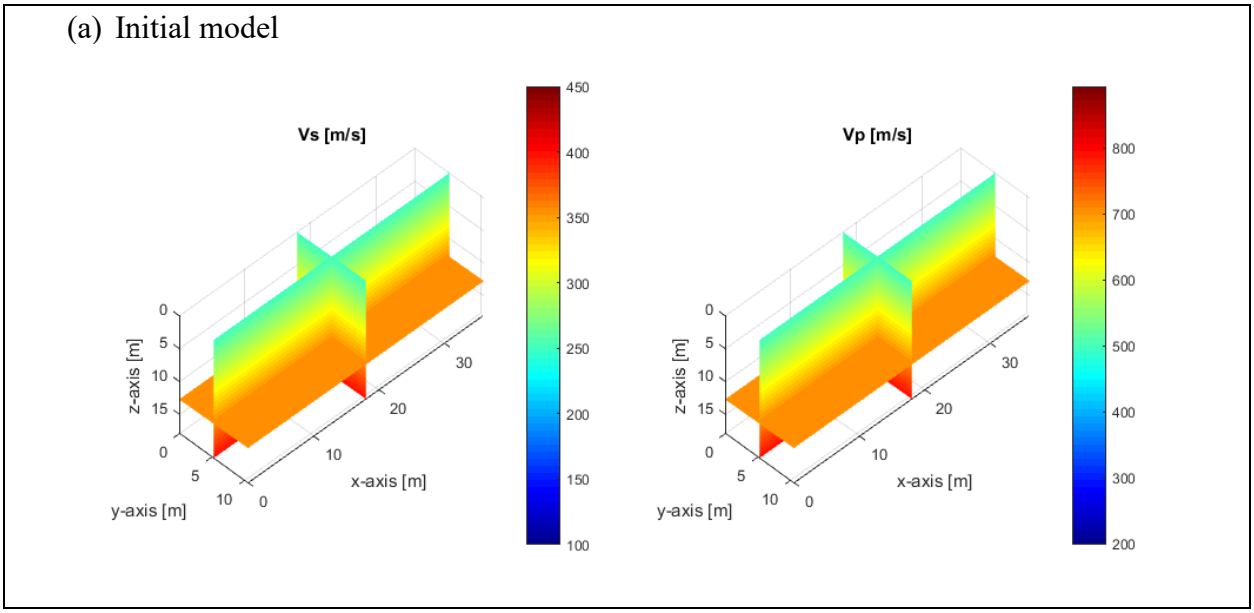

Figure 5.4: Field experiment: distribution of V_S and V_P (m/s): (a) initial model used at the beginning of inversion and (b) final inverted models at 5-30 Hz.

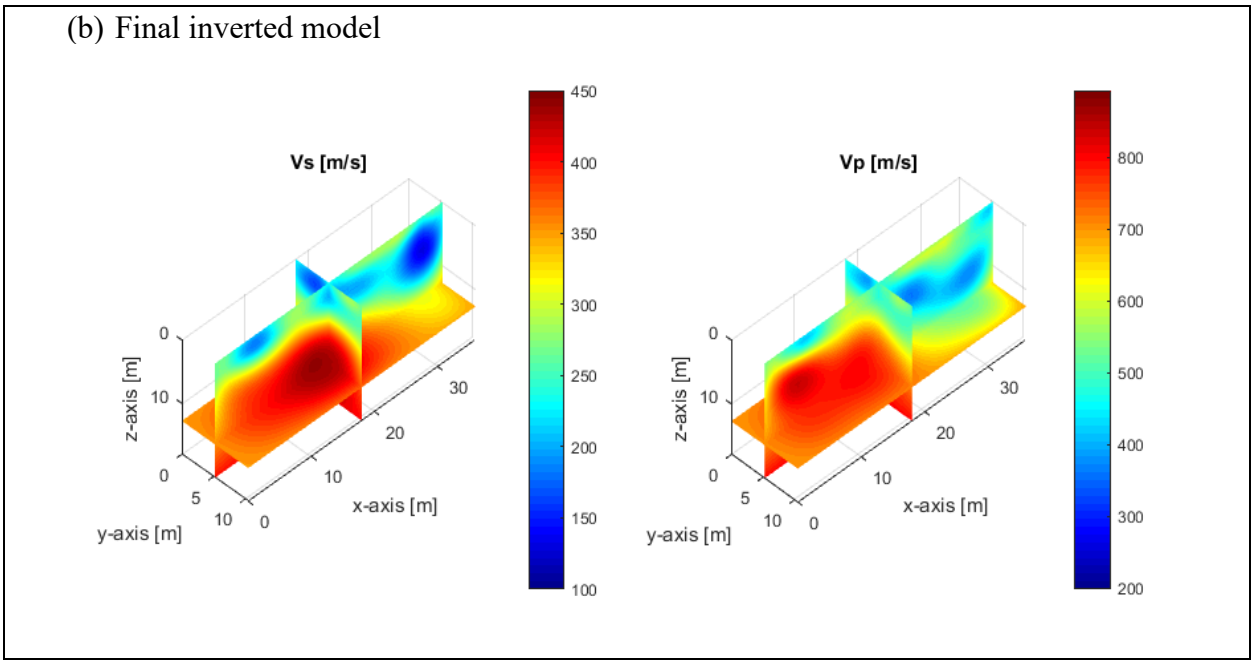

Figure 5.4: Field experiment: distribution of V_S and V_P (m/s): (a) initial model used at the beginning of inversion and (b) final inverted models at 5-30 Hz.

Figure 5.5 shows the least-squares errors for all 30 iterations of both inversion runs, which were normalized by the initial error. The error reduced from 1.0 to about 0.62 in the first run, and just below that in the second run. The error increased at the start of 5-30 Hz, because the model was not setup to characterize the shorter wavelength data initially. Shown in Figure 5.6 is a comparison of observed data at 5 - 30 Hz, and estimated data associated with the initial model and the final inverted result at iteration 30 for a sample shot. The agreement between observed and estimated data improved during inversion. The observed and final estimated waveform data agree well for most channels in Figure 5.6 b. No cycle skipping is observed; suggesting the 1D initial model established from the spectral analysis was a good initial velocity estimate.

The final inverted results for data at 5 - 30 Hz are shown in Figure 5.4b. The Vs profile (Figure 5.4b, left) consists of softer layers (Vs ~ 150 m/s [500 ft/s] - 300 m/s [1,000 ft/s]) with a buried low-velocity zone at about 5-m (16-ft) depth, underlain by a stiffer layer (Vs ~ 400 m/s [1,330 ft/s]). The Vp profile (Figure 5.4b, right) is consistent with the Vs profile. Based on soil

types from SPT borings, the softer layers and stiffer layer are soils and weathered limestone, respectively. For better viewing, the lateral variation, Figure 5.7 shows Vs profiles along 4 receiver lines at y = 0, 3, 6, and 9 m (y = 0, 10, 20, and 30 ft), together with the 4 SPT locations. Variation of soil layers is consistent along y-direction with shallower weathered limestone to the left of the test domain.

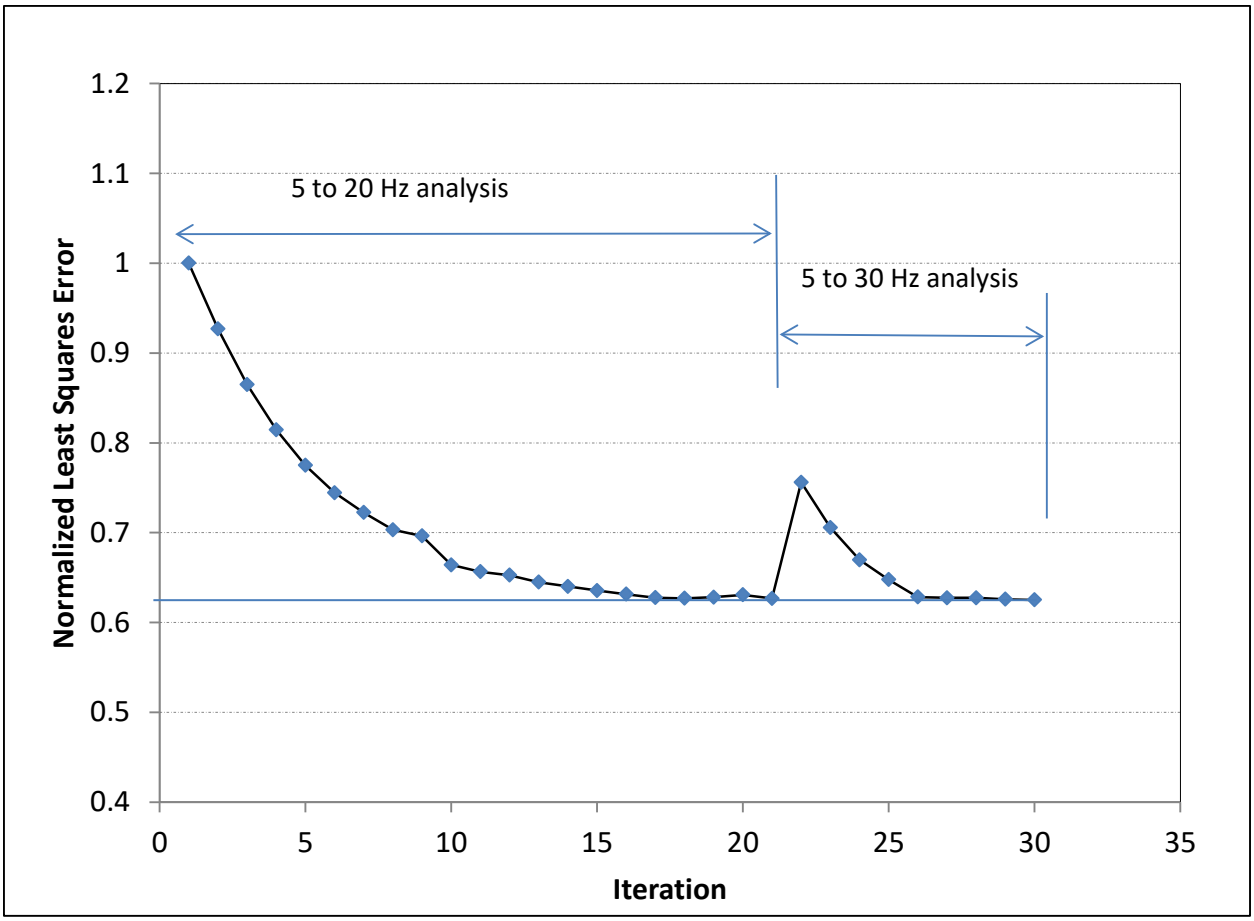

Figure 5.5: Field experiment: normalized least squares error versus the inversion iteration number for both inversion runs at 5-20 Hz and 5-30 Hz. The error defines the degree of match between the estimated and observed waveforms during the inversion analysis. The error increases at higher frequencies because the model is not yet appropriate to produce the recorded wave propagation of shorter wavelengths.

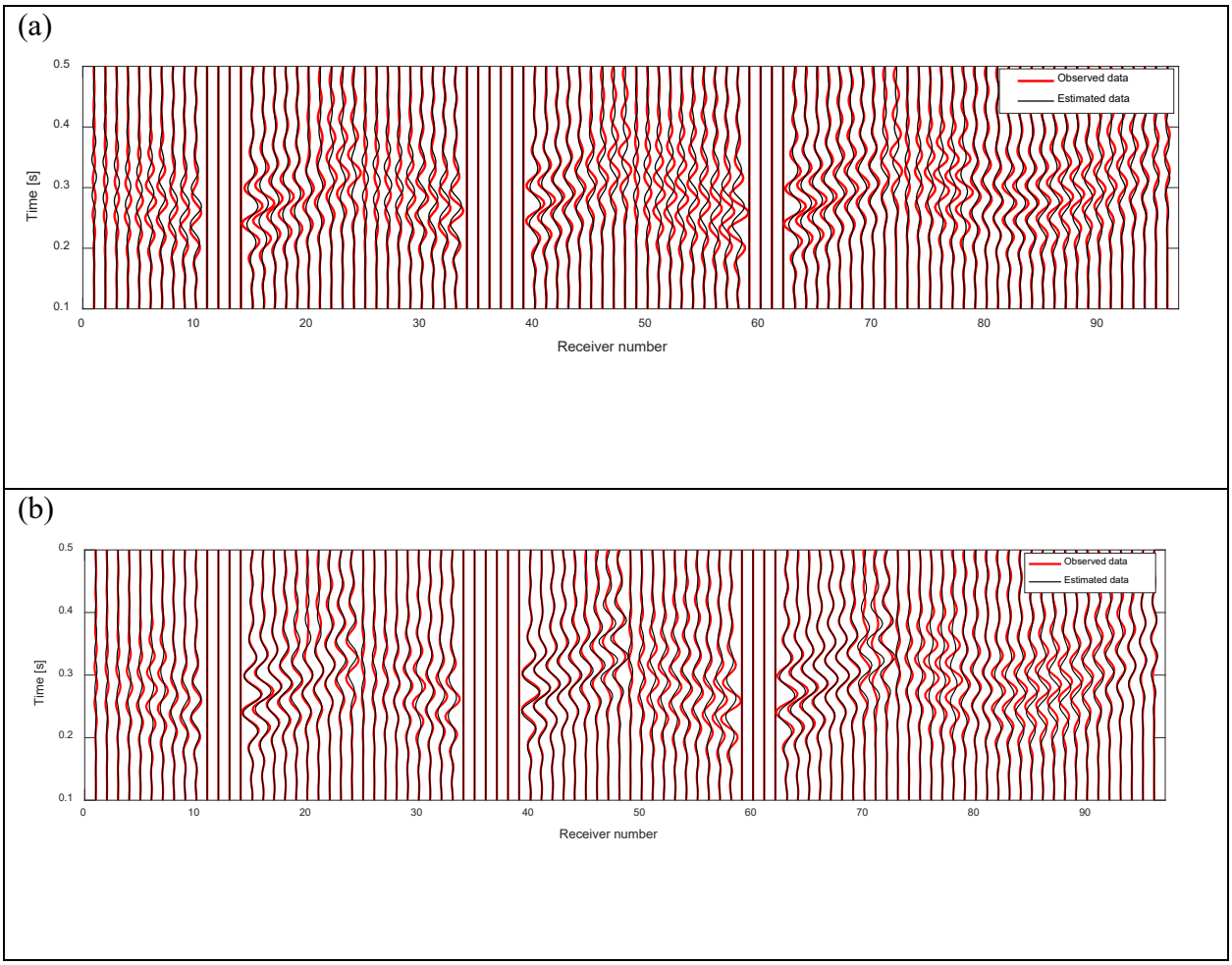

Figure 5.6: Field experiment: waveform comparison for a sample shot associated with (a) the initial model and (b) the final inverted model. Poor channels near the source are removed from analysis.

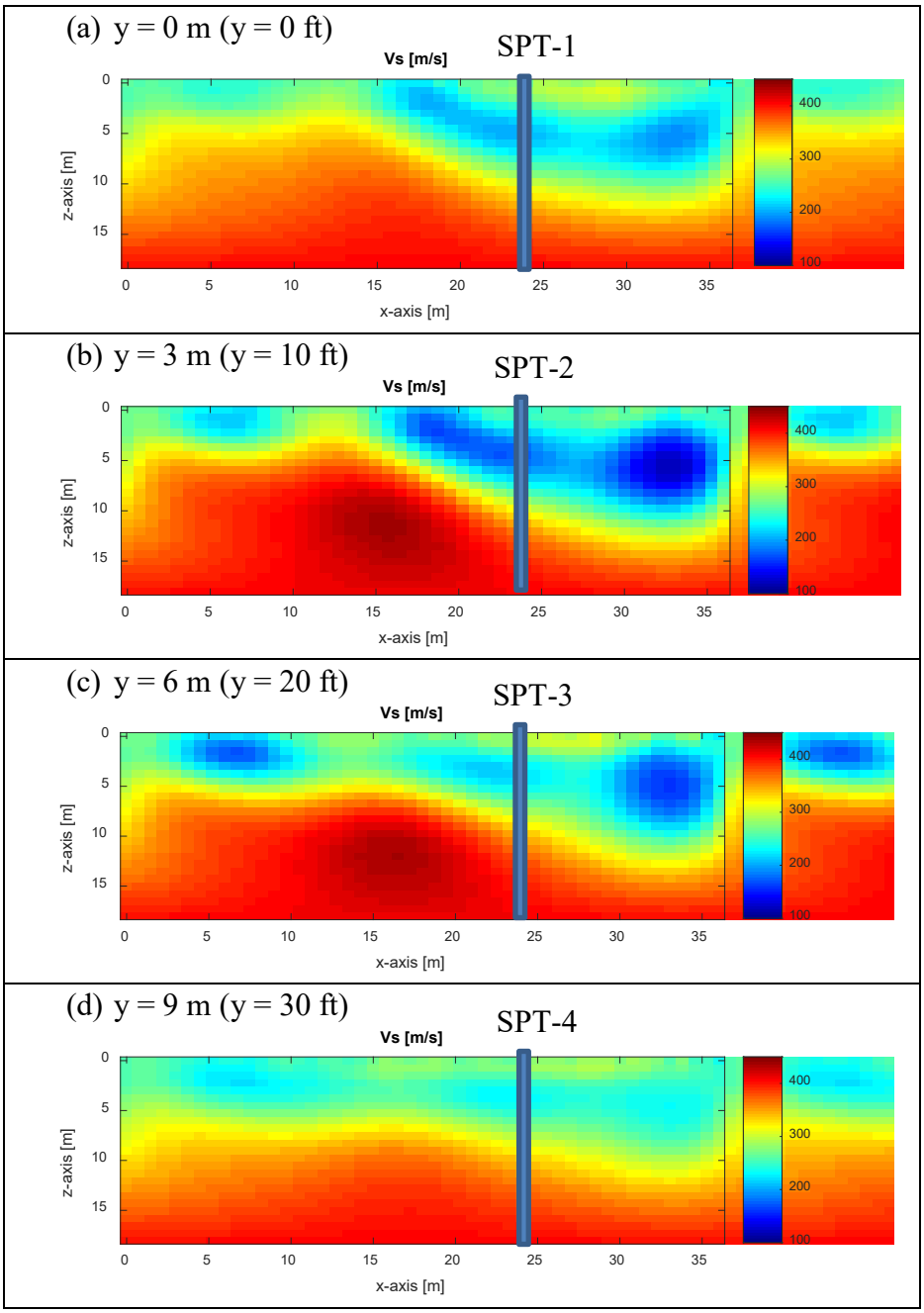

Figure 5.7: Field experiment: inverted V_S and SPT locations along four receiver lines at y= 0, 3, 6, and 9 m (y= 0, 10, 20, and 30 ft)

Shown in Figure 5.8 are the initial Vs values, the final inverted Vs values at 5-30 Hz, and SPT N-values at 4 locations. The depths of four SPTs are about 21-m (70-ft) depth. The final inverted Vs values are very different from the initial values, suggesting the Vs profiles have changed (updated) significantly during inversion analysis, particularly at depths less than 10 m

(33 ft). The final inverted Vs and SPT results generally agree at all four locations. Both show soft materials from 0 m (0 ft) to 5 m (16 ft) depth, linearly increasing stiffness with depth from 5 m (16 ft) to 10 m (33 ft) depth, and stiffer materials below 10 m (33 ft) depth. The low-velocity zone at about 5 m (16 ft) depth identified by the waveform analysis was confirmed by the SPT results, particularly at the SPT-3 and SPT-4 locations, Figure 5.8. There is discrepancy between the Vs (higher values) and SPT N-values at depths less than 2 m (7 ft) of SPT-1 and SPT-2. The discrepancies are likely due to inversion artifacts near source locations that could not be suppressed by Gauss-Newton inversion. Also, the SPT N-values appear more erratic than Vs values. This is because N-values represent more local properties than do Vs values, which are averaged within cell volumes ($0.75 \times\ 0.75 \times\ 0.75\ m$ [$2.5' \times 2.5' \times 2.5'$] each).

Results from this seismic dataset analyzed by a cross-adjoint 3-D FWI (Nguyen and Tran, 2018) are also shown, in which the same initial model and frequency content were used. Apparently, both Gauss-Newton and cross-adjoint methods produce good results for this dataset. However, the inverted Vs from the Gauss-Newton method are more consistent with the SPT N-values in both trend and magnitudes, particularly at SPT-1 and SPT-4. The cross-adjoint 3-D FWI tends to overpredict the low-velocity zones.

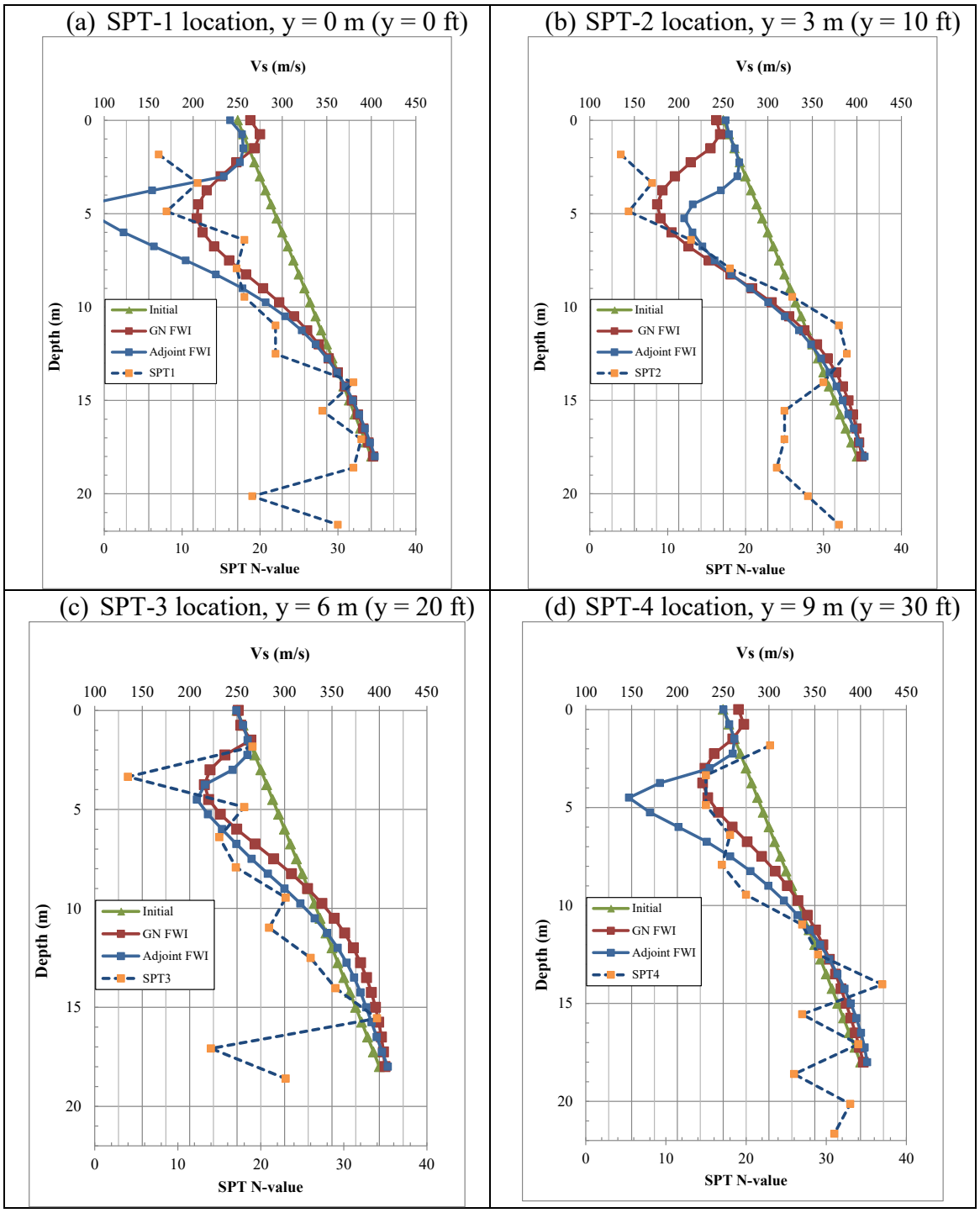

Figure 5.8: Comparison between V_S and SPT N-values at the 4 invasive test locations. GN FWI and adjoint FWI denote results from Gauss-Newton and cross-adjoint waveform inversion methods, respectively.

5.3 UF campus buried pipe detection

For the purpose of shallow void detection, the 3-D FWI approach was first field tested on a known stormwater pipe located on the campus of the University of Florida. The pipe is high-density polyethylene (HDPE), corrugated, 1 m in diameter and buried approximately 3 m (10 ft) beneath the ground surface. The pipe spans diagonally across source/receiver grid layout (Figure 5.9a). A 2-D array of 91 sources (shots) and 72 receivers (4.5 Hz vertical geophones) at 1.5 m (5 ft) spacing was placed on the ground surface (Figure 5.9b), covering a test area of 18 x 9 square meters (60 x 30 ft^2). A 45-N sledgehammer source was used to generate seismic waves at each of 91 source locations and the generated wave-fields were simultaneously recorded by each of the 72 geophones.

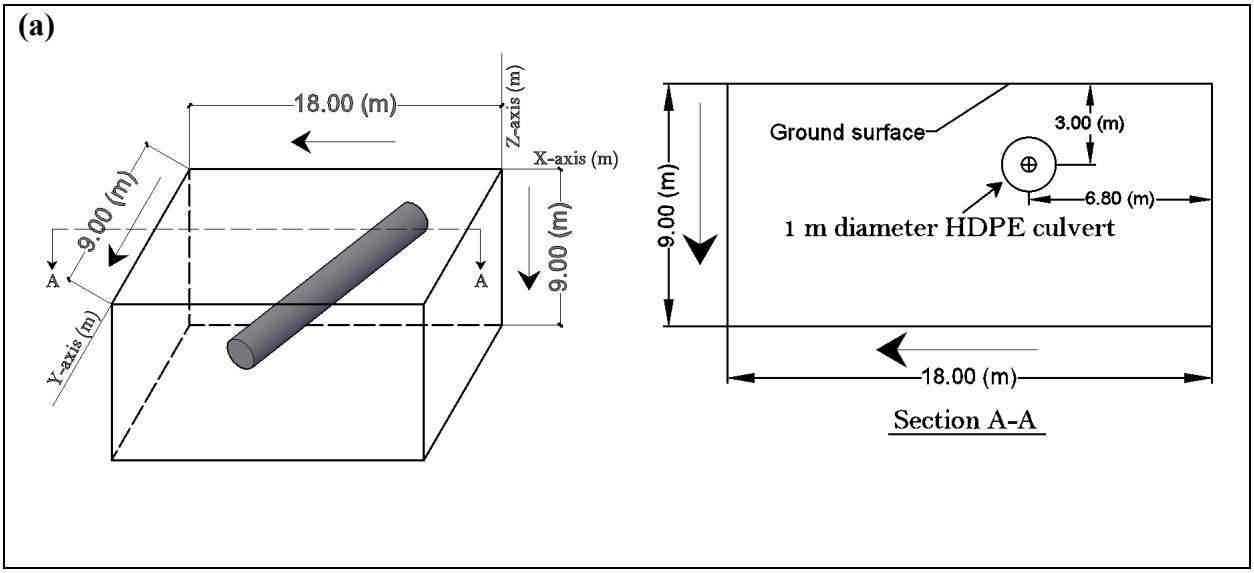

Figure 5.9: Field experiment on culvert: (a) 3-D depiction of pipe location with respect to the test area (left), vertical view of the pipe at y = 4 m (y = 13 ft) (right), and (b) true-to-scale meshing and test configuration on pipe.

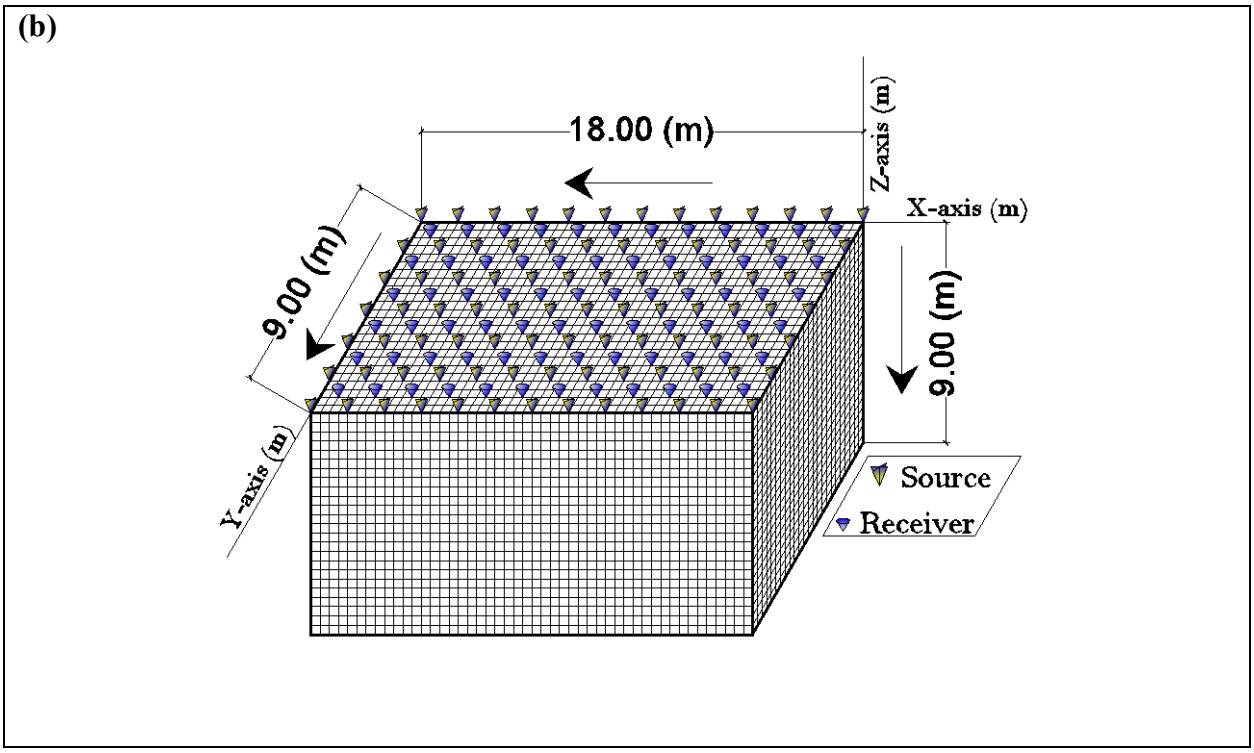

Figure 5.9: Field experiment on culvert: (a) 3-D depiction of pipe location with respect to the test area (left), vertical view of the pipe at y = 4 m (y = 13 ft) (right), and (b) true-to-scale meshing and test configuration on pipe.

The FWI analyses began with the spectral analysis of measured data from a row of 12 geophones as shown in Figure 5.10, to assess initial domain velocities. Evident, the phase velocity is almost constant at 180 m/s (600 ft/s) for the wide frequency range from 10 to 60 Hz. Thus, a homogeneous model of 180 m/s (600 ft/s) for Vs was chosen as the initial model, and Vp was taken as twice of Vs. The medium depth of 9 m (30 ft) was selected, since it represents half of the larger lateral test dimension (18 m [60 ft]). Note, a deeper medium could have been chosen; however, limited source energy (45 N) and high utilized frequencies (fc =45 Hz) would make large depth detection non-feasible in this scenario.

The entire inversion was performed with one set of iterations with a frequency bandwidth of 10-60 Hz and a central frequency of 45 Hz. An 18 × 9 × 9 m ($60' \times 30' \times 30'$) (length ×

width × depth) numerical grid with a grid spacing of 0.375 m (1.25 ft) was used for the forward simulation and model updating (Figure 5.9b). The grid spacing of 0.375 m (1.25 ft) was selected as a quarter of shot/receiver spacing (1.5 m [5 ft]) for conveniently assigning shot/receiver locations for the numerical nodes.

Similar to that of Gainesville soil-rock characterization analysis, the estimated wave fields were corrected by an offset-dependent correction factor of the form $y(r) = A.r^{\alpha}$ with the offset denoted by *r*. Factor *A* and exponent α were determined in an iterative least-squares inversion process that minimizes the energy of the waveform residuals. The values of *A* and α were determined at the beginning of each update and kept constant throughout the entire iteration. The correction factor *y(r)* only accounts for material damping inherent in the field data, whereas the 3-D nature of the numerical simulation in the forward modeling already accounts for the geometrical spreading/damping.

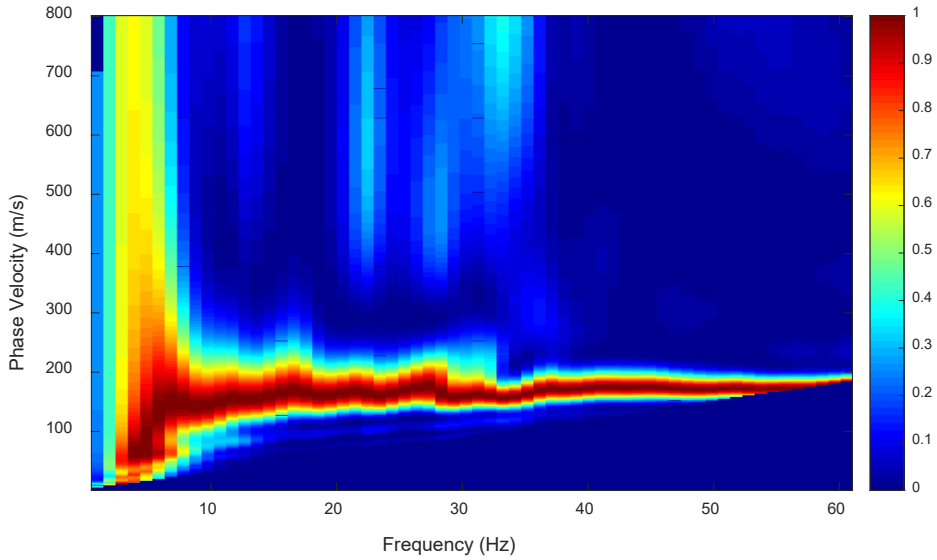

Figure 5.10: Field experiment on pipe: spectral analysis of measured data for one sample shot and one line of 12 geophones.

The inversion analysis stopped when it reached the preset maximum number of iterations (40 iterations). It took about 15 hours on a desktop computer (32 cores of 3.46 GHz each and 256 GB of memory). As shown in Figure 5.11, the least-squares error consistently decreased during the inversion process from the normalized value of 1.0 at the beginning of the inversion run to 0.63 for the last iteration. Shown in Figure 5.12 is the wave field comparison of a sample shot for the measured data from the field experiment, and the estimated data associated with the initial model (iteration 1) and the final inverted model (iteration 40). Evident, the waveform match improved for all 72 channels during inversion. No cycle skipping or matching of wrong peaks is observed, suggesting the sufficiency of the homogenous initial model.

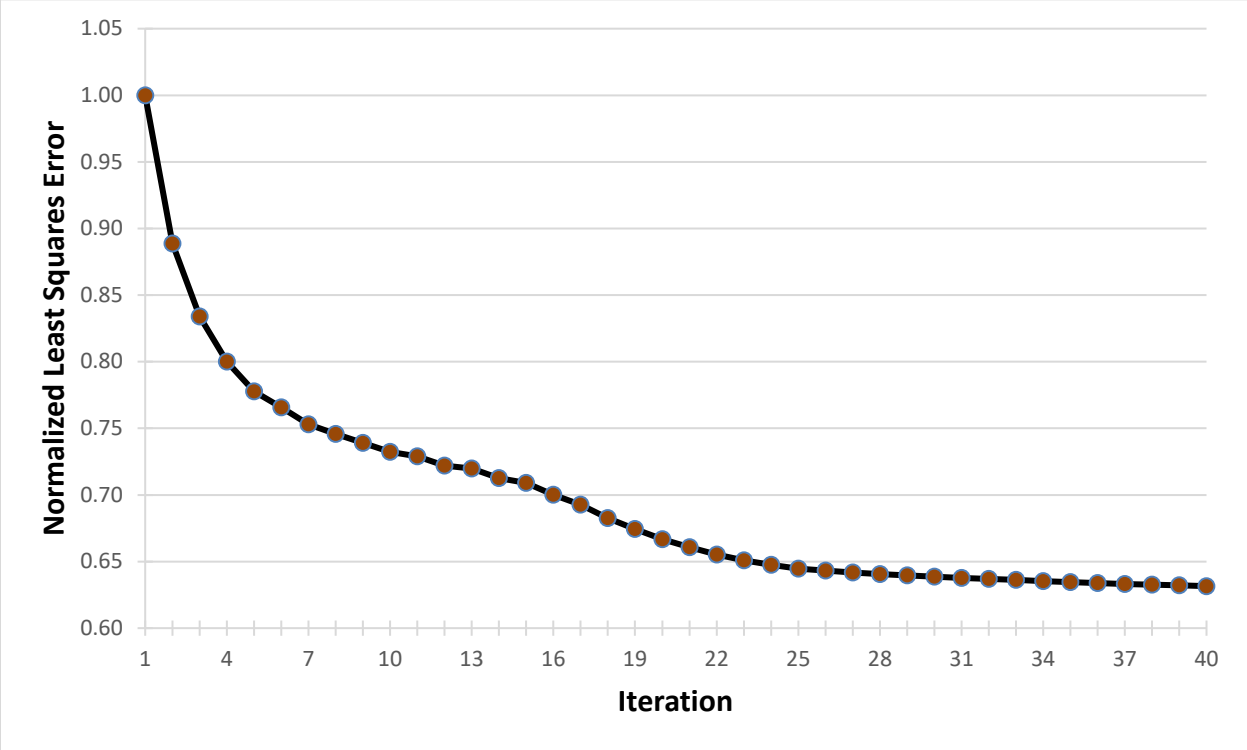

Figure 5.11: Field experiment on pipe: normalized least squares error for the entire inversion analysis (iterations 1 to 40) on data at the frequency bandwidth of 10-60 Hz

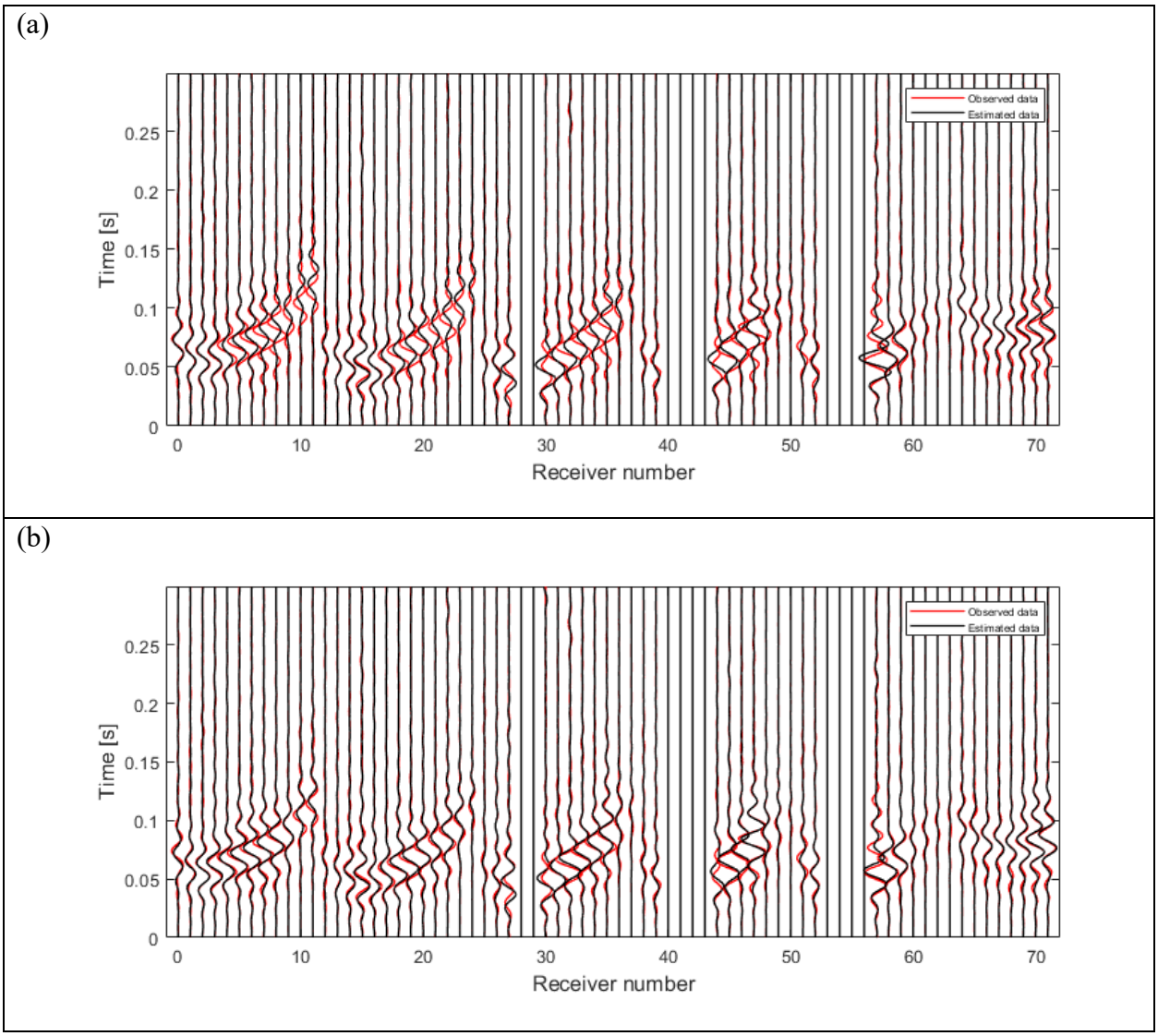

Figure 5.12: Field experiment on pipe: waveform comparison between the observed data and the estimated data associated with (a) the initial model and (b) the final inverted model for a sample shot.

Shown in Figure 5.13 is the inverted Vs profile, with 3-D perspective views having a horizontal cut at depth z = 3 m (z = 10 ft) (Figure 5.13a, left) and a vertical cut at distance y = 4.5 m (y = 15 ft) (Figure 5.13a, right). Evident from the figure, the FWI method successfully identified the existence of the pipe, as well as accurately characterizing its depth, diameter, and direction. Figure 5.13b presents a rendering of the results from two different views which

clearly show the position, direction, and depth of the pipe in 3-D domain. The inverted Vp profile is very similar to Vs, and is not presented.

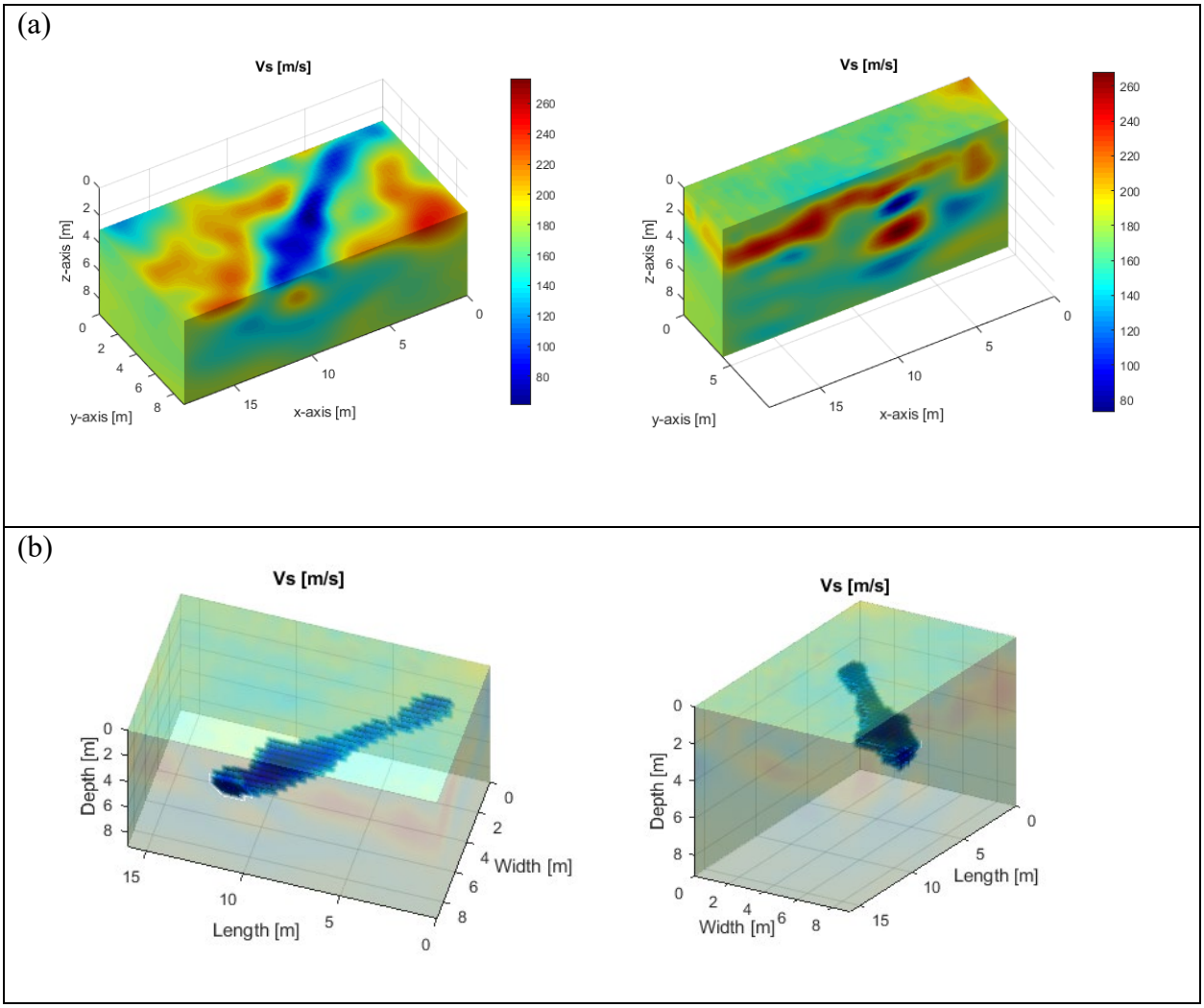

Figure 5.13: Field experiment on pipe: (a) perspective view of the inverted result, and (b) 3-D rendering of the result at two view angles.

5.4 Newberry sinkhole detection

Next, the 3-D FWI approach was performed on seismic surface datasets gathered at a retention pond in Newberry, Florida. The site has a history of pre-collapsed sinkholes as well as unknown buried voids. In addition, the test site is known to consist of medium dense, fine sand and silt underlain by highly variable limestone (pinnacles). The top of limestone varies from 2 m

(7 ft) to 10 m (33 ft) in depth. For the seismic testing, the entire testing area was divided into two adjoining test zones marked as zone 1 and 2, each covering an area of 18 × 36 m^2 ($60 \times 120\ ft^2$) (Figure 5.14a). Note, the survey was considered Class A prediction of buried voids (i.e. blind), as the test area was an open and flat field with no indication of subsidence or chimneys. In addition, no previous knowledge (i.e. invasive tests) of voids and soil-rock layering existed at the test area.

The seismic survey was conducted in a test configuration of 72 receivers and 91 shots located in 2-D uniform grids on the ground surface (Figure 5.15) for each test area. The receiver and source grids were 6 × 12 and 7 × 13, respectively, both at 3 m (10 ft) spacing. A propelled energy generator with 40 kg (88 lbf) drop-weight (Figure 5.14b) was used to generate seismic waves at each of the 91 source locations, and the surface wave-field was simultaneously recorded with 72 4.5-Hz vertical geophones.

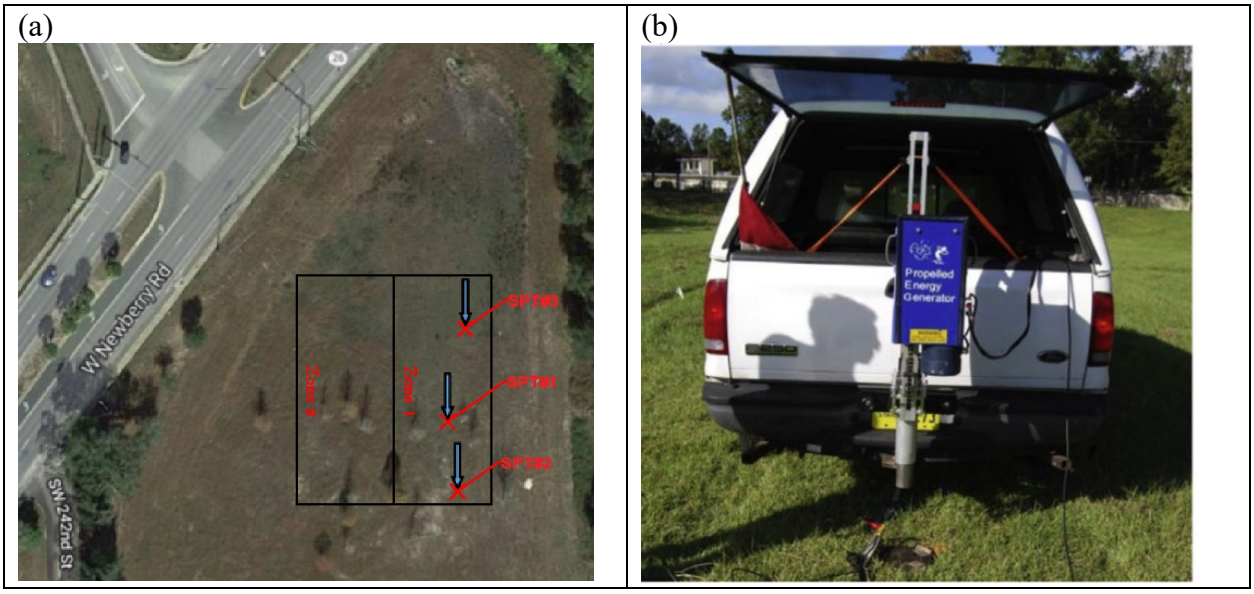

Figure 5.14: Newberry test site: (a) location of the test zones and SPT tests and (b) propelled Energy Generator (PEG) used to generate seismic waves

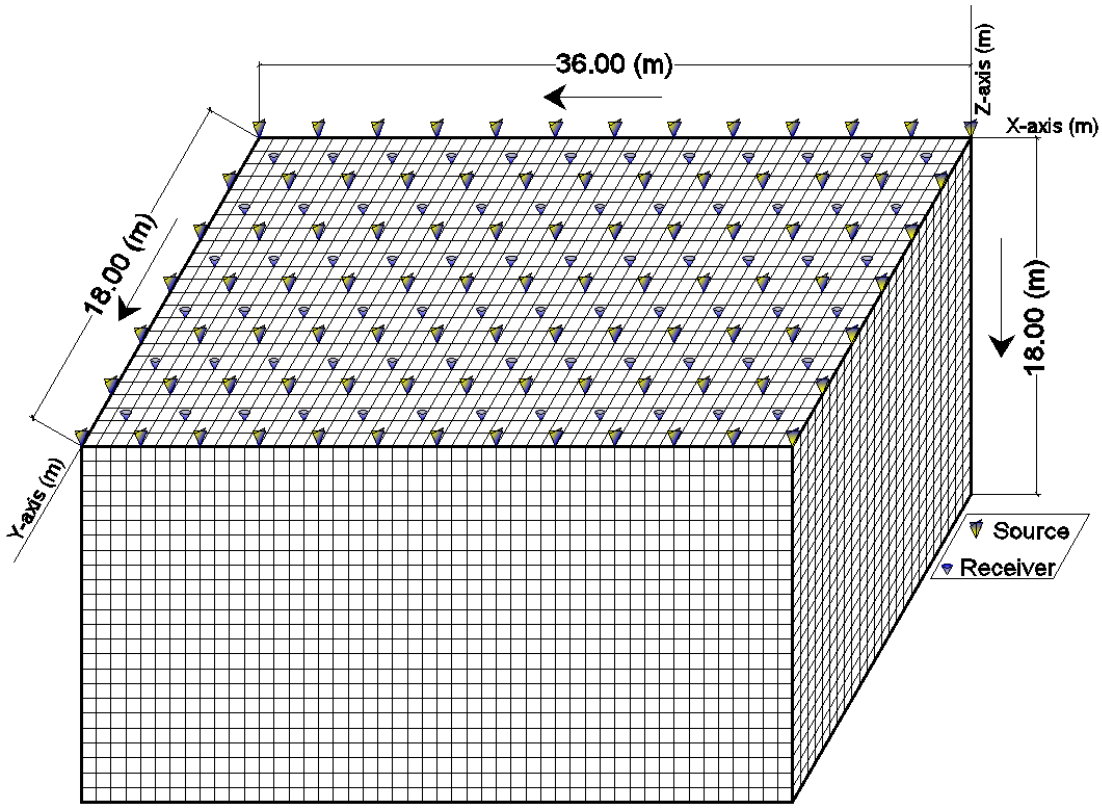

Figure 5.15: Newberry field experiment on unknown voids: true-to-scale meshing and test configuration

5.4.1 Data analysis of test zone 1

The analyses began with a spectral analysis of the measured wave-fields (sample shot and one line of 12 geophones) to develop initial velocity profile for the domain. Evident from Figure 5.16, phase wave velocities are from 250 m/s (830 ft/s) to 600 m/s (2,000 ft/s) at a frequency range of 7 to 35 Hz. Vs near the ground surface associated with high frequencies was known to be approximately 250 m/s (820 ft/s), and Vs of the half space was assumed as 600 m/s (2,000 ft/s). Based on the results of the spectral analysis (Figure 5.16), The initial model (Figure 5.17a) was established having Vs increasing with depth from 250 m/s (830 ft/s) at the surface to 600 m/s (2,000 ft/s) (Vs of the half space) at the bottom of the model. The depth of model was taken as a half of the longer dimension of the test area (or 18 m [60 ft]) to maintain good signal coverage in the analyzed domain. The Vp was calculated from Vs using a constant Poisson's

ratio of 1/3 for the entire medium, which typically varies from 1/4 to 1/2 for general soil-rock. It is noted the no prior information of any subsurface features is needed for the initial model. Again, a mass density of 1,800 kg/m^3 (112.37 lb/ft^3) was assumed as an average value for both soil and limestone for the entire domain during the inversion analysis.

For the analyses, a 36 × 18 × 18 m ($120' \times 60' \times 60'$) (length × width × depth) numerical grid with a grid spacing of 0.75 m (2.5 ft) was used during the forward simulation and model updating (Figure 5.15). The grid spacing of 0.75 m (2.5 ft) was selected as a quarter of shot/receiver spacing. The measured data was filtered through two frequency bandwidths of 5-25 Hz and 5-35 Hz prior to running the FWI analysis. Like the previous case of pipe detection, the synthetic data generated by the elastic forward solver were corrected for amplitude reduction caused by intrinsic attenuation effects (material damping) by applying an offset-dependent correction factor for each iteration.

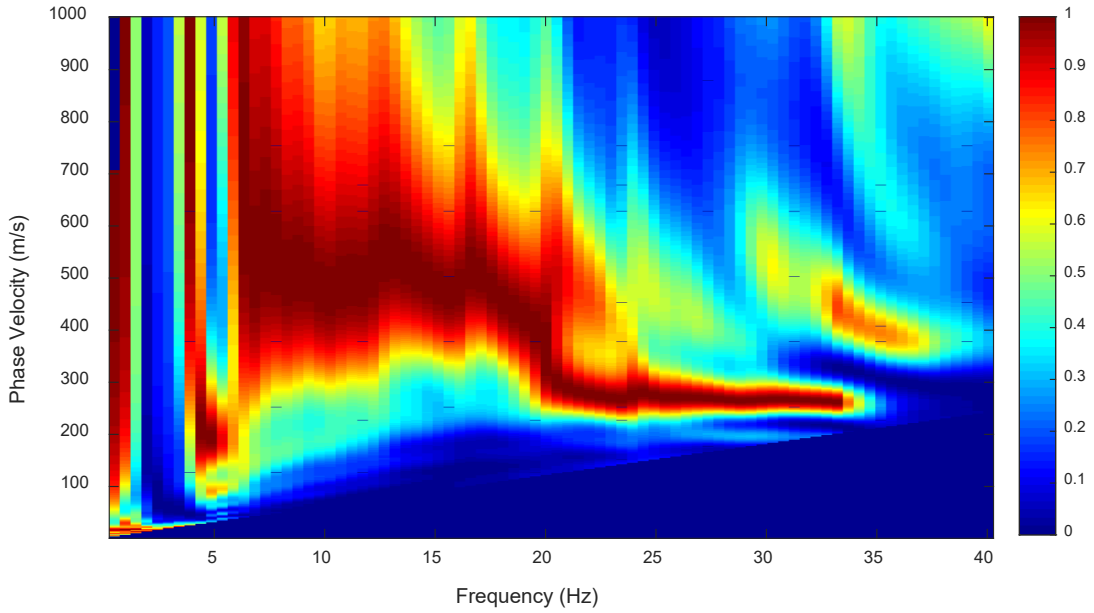

Figure 5.16: Field experiment of Newberry site (test zone 1): spectral analysis of measured data for one sample shot and one line of 12 geophones.

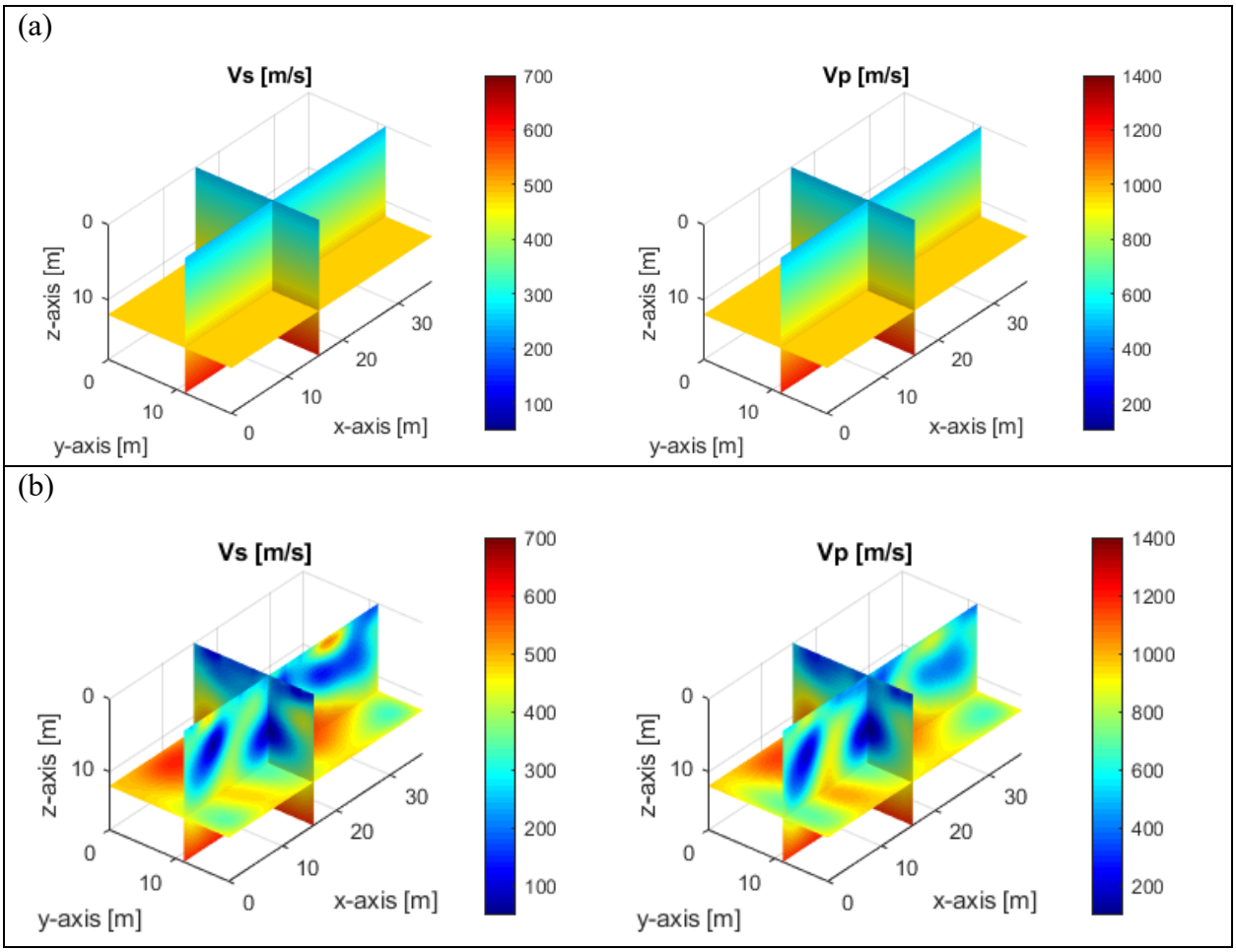

Figure 5.17: Field experiment of Newberry site (test zone 1): (a) distribution of V_S and V_P (m/s) for the initial model used at the beginning of inversion, (b) distribution of V_S and V_P (m/s) for the final inverted models at 25 Hz central frequency.

Two inversion runs were performed. The first analysis began with data having a frequency range of 5-25 Hz using the initial model (Figure 5.17a) as input. Next, the inversion result of the first analysis (i.e. cell properties) were used as the input model for the second run with data having the frequency range of 5-35 Hz. Both inversion runs stopped after 20 iterations at the preset maximum number of iterations. The FWI algorithm was able to consistently improve on the initial model, and decrease the error to about 50% of the initial error at the end of the 5-35 Hz frequency analysis (Figure 5.18).

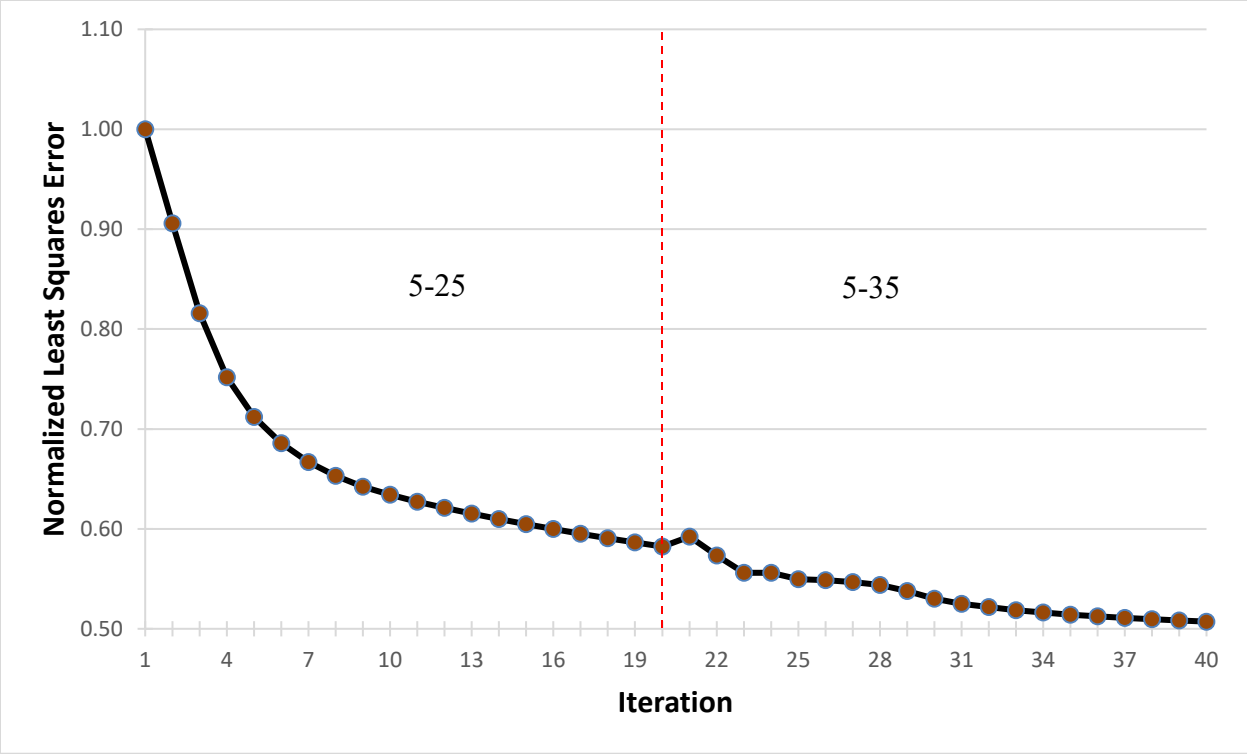

Figure 5.18: Field experiment of Newberry site (test zone 1): normalized least squares error for the entire inversion analysis (iterations 1 to 40).

Shown in Figure 5.19 is the wave-field comparison of a sample shot for the observed data from the field measurements with the estimated velocities associated with the initial model (iteration 1) and the final inverted model (iteration 40). Evidently, the waveform match improved significantly during the inversion analysis. The observed and the final estimated velocities are well matched (Figure 5.19b), suggesting the sufficiency of the initial model and the ability of the FWI method to find the optimum solution to the nonlinear inversion problem.

The final inverted results on the 5-35 Hz data are shown in Figure 5.17b. The Vs profile (Figure 5.17b, left) consists of a softer layer (Vs ~ 150 - 300 m/s [Vs ~ 500 – 1,000 ft/s]), underlain by a stiffer layer (Vs ~ 400 - 700 m/s [Vs ~ 1,330 – 2,330 ft/s]). There are three buried low-velocity zones at the left, middle and right of the profile. The Vp profile (Figure 5.17b, right) is consistent with the Vs profile, including the softer and stiffer layers, and the three low-

velocity anomalies. Based on soil types from the SPT boring, the softer and stiffer layers are fine sand with silt and weathered limestone, respectively.

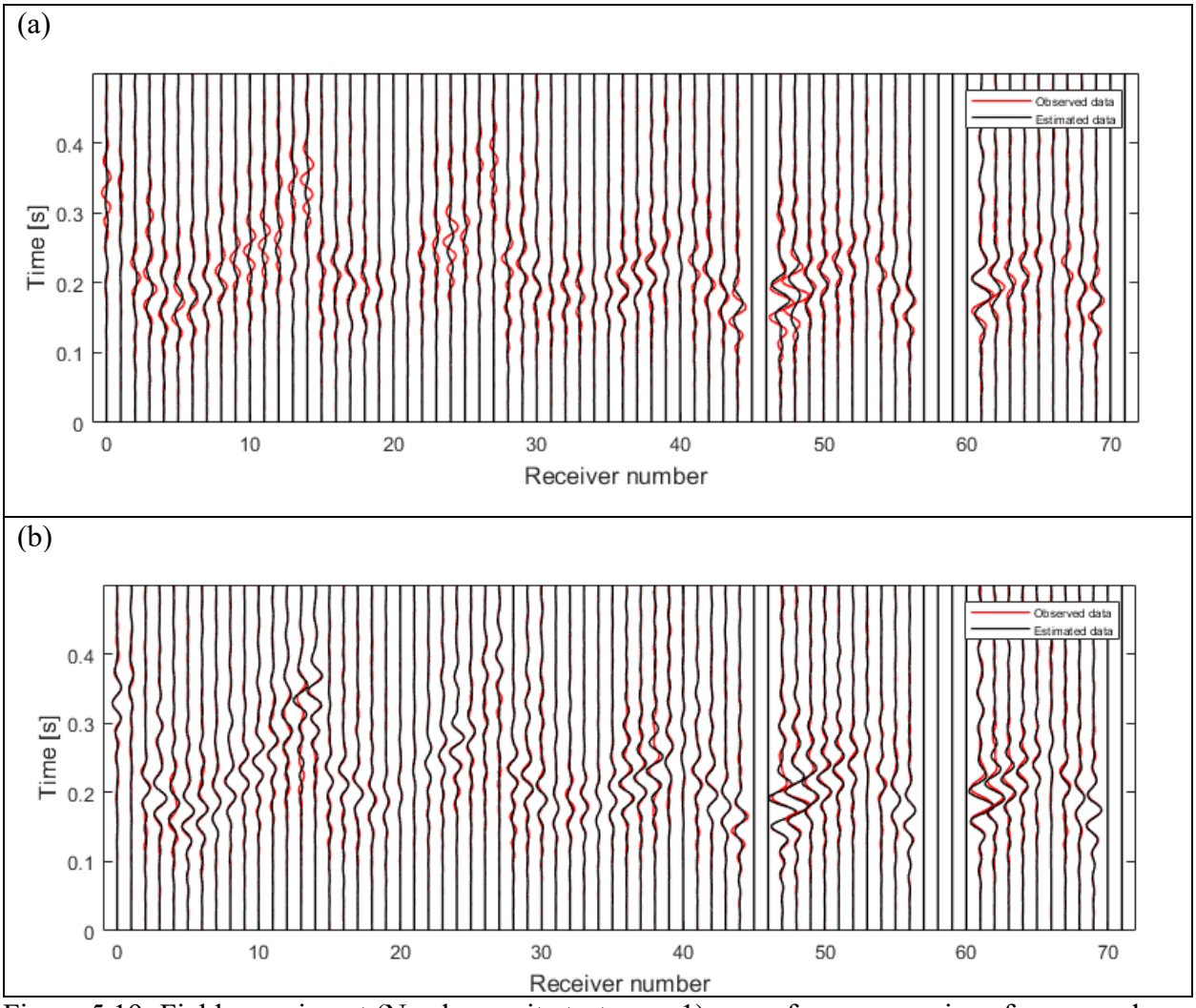

Figure 5.19: Field experiment (Newberry site test zone 1): waveform comparison for a sample shot associated with (a) the initial mode and (b) the final inverted model. Poor channels are removed from the waveform analyses.

For better viewing of subsurface features, Figure 5.20 presents a 3-D rendering of the final inverted Vs and Vp profiles. In the Vs image, cells with Vs < 100 m/s (Vs < 330 ft/s) (low-velocity anomalies) or Vs > 400 m/s (Vs > 1,330 ft/s) (limestone) are shown, whereas cells with 100 m/s < Vs < 400 m/s (330 ft/s < Vs < 1,330 ft/s) are made to be transparent. Similarly, cells with Vp < 400 m/s (Vp < 1,330 ft/s) (low-velocity anomalies) and Vp > 800 m/s (Vp > 2,660

ft/s) (limestone) are shown in the Vp image. Three low-velocity anomalies and variable limestone are clearly displayed in both Vs and Vp images.

To verify the seismic results, SPT borings were performed by SMO personnel at the three anomalies (Figure 5.14a). All three SPTs ended at the top of limestone bedrock. Shown in Figure 5.21 are the locations, depths, and recorded SPT N-values. The existence of two voids were confirmed at the locations marked by SPT#1 and SPT#3. This was verified by loss of circulation and drop of hammer and rod within the borehole. The void at SPT #1 is from 4 m to 7 m (13 ft to 23 ft) depth (i.e. large void), whereas the void at SPT #3 was smaller, i.e., from 4 m to 5 m (13 ft to 16 ft) depth. The SPT #2 location showed low N-values (2 to 6), suggesting the existence of a very soft material at the marked location. However, no void was encountered at this location. Note, the top of bedrock identified at 6 ~ 7 m (20 ~ 23 ft) depths in the seismic survey (Vs ~ 500 m/s [Vs ~ 1,640 ft/s]) also agreed with the SPT results.

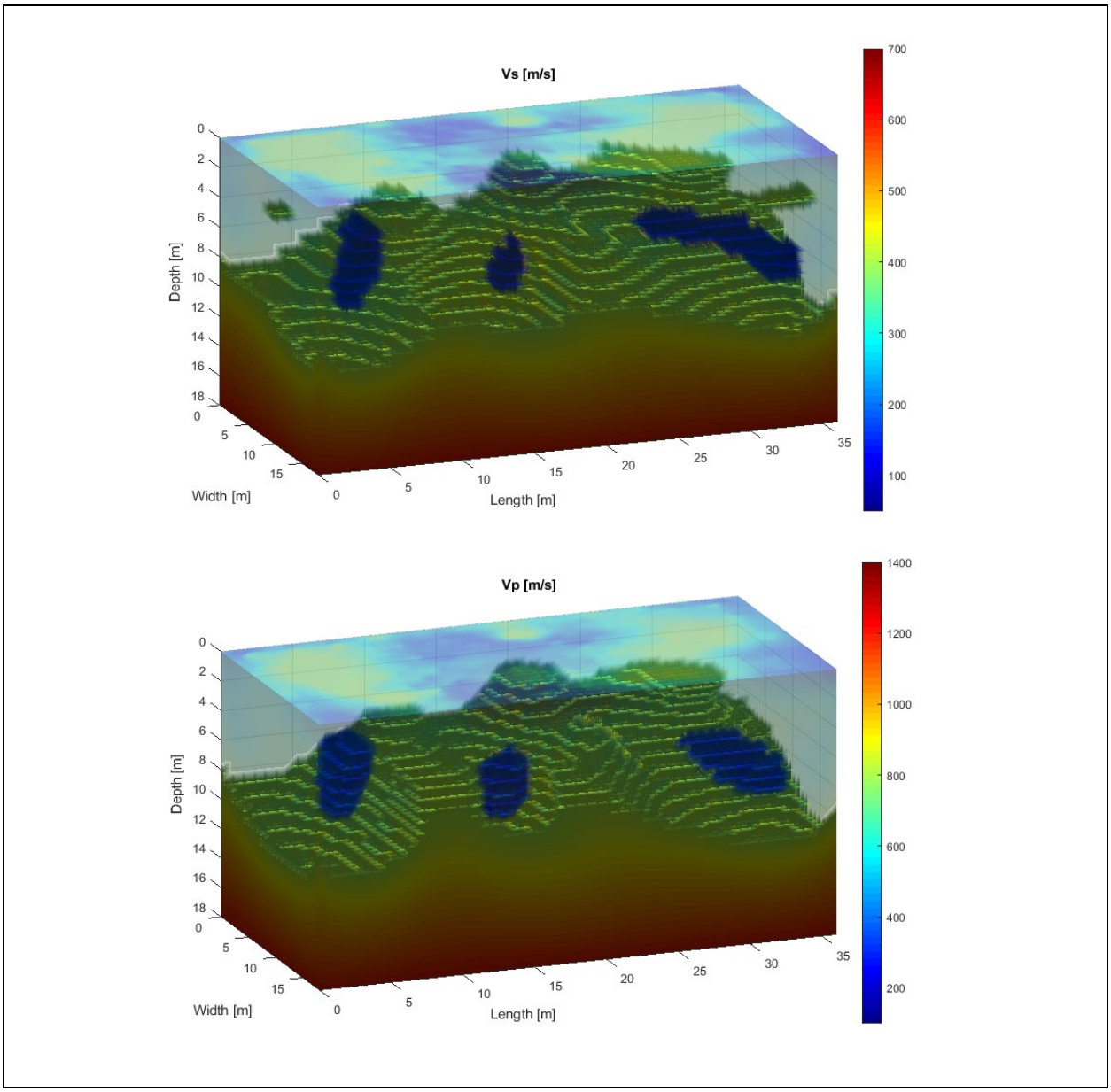

Figure 5.20: Field experiment of Newberry site (test zone 1): 3-D rendering of the final inverted result for the V_P and V_S.

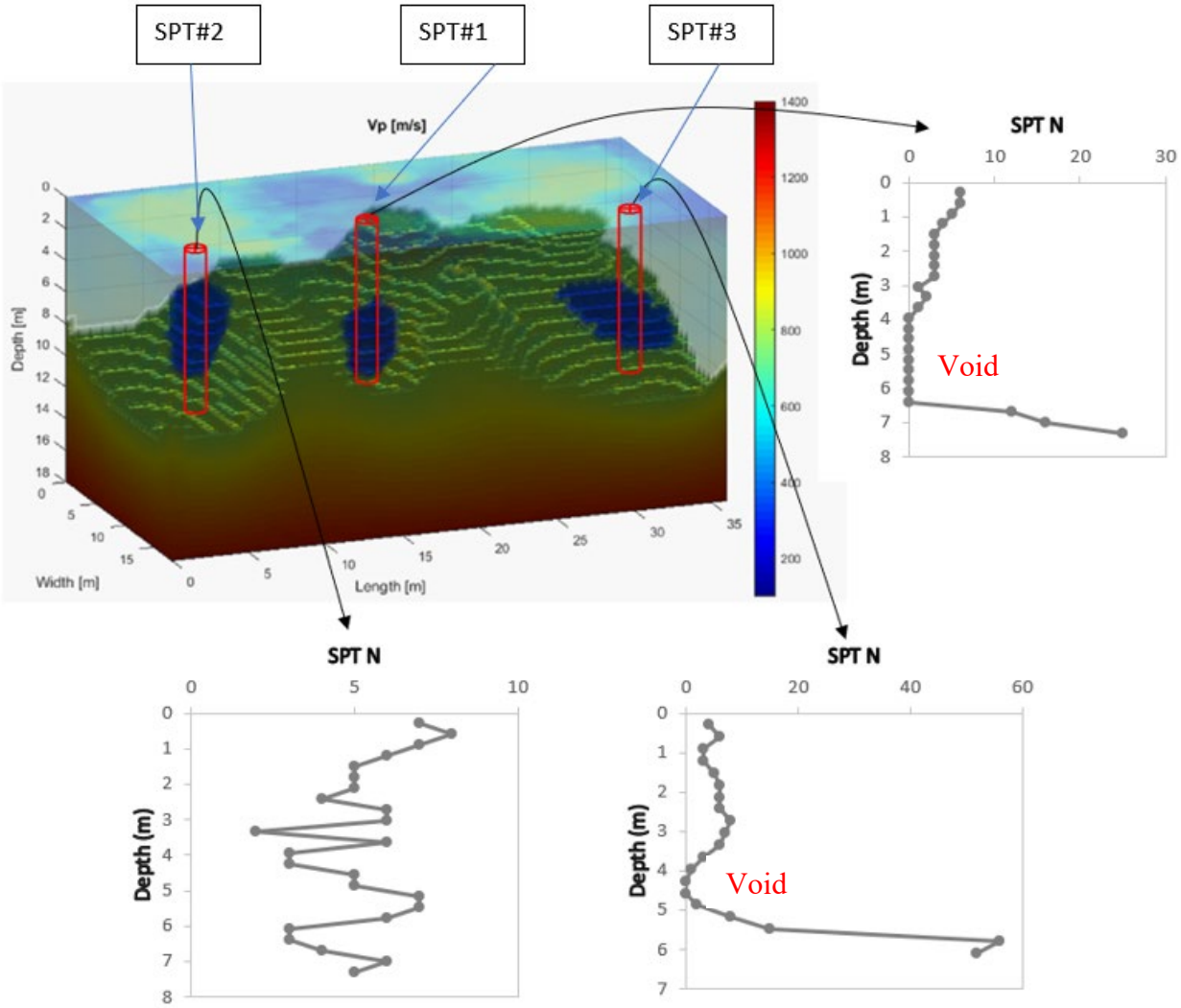

Figure 5.21: Field experiment of Newberry site (test zone 1): SPT locations, depths, and N-values. Two voids are confirmed at SPT#1 and SPT#3, and soft soil zone exists at SPT #2.

5.4.2 Data analysis of test zone 2

Zone 2 of the Newberry site (Figure 5.14a) was also analyzed with the 3-D FWI algorithm using the same initial velocity profile shown in Figure 5.22a with the same process. That is, the inversion began with frequency dataset restrained between 5-25 Hz to give preliminary results which were used for input for the second stage (frequency 5-35 Hz) to find the final cell velocities. The error consistently decreased throughout the entire inversion process from a normalized value of 1.0 at the beginning of the 1st inversion to less than 0.6 at the end of the 2nd stage analysis (Figure 5.23). Shown in Figure 5.24 is the waveform match between the field and inverted data for a sample shot. Evident, a very good match was achieved from the final inversion analysis.

Final inverted results presented in Figure 5.22b clearly shows a soil layer (Vs ~ 150 - 300 m/s [Vs ~ 500 – 1,000 ft/s]), underlain by weathered limestone (Vs ~ 500 - 700 m/s [Vs ~ 1,640 – 2,330 ft/s]). The Vp profile is consistent with the Vs profile. The 3-D rendering (Figure 5.22c) shows the existence of a low velocity anomaly at the edge of the test domain (length = 10 m [33 ft], width = 0 m [0 ft] and depth = 4 m [13 ft]) for both the Vs and Vp. The location of the characterized anomaly, i.e., being very close to the edge of the test zone, did not warrant a recommendation for invasive verification using an SPT test. The actual anomaly could be just outside of test area, and still shows up at the edge of analyzed domain because the reflected signals from the anomaly may appear in the field data.

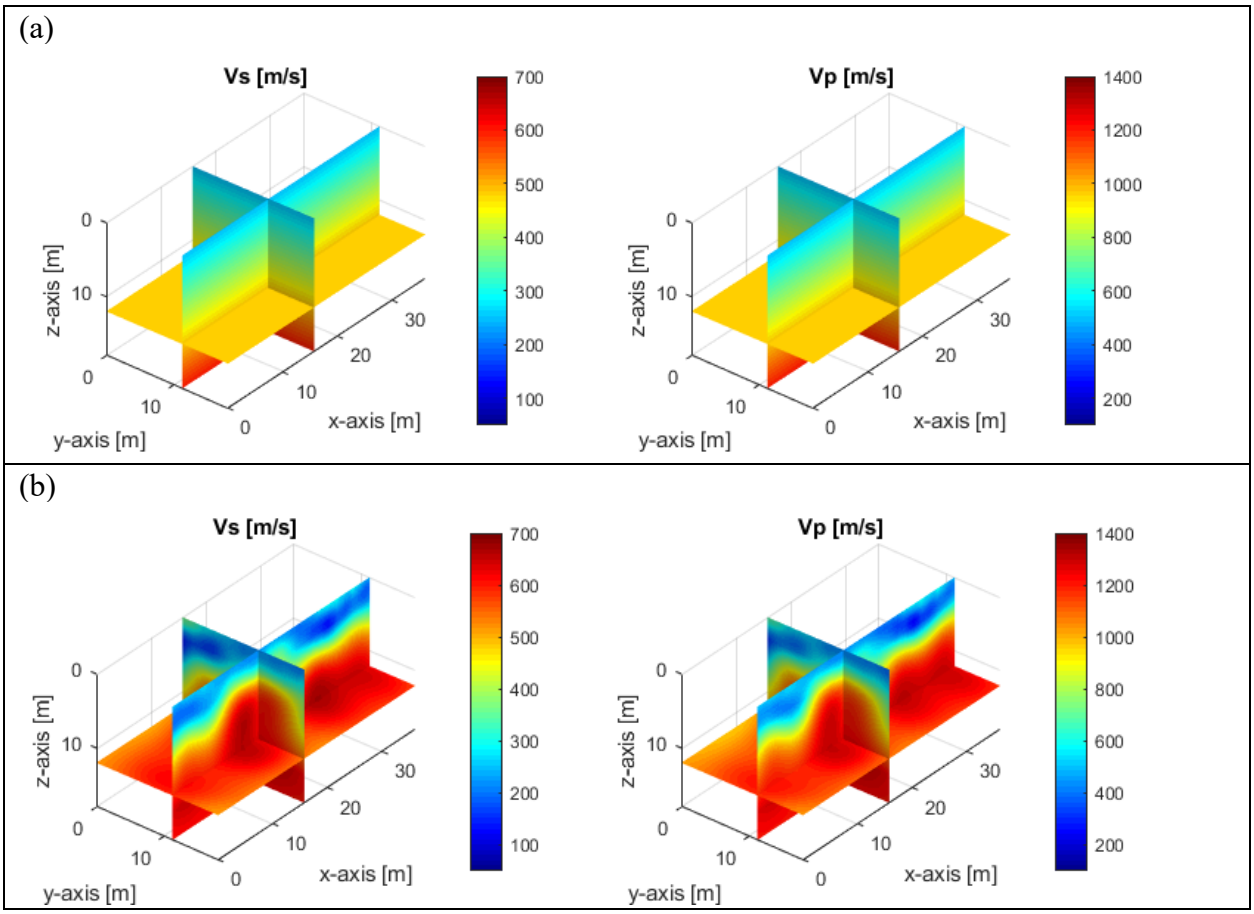

Figure 5.22: Field experiment of Newberry site (test zone 2): (a) distribution of V_S and V_P (m/s) for the initial model used at the beginning of inversion; (b) distribution of V_S and V_P (m/s) for the final inverted models at 25 Hz central frequency; and (c) 3-D rendering of the final inverted result for the V_S and V_P.

(c)

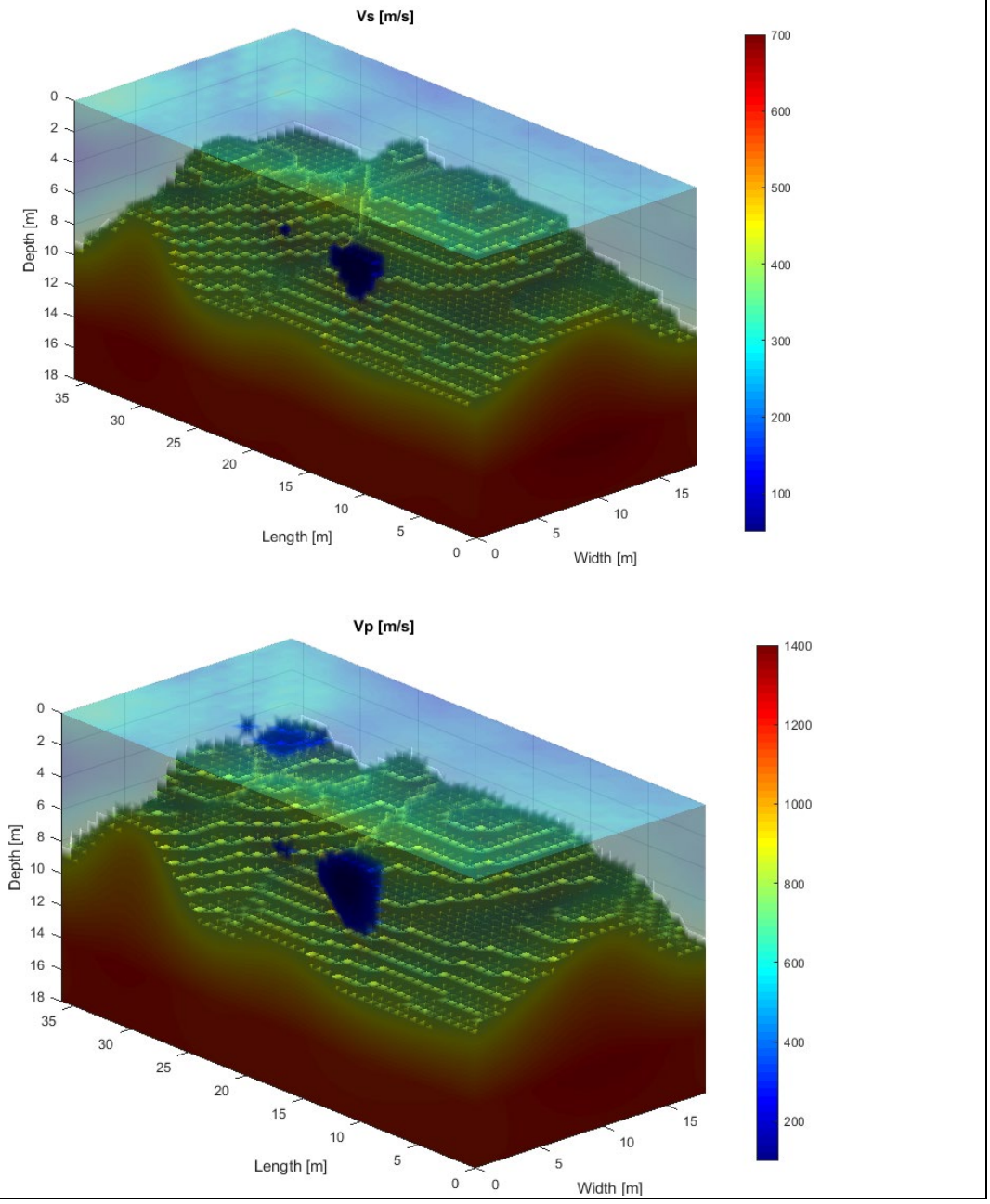

Figure 5.22: Field experiment of Newberry site (test zone 2): (a) distribution of V_S and V_P (m/s) for the initial model used at the beginning of inversion; (b) distribution of V_S and V_P (m/s) for the final inverted models at 25 Hz central frequency; and (c) 3-D rendering of the final inverted result for the V_S and V_P.

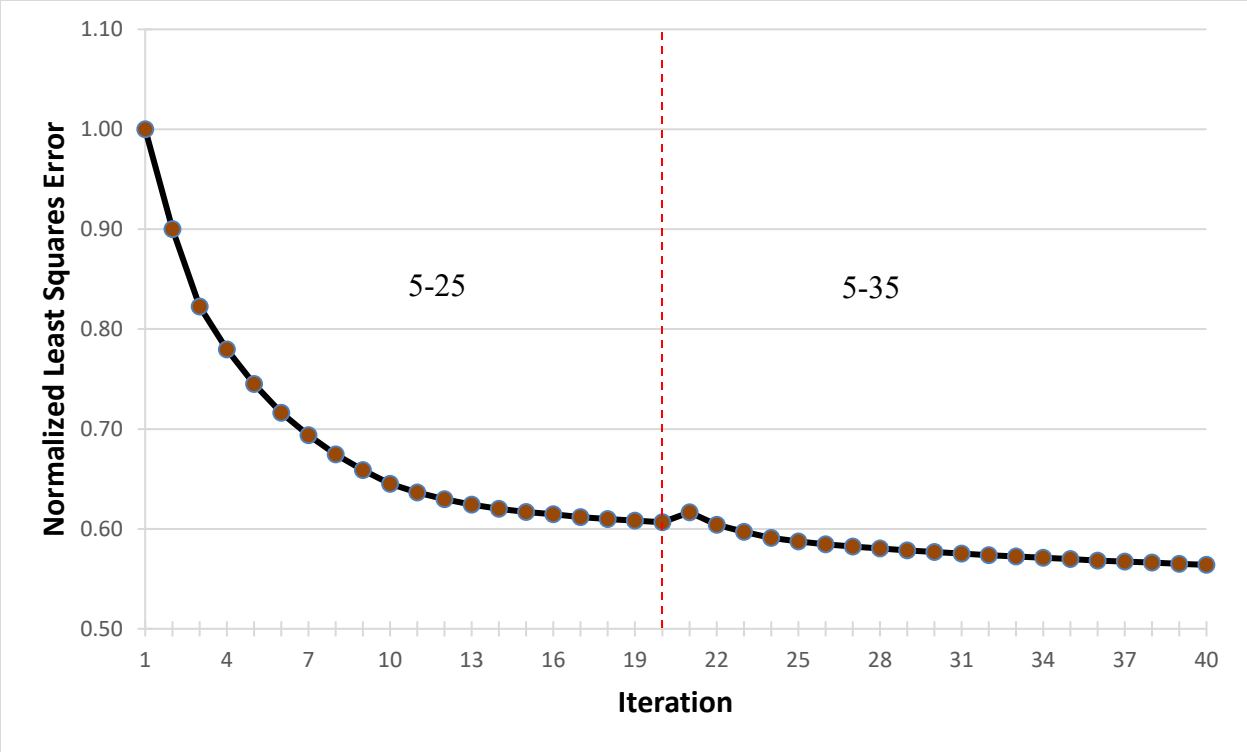

Figure 5.23: Field experiment of Newberry site (test zone 2): normalized least squares error for the entire inversion run (iterations 1 to 40).

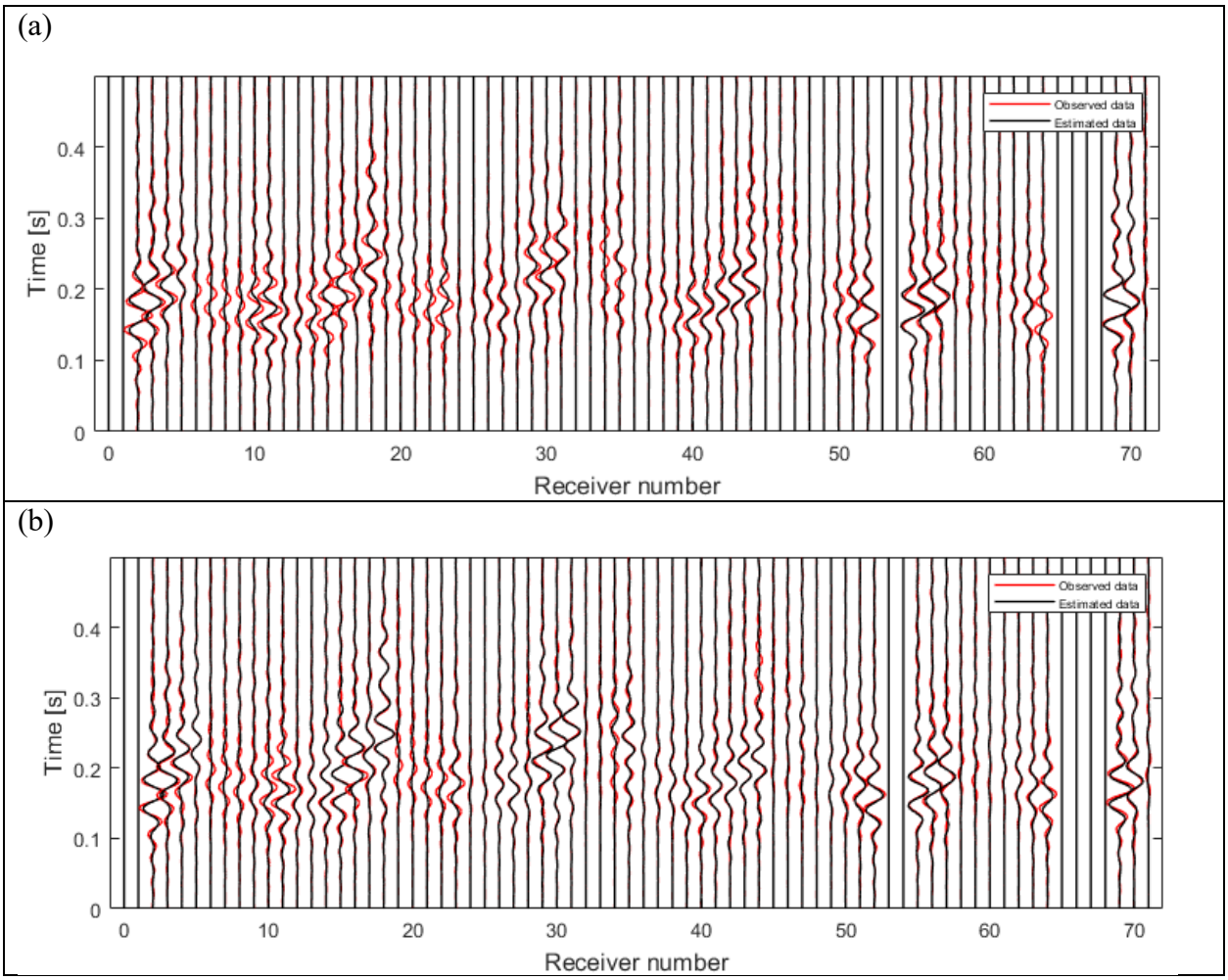

Figure 5.24: Field experiment of Newberry site (test zone 2): waveform comparison for a sample shot associated with (a) the initial mode and (b) the final inverted model

5.5 Miami bridge test site using surface data with the large source

5.5.1 Test configuration and field testing

Due to the depth of the void, surface-based testing was carried out using a larger source shown in Figure 5.25. The source weighted 340 kg (750 lbf) and was dropped from a height of 45 cm (18 in). The impact area was measured at 0.16 m^2 (1.7 ft^2). The system was operated through a remote control that both raised and dropped the weight. The test area was surrounded by embankments in the lateral direction facing north-south, and hence test lines were placed in the east-west direction (Figure 5.25). Based on available information from previous invasive testing (SPT and sonar), it was known that part of the void is located underneath the two embankments placed north and south of the testing area, and hence lies outside of the accessible testing area on the surface. Note, seismic waves can still penetrate to zones that lie outside of the testing area and they can be detected beyond the testing zone.

Given the available information of the void location and the existence of the two embankments, 72 geophones were placed in a 4×18 grid with a grid spacing of 3 m×4.5 m ($10' \times 15'$), respectively (Figure 5.26). The whole test area spanned 9 m (30 ft) in the north-south, and 76.5 m (250 ft) in the east-west directions (Figure 5.26). A grid of 46 shots were located and marked in the testing area. The shots were placed in the east-west direction at 4.5 m (15 ft) spacing, and in the north-south direction at 3 m (10 ft) spacing. The placement was performed in a staggered grid configuration shown in Figure 5.26 to facilitate source placement, and to reduce source-receiver coupling.

Figure 5.25: Miami test site: Large source used to generate seismic waves

Based on the above testing setup, the source was moved to the desired location for each shot and dropped with the force of gravity. The induced ground motion was picked up by the 72 geophones and a signal was recorded for each. Note that the pulse generated through the act of dropping the weight contains a variety of frequencies, and as a result had to be filtered before being used in the actual FWI analysis. The sampling rate of the seismographs was 0.5 ms for all the recorded wavefields. This allows frequencies as high as 1,000 Hz to be accurately sampled. It should be noted that this is the highest frequency that can be accurately sampled with the utilized equipment and it was not used during the analysis. Of importance, was that the source had sufficient energy at the lower frequencies (5-20 Hz) to allow for deep void detection.

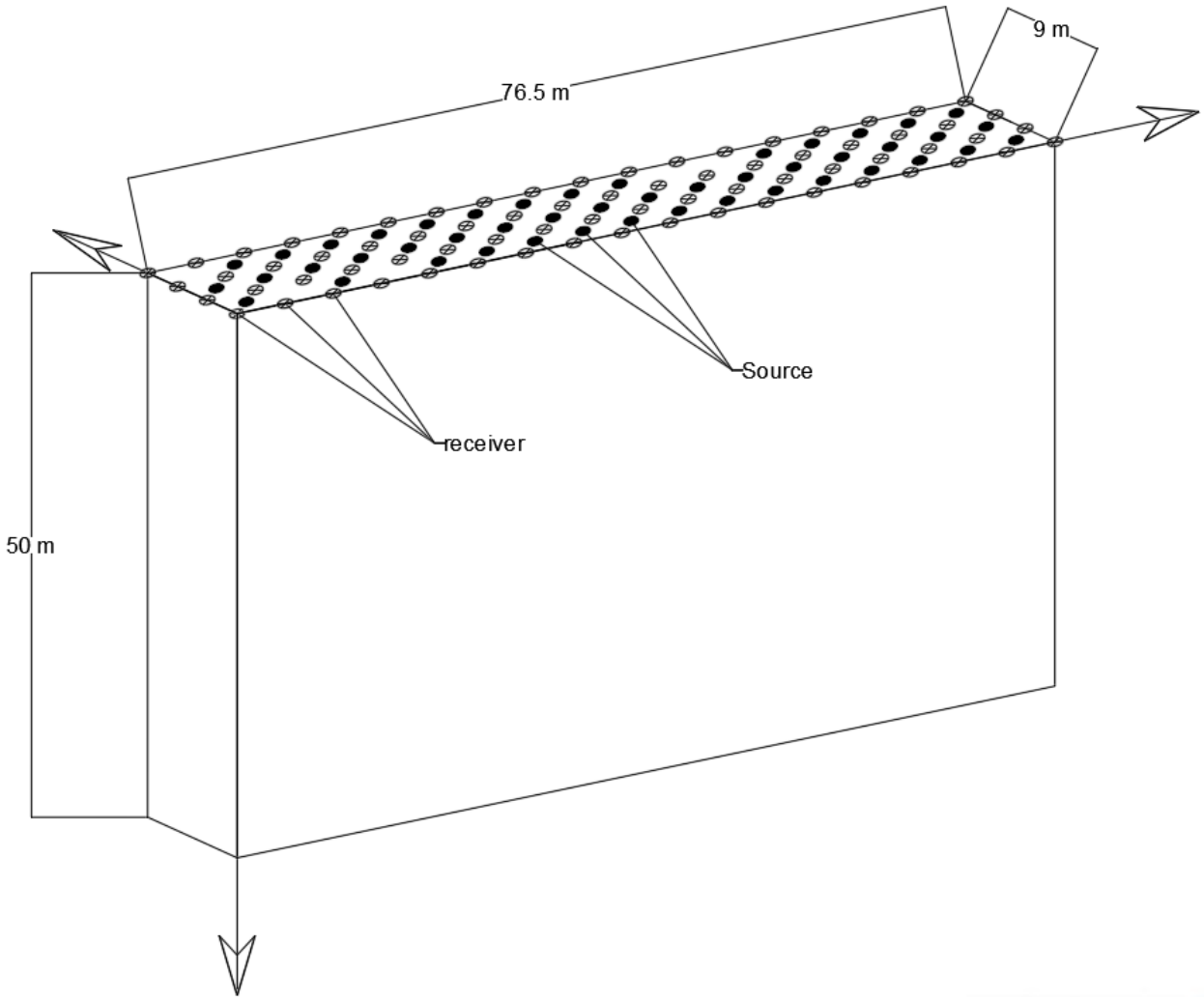

Figure 5.26: testing configuration used for surface-based analysis

5.5.2 Analysis, results, and discussions

A medium size of 50 × 85.5 × 15 m (166 × 285 × 50 ft) (depth × length × width) was used during the analysis. The analyzed medium size was chosen to be larger than the testing size shown in Figure 5.26 to capture void image that lied outside of the testing area. A grid spacing of 1.5 × 1.125 × 1.5 m (5 × 3.7 × 5 ft) (depth × length × width) was used to facilitate the source and receiver placement on the numerical grid. Based on the spectral analysis of the recorded

wavefields, a homogenous initial velocity of 400 m/s (1,330 ft/s) for Vs, and twice that for Vp was chosen for the analysis (Figure 5.27a).

The analysis began with the data filtered for the frequency window of 5-15 Hz, with center frequency of 12 Hz, for 5 iterations for the first stage. The error decreased from a normalized value of 1 at the start of the inversion to 0.98 at the end of the first stage (Figure 5.28). The results of the first inversion stage was then used as input to the second stage using a center frequency of 20 Hz, and a frequency window of 5-25 Hz. The inversion was able to vector towards the local minimum faster in the second stage and the error decreased to a normalized value of 0.65 at the end of the inversion (Figure 5.28). Note, that the first stage was run at lower number of iterations to reveal larger features and make the velocity model ready for the second stage. This staged increase in the frequency is usually employed to force the optimization algorithm to vector towards the appropriate local minimum. Shown in Figure 5.29 is the wavefield comparison for a sample shot at the end of the inversion (25 iterations) for the measured and estimated results. Evident, the observed and estimated waveform data agree quite well for all the recorded time (i.e. FWI).

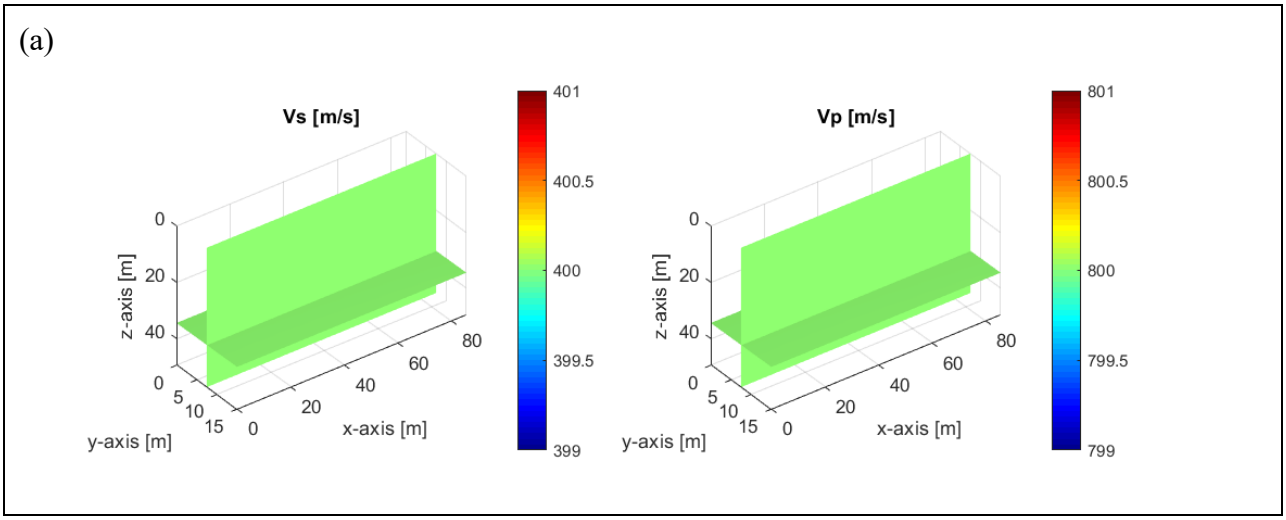

Figure 5.27: Field experiment (large source): (a) distribution of V_S and V_P for the initial velocity model used at the beginning of the analysis; (b) distribution of V_S and V_P for the final inverted result at the end of the 5-25 Hz frequency stage

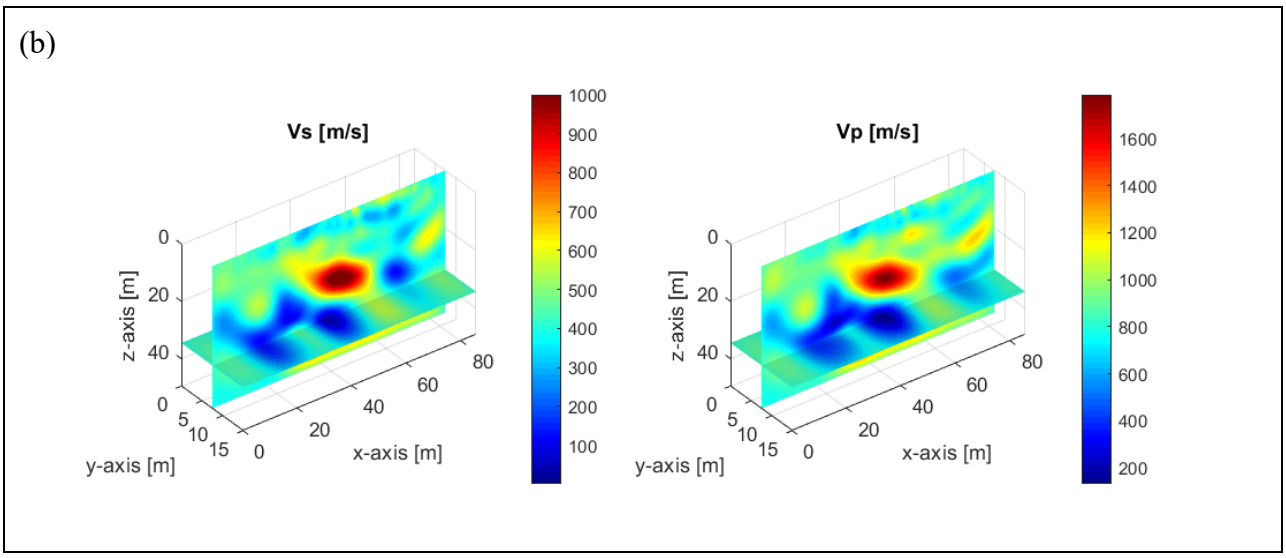

Figure 5.27: Field experiment (large source): (a) distribution of V_S and V_P for the initial velocity model used at the beginning of the analysis; (b) distribution of V_S and V_P for the final inverted result at the end of the 5-25 Hz frequency stage

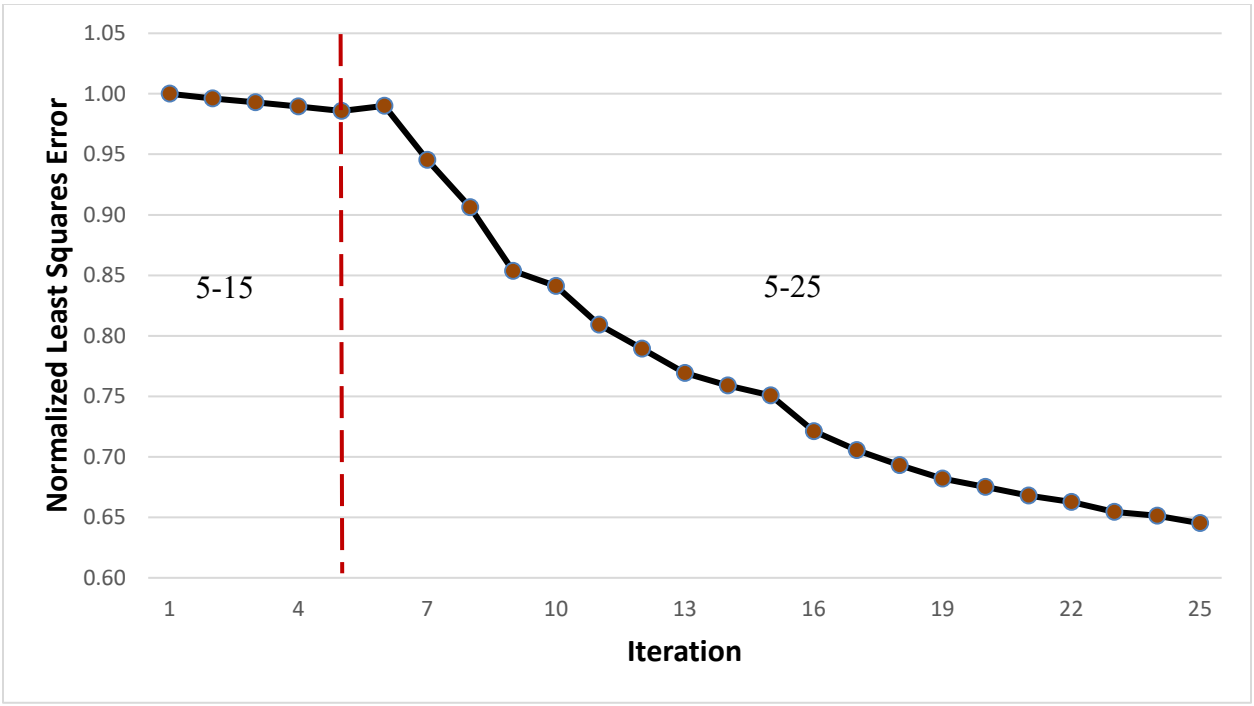

Figure 5.28: Field experiment (large source): normalized least squares error for the entire inversion run

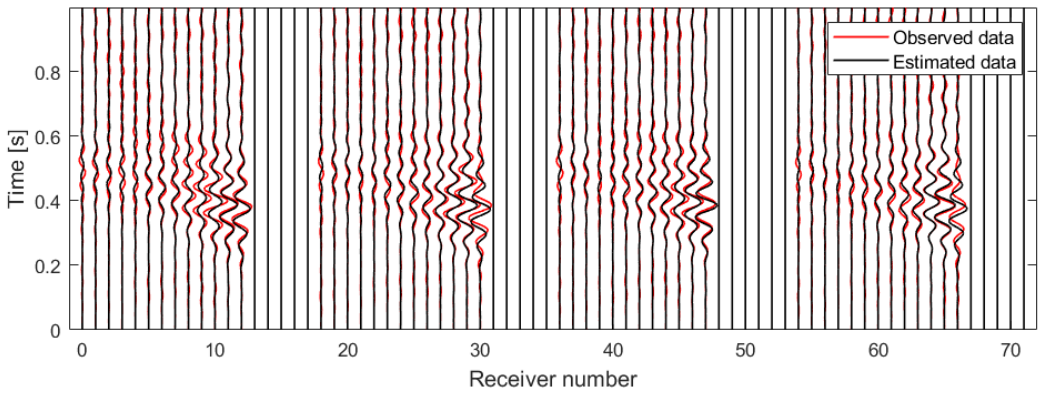

Figure 5.29: Field experiment (large source): wavefield comparison for a sample shot at the end of the inversion (25 iterations)

Shown in Figure 5.27b is the velocity profile for the final inverted results. The existence of the deep void is confirmed underneath the high velocity zone located at the medium's center. There are some indications of another low velocity zone connected to the deep void. This most likely represents the existence of patches of weak soil around the deep void. Shown in Figure 5.30 is 3-D rendering of the final inverted results at four different view angles, and the top-down view of the void. The true extent of the void is revealed, laterally spanning the entire test area in the north-south direction to the outer edges of the analyzed domain. There is also indication of a localized high velocity zone on top of the void, made transparent in the rendering.

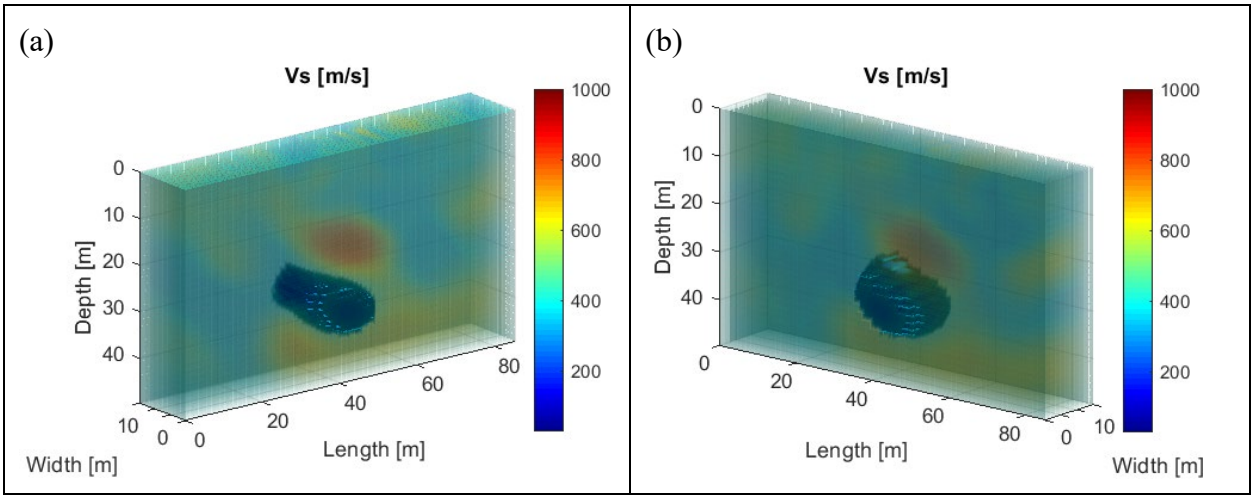

Figure 5.30: Field experiment (large source): 3-D rendering of the final inverted result at (a-d) various viewing angles and (e) the top-down view.

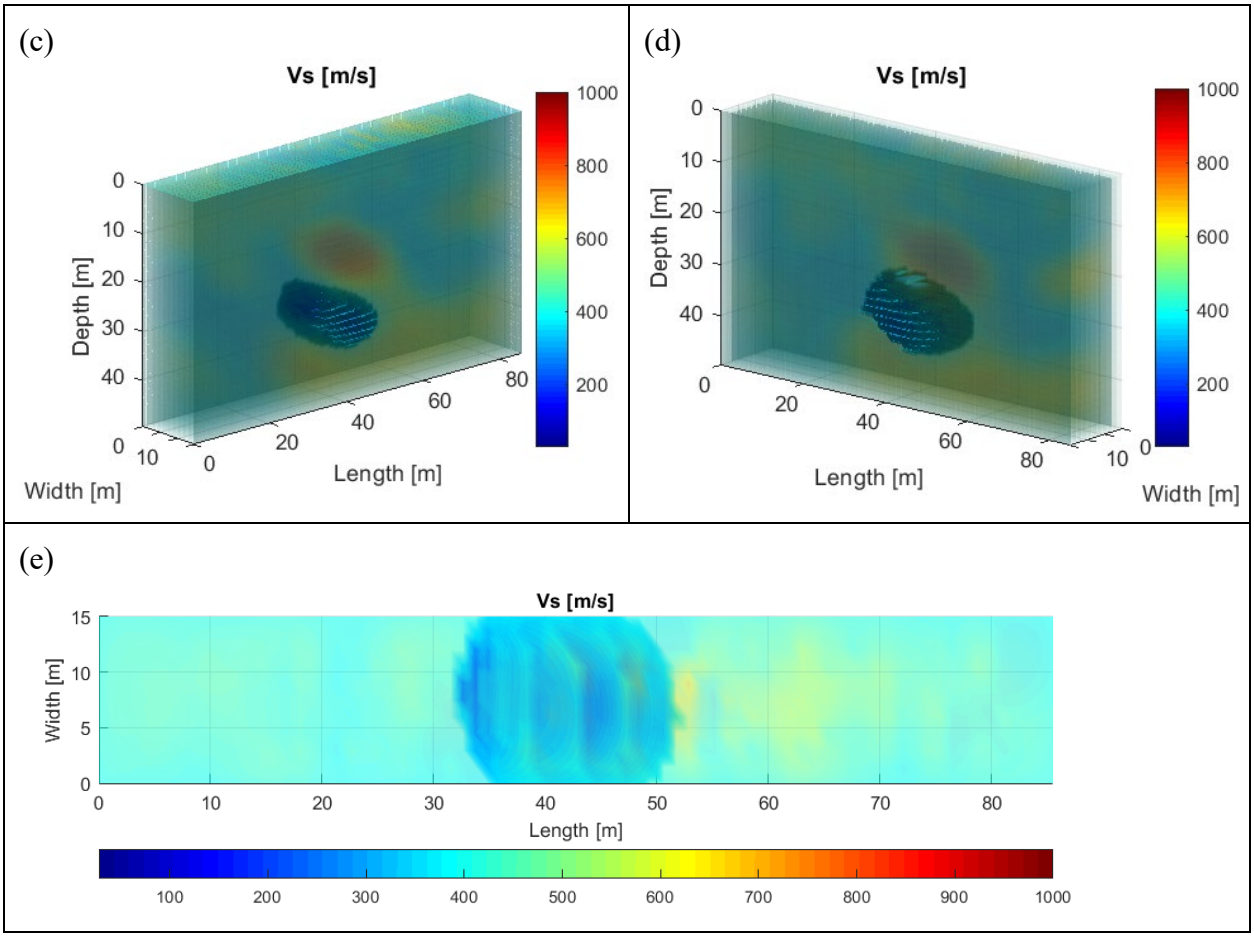

Figure 5.30: Field experiment (large source): 3-D rendering of the final inverted result at (a-d) various viewing angles and (e) the top-down view.

Shown in Figure 5.31 is the overlay of the void location using the top down view of the rendering results (Figure 5.30e) and the result of the sonar field analysis performed at the test site (Figure 5.31a), along with side overlays of the void in the north-south and east-west directions (Figure 5.31b, c). A good overall match on center depth and location between seismic and sonar image of the void extents is seen. The sonar image extends beyond the north-south boundaries of the inverted zone. Overall, the void is measured at about 20 m (66 ft) in lateral diameter, consistent with the sonar image. A vertical side view of the void in the north-south direction facing south (Figure 5.31b) shows the void depth for the inverted results from 25 m (83 ft) at its

shallowest to 40 m (133 ft) at its deepest. A Vertical side view of the void in the east-west direction facing east (5.31c) shows its lateral extents go beyond the analyzed zone. There is some mismatch in the void dimensions in depth for the inverted and sonar results. This is because of the uneven illumination of the void features from all directions (limited on North and South sides) by the surface source.

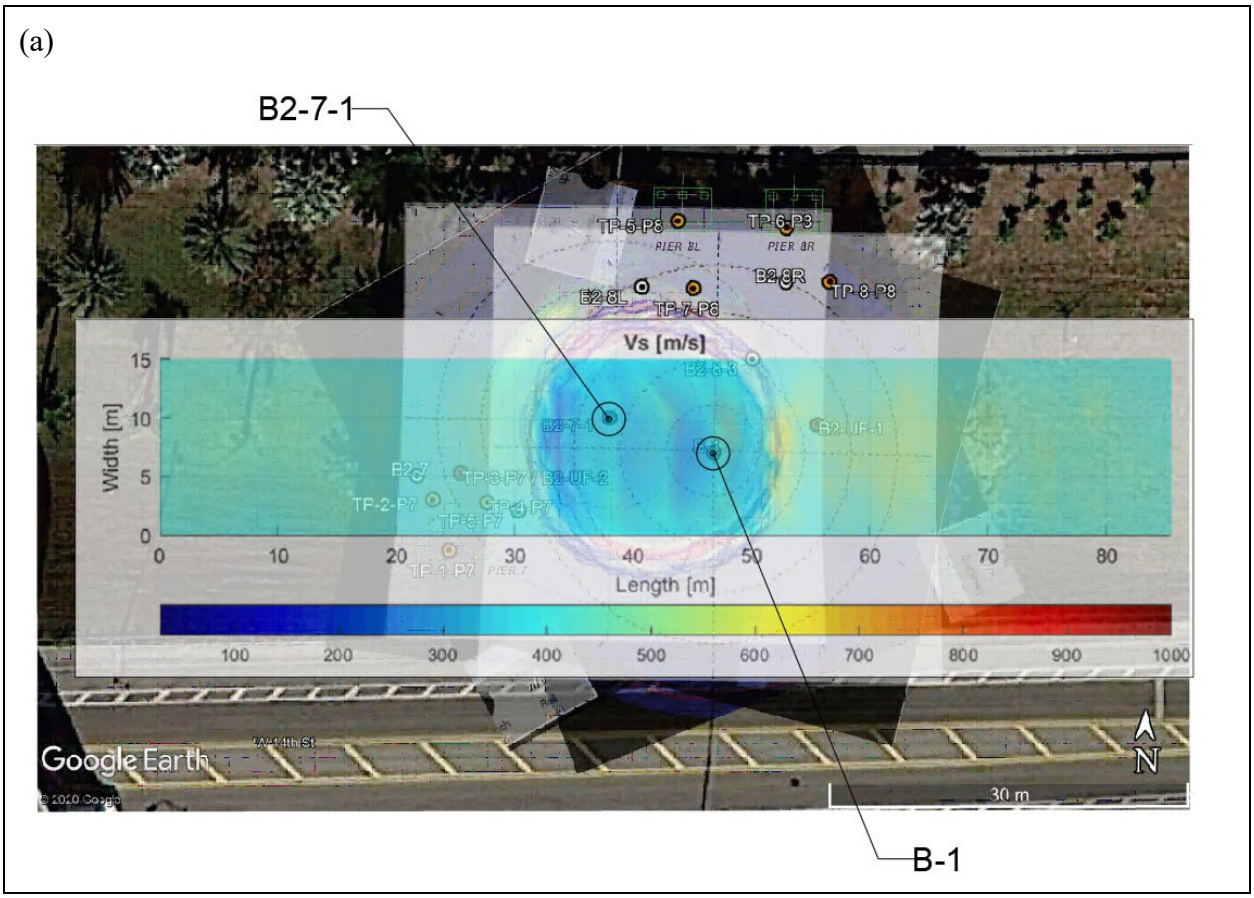

Figure 5.31: Field experiment (large source): (a) overlay of the final inverted result and void location from sonar analysis (B2-7-1 and B-1 locations are used to draw SPT comparison plots in Figure 5.32); (b) side view overlay of the inverted and sonar imaging in the north-south direction facing south; (c) side view overlay of the inverted and sonar imaging in the east-west direction facing east.

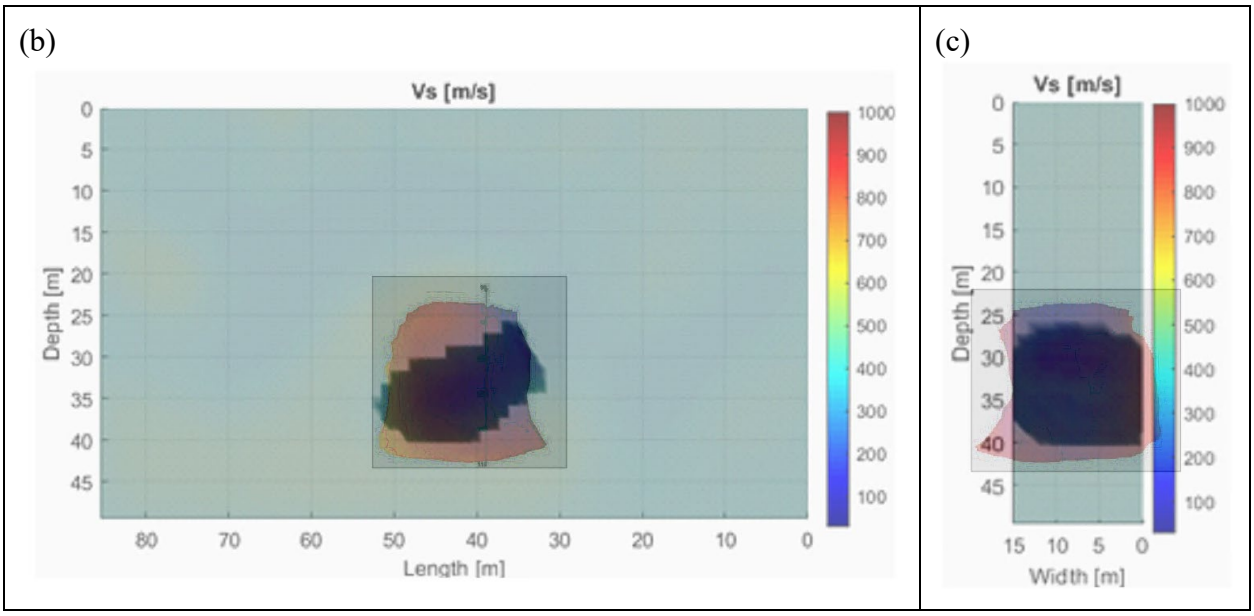

Figure 5.31: Field experiment (large source): (a) overlay of the final inverted result and void location from sonar analysis (B2-7-1 and B-1 locations are used to draw SPT comparison plots in Figure 5.32); (b) side view overlay of the inverted and sonar imaging in the north-south direction facing south; (c) side view overlay of the inverted and sonar imaging in the east-west direction facing east.

Shown in Figure 5.32 is the comparison of the SPT N-values and the final velocity profile for the Vs at two locations determined in Figure 5.31a. Overall, a good match is observed verifying the existence of the void and the high velocity zone on top of the void. The SPT results are more erratic than the inverted velocity results. This is due to the higher sensitivity of the invasive SPT test to local variations in soil density and material properties compared to the geophysical inversion method. The inversion method updates individual velocity cells based on their combined contribution to the recorded wavefield, and therefore averages over a larger volume of the underlying material. Also, using regularization during the inversion process forces additional smoothing of individual velocity cubes in the numerical domain, increasing stability of the optimization algorithm.

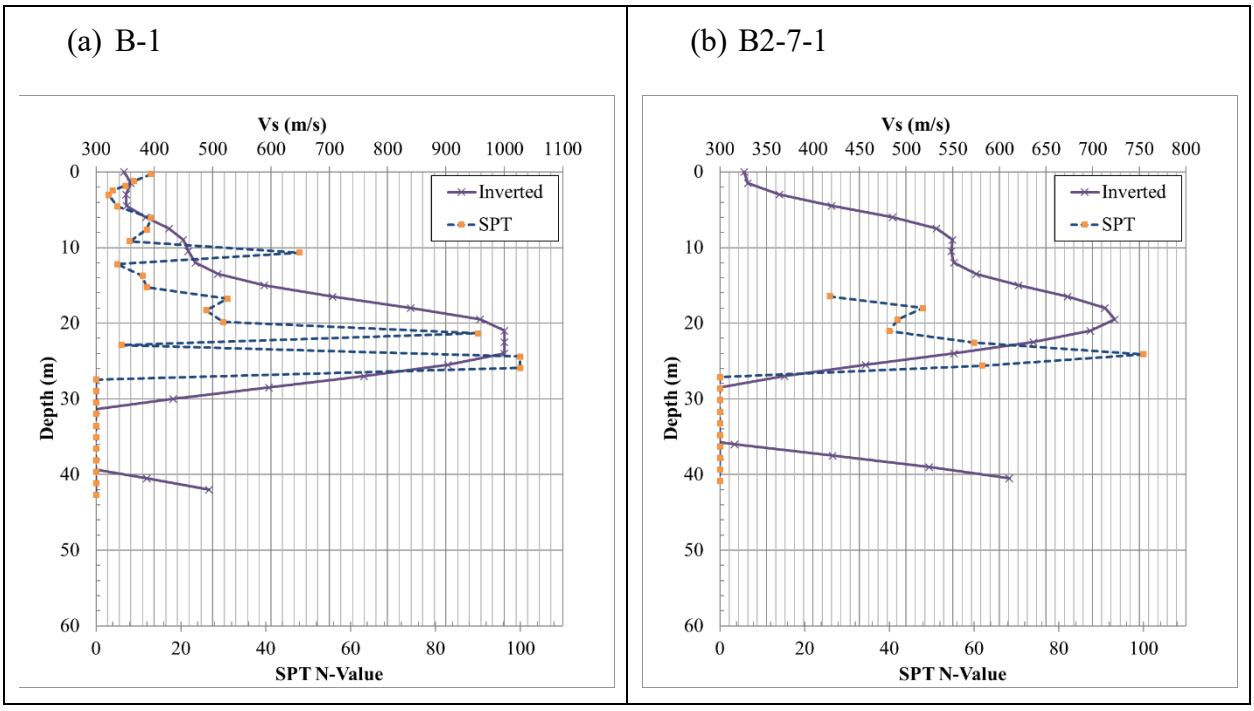

Figure 5.32: Field experiment (large source): Comparison of the velocity profile and final inverted results at two SPT locations shown in Figure 5.31a.

5.6 Coupled SPT and 3-D FWI at the Newberry test site

To extend the void detection range of the FWI method in situations where there is limited source energy or lack of ground access on the surface, an in-depth source using a novel SPT seismic approach was tested. Initially, data gathered from an in-depth source (SPT hammer strike) was used in the inversion analysis at Newberry, Florida test site. In total, 36 4.5-Hz vertical geophones covering a 6 × 6 grid of 3 m (10 ft) spacing were placed on the ground surface (Figure 5.33a). FDOT State Material Office's CME 75 SPT rig was used for the in-depth seismic source. An automatic SPT hammer, 63.5 kg (140 lb) with a drop height of 760 mm (30 inch), was used to generate seismic wavefields at each source location at varying depths (Figure 5.33b). To record the seismic data, a trigger was mounted on the SPT rod to activate the seismograph. Seismic wavefields from 16 SPT blows were recorded, together with the 16 depths

of the SPT spoon as source locations (Figure 5.33a right). As the source locations were dictated by the advancement of the SPT spoon, they are not located uniformly with depth.

For comparison, a surface-based test was also conducted with 49 source locations covering a 7×7 grid of 3 m spacing on the ground surface (Figure 5.34). A propelled energy generator (PEG) with 40 kg (88 lbf) dropped weight (40 kg) was used to induce seismic waves on the ground surface. The same 36 geophones on the 6 × 6 grid of 3 m (10 ft) spacing were used to record surface-based data. Note, limited energy of the surface-based source, and limited ground access on the surface makes deep void recovery in this situation more challenging.

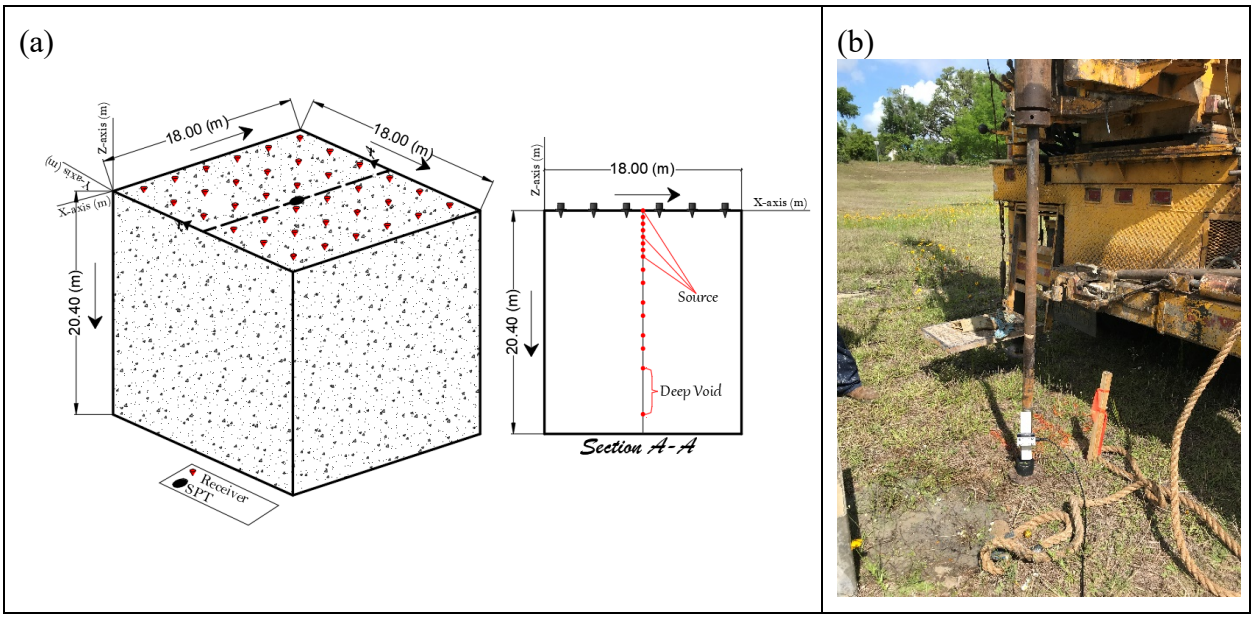

Figure 5.33: (a) field test configuration and (b) the SPT rig testing pictures. The SPT-source locations are not uniform as the source locations are controlled by the advancement of SPT spoon during field experiment.

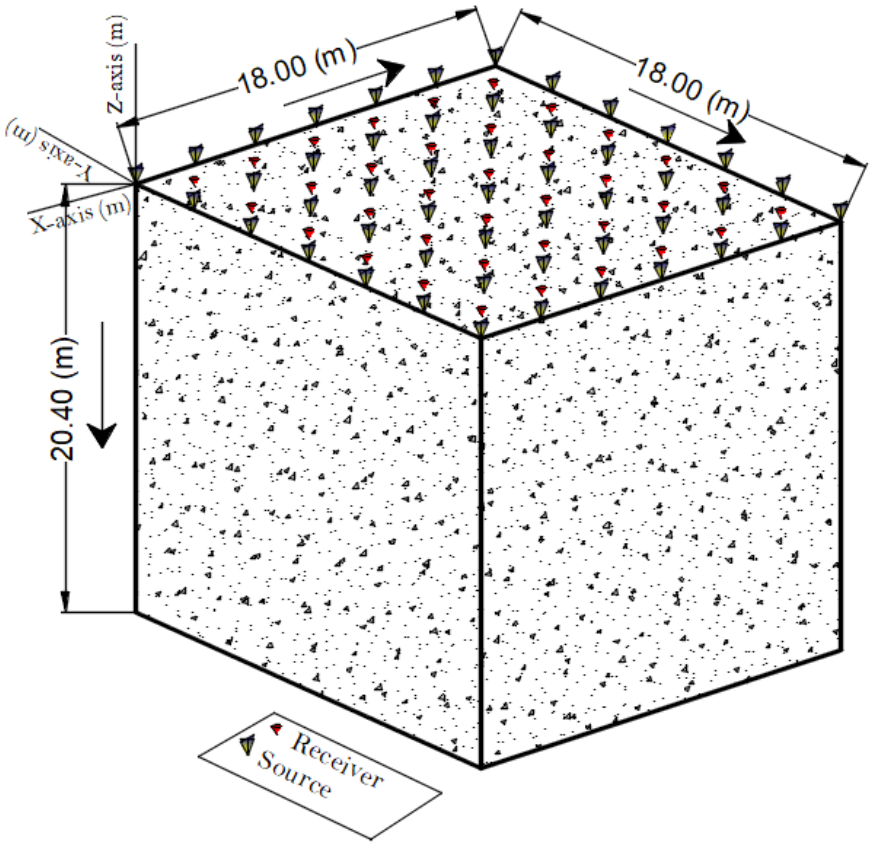

Figure 5.34: Field test configuration of the surface-based geometry.

To get a suitable initial model for waveform analysis, a spectral analysis of surface waves was performed using a line of six geophones on the ground surface (Figure 5.35). The results suggested a Rayleigh wave velocity of about 200 m/s (666 ft/s) to 350 m/s (1,160 ft/s) at the frequency spectrum of 10 to 30 Hz. A linearly increasing initial velocity model was developed with Vs of 200 m/s (666 ft/s) at the surface to 350 m/s (1,160 ft/s) at the half space of the analyzed medium (Figure 5.36a left). Vp was determined using Vs and an assumed Poisson's ratio of 0.3 or almost two times that of Vs (Figure 5.36a right). A mass density of 1,800 kg/m^3 (112 lb/ft^3) was assumed as the characteristic density for general soil-rock and kept constant throughout the analysis. It is noted that waveforms are not very sensitive to the mass density, which does not need to be exactly determined for the inversion analysis.

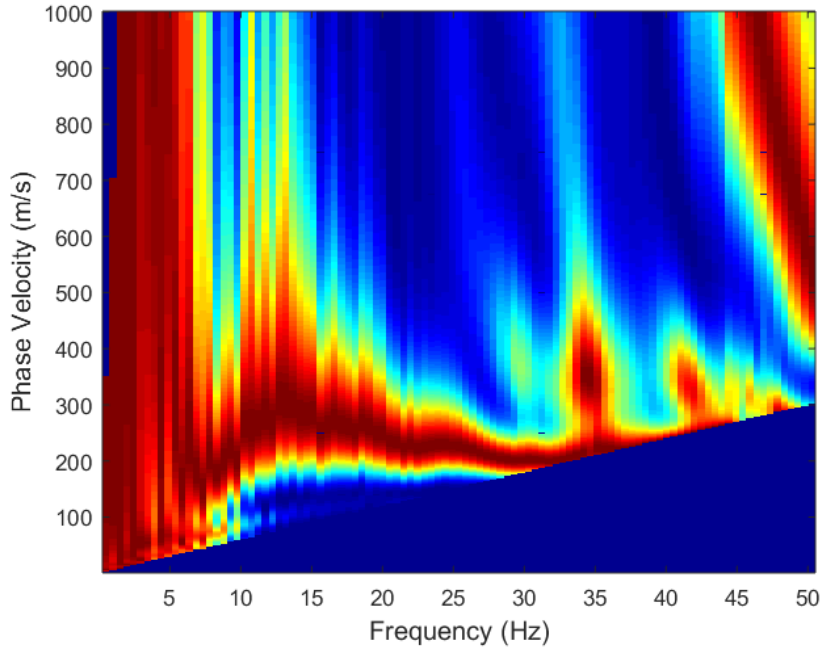

Figure 5.35: Spectral analysis of the surface field data of one line of receivers.

5.6.1 SPT-source data

A medium of 20.4 × 18 × 18 (67 × 60 × 60 ft) (depth × length × width) with a grid spacing of 0.6 × 0.75 × 0.75 m (2 × 2.5 × 2.5 ft) (depth × length × width) was used during the analysis (Figure 5.33a). The source locations (actual depths of the SPT spoon) were rounded to the nearest grid points based on the vertical grid spacing of 0.6 m (2 ft) used in the numerical analysis. The measured field data of the SPT source were filtered through two frequency bandpasses of 10-30 Hz and 10-40 Hz and used for two inversion runs.

Similar to previous analyses, the estimated data generated from the elastic forward solver were adjusted by an offset dependent correction factor in the form of $y(r)=Ar^{\alpha}$, where r is the source-receiver distance. Parameters A and α are determined through an iterative inversion process to minimize the energy of the waveform residuals. These parameters are determined at the beginning of each inversion run and kept constant for each run.

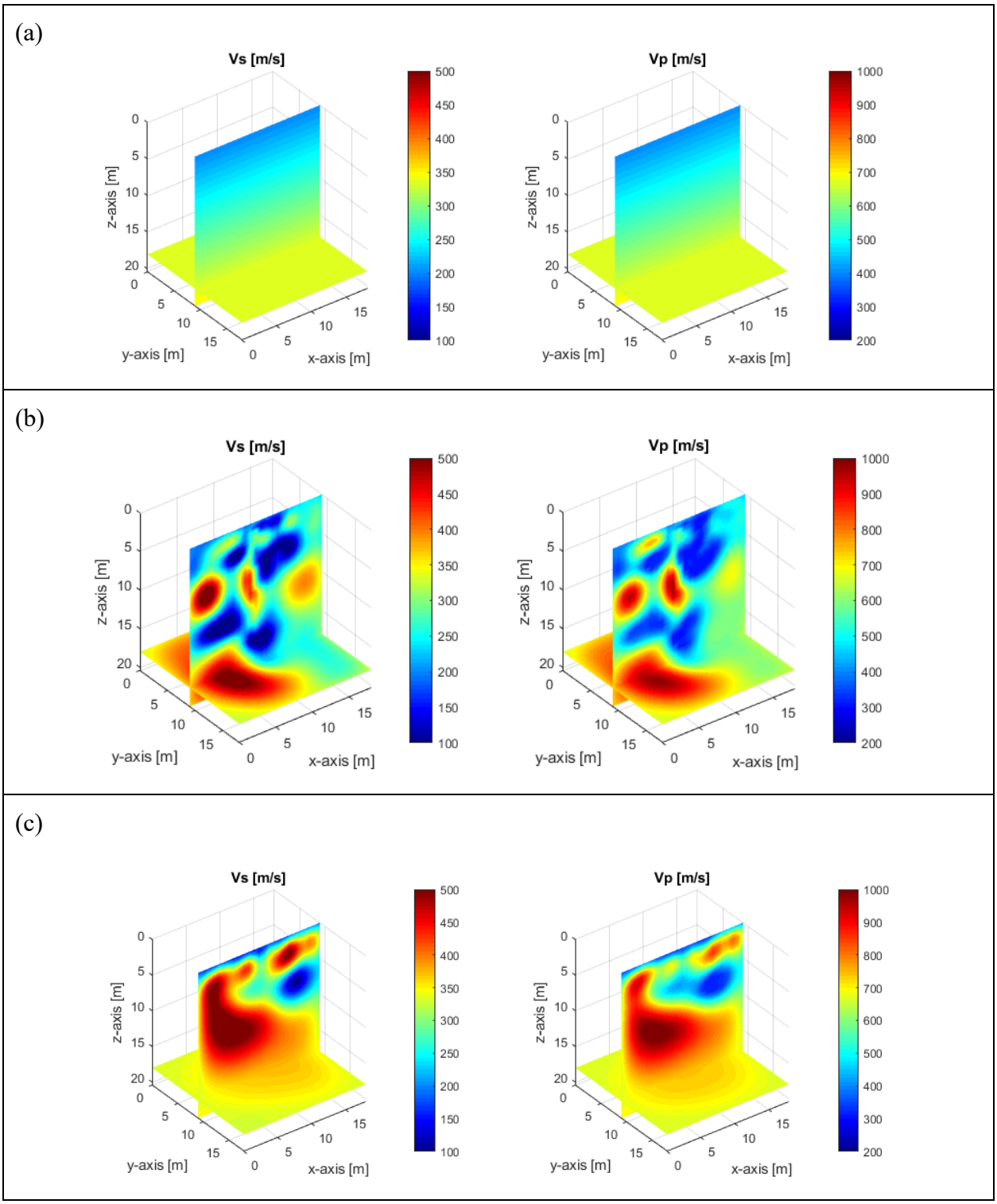

Figure 5.36: Field experiment: (a) distribution of V_S and V_P for the initial model, (b) the inverted result for SPT source data, and (c) the inverted result for surface-based data.

The first inversion started with the initial model (Figure 5.36a), using the filtered data of 10-30 Hz. The second inversion continued with the result of the first inversion as the input

velocity model, and the filtered 10-40 Hz surface data. Both inversions ran for the preset 100 iterations. The error reduced continuously from a normalized value of 1.0 at the start of the inversion process to 0.63 at the end of the first inversion stage (100 iterations), and to 0.58 at the end of the second stage at 200 iterations (Figure 5.37). No spike in the normalized error at the transition of the two frequency stages was observed. This means that less wave energy from 30-40 Hz was added to the wavefield with the increase of frequency. In addition, most subsurface features had already been revealed by the first frequency stage, and the velocity model was ready to accept the higher frequencies.

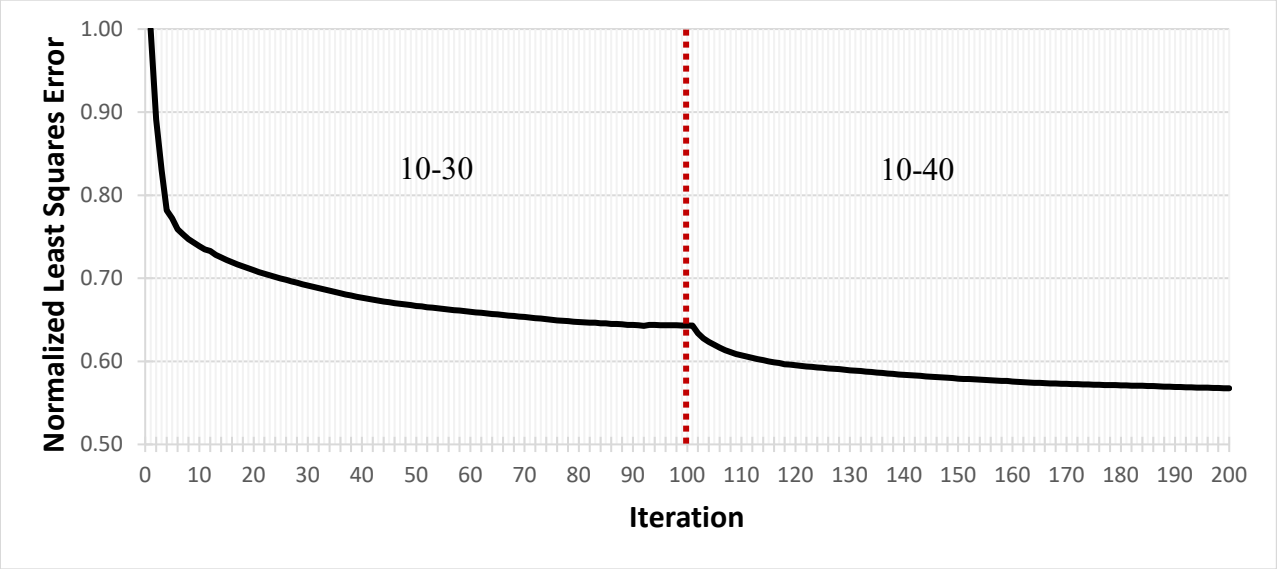

Figure 5.37: Field experiment: normalized least squares error for SPT source data.

Shown in Figure 5.38 is the waveform comparison between the observed (measured) data from a sample SPT-source and estimated data associated with the initial model (Figure 5.38a) and the final inverted result (Figure 5.38b). As seen in the observed data, the seismic waveforms generated from the SPT blow were well recorded on the ground surface, with a consistent wave propagation pattern and magnitude. During inversion, the waveform match improved for most of

the channels. No cycle skipping or matching of the wrong peaks is seen, suggesting the sufficiency of the initial model.

Shown in Figure 5.36b is the final inverted result for the SPT-source data. Vs profile (Figure 5.36b, left) consists of a soft layer from the ground surface to about 7 m (23 ft) depth with shallow low-velocity anomalies, underlain by a stiff layer. Based on SPT samples, the soft and stiff layers are soil and weathered limestone, respectively. Interestingly, there exist two connected voids with very low Vs values (40 -100 m/s [133-333 ft/s]) buried inside the limestone layer, at 14 m to 18 m (46-60 ft) depth. One of them lies outside of the SPT boring and was not identified by the SPT. Vp profile (Figure 5.36b, right) is consistent with the Vs profile, including soil/limestone layers and low-velocity anomalies/voids.

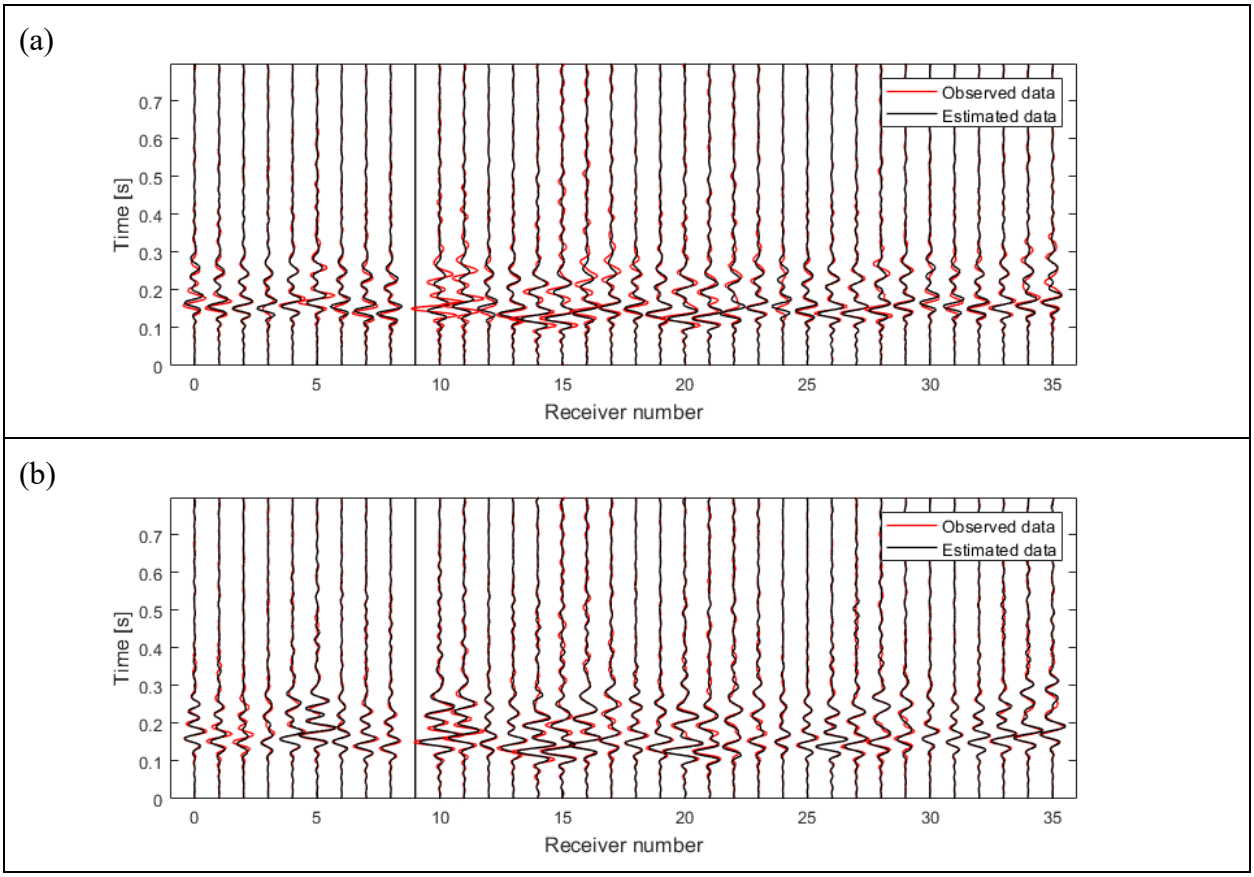

Figure 5.38: Field experiment: waveform comparison between the observed data from the SPT-source and estimated data for a sample shot associated with (a) the initial model and (b) the final inverted result at iteration 200. Channel 9 with poor data is removed from analysis.

5.6.2 Surface-based data for comparison with SPT source

The surface-based data was also inverted using the same initial model as that of the SPT-source data (Figure 5.36a). The same frequency bandpasses of 10-30 Hz and 10-40 Hz and the same number of iterations were also used during the surface-based inversion analysis. The final inverted results of the surface-based data (Figure 5.36c) revealed one shallow low-velocity zone at the right of the medium, and a high-velocity zone at the left of the medium. As expected, the deep voids inside the limestone layer cannot be identified from the surface-based experiment. Again, this is due to the limited test area on the surface (18 x 18 m [60 x 60 ft]) and large reflections of surface source energy at the soil/limestone boundary, as well as the limited energy from the PEG source at lower frequencies (5-20 Hz range).

For better viewing of subsurface features, Figure 5.39 shows the 3-D renderings of Vs and Vp of the initial model, and inverted results of the SPT-source and surface-based data. Again, the two deep voids (14 -18 m [46-60 ft] depth) are clearly shown in the result of the SPT-source data (Figure 5.39b, left), but not in the result of the surface-based data (Figure 5.39c). The Vp renderings are similar to the Vs renderings, except the two deep voids are merged into a big one (Figure 5.39b, right).

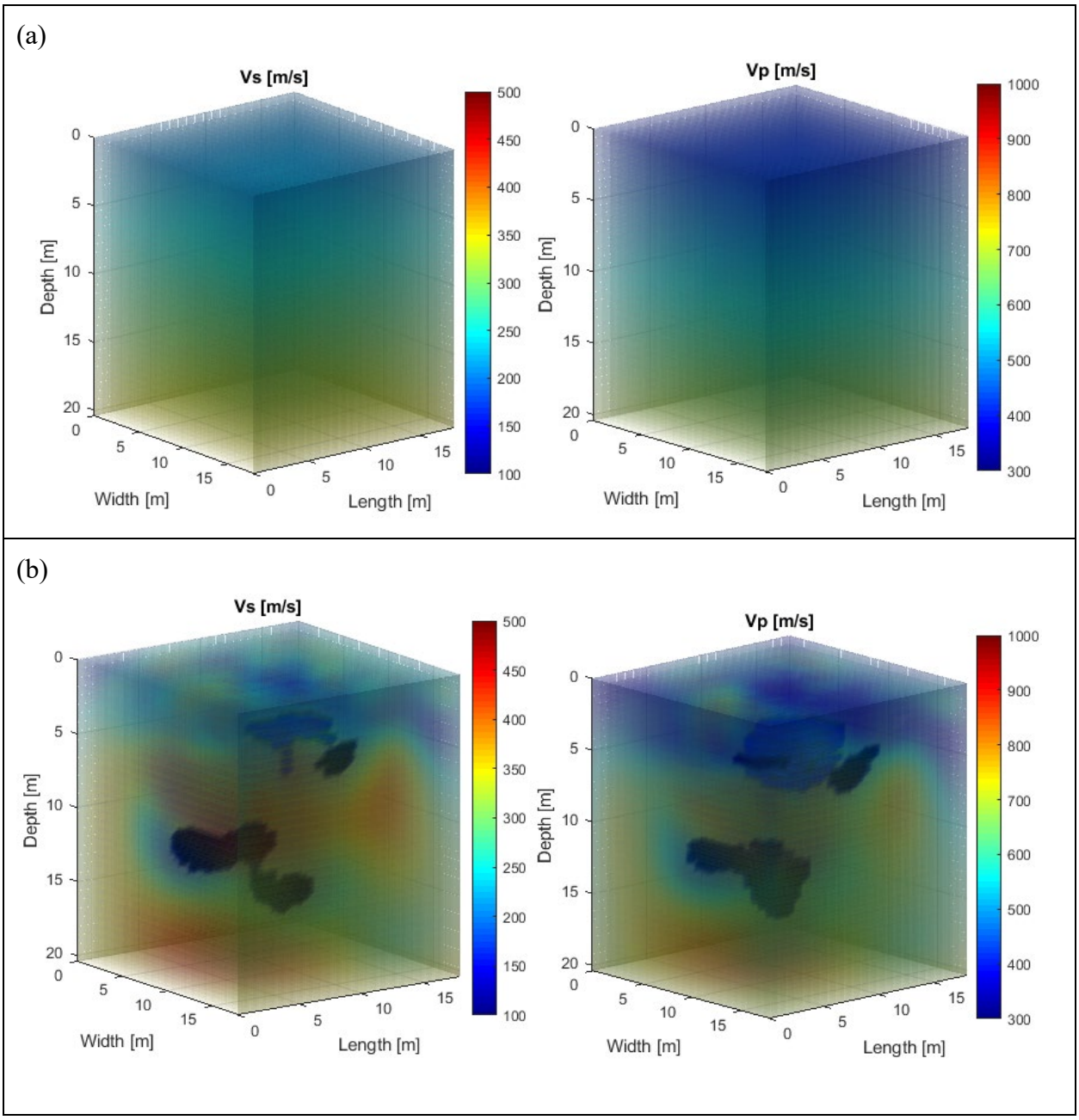

Figure 5.39: Field experiment: 3-D rendering of the V_S (left) and V_P (right) in m/s for (a) the initial model, (b) the final inverted result of the SPT-source data and (c) the final inverted result of the surface-based data

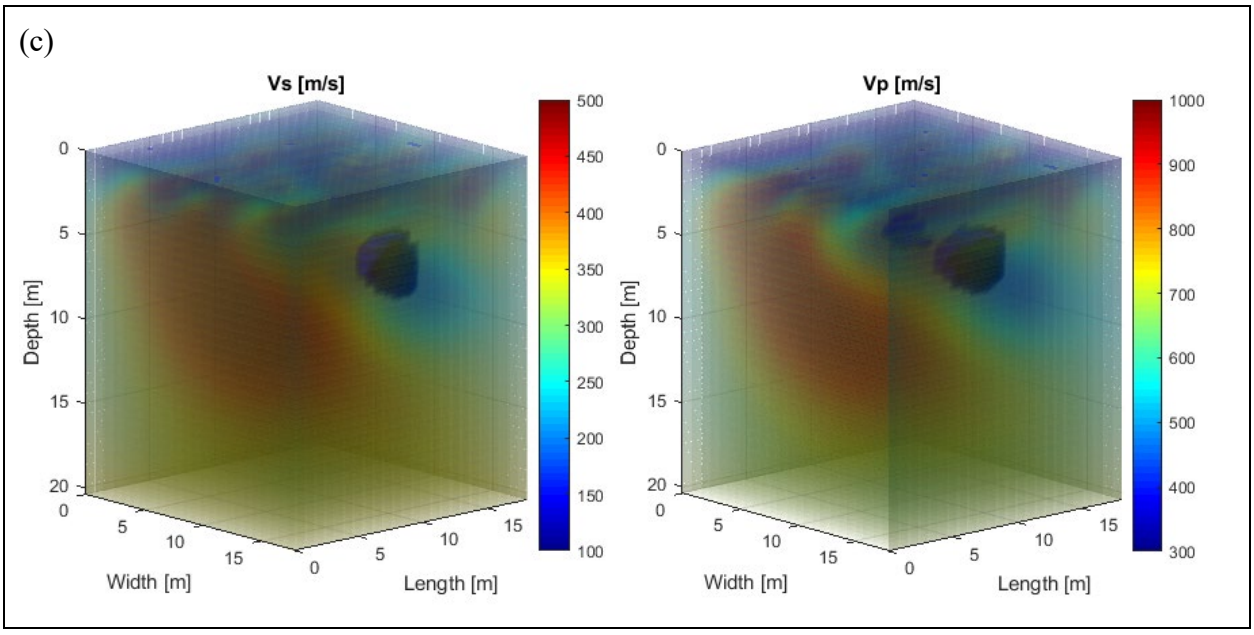

Figure 5.39: Field experiment: 3-D rendering of the V_S (left) and V_P (right) in m/s for (a) the initial model, (b) the final inverted result of the SPT-source data and (c) the final inverted result of the surface-based data

Shown in Figure 5.40 is the comparison of the initial Vs, the inverted Vs (iteration 200, SPT source inversion) and the SPT N-values along the vertical source line at the center of the medium. The initial and inverted Vs values were sampled at each grid point along the depth. A good overall match of the SPT N-values and the inverted Vs profile is observed, including identification of low-velocity zones at about 1 m (3 ft) and 15 m (50 ft) depths and high-velocity zones at about 4 m (13 ft) and 9 m (30 ft) depths. The inverted Vs profile is not as erratic as the SPT N-values. This is due to the regularization used in the inversion, which partially ties adjacent cells and smooths velocity models. Reducing the regularization level can increase the model contrast and improve the match with SPT N-values. However, it leads to less optimization stability and produces more inversion artifacts.

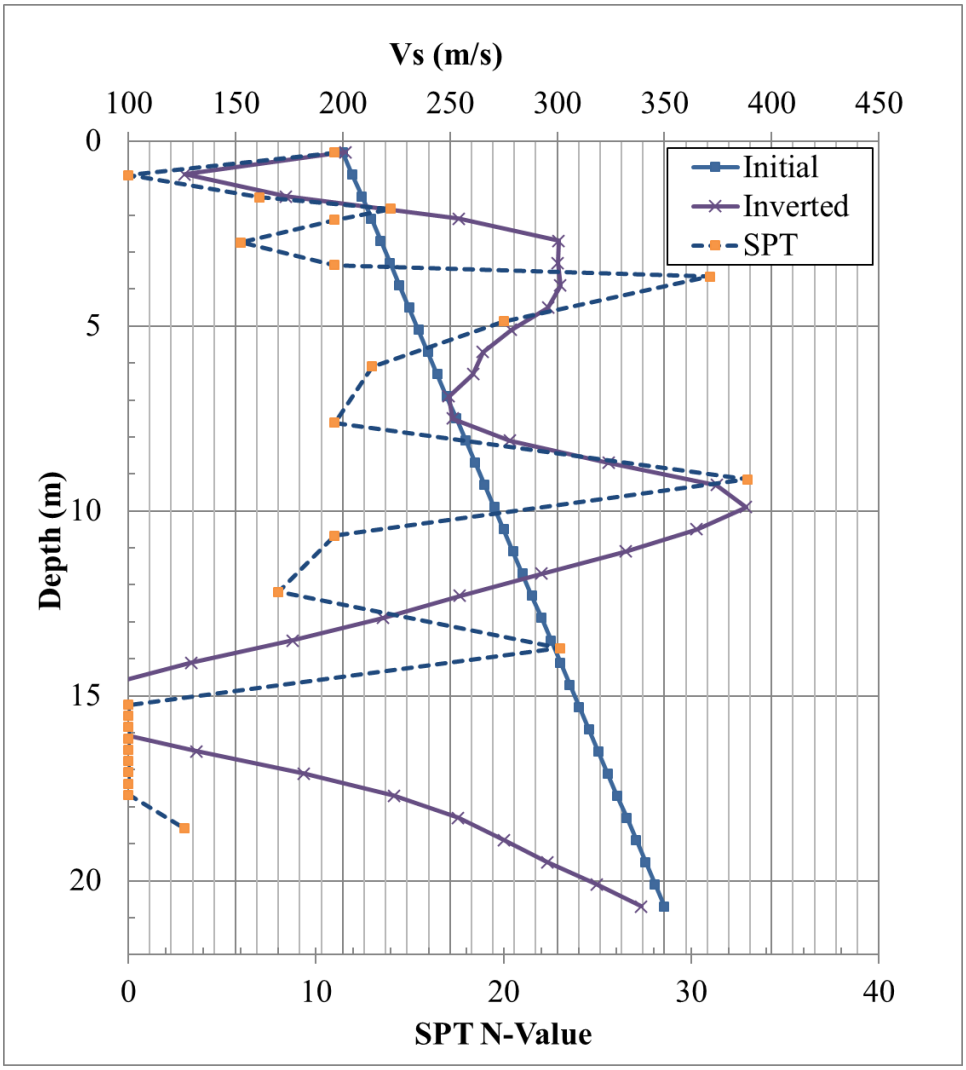

Figure 5.40: Comparison of the velocity variation with the SPT N-values for the final inverted result of the SPT-source seismic data and the initial velocity.

5.7 Coupled SPT and 3-D FWI at the Miami test site

5.7.1 Test configuration and field testing

In-depth source testing using the SPT-seismic approach was subsequently carried out at two different locations outside of the void region. The goal was to further study the novel SPT seismic approach to see if using SPT blows as the source can help determine the existence of the deep void and appraise the accuracy of the inverted results. Using the SPT hammer as the source allows for the generation of seismic waves from soil-rock mass at great depths by drastically

reducing surface wave contribution and increasing the body waves in surface data. Strong body wave signals at ground surface from a source at appreciable depth ensures identification of layering, zones, anomalies, etc. by the volume of soil between the source and receivers. For instance, being able to detect voids and anomalies outside of the SPT testing zone in the earlier stages of field investigations (first or second SPTs) allows for targeted subsequent SPT borings and aids in decreasing uncertainty in later stages of project design.

An automatic SPT rig (Figure 5.41) was used for a boring on the southwest and one on the northeast of the deep void. The goal was to illuminate the targeted void from both opposite directions using in-depth seismic waves without physically intersecting the void. Shown in Figure 5.42 is the testing configuration used for data acquisition during both SPT borings. In total, 72 geophones located in a 4 × 18 grid of 3 × 4.5 m (10 ×15 ft) spacing were used on the ground surface. Two lines of sources were applied each to a depth of 52.5 m (172 ft). The SPT hammer was dropped at every 1.5 m (5 ft) interval and the data was collected by all the 72 geophones simultaneously. In total, 70 SPT locations in depth were recorded for the analysis (35 each line). At each in-depth location, data was collected for multiple singular hammer drops, and the data was summed (stacked). This is good practice for seismic testing, as it helps with reducing unwanted ambient noise (e.g. car passing) in the data during the analysis.

Figure 5.41: Miami test site: in-depth source using SPT seismic approach used to generate seismic waves

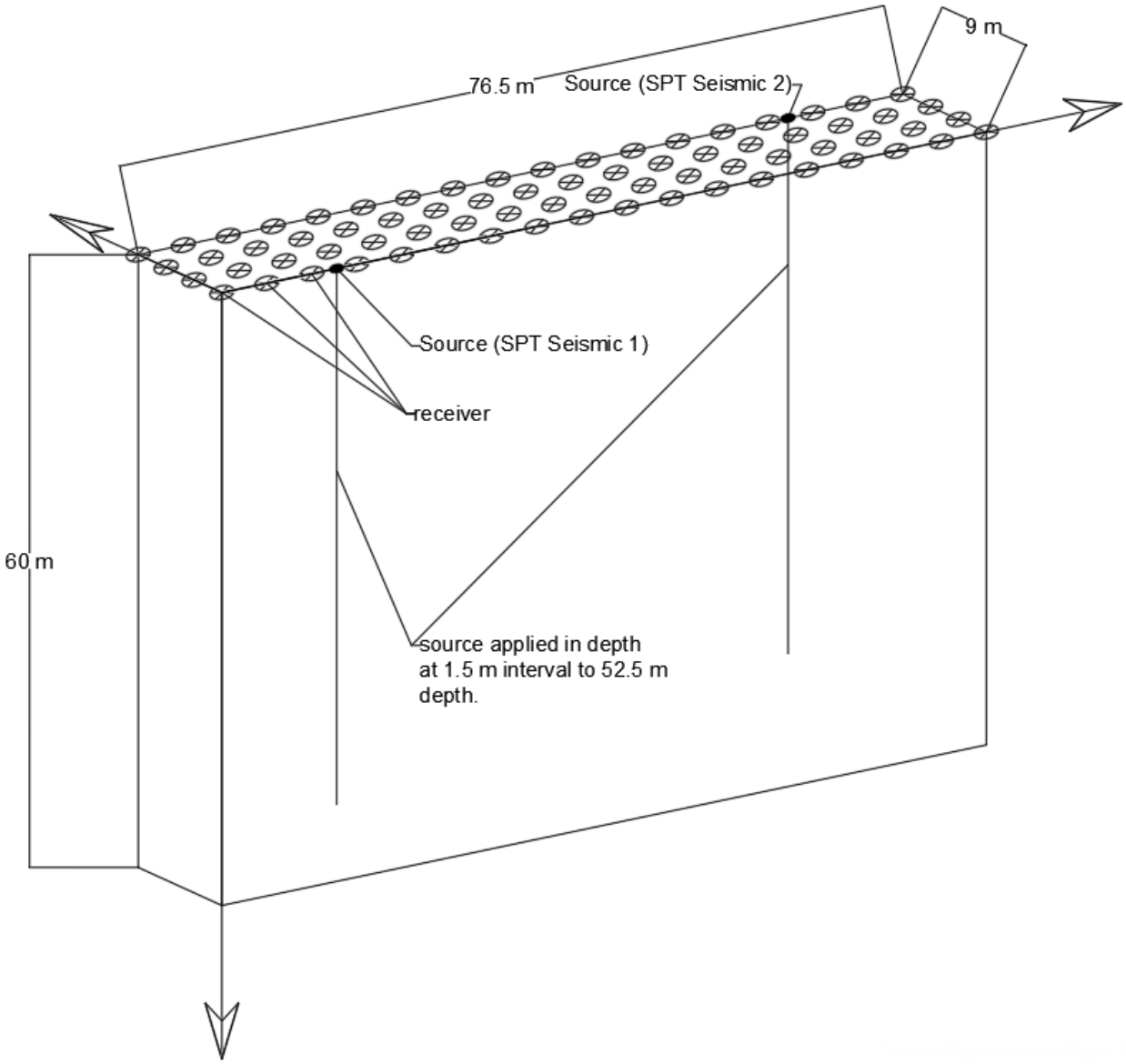

Figure 5.42: testing configuration used for in-depth source based on SPT seismic approach

5.7.2 Analysis, results, and discussions

The acquired data was stacked at each testing depth and used in the inversion analysis. A medium size of 60 × 85.5 × 15 m (200 × 285 × 50 ft) (depth × length × width) was used in the numerical analyses. Given the reasons mentioned for the surface-based method (Section 5.5), the medium size was chosen to be larger than the testing configuration shown in Figure 5.42, to

capture void features that lie outside of the testing zone. A homogeneous initial velocity model was chosen based on spectral analysis of the data (Figure 5.43a).

The inversion began with the data filtered at 5-25 Hz at a center frequency of 17 Hz for the first stage using the initial model shown in Figure 5.43a. The implemented Gauss-Newton optimization algorithm successfully vectored towards a local minimum and the error decreased to a normalized value of 0.94 at the end of the predefined 100 iterations (Figure 5.44). Note, the amount of data embedded in the SPT-seismic approach is larger compared to the surface-based method due to the addition of diffraction/transmission effects. Therefore, more iterations are required to reach convergence (compared to surface-based method).

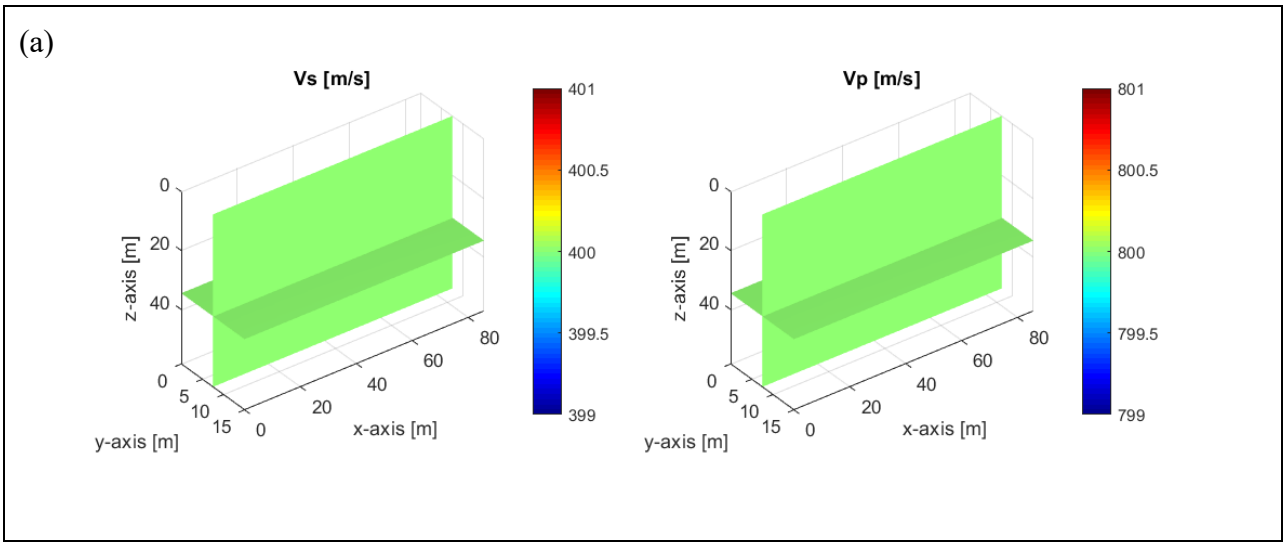

Figure 5.43: Field experiment (SPT seismic): (a) distribution of V_S and V_P for the initial velocity model used at the beginning of the analysis; (b) distribution of V_S and V_P for the final inverted result at the end of the 5-35 Hz frequency stage

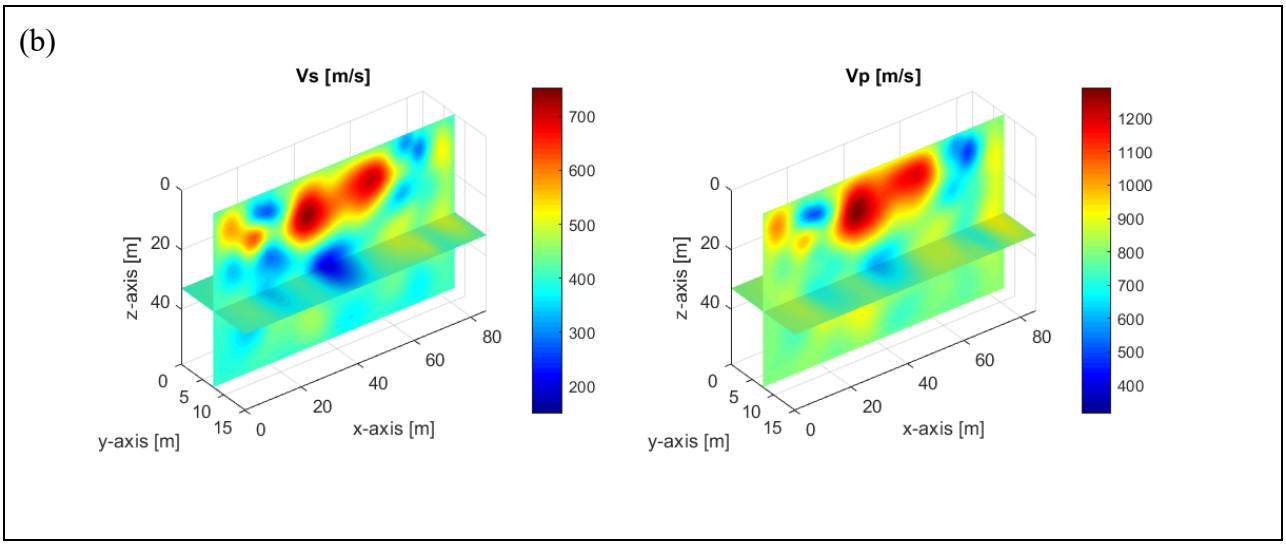

Figure 5.43: Field experiment (SPT seismic): (a) distribution of V_S and V_P for the initial velocity model used at the beginning of the analysis; (b) distribution of V_S and V_P for the final inverted result at the end of the 5-35 Hz frequency stage

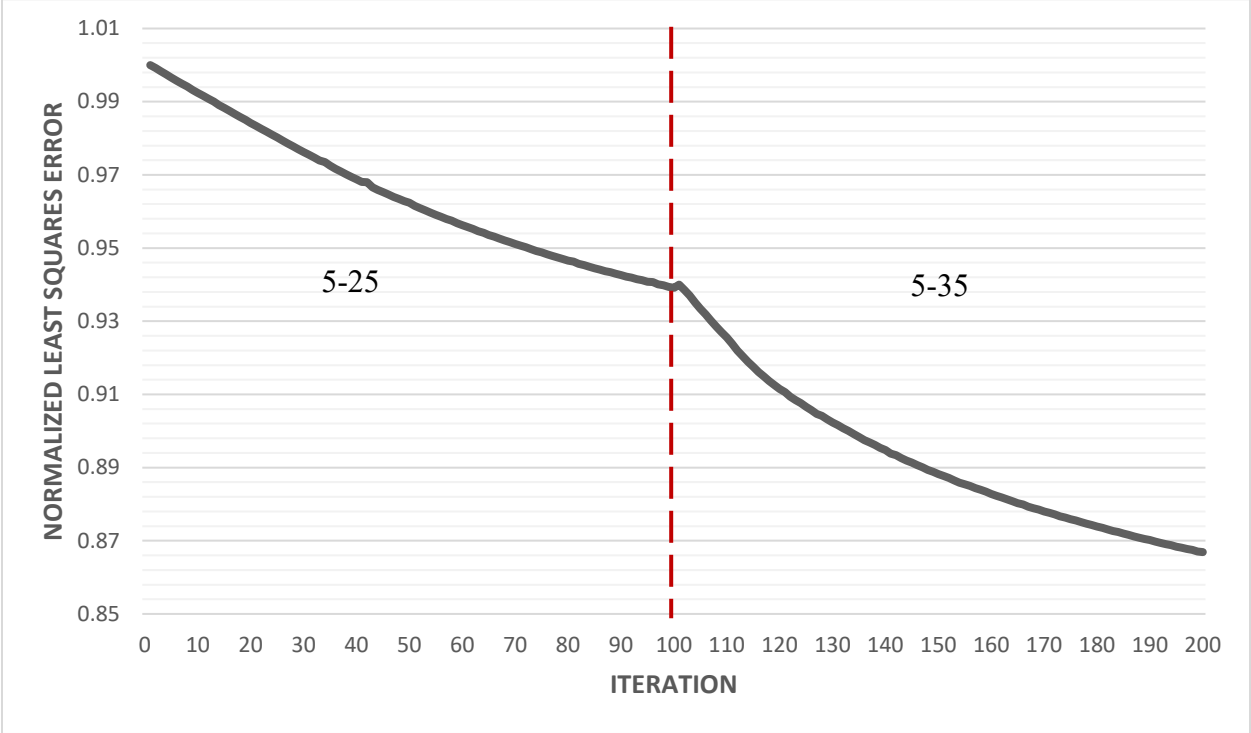

Figure 5.44: Field experiment (SPT seismic): normalized least-squares error for the entire inversion run

The waveform data was then filtered through a 5-35 Hz window, using a central frequency of 25 Hz, and used in the second stage with the results of the velocity profile from the previous stage as the input model. The error further decreased to 0.87 at the end of the inversion process (200 iterations). Shown in Figure 5.45 is the waveform comparison from the final inverted result (200 iterations) and the initial model for a sample shot. Overall, the phase and amplitude match improved for most channels. There is still some mismatch in the final inverted results. This can be attributed to the noise that remained in the data during the inversion analysis, which cannot be accounted for through the forward simulation.

Shown in Figure 5.43b is the final inverted result at the end of the 200 iterations for Vs and Vp profile. There is an indication of a large void at the center. The void is overlain by a large high velocity zone closer to the surface. Shown in Figure 5.46a to 5.46e are the 3-D renderings of the final inverted result at different viewing angles and the top-down view, respectively. The true extent of the void is revealed, spanning the entire testing area laterally to outside of the analysis region. There is indication of a high velocity zone on top of the void and a low velocity zone to the left. Overall, the features match those of the surface-based testing (Figure 5.30) in type and relative positions.

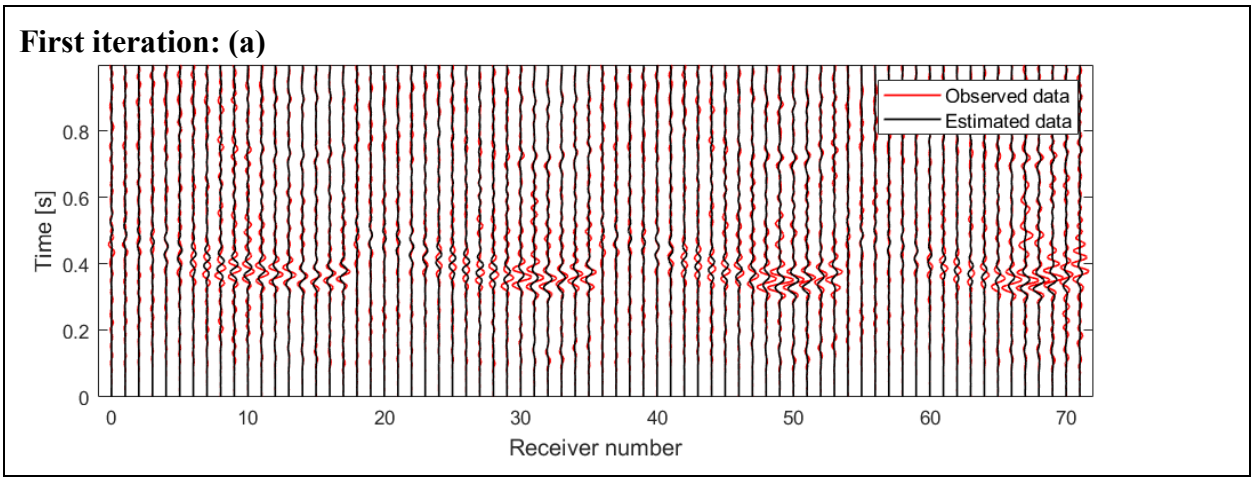

Figure 5.45: Field experiment (SPT seismic): wavefield comparison for a sample shot between (a) the initial model and (b) the final inverted model.

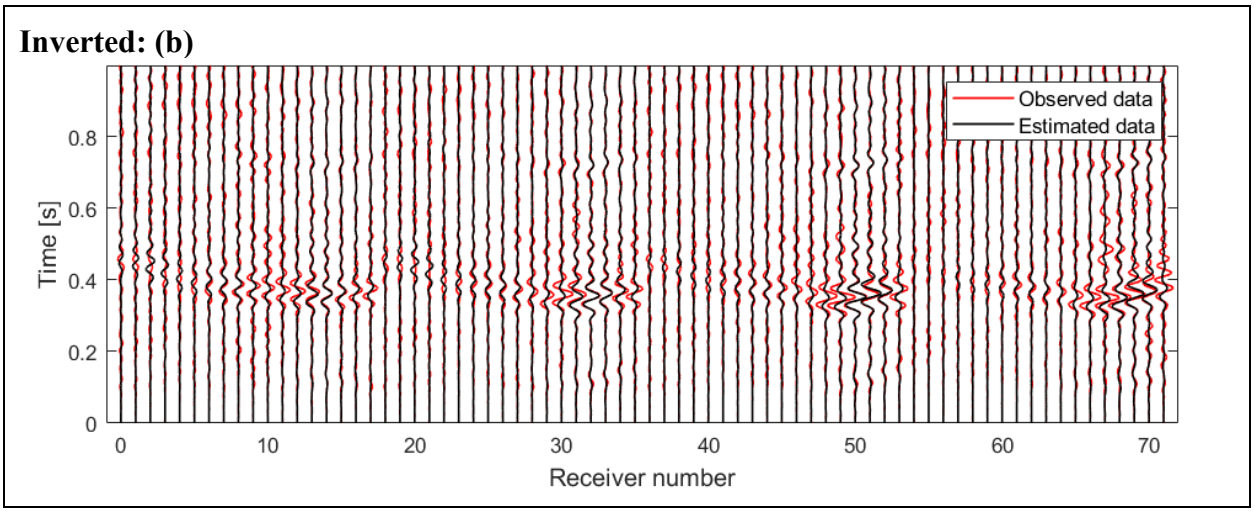

Figure 5.45: Field experiment (SPT seismic): wavefield comparison for a sample shot between (a) the initial model and (b) the final inverted model.

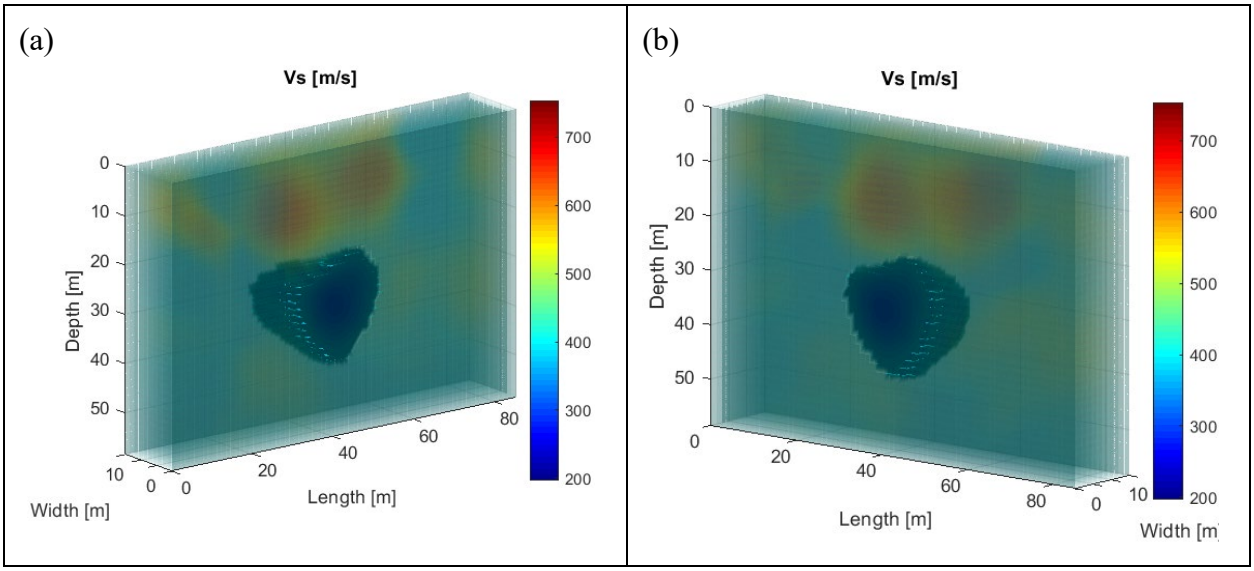

Figure 5.46: Field experiment (SPT seismic): 3-D rendering of the final inverted result at (a-d) various viewing angles and (e) the top-down view.

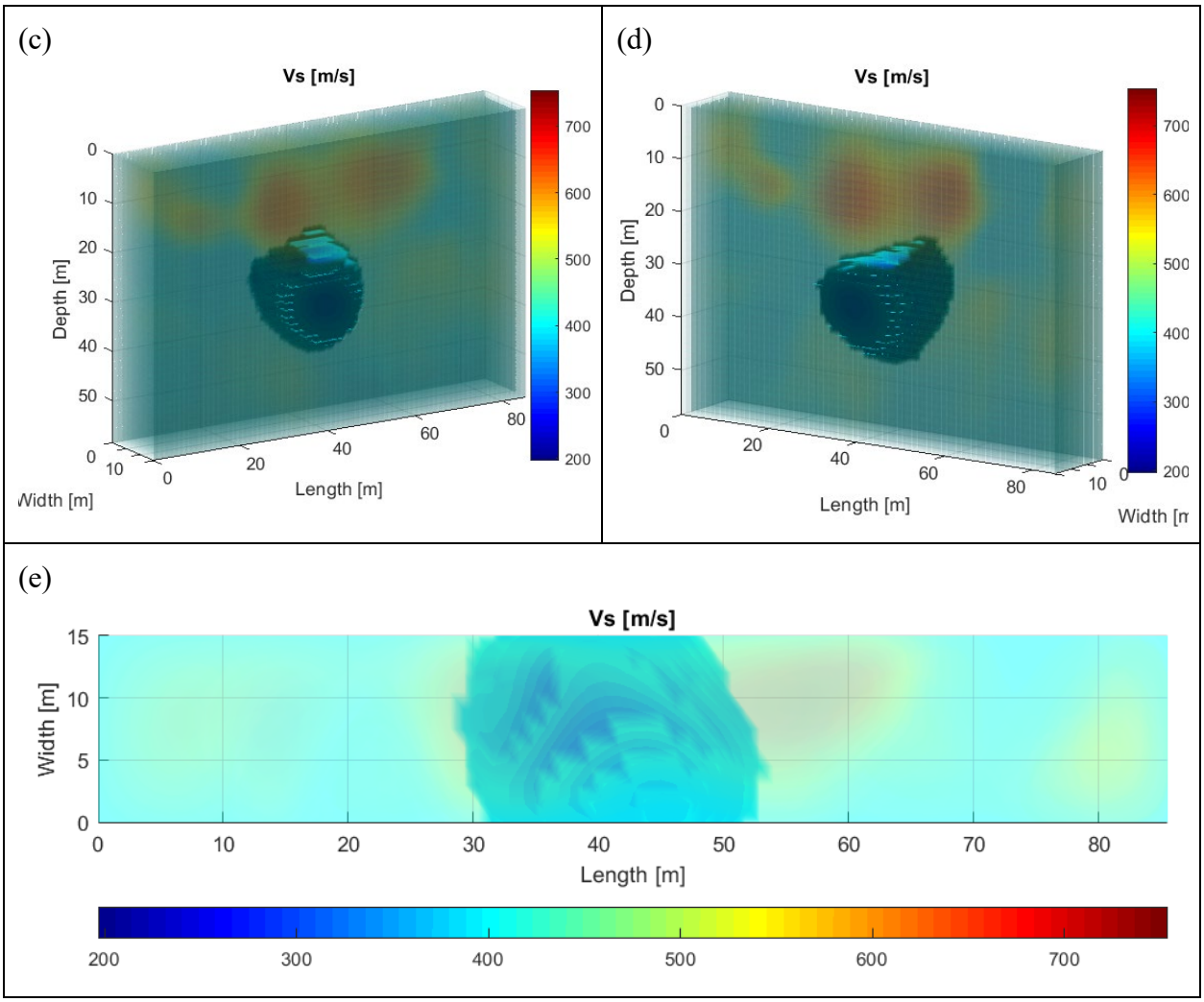

Figure 5.46: Field experiment (SPT seismic): 3-D rendering of the final inverted result at (a-d) various viewing angles and (e) the top-down view.

Shown in Figure 5.47a is the top-down overlay of the void using Figure 5.46e and the results of the sonar analysis performed at the site. The void is matched well at the center and both results show lateral extensions to outside of the testing zone. Shown in Figure 5.47b is the side overlay comparison of the void in the north-south direction facing south, for the inverted and sonar results. The void extent is determined from about 22 m (72 ft) at its shallowest to 42 m (138 ft) at its deepest. The void dimension in depth was estimated to be 20 m (66 ft) from the inverted results. Shown in Figure 5.47c is the side overlay comparison of the inverted and sonar

images in the east-west direction, facing east. The sonar image extends beyond the analyzed domain. Overall, agreement between the two results is quite good in all directions.

The locations of four SPT borings are shown in Figure 5.47a. B2-7-1 and B-1 are physically intersecting the void and were used to verify the inverted results in the zone above and inside the void. B2-UF-2 and B2-UF-1 are the positions of the shots (SPT Seismic 1 and SPT Seismic 2 in Figure 5.42) used to generate the data. These were also used in verification of the results for in-depth source data.

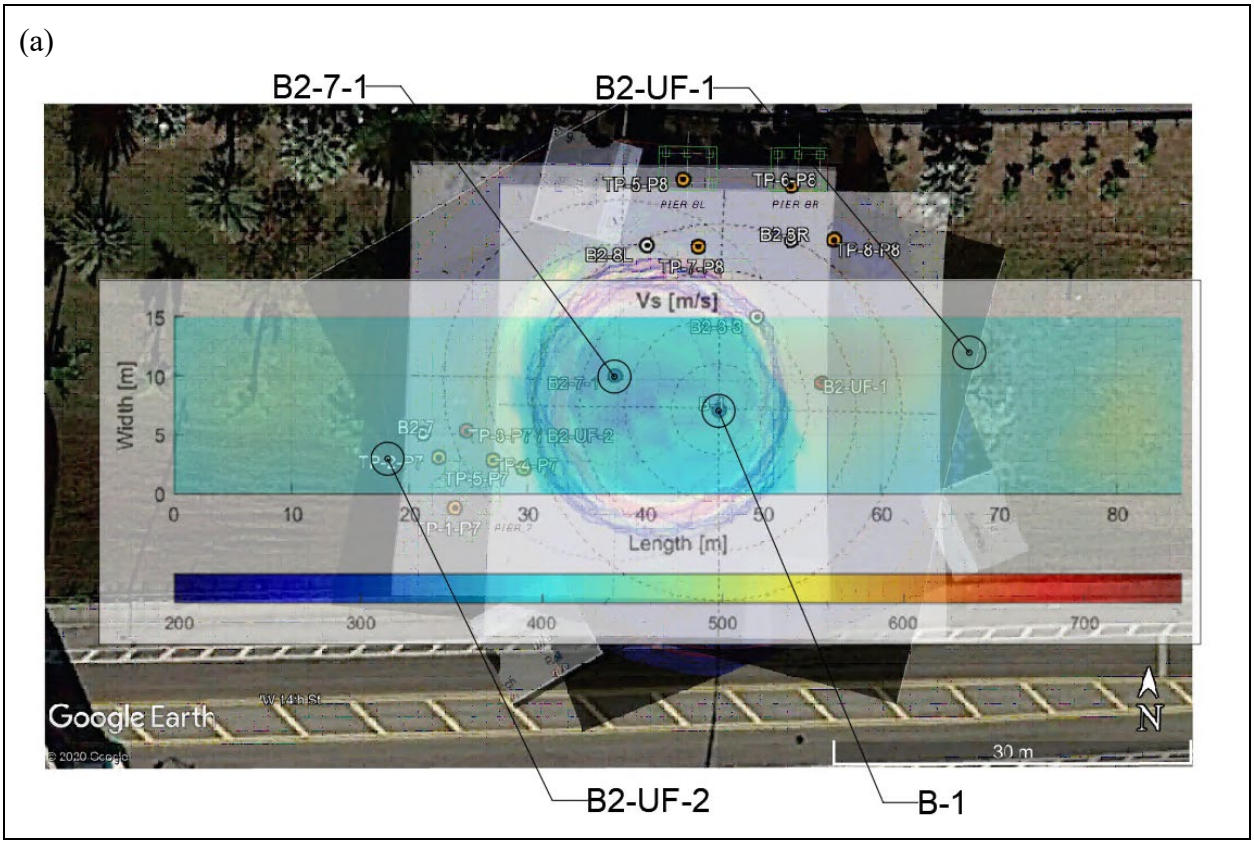

Figure 5.47: Field experiment (SPT seismic): (a) overlay of the final inverted result and void location from sonar analysis. B2-7-1, B-1, B2-UF-1 and B2-UF-2 locations are used to draw SPT comparison plots in Figure 5.48; (b) side view overlay of the inverted and sonar imaging in the north-south direction facing south; (c) side view overlay of the inverted and sonar imaging in the east-west direction facing east.

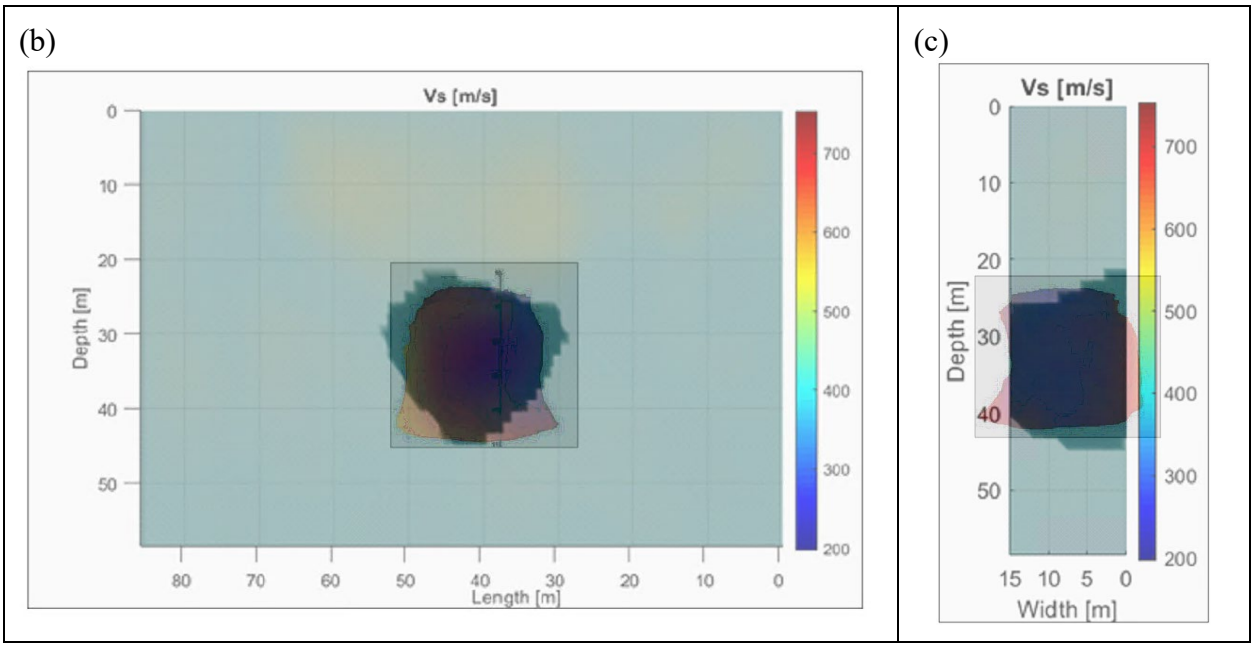

Figure 5.47: Field experiment (SPT seismic): (a) overlay of the final inverted result and void location from sonar analysis. B2-7-1, B-1, B2-UF-1 and B2-UF-2 locations are used to draw SPT comparison plots in Figure 5.48; (b) side view overlay of the inverted and sonar imaging in the north-south direction facing south; (c) side view overlay of the inverted and sonar imaging in the east-west direction facing east.

Shown in Figure 5.48 are the SPT N-value comparison with the Vs velocity of the final inverted result at the four locations shown in Figure 5.47a. It is seen that the position of the void in depth is well matched in B-1 and B2-7-1. The high velocity zone is also verified but at different depths. The match of the high velocity zone and deeper is not as good as that observed in the surface-based testing (Figure 5.32). This is attributed to a number of contributing factors: 1) the volume of material characterized was significant, 76,950 m^3 (100,647 yd^3) which limited the size of each cell (more cells required more computer RAM) and the wavelength of passing waves, and limits the smallest size of zone that can be characterized, Figures 5.48c and 5.48d; 2) larger volumes lead to longer times for slower wave speeds to arrive at the ground surface and the likelihood for ambient noise to occur within traces (i.e. need to continuously monitor and stack SPT blows). There is also the issue of regularization and averaging of adjacent cells used

during the inversion. Reducing the regularization can help the inversion algorithm adapt to sudden variations in the data better, improving the velocity match. However, this comes at the cost of less optimization stability and creation of numerical artifacts in the final inverted results. Consequently, it is recommended that further research is warranted in characterizing geotechnical properties (e.g. SPT N-value) in rock at depths greater than 20 m (66 ft).

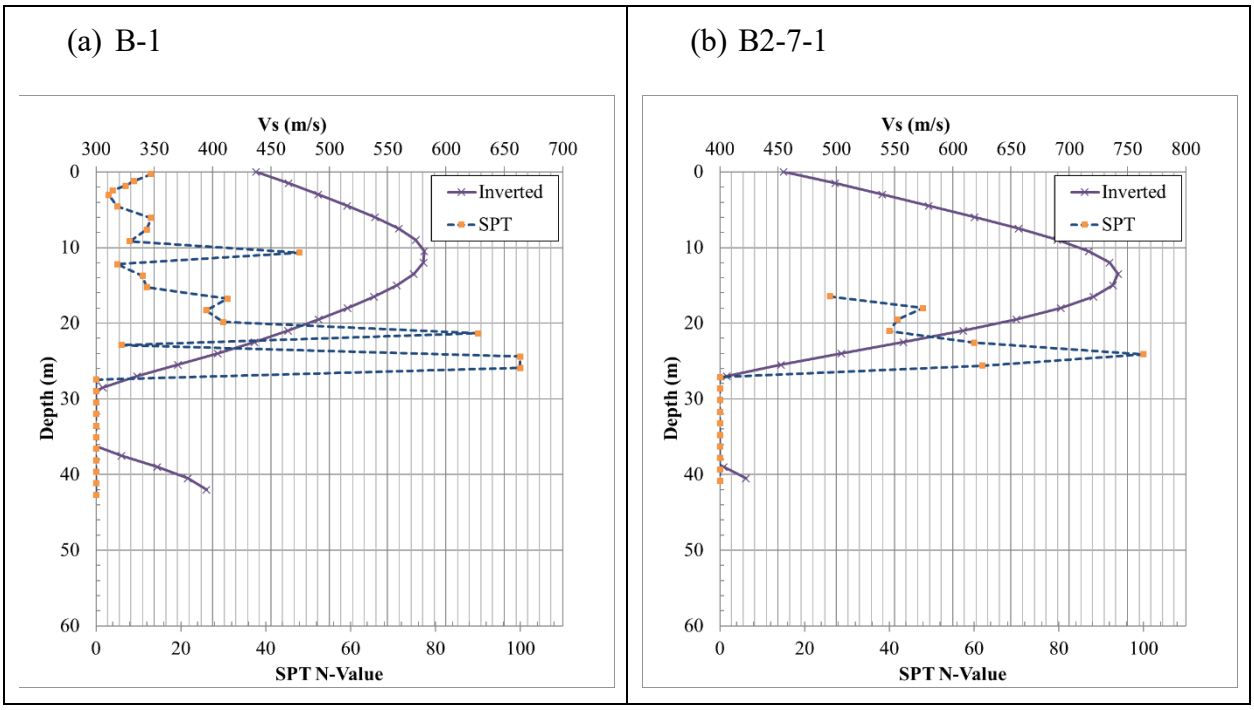

Figure 5.48: Field experiment (SPT seismic): Comparison of the velocity profile and final inverted results at four SPT locations shown in figure 5.47a.

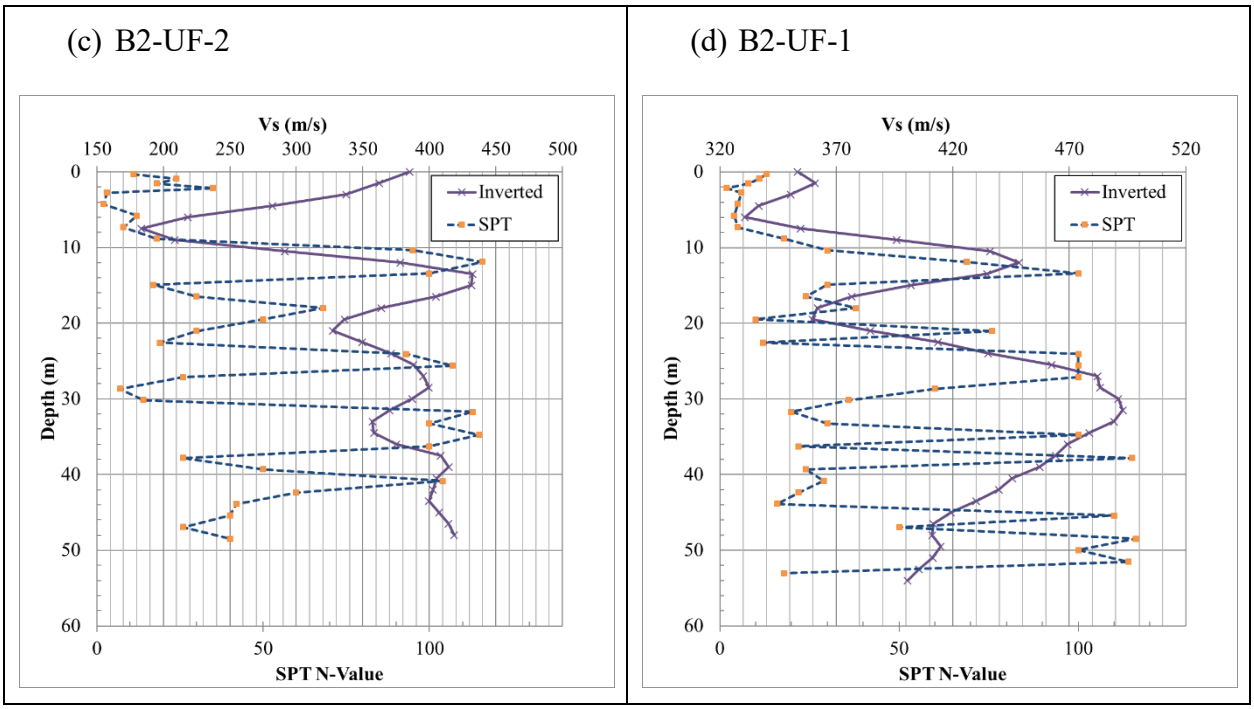

Figure 5.48: Field experiment (SPT seismic): Comparison of the velocity profile and final inverted results at four SPT locations shown in figure 5.47a.

5.8 Conclusion

The focus of the field work was the full-scale field collection of seismic data, subsequent data analysis using 3-D FWI (Chapter 2) and validation of both anomalies and properties (blow count) with invasive logging (SPT) or visual observations (pipe plans). Of interest was recovering shallow and deep subsurface anomalies/voids and characterizing variable soil-rock layers, as well as pinnacles. The method was first tested on the data gathered at a site located in Gainesville, Florida to assess its performance on imaging soil-rock layering and pinnacle formations. It was then tested on the University of Florida main campus, where a stormwater pipe was located directly beneath the testing area. The goal was to see if the FWI method could accurately detect and characterize the known shallow cavity and to verify its existence when used with noisy field data (compared to noise-free synthetic data).

Next, the method was used on field data collected at a retention pond in Newberry, Florida in a blind study, where no previous knowledge of the void and soil-rock layering existed. Subsequently, tests were done at a bridge site in Miami, Florida, where a deep void was identified. A larger surface source (750 lbf drop weight) was used for this test to produce more energy at lower frequencies (5-20 Hz), and to increase wave penetration depth. The goal was to see if the larger source (compared to the PEG) can better characterize the deep void using surface testing only.

It was finally tested with in-depth source field data using a novel SPT seismic approach, where an SPT hammer was used to generate seismic waves at varying depths and the seismic response was recorded on the ground surface. Note, the SPT seismic approach does not require a surface-based source and is performed only using surface-based receivers and the drop of the SPT hammer at varying depths. SPT seismic tests using the drop of the SPT hammer were initially conducted at a site in Newberry, Florida. The goal was to see if the SPT seismic approach could be used to detect a deep void (more than 15 m [49 ft] deep), and to appraise the feasibility of SPT-source seismic method. A surface test with the 40 kg (88 lbf) PEG source was also carried out at this stage using the same geophone location on the ground surface as that used in the SPT seismic test. The goal of this surface source was to use it as a comparison measure with the in-depth SPT source, to see any possible improvements in the resolution of deeper cells. Note, the surface-based source testing is inverted separately without any need for SPT-source seismic data. In other words, each source type (SPT or surface-based) is inverted separately. Finally, very deep SPT source test (>150 ft) was carried out at the Miami bridge site. This test was carried out to identify if the novel SPT-seismic approach could be used on typical Florida

stratigraphy including variable rock strength and if it could detect deep voids outside of the SPT testing line (not intersecting SPT line).

The results of the field experiment at Gainesville site showed that the method could successfully recover soil-rock variable layering and recognize pinnacle formations. Studies on the known pipe showed that the FWI analysis identified the existence, direction, depth and diameter of the pipe. The blind 3-D seismic analysis of the Newberry site revealed that 3-D FWI method had excellent capability in detecting buried voids/low-velocity shallow anomalies and characterizing variable soil-rock layers. Application of the large surface-based drop weight showed that increasing the energy and impact size of the source can improve in-depth resolution, providing better characterization at greater depths compared to the smaller PEG source.

Finally, in-depth source testing using the novel SPT seismic approach showed that the method can be used to generate high resolution images of voids at large depths with limited surface area. Testing of the in-depth SPT source at the Miami bridge site showed the ability of the method to reveal anomalies that lie outside of the SPT testing line. Both tests (Newberry and Miami sites) were verified with their associated SPT N-values. SPT N-values, loss of drilling fluid, and spoon samples all showed good correlation to the seismic survey results for soil, rock, voids and pinnacle placement.

CHAPTER 6

SUMMARY

6.1 General

This research was focused on the development and field testing of a 3-D FWI seismic algorithm, as well as optimization of the testing configuration, and establishing maximum void detection depth. The goal was to tackle some of the challenges faced in the 2-D treatment of the inversion problem. Generally, a 2-D approach requires the receiver and source line to be directly placed above the void. This creates problems in field applications, as the void location is unknown, which requires many receiver-source lines be completed in order to map the underground features. Moreover, out-of-plane scattering of the seismic wave is not well simulated in a 2-D approach. This adds an element of uncertainty in the objective function that can never be properly accounted (e.g. distortion, misalignment, etc.) for in the numerical simulation and hence leads to the formation of artefacts in the final inverted results. Utilizing a 3-D approach provides a solution for these issues, and promises easier field implementation and faster overall analysis runtime. A discussion of each main aspect of this study follows.

6.2 Development of a 3-D full waveform inversion method

A 3-D FWI technique was developed and discussed in detail in Chapter 2. Robust and well-known techniques for numerical wave modelling and optimization were used to ensure high reliability (i.e. likelihood of solution/image) for field applications. Elastic wave equations were solved using a 2^{nd} order accuracy (time and space) finite difference scheme, and a perfectly matched layer (PML) boundary truncation technique was employed in the forward simulation. During the inversion process, waveforms are created using the forward simulation, and are then compared with the recorded field data to get the residual. This residual (also known as objective function) is then minimized through an optimization technique by updating material parameters

(Vs and Vp) cell by cell in the numerical domain. The process of using wave equation and updating the parameter space, allows for the creation of a high resolution visual image of subsurface features. Progressive increasing frequency source data, using virtual source and reciprocity of the wave fields, and parallelization of computations were other aspects of the developed method. The method was tested on a synthetic data set of varying layer interface, and promising results for subsurface characterization were obtained.

6.3 Optimization of testing configuration and verification of void detection depth

Chapters 3 and 4 were dedicated to optimizing testing configuration and establishing maximum void detection depth, respectively. Various receiver-source spacing were tried in Chapter 3, using two void sizes of 4.5 m [15 ft] and 3 m [10 ft] sources and receivers were placed in a staggered pattern on the ground surface to reduce coupling and facilitate field testing. The results suggested that the best resolution is achieved if sources/receivers that are placed at a spacing equal to the void size. Further decreasing the spacing (i.e. less than the void size) was found not to improve the detection resolution, and only increased data redundancy. Similarly, in Chapter 4 a void was placed at various depths using the best testing configuration of Chapter 3 to determine its detection depth. It was revealed that voids deeper than 3 times their diameter are not reliably detected using a surface-based testing method at the frequencies considered. Utilizing alternate testing methods as shown in Chapter 5, for increasing dominancy of low frequencies through source modification can extend void detection depths, and are explained more in the following section.

6.4 Field verification of the developed FWI method and in-depth source testing

Finally, the developed 3-D FWI method was tested on noisy field data to verify its utility in practice. It was expected that the 3-D approach would produce detailed subsurface features using a 2-D array of source/receivers on the ground surface. Furthermore, voids up to 3 times

their size were expected to be detected and accurately defined. In total, 5 field testing case were presented in this study. The first field test was on data gathered at a retention pond in Gainesville, Florida. The site was known from previous studies to contain highly variable soil-rock interface. The inversion method was employed in progressive frequency stages, and the results were verified against invasive SPT data for validation. A good match was observed, indicating the good ability of the 3-D FWI method in characterizing high variable layering features.

The method was then testing on its void detection ability. Initially, a known stormwater pipe located at the University of Florida main campus in Gainesville, was chosen for the study. It was observed that the method could detect the depth and direction of the pipe in a 3-D space and characterize its shape. It was then tested in a blind prediction test on a retention pond in Newberry, Florida. The inversion results indicated the existence of 3 shallow voids. Invasive SPT tests verified the existence of 2 of the voids and showed a very low velocity zone at the location of the 3rd void.

Subsequently, a large weight drop hammer source capable of creating more energy at lower frequencies was tried at a bridge construction site in Miami, Florida. The goal was to see if increasing low frequency dominancy of the propagating wave can help with increasing in-depth resolution. The test site was known to contain a large void (20 m [66 ft] in diameter) located at more than 20 m (66 ft) in depth. The results showed that using the larger source could enable the inversion algorithm to locate the deep void. Comparison of the void features with SPT N-values and sonar analysis was also undertaken at the test site. Generally, there was good agreement between the seismic inverted, SPT and sonar results. For instance, location of the void and velocity zone at and above the void were well recovered and characterized.

Finally, for the cases were surface access to the test site is limited, or when the source has limited capabilities (i.e., low energy at low frequencies), the coupled SPT-seismic was considered. This was achieved by using the SPT hammer as a source (SPT-seismic) and generating body waves from various depths within the ground. Tests were carried out at the Newberry and Miami locations. For the Newberry site, inversion results revealed two deep voids (more than 3 void diameters) that were not identified by surface testing (due to limited surface area and source capability). It was then tested at a bridge construction site in Miami, Florida. In-depth sources were applied outside of the void region. The goal was to see if the SPT-seismic approach could detect voids that lie outside of the SPT testing line. Existence of the void and its overall dimensions were detected and characterized. Inversion results were compared with invasive SPT N-values and sonar images performed at the test site. Overall, a very good match for the location of the void was achieved.

It is believed that the breadth and depth of field tests performed in this study provide a very good reference regarding the capabilities of FWI techniques in general and how they can be applied to various field conditions. Techniques regarding the visualization of the underlying sub-surface image in three-dimensional space and interpretation of the produced images were other areas that were developed, applied and illustrated in this work. Finally, application of the presented 3-D full inversion method can be a good supplement to the traditional invasive testing and has the potential of revealing a large volume of underlying features including layering, zones, voids, and associated variability of soil and rock to appreciable depths.

REFERENCES

Bristow, C. S., & Jol, H. M. (Eds.). (2003). Ground penetrating radar in sediments. Geological Society of London.

Ben-Hadj-Ali, H., Operto, S., & Virieux, J. (2008). Velocity model building by 3D frequency-domain, full-waveform inversion of wide-aperture seismic data3D full-waveform tomography. *Geophysics*, *73*(5), VE101-VE117.

Bretaudeau, F., Brossier, R., Leparoux, D., Abraham, O., & Virieux, J. (2013). 2D elastic full-waveform imaging of the near-surface: application to synthetic and physical modelling data sets. *Near Surface Geophysics*, *11*(3), 307-316.

Butzer, S., Kurzmann, A., & Bohlen, T. (2013). 3D elastic full-waveform inversion of small-scale heterogeneities in transmission geometry. *Geophysical Prospecting*, *61*(Challenges of Seismic Imaging and Inversion Devoted to Goldin), 1238-1251.

Chen, Y. L., & Chow, J. J. (2007). Ground penetrating radar signal processing improves mapping accuracy of underground voids and seawater table: an application in deteriorating coastal structure, Nanfangao Port, Taiwan. *Environmental Geology*, *53*(2), 445-455.

Cardarelli, E., Cercato, M., Cerreto, A., & Di Filippo, G. (2010). Electrical resistivity and seismic refraction tomography to detect buried cavities. *Geophysical Prospecting*, *58*(4), 685-695.

De Vore, S. L. (1998). Ground-penetrating radar: An introduction for archaeologists. *Geoarchaeology: An International Journal*, *13*(5), 527-528.

Daniels, D. J. (2005). Ground Penetrating Radar. Encyclopedia of RF and Microwave Engineering. John Willy & Sons.

DiFrancesco, D., & Talwani, M. (2002, May). Time lapse gravity gradiometry for reservoir monitoring. In *64th EAGE Conference & Exhibition* (pp. cp-5). European Association of Geoscientists & Engineers.

Epanomeritakis, I., Akçelik, V., Ghattas, O., & Bielak, J. (2008). A Newton-CG method for large-scale three-dimensional elastic full-waveform seismic inversion. *Inverse Problems*, *24*(3), 034015.

Fichtner, A., Kennett, B. L., Igel, H., & Bunge, H. P. (2009). Full seismic waveform tomography for upper-mantle structure in the Australasian region using adjoint methods. *Geophysical Journal International*, *179*(3), 1703-1725.

Fathi, A., Poursartip, B., Stokoe II, K. H., & Kallivokas, L. F. (2016). Three-dimensional P-and S-wave velocity profiling of geotechnical sites using full-waveform inversion driven by field data. *Soil Dynamics and Earthquake Engineering*, *87*, 63-81.

Fathi, A., Kallivokas, L. F., & Poursartip, B. (2015). Full-waveform inversion in three-dimensional PML-truncated elastic media. *Computer Methods in Applied Mechanics and Engineering*, *296*, 39-72.

Greenfield, R. J. (1979). Review of geophysical approaches to the detection of karst. *Bulletin of the association of engineering geologists*, *16*(3), 393-408.

Grandjean, G., & Leparoux, D. (2004). The potential of seismic methods for detecting cavities and buried objects: experimentation at a test site. *Journal of Applied Geophysics*, *56*(2), 93-106.

Hawkins Jr, M. F. (1956). A note on the skin effect. *Journal of Petroleum Technology*, *8*(12), 65-66.

Hansen, R. O. (2001). Gravity and magnetic methods at the turn of the millennium. *Geophysics*, *66*(1), 36-37.

Ha, W., Kang, S. G., & Shin, C. (2015). 3D Laplace-domain waveform inversion using a low-frequency time-domain modeling algorithm. *Geophysics*, *80*(1), R1-R13.

Jol, H. M. (Ed.). (2008). *Ground penetrating radar theory and applications*. Elsevier.

Komatitsch, D., & Martin, R. (2007). An unsplit convolutional perfectly matched layer improved at grazing incidence for the seismic wave equation. *Geophysics*, *72*(5), SM155-SM167.

LaFehr, T. R. (1980). Gravity method. *Geophysics*, *45*(11), 1634-1639.

Lai, W. W., Chang, R. K., & Sham, J. F. (2018). A blind test of nondestructive underground void detection by ground penetrating radar (GPR). *Journal of Applied Geophysics*, *149*, 10-17.

McKenna, J. R., Rim, H., & Li, Y. (2015). Feasibility and limitations of void detection using gravity gradiometry. *IEEE Transactions on Geoscience and Remote Sensing*, *54*(2), 881-891.

Métivier, L., Brossier, R., Merigot, Q., Oudet, E., & Virieux, J. (2016). An optimal transport approach for seismic tomography: Application to 3D full waveform inversion. *Inverse Problems*, *32*(11), 115008.

Mirzanejad, M., & Tran, K. T. (2019). 3D viscoelastic full waveform inversion of seismic waves for geotechnical site investigation. *Soil Dynamics and Earthquake Engineering*, *122*, 67-78.

Nguyen, T. D., & Tran, K. T. (2018). Site characterization with 3D elastic full-waveform tomography. *Geophysics*, *83*(5), R389-R400.

Plessix, R. É. (2009). Three-dimensional frequency-domain full-waveform inversion with an iterative solver. *Geophysics*, *74*(6), WCC149-WCC157.

Paterson, N. R., & Reeves, C. V. (1985). Applications of gravity and magnetic surveys; the state-of-the-art in 1985. *Geophysics*, *50*(12), 2558-2594.

Park, C. B., Miller, R. D., & Xia, J. (1999). Multichannel analysis of surface waves. *Geophysics*, *64*(3), 800-808.

Romdhane, A., Grandjean, G., Brossier, R., Réjiba, F., Operto, S., & Virieux, J. (2011). Shallow-structure characterization by 2D elastic full-waveform inversion. *Geophysics*, *76*(3), R81-R93.

Sudha, K., Israil, M., Mittal, S., & Rai, J. (2009). Soil characterization using electrical resistivity tomography and geotechnical investigations. *Journal of Applied Geophysics*, *67*(1), 74-79.

Slob, E., Sato, M., & Olhoeft, G. (2010). Surface and borehole ground-penetrating-radar developments. *Geophysics*, *75*(5), 75A103-75A120.

Shen, X., Ahmed, I., Brenders, A., Dellinger, J., Etgen, J., & Michell, S. (2018). Full-waveform inversion: The next leap forward in subsalt imaging. *The Leading Edge*, *37*(1), 67b1-67b6.

Sheen, D. H., Tuncay, K., Baag, C. E., & Ortoleva, P. J. (2006). Time domain Gauss—Newton seismic waveform inversion in elastic media. *Geophysical Journal International*, *167*(3), 1373-1384.

Tran, K. T., & Hiltunen, D. R. (2011). Inversion of first-arrival time using simulated annealing. *Journal of Environmental & Engineering Geophysics*, *16*(1), 25-35.

Tran, K. T., & Hiltunen, D. R. (2012). Inversion of combined surface and borehole first-arrival time. *Journal of geotechnical and geoenvironmental engineering*, *138*(3), 272-280.

Tran, K. T., McVay, M., Faraone, M., & Horhota, D. (2013). Sinkhole detection using 2D full seismic waveform tomography Sinkhole detection by FWI. *Geophysics*, *78*(5), R175-R183.

Tran, K. T., & McVay, M. (2012). Site characterization using Gauss–Newton inversion of 2-D full seismic waveform in the time domain. *Soil Dynamics and Earthquake Engineering*, *43*, 16-24.

Tran, K. T., Mirzanejad, M., McVay, M., & Horhota, D. (2019). 3-D time-domain Gauss–Newton full waveform inversion for near-surface site characterization. *Geophysical Journal International*, *217*(1), 206-218.

Tran, K. T., & Sperry, J. (2018). Application of 2D full-waveform tomography on land-streamer data for assessment of roadway subsidence. *Geophysics*, *83*(3), EN1-EN11.

Virieux, J. (1986). P-SV wave propagation in heterogeneous media; velocity-stress finite-difference method. *Geophysics*, *51*(4), 889-901.

Virieux, J., & Operto, S. (2009). An overview of full-waveform inversion in exploration geophysics. *Geophysics*, *74*(6), WCC1-WCC26.

Vigh, D., Kapoor, J., Moldoveanu, N., & Li, H. (2011). Breakthrough acquisition and technologies for subsalt imaging. *Geophysics*, *76*(5), WB41-WB51.

Wightman, W., Jalinoos, F., Sirles, P., & Hanna, K. (2003). Applications of geophysical methods to related highway problems. *FHWA Technical manual*.

Warner, M., Ratcliffe, A., Nangoo, T., Morgan, J., Umpleby, A., Shah, N., Vinje, V., Štekl, I., Guasch, L., Win, C, & Conroy, G. (2013). Anisotropic 3D full-waveform inversion. Geophysics, 78(2), R59-R80.